

## Stellingen

behorende bij het proefschrift :

"Wave propagation, localisation and dispersion in softening solids"

van L.J. Sluys

1. De voorspellende waarde van een (dynamische) bezwijkanalyse met een klassiek *strain softening* model is van nul en generlei waarde.
2. Het gebruik van een scheurenergiemodel (of scheurbandbreedtemodel), voorgesteld door Bažant en Oh (1983), kan leiden tot resultaten die onafhankelijk zijn van de fijnheid van het gekozen elementennet. Echter, de resultaten zijn wel afhankelijk van de richting van de lijnen in het elementennet (*mesh alignment*), waardoor het bezwijkmechanisme en dus ook de bezwijkbelasting nog steeds discretisatie afhankelijk zijn.
3. Een adequate continuümformulering voor *strain softening* moet tenminste leiden tot (i) een goed gesteld mathematisch probleem, (ii) de incorporatie van een lengteschaal en (iii) een dispersieve golfvoortplanting in de lokalisatiezone.
4. Het toevoegen van reksnelheidsafhankelijkheid of afhankelijkheid van een tweede-orde rekgradient aan de constitutieve relatie voor een *strain softening* continuüm leidt tot resultaten die invariant zijn met betrekking tot de fijnheid en de oriëntatie van de eindige elementen configuratie.
5. Een micro-polaire (Cosserat) formulering van het *strain softening* continuüm leidt bij verfijning van het elementennet tot convergentie naar een lokalisatiezone met een eindige breedte als afschuiving (*mode-II* lokalisatie) en niet decohesie (*mode-I* lokalisatie) het dominante bezwijkmechanisme is.
6. In analyses waarin golfvoortplanting en lokalisatie worden beschouwd geeft het gebruik van een consistente massamatrix nauwkeurigere resultaten dan een *lumped* massamatrix, onafhankelijk van de toegepaste tijdsintegratiemethode.
7. Waar de lokalisatie van deformatie vaak de inleiding is tot het bezwijken van een constructie is de lokalisatie van populatie vaak de inleiding tot het bezwijken van een beschaving.

8. De parallellen tussen lokalisatietheorieën in de vaste stoffen mechanica en grenslaagtheorieën in de vloeistofmechanica zijn voor de civiel ingenieur moeilijk te bepalen door de ontkoppeling van "droge" en "natte" mechanica in een vroeg stadium van de studie.
9. De oorzaak van het niet overeenstemmen van experiment en numerieke simulatie wordt ten onrechte altijd gezocht bij de laatste.
10. Het uitvoeren van een evaluerende opdracht in de afstudeerfase is niet bevorderlijk voor het creëren, dan wel aanscherpen, van een kritische houding ten opzichte van het eigen werk.
11. Universitair onderzoek moet ten dienste staan aan de hoofdtaak van de universiteit, namelijk het onderwijs. Het onderwijs is meer gebaat bij fundamenteel onderzoek dan bij technologieontwikkeling, terwijl subsidiërende instanties van universitair onderzoek juist de voorkeur geven aan technologieontwikkeling met een hoog utiliteitsgehalte.
12. Het vergroten van de gebruikersvriendelijkheid van eindige elementen methode programmatuur vereist minder kennis van de gebruiker en vergroot de kans op onoordeelkundig gebruik.
13. Het samenkomen in de bekende vakantiecentra en het beperkte vermogen zich aan te passen aan lokale eet-en leefgewoonten toont al enigszins de hypocriete houding van Nederlanders ten opzichte van integratie van allochtonen.
14. Het argument dat het legaliseren van dopinggebruik in de sport de gelijke kansen bevordert is onjuist omdat de kapitaalkrachtige landen de betere atleten kunnen gaan bouwen.

553883

3172801

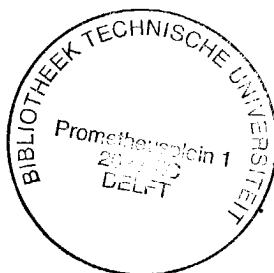
TR diss 2082

*2070*

**TR diss  
2082**

**WAVE PROPAGATION, LOCALISATION AND  
DISPERSION IN SOFTENING SOLIDS**

# WAVE PROPAGATION, LOCALISATION AND DISPERSION IN SOFTENING SOLIDS



## PROEFSCHRIFT

ter verkrijging van de graad van doctor aan de Technische Universiteit  
Delft, op gezag van Rector Magnificus, prof.dr.s. P.A. Schenck,  
in het openbaar te verdedigen ten overstaan van een commissie door het  
College van Dekanen daartoe aangewezen,  
op 23 juni 1992 te 16.00 uur

door

LAMBERTUS JOHANNES SLUYS

geboren te Schoonhoven  
civiel ingenieur

Dit proefschrift is goedgekeurd door de promotor :  
Prof.dr.ir. R. de Borst

CIP-GEGEVENS KONINKLIJKE BIBLIOTHEEK, DEN HAAG

Sluys, Lambertus Johannes

Wave propagation, localisation and dispersion in softening  
solids / Lambertus Johannes Sluys. - [S.l. : s.n.]

Proefschrift Technische Universiteit Delft. - Met lit.

opg. - Met samenvatting in het Nederlands.

ISBN 90-9005139-2

Trefw.: breuken (materiaalkunde).

Printed by : W.D. Meinema B.V. Delft

Cover design : J. Coemans

## ACKNOWLEDGEMENTS

The research reported in this thesis has been carried out at the Civil Engineering Department of Delft University of Technology.

I would like to gratefully acknowledge my supervisor Professor René de Borst for his encouragement and comprehensive guidance during the study.

Furthermore, I wish to record thanks to the colleagues of the Computational Mechanics Group of the Civil Engineering Department for their interest and support during the work, in particular to Albert Allaart, Peter van den Bogert, Peter Feenstra, Jerzy Pamin, Han Schellekens and Harold Thung.

I would also like to direct acknowledgements to Jaap Weerheijm (Prins Maurits Laboratory TNO), Harry Dieterman (Delft University of Technology) and Hans Mühlhaus (CSIRO Division of Geomechanics) for the stimulating and fruitful discussions on the subject.

The models described in this thesis have been implemented in the DIANA finite element program of TNO Building and Construction Research.

The financial support provided by the Prins Maurits Laboratory of TNO is gratefully acknowledged.

## CONTENTS

1. INTRODUCTION . . . . .	1
1.1 Aims and scope of the study . . . . .	1
1.2 Outline of the thesis . . . . .	3
1.3 Notation . . . . .	4
2. FORMULATION OF THE INITIAL VALUE PROBLEM . . . . .	5
2.1 Preliminary equations . . . . .	5
2.2 Weak formulation of the IVP . . . . .	6
2.3 Discretisation of the IVP . . . . .	7
3. STRAIN SOFTENING AND LOCALISATION OF DEFORMATION - PROBLEM STATEMENT . . . . .	15
3.1 Softening and a translation to strain softening . . . . .	15
3.2 Mathematics of strain-softening continuum . . . . .	18
3.3 Analytical solution of a classical strain-softening bar . . . . .	21
3.4 Constitutive equations for strain softening . . . . .	26
3.4.1 Smearred crack model . . . . .	27
3.4.2 Softening plasticity model . . . . .	29
3.5 Numerical analyses . . . . .	32
3.5.1 Example 1 : One-dimensional bar problem in tension . . . . .	32
3.5.2 Example 2 : Impact tensile test on a double-notched specimen . . . . .	35
3.5.3 Example 3 : Impact biaxial test . . . . .	42
3.6 Solution techniques . . . . .	47
Appendix 3A : Shear band inclination in biaxial test . . . . .	50
4. RATE-DEPENDENT CRACK MODEL . . . . .	55
4.1 Formulation of a rate-dependent crack model . . . . .	55
4.2 Wave propagation in a rate-dependent bar . . . . .	57
4.3 Algorithmic aspects . . . . .	61
4.4 Numerical analyses . . . . .	63
4.4.1 Example 1 : One-dimensional bar problem in tension . . . . .	63
4.4.2 Example 2 : Impact tensile test on a double-notched specimen . . . . .	67
4.5 Power law model . . . . .	75
4.5.1 Model formulation . . . . .	75
4.5.2 Algorithmic aspects . . . . .	77

4.5.3 Numerical results . . . . .	78
5. GRADIENT-DEPENDENT MODEL . . . . .	81
5.1 Formulation of a gradient-dependent plasticity model . . . . .	81
5.2 Wave propagation in a one-dimensional gradient-dependent bar . . . . .	82
5.3 Algorithmic aspects . . . . .	86
5.4 Numerical analyses . . . . .	89
5.4.1 Example 1 : One-dimensional bar problem in tension . . . . .	90
5.4.2 Example 3 : Impact biaxial test . . . . .	94
6. VISCOPLASTIC MODELS . . . . .	103
6.1 Constitutive equations for viscoplasticity . . . . .	103
6.1.1 Perzyna viscoplasticity . . . . .	104
6.1.2 Duvaut-Lions viscoplasticity . . . . .	106
6.2 Algorithmic aspects . . . . .	107
6.2.1 Perzyna model . . . . .	107
6.2.2 Duvaut-Lions model . . . . .	110
6.3 Numerical analyses . . . . .	112
6.3.1 Example 1 : One-dimensional bar problem in shear . . . . .	112
6.3.2 Example 3 : Impact biaxial test . . . . .	116
6.4 The big picture : A comparison of rate-dependent models . . . . .	125
7. COSSERAT CONTINUUM MODEL . . . . .	129
7.1 Cosserat theory . . . . .	129
7.2 Additional material parameters . . . . .	134
7.3 Wave propagation in a Cosserat shear layer . . . . .	135
7.4 Numerical analyses . . . . .	140
7.4.1 Shear layer problem . . . . .	140
7.4.2 Example 3 : Impact biaxial test . . . . .	148
Appendix 7A : Analytical eigenmode analysis of shear layer . . . . .	155
8. CONCLUSIONS . . . . .	157
REFERENCES . . . . .	161
SUMMARY . . . . .	167
SAMENVATTING . . . . .	169



# 1. INTRODUCTION

## 1.1 AIMS AND SCOPE OF THE STUDY

Dynamic problems are generally classified depending on the spectral characteristics of the excitation. We deal with wave propagation problems if the high-frequency modes of the loading pulse dominate the response of the structure. In the wave-like solution the behaviour at the wave front and wave reflection are important phenomena. Problems that fall into this category are shock responses from explosive or impact loadings. On the other hand, propagating waves are negligible if a relatively small number of low frequencies govern the response. Examples of these problems, commonly called structural dynamics problems, are seismic responses and responses to machine vibrations. In this thesis we confine the attention to the response in wave propagation problems under impact loadings.

A large number of engineering materials including metals, polymers, soils, concrete and rock are classified as *softening* materials. These materials show a reduction of the load-carrying capacity accompanied by increasing localised deformations after reaching the limit load, i.e. the load-displacement characteristic exhibits a descending branch. For a continuum description of this type of structural behaviour the standard procedure to derive stress-strain relations, which consists of an affine mapping from the measured load-displacement relation onto a stress-strain diagram, i.e. stress and strain are computed as the quotients of the force and the virgin load-carrying cross-section, and of the displacement and the length of the specimen, respectively, then leads to a negative slope of the stress-strain diagram. This is commonly called *strain softening*.

Beyond a critical load level softening causes all further deformation to localise in small bands, which are often a precursor to failure. We can observe two types of localisation. Firstly, if the cohesive properties of the material are more critical than the frictional properties localisation of deformation takes place in fracture zones (mode-I localisation). However, in the opposite case localisation becomes manifest along shear bands (mode-II localisation). Although the mode of failure differs, fracture and shear banding are treated along the same lines in this thesis.

Localisation of deformation is subject to an intense debate. For instance, at a micro level the materials scientists study the internal damage processes that drive the abrupt change of a smooth displacement pattern into a failure mode of highly localised deformations. At the same time at a macro or phenomenological level numerical research is carried out to arrive at a proper modelling of strain softening in a mathematical sense. This study belongs to the latter category and focuses on a correct representation of strain softening to obtain a well-posed nonlinear initial value problem.

The straightforward use of the strain-softening model in a classical continuum generally does not result in a well-posed problem. The field equations that describe the motion of the

body lose hyperbolicity and become elliptic as soon as strain softening occurs. In fact, the domain is split up into an elliptic part, in which the waves have imaginary wave speeds and are not able to propagate (standing waves), and into a hyperbolic part with propagating waves. The initial value problem becomes ill-posed and can no longer be a proper description of the underlying physical problem. Because of the inability of the standing waves to propagate, localisation zones stay confined to a line with zero thickness (or a discrete plane in a three-dimensional continuum). Spurious wave reflections occur on these localisation zones with zero thickness and the energy consumed in the failure zones is zero. These results are in contradiction with experimental data, which for mode-I as well as for mode-II localisation show finite widths of the localisation zone and finite values for the energy consumption and the wave reflection. The finite element solution tries to capture the localisation zone of zero thickness which results in a *mesh sensitivity*. A clear description of the fundamental problems of classical strain-softening models is a first objective of this study.

For proper failure analyses the above observations are unacceptable and we must therefore rephrase our continuum description of the softening solid such that it is able to capture zones of highly localised deformation. The main goal of the present study is to scrutinise approaches which may remedy the deficiencies. For a proper mathematical modelling of the softening solid extra or higher-order derivative terms are necessary in the continuum description. Such enriched, or higher-order continua do not necessarily lose hyperbolicity at the onset of strain softening and admit a solution with real wave speeds. In this thesis we suggest three so-called regularisation techniques to solve mesh sensitivity, namely (i) the addition of viscous, or higher-order time derivatives, (ii) the addition of higher-order deformation gradients, and (iii) the use of a micro-polar (Cosserat) continuum. A proper modelling of the softening solid is obtained if the numerical results converge to a finite size of the localisation zone upon mesh refinement with unique properties with respect to energy consumption and wave reflection. Below a certain discretisation level at which accuracy of the results is obtained a refinement of the mesh as well as a change of orientation of the mesh lines should not affect the numerical outcome.

The use of higher-order continuum models should not be considered as a further sophistication of the strain-softening solid but as a necessity to carry out failure analyses with a localised failure pattern. The models have been defined as simple as possible in order to be able to extend the models to composite softening materials as (fibre-)reinforced concrete. Furthermore, it is noted that the models are in a preliminary stage and tuning of the results to experimental data has not been done extensively. So far, the prime aim was not the exact simulation of the experimentally measured response, rather it was the purpose to model the softening solid properly in a mathematical sense.

## 1.2 OUTLINE OF THE THESIS

Chapter 2 starts with the basic equilibrium, constitutive and kinematic equations for the motion of an inelastic body. By means of the finite element representation of the virtual work equation the semi-discrete nonlinear set of equations will be derived. Finally, the implicit time integration is carried out to arrive at a fully discretised wave propagation problem.

In Chapter 3 the problem is stated and the fundamental notions softening, strain softening and localisation are explained. An analytical and numerical treatment of a strain-softening bar (Example 1) shows the physically meaningless solution for the localisation zone. The non-dispersive behaviour of waves and the absence of an internal length scale are the basic deficiencies of the classical strain-softening model. Consequently, we observe a pathological mesh sensitivity for mode-I localisation (fracture in a tensile test - Example 2) and mode-II localisation (shear banding in a biaxial test - Example 3). Mesh sensitivity is demonstrated for the fineness of the discretisation and for the orientation of the mesh lines (mesh alignment).

In the next chapters the regularisation techniques will be discussed. In Chapter 4 and Chapter 5 we focus on failure by decohesion (mode-I localisation) and in Chapter 5 we focus attention on failure by frictional slip (mode-II localisation) which will also be treated in the Chapters 6 and 7.

In Chapter 4 we discuss a rate-dependent smeared crack model as a first method to regularise the initial value problem. It will be shown that inclusion of a first-order time derivative term in the constitutive equations prevents the field equations from becoming elliptic. Dispersive waves and the presence of an implicit length scale makes it possible for the rate-dependent continuum to capture localisation of deformation in a proper manner. Examples 1 and 2 (mode-I localisation problems) will be used to assess the performance of the model.

In Chapter 5 the enrichment of the continuum with higher-order spatial derivatives of the inelastic state variables is proposed. We use a model in which the second-order gradient of the equivalent plastic strain is incorporated in the yield function. The dispersive character of wave propagation in a gradient-dependent continuum is demonstrated, resulting in an expression for the width of the localisation zone. Numerical results will be presented for mode-I localisation (Example 1) as well as for mode-II localisation (Example 3).

In Chapter 6 the inclusion of rate-effects in plasticity models (viscoplastic models) is considered in order to carry out mode-II localisation analyses. As an extension to Chapter 4, in which the mathematical well-posedness is demonstrated, the viscoplastic theories according to Perzyna and to Duvaut and Lions will be analysed. In the numerical analyses the attention is focused on the sensitivity of the discretisation of the biaxial test (Example 3) with respect to fineness and orientation of the finite elements.

The third method, treated in Chapter 7, is the use of a micro-polar or Cosserat continuum model. The model is based on the idea that a macro-structure consists of micro-elements with a finite length, which implies the introduction of a length scale parameter. The regularising effect comes from the introduction of couple stresses and micro-curvatures, so that extra

rotational degrees-of-freedom are defined. In the numerical analyses shear banding has been analysed for a simple one-dimensional shear layer and for the biaxial test (Example 3).

In Chapter 8 the three methods will be compared and the merits and limitations of each of the proposed approaches will be summarised.

### 1.3 NOTATION

In this study we will use the matrix-vector notation. Only for a few equations in Chapter 7 we make use of the tensor notation to obtain a more compact format. Matrices and vectors can be distinguished by bold-faced characters. A list of symbols is not included separately because some symbols have more than one meaning. To avoid confusion the symbols are defined when they first appear in the text.

## 2. FORMULATION OF THE INITIAL VALUE PROBLEM

In this chapter the equations of motion of the inelastic body will be derived. In the derivation a restriction is made to small displacement gradients. We use the finite element representation of the virtual work equation to derive the semi-discrete initial value problem (IVP). A full discretisation is obtained if the time integration has been carried out. The treatment is applied to the special case of wave propagation in the softening solid.

### 2.1 PRELIMINARY EQUATIONS

In a general three-dimensional continuum the equations of motion of an elementary volume  $V$  without damping can be written as

$$\mathbf{L}^T \boldsymbol{\sigma} + \mathbf{p} = \mathbf{R} \ddot{\mathbf{u}}, \quad (2.1)$$

in which  $\boldsymbol{\sigma}$  is a vector containing the stress components ( $\sigma_{xx}, \sigma_{yy}, \sigma_{zz}, \sigma_{xy}, \sigma_{yz}, \sigma_{zx}$ ), while in the vector  $\mathbf{u}$  the displacement components are assembled ( $u_x, u_y, u_z$ ). A superimposed dot denotes differentiation with respect to time and a superimposed double dot implies that a quantity is differentiated twice, which means that  $\ddot{\mathbf{u}}$  is the acceleration vector. The density matrix  $\mathbf{R}$  is equal to  $\text{diag}[\rho, \rho, \rho]$  with density  $\rho$ . In the vector  $\mathbf{p}$  the body forces are assembled. The kinematic equations

$$\boldsymbol{\varepsilon} = \mathbf{L} \mathbf{u}, \quad (2.2)$$

set the relations between the strain components ( $\varepsilon_{xx}, \varepsilon_{yy}, \varepsilon_{zz}, 2\varepsilon_{xy}, 2\varepsilon_{yz}, 2\varepsilon_{zx}$ ), assembled in the vector  $\boldsymbol{\varepsilon}$  and the displacement components. In eq.(2.1) and (2.2) the differential operator matrix  $\mathbf{L}$  is defined as

$$\mathbf{L} = \begin{bmatrix} \frac{\partial}{\partial x} & 0 & 0 \\ 0 & \frac{\partial}{\partial y} & 0 \\ 0 & 0 & \frac{\partial}{\partial z} \\ \frac{\partial}{\partial y} & \frac{\partial}{\partial x} & 0 \\ 0 & \frac{\partial}{\partial z} & \frac{\partial}{\partial y} \\ \frac{\partial}{\partial z} & 0 & \frac{\partial}{\partial x} \end{bmatrix}, \quad (2.3)$$

and the superscript T is the transpose symbol. The constitutive equations can be given in the

general rate format

$$\dot{\boldsymbol{\sigma}} = \mathbf{D}_c \dot{\boldsymbol{\epsilon}}, \quad (2.4)$$

with matrix  $\mathbf{D}_c$  containing the tangent stiffness moduli. In the nonlinear calculations treated in this thesis, we apply a decomposition of the total strain rate  $\dot{\boldsymbol{\epsilon}}$  into the elastic strain rate  $\dot{\boldsymbol{\epsilon}}_e$  and the inelastic strain rate  $\dot{\boldsymbol{\epsilon}}_i$  according to

$$\dot{\boldsymbol{\epsilon}} = \dot{\boldsymbol{\epsilon}}_e + \dot{\boldsymbol{\epsilon}}_i. \quad (2.5)$$

The stress rate must satisfy

$$\dot{\boldsymbol{\sigma}} = \mathbf{D}_e \dot{\boldsymbol{\epsilon}}_e, \quad (2.6)$$

with matrix  $\mathbf{D}_e$  containing the elastic stiffness moduli according to

$$\mathbf{D}_e = \begin{bmatrix} 2\mu a_1 & 2\mu a_2 & 2\mu a_2 & 0 & 0 & 0 \\ 2\mu a_2 & 2\mu a_1 & 2\mu a_2 & 0 & 0 & 0 \\ 2\mu a_2 & 2\mu a_2 & 2\mu a_1 & 0 & 0 & 0 \\ 0 & 0 & 0 & 2\mu & 0 & 0 \\ 0 & 0 & 0 & 0 & 2\mu & 0 \\ 0 & 0 & 0 & 0 & 0 & 2\mu \end{bmatrix}, \quad (2.7)$$

with  $a_1 = (1-\nu)/(1-2\nu)$ ,  $a_2 = \nu/(1-2\nu)$  and shear modulus  $\mu = E/(2(1+\nu))$ , in which  $\nu$  Poisson's ratio and  $E$  Young's modulus. Substitution of eq.(2.5) into (2.6) leads to

$$\dot{\boldsymbol{\sigma}} = \mathbf{D}_e (\dot{\boldsymbol{\epsilon}} - \dot{\boldsymbol{\epsilon}}_i), \quad (2.8)$$

which can be used for the derivation of the tangent stiffness matrix. If the inelastic strain rate  $\dot{\boldsymbol{\epsilon}}_i$  can be written in an explicit format substitution into eq.(2.8) yields the matrix  $\mathbf{D}_c$ . At the boundary  $S$  of the body it is required that either

$$\mathbf{t} - \boldsymbol{\sigma} \bar{\mathbf{n}} = \mathbf{0}, \quad (2.9)$$

with  $\mathbf{t}$  the boundary traction and  $\bar{\mathbf{n}}$  the outward normal to the surface of the body, or

$$\mathbf{u}_{\bar{\mathbf{n}}} = \mathbf{u}_s, \quad (2.10)$$

with  $\mathbf{u}_{\bar{\mathbf{n}}}$  the displacements at the boundary and  $\mathbf{u}_s$  the prescribed displacements.

## 2.2 WEAK FORMULATION OF THE IVP

While eq.(2.1) describes the motion of the body in a strong sense, a weak form of these equations is obtained by setting

$$\int_V \delta \mathbf{u}^T [\mathbf{L}^T \boldsymbol{\sigma} - \mathbf{R} \ddot{\mathbf{u}} + \mathbf{p}] dV = 0, \quad (2.11)$$

in which  $\delta$  denoting the variation of a quantity. With aid of Green's theorem

$$\int_V \delta \mathbf{u}^T [\mathbf{L}^T \boldsymbol{\sigma}] dV = - \int_V \delta \boldsymbol{\varepsilon}^T \boldsymbol{\sigma} dV + \int_S \delta \mathbf{u}^T [\boldsymbol{\sigma} \bar{\mathbf{n}}] dS, \quad (2.12)$$

eq.(2.11) can be transformed into

$$\int_V \delta \mathbf{u}^T [\mathbf{R} \ddot{\mathbf{u}}] dV + \int_V \delta \boldsymbol{\varepsilon}^T \boldsymbol{\sigma} dV = \int_V \delta \mathbf{u}^T \mathbf{p} dV + \int_S \delta \mathbf{u}^T \mathbf{t} dS, \quad (2.13)$$

in which eq.(2.9) has been substituted. Note that in the derivation of eq.(2.13) no assumptions have been made with regard to the material behaviour.

If eq.(2.13) is considered to be valid at time  $t + \Delta t$  the evolution of the stress follows from

$$\boldsymbol{\sigma}^{t+\Delta t} = \boldsymbol{\sigma}^t + \int_t^{t+\Delta t} \dot{\boldsymbol{\sigma}} d\tau. \quad (2.14)$$

If the constitutive relation (2.4) is substituted in eq.(2.14) we can rewrite the virtual work equation (2.13) into

$$\int_V \delta \mathbf{u}^T [\mathbf{R} \ddot{\mathbf{u}}^{t+\Delta t}] dV + \int_V \delta \boldsymbol{\varepsilon}^T \int_t^{t+\Delta t} \mathbf{D}_c \dot{\boldsymbol{\varepsilon}} d\tau dV = \int_V \delta \mathbf{u}^T \mathbf{p}^{t+\Delta t} dV + \int_S \delta \mathbf{u}^T \mathbf{t}^{t+\Delta t} dS - \int_V \delta \boldsymbol{\varepsilon}^T \boldsymbol{\sigma}^t dV. \quad (2.15)$$

### 2.3 DISCRETISATION OF THE IVP

We shall consider the finite element representation of the virtual work equation (2.15) for the dynamic motion of the inelastic body. First, we will discuss the spatial discretisation of the problem and then the time integration is treated. The body can be divided into a finite number of elements. For each element the continuous displacement field  $\mathbf{u}$  can be interpolated by

$$\mathbf{u} = \mathbf{H} \mathbf{a}, \quad (2.16)$$

and the continuous acceleration field by

$$\ddot{\mathbf{u}} = \mathbf{H} \ddot{\mathbf{a}}, \quad (2.17)$$

in which the matrix  $\mathbf{H}$  contains the interpolation polynomials and  $\mathbf{a}$  and  $\ddot{\mathbf{a}}$  the nodal displacements and nodal accelerations, respectively. Combining eqs.(2.2) and (2.16) and introducing the strain-nodal displacement matrix

$$\mathbf{B} = \mathbf{LH}, \quad (2.18)$$

the relation between the strains and the nodal displacements is obtained as

$$\boldsymbol{\varepsilon} = \mathbf{B}\mathbf{a} , \quad (2.19)$$

or in rate format as

$$\dot{\boldsymbol{\varepsilon}} = \mathbf{B}\dot{\mathbf{a}} . \quad (2.20)$$

We can now substitute eqs.(2.16), (2.17), (2.19) and (2.20) into the virtual work expression (2.15), which yields

$$\begin{aligned} \delta\mathbf{a}^T \int_V \mathbf{H}^T \mathbf{R} \mathbf{H} \ddot{\mathbf{a}}^{t+\Delta t} dV + \delta\mathbf{a}^T \int_V \int_t^{t+\Delta t} \mathbf{B}^T \mathbf{D}_c \mathbf{B} \dot{\mathbf{a}} d\tau dV = \\ \delta\mathbf{a}^T \int_V \mathbf{H}^T \mathbf{p}^{t+\Delta t} dV + \delta\mathbf{a}^T \int_S \mathbf{H}^T \mathbf{t}^{t+\Delta t} dS - \delta\mathbf{a}^T \int_V \mathbf{B}^T \boldsymbol{\sigma}^t dV . \end{aligned} \quad (2.21)$$

Here, we consider eq.(2.21) on a structural level and the solution method for the nonlinear set of algebraic equations determines the time integral. In this study we use the incremental iterative Newton-Raphson solution method and an Euler forward method is used for the determination of  $\int_V \mathbf{B}^T \mathbf{D}_c \mathbf{B} \dot{\mathbf{a}} d\tau$ . In the zero-th iteration we start from the stress-strain matrix at time  $t$ , i.e.  $\mathbf{D}_c^t$ . Furthermore, we define the incremental nodal displacement vector as

$$\Delta\mathbf{a} = \mathbf{a}^{t+\Delta t} - \mathbf{a}^t = \int_t^{t+\Delta t} \dot{\mathbf{a}} d\tau . \quad (2.22)$$

Since we assume that identity (2.21) must hold for any admissible  $\delta\mathbf{a}$  we obtain for the zero-th iteration at time  $t+\Delta t$

$$\int_V \mathbf{H}^T \mathbf{R} \mathbf{H} \dot{\mathbf{a}}^{t+\Delta t} dV + \int_V \mathbf{B}^T \mathbf{D}_c^t \mathbf{B} \Delta\mathbf{a} dV = \int_V \mathbf{H}^T \mathbf{p}^{t+\Delta t} dV + \int_S \mathbf{H}^T \mathbf{t}^{t+\Delta t} dS - \int_V \mathbf{B}^T \boldsymbol{\sigma}^t dV . \quad (2.23)$$

If we introduce the notations

$$\mathbf{M} = \int_V \mathbf{H}^T \mathbf{R} \mathbf{H} dV \quad (2.24)$$

for the mass matrix,

$$\mathbf{K}^t = \int_V \mathbf{B}^T \mathbf{D}_c^t \mathbf{B} dV \quad (2.25)$$

for the stiffness matrix,

$$\mathbf{f}^{t+\Delta t} = \int_V \mathbf{H}^T \mathbf{p}^{t+\Delta t} dV + \int_S \mathbf{H}^T \mathbf{t}^{t+\Delta t} dS \quad (2.26)$$

for the external load vector and



$$\mathbf{f}_{int}^t = \int_V \mathbf{B}^T \boldsymbol{\sigma}^t dV \quad (2.27)$$

for the internal force vector, we can rewrite eq.(2.23) into

$$\mathbf{M} \ddot{\mathbf{a}}^{t+\Delta t} + \mathbf{K}^t \Delta \mathbf{a} = \mathbf{f}^{t+\Delta t} - \mathbf{f}_{int}^t. \quad (2.28)$$

Eq.(2.28) represents the semi-discrete nonlinear equation of motion governing the response of a system of finite elements. After the spatial integration of the virtual work equation we apply the direct time integration method to obtain a full discrete equation of motion.

In the above derivation we have tacitly assumed that the equation of motion is satisfied at time  $t + \Delta t$  which corresponds to an implicit time integration of the field equations. If we would consider the equation of motion at time  $t$  we speak of an explicit time integration scheme. An explicit time integration scheme can have major advantages in reducing the computational effort per time step. The explicit scheme does not require factorisation of the stiffness matrix and storage of the system matrices is not necessary if a lumped mass matrix is used. Two shortcomings of the use of an explicit time integration scheme are the time step restriction and the absence of knowledge whether the exact path of dynamic "equilibrium" has been traced. The first problem concerns the stability of the solution. For linear problems a critical time step can be calculated, which is dependent on the smallest period in a system (Bathe 1982, Hughes 1987). For time steps larger than this critical value the initial conditions are amplified artificially in the course of time which makes the calculation meaningless. For nonlinear problems with softening a critical time step cannot be obtained and it is not even clear whether a stable time step exists for explicit time integration. More important is the second issue concerning the accuracy of the solution. Strong nonlinearities during a time step are not taken into account for the determination of the state variables at time  $t + \Delta t$ . Therefore, small solution errors arise which are not corrected but, on the contrary, can accumulate in significant solution errors. In this study the implicit time integration method is applied for two reasons. Firstly, we can obtain an unconditionally stable scheme and we avoid time step restrictions (only if the time integration of the nonlinear constitutive equations is also done implicitly). Secondly, iterations within a time step can be used to assure dynamic "equilibrium" and improve the solution accuracy.

One of the popular classes of implicit time integrators is the Newmark family. The main assumption is that the acceleration varies linearly over the time step. Therefore we use the formulae

$$\dot{\mathbf{a}}^{t+\Delta t} = \dot{\mathbf{a}}^t + [(1-\gamma)\ddot{\mathbf{a}}^t + \gamma\ddot{\mathbf{a}}^{t+\Delta t}] \Delta t \quad (2.29)$$

and

$$\mathbf{a}^{t+\Delta t} = \mathbf{a}^t + \dot{\mathbf{a}}^t \Delta t + [(1/2 - \beta)\ddot{\mathbf{a}}^t + \beta\ddot{\mathbf{a}}^{t+\Delta t}] \Delta t^2. \quad (2.30)$$

Eqs.(2.29) and (2.30) with the semi-discrete equation of motion (2.28) result in a system of

equations with the unknown variables  $\mathbf{a}$ ,  $\dot{\mathbf{a}}$  and  $\ddot{\mathbf{a}}$  at time  $t + \Delta t$ , so that the problem is determined if the boundary and initial conditions are known. The parameters  $\beta$  and  $\gamma$  determine the stability and accuracy of the method. We can rewrite eq.(2.30) into

$$\ddot{\mathbf{a}}^{t+\Delta t} = c_0 \Delta \mathbf{a} - c_1 \dot{\mathbf{a}}^t - c_2 \ddot{\mathbf{a}}^t, \quad (2.31)$$

where the coefficients are given by

$$c_0 = \frac{1}{\beta \Delta t^2}, \quad c_1 = \frac{1}{\beta \Delta t}, \quad c_2 = \frac{1}{2\beta} - 1, \quad (2.32)$$

and substitute the result into eq.(2.28) which yields

$$\hat{\mathbf{K}} \Delta \mathbf{a} = \hat{\mathbf{f}}, \quad (2.33)$$

where

$$\hat{\mathbf{K}} = \mathbf{K}^t + c_0 \mathbf{M} \quad (2.34)$$

$$\hat{\mathbf{f}} = \mathbf{f}^{t+\Delta t} + \mathbf{M}(c_1 \dot{\mathbf{a}}^t + c_2 \ddot{\mathbf{a}}^t) - \mathbf{f}_{int}^t. \quad (2.35)$$

The matrix  $\hat{\mathbf{K}}$  and vector  $\hat{\mathbf{f}}$  are called the dynamic tangent matrix and the effective load vector, respectively. As mentioned above we make use of Newton's method to solve the non-linear set of algebraic equations in order to obtain dynamic "equilibrium". If we substitute  $^{(i)}\boldsymbol{\sigma}^{t+\Delta t} = ^{(i-1)}\boldsymbol{\sigma}^{t+\Delta t} + ^{(i)}\Delta\Delta\boldsymbol{\sigma}$  into eq.(2.13), with  $\Delta\Delta\boldsymbol{\sigma}$  as a delta-incremental stress field, and proceed in a similar manner the semi-discrete equation of motion for the  $i$ -th iteration becomes

$$\mathbf{M}^{(i)} \ddot{\mathbf{a}}^{t+\Delta t} + ^{(i-1)}\mathbf{K}^{t+\Delta t} ^{(i)}\Delta\Delta\mathbf{a} = \mathbf{f}^{t+\Delta t} - ^{(i-1)}\mathbf{f}_{int}^{t+\Delta t}. \quad (2.36)$$

in which  $\mathbf{M}$  and  $\mathbf{f}^{t+\Delta t}$  are as defined above. The delta-incremental displacement field  $\Delta\Delta\mathbf{a}$  is defined as

$$^{(i)}\Delta\Delta\mathbf{a} = ^{(i)}\mathbf{a}^{t+\Delta t} - ^{(i-1)}\mathbf{a}^{t+\Delta t}, \quad (2.37)$$

which implies that

$$^{(i)}\mathbf{a}^{t+\Delta t} = \mathbf{a}^t + ^{(i-1)}\Delta\mathbf{a} + ^{(i)}\Delta\Delta\mathbf{a}. \quad (2.38)$$

By means of eq.(2.38) we can rewrite eq.(2.31) now into

$$^{(i)}\ddot{\mathbf{a}}^{t+\Delta t} = c_0 ^{(i)}\Delta\Delta\mathbf{a} + c_0 ^{(i-1)}\Delta\mathbf{a} - c_1 \dot{\mathbf{a}}^t - c_2 \ddot{\mathbf{a}}^t, \quad (2.39)$$

which is equivalent to

$$^{(i)}\ddot{\mathbf{a}}^{t+\Delta t} = c_0 ^{(i)}\Delta\Delta\mathbf{a} + ^{(i-1)}\ddot{\mathbf{a}}^{t+\Delta t}. \quad (2.40)$$

Finally, the discretised equation of motion for iteration  $i$  is obtained by substitution of eq.(2.40) into eq.(2.36) which yields

Box 2.1 : Summary of algorithm for Newmark time integration scheme.

1. Calculate constants :

$$c_0 = 1/(\beta\Delta t^2), \quad c_1 = 1/(\beta\Delta t), \quad c_2 = 1/(2\beta) - 1, \quad c_3 = (1 - \gamma)\Delta t, \quad c_4 = \gamma\Delta t$$

2. Initialise :  $\mathbf{a}^0, \dot{\mathbf{a}}^0, \ddot{\mathbf{a}}^0$

3. Compute :  $\hat{\mathbf{K}} = \mathbf{K}^t + c_0\mathbf{M}$

$$\hat{\mathbf{f}} = \mathbf{f}^{t+\Delta t} + \mathbf{M}(c_1\dot{\mathbf{a}}^t + c_2\ddot{\mathbf{a}}^t) - \mathbf{f}_{int}^t$$

4. Solve for incremental displacements :

$$\hat{\mathbf{K}}\Delta\mathbf{a} = \hat{\mathbf{f}}$$

5.  $i = 1, {}^{(0)}\Delta\mathbf{a} = \Delta\mathbf{a}$

6. Compute :  ${}^{(i-1)}\ddot{\mathbf{a}}^{t+\Delta t} = c_0 {}^{(i-1)}\Delta\mathbf{a} - c_1\dot{\mathbf{a}}^t - c_2\ddot{\mathbf{a}}^t$

$$\hat{\mathbf{K}} = {}^{(i-1)}\mathbf{K}^{t+\Delta t} + c_0\mathbf{M}$$

$$\hat{\mathbf{f}} = \mathbf{f}^{t+\Delta t} - \mathbf{M}{}^{(i-1)}\ddot{\mathbf{a}}^{t+\Delta t} - {}^{(i-1)}\mathbf{f}_{int}^{t+\Delta t}$$

7. Solve for delta-incremental displacements :

$$\hat{\mathbf{K}} {}^{(i)}\Delta\Delta\mathbf{a} = \hat{\mathbf{f}}$$

8. Compute :  ${}^{(i)}\Delta\mathbf{a} = {}^{(i-1)}\Delta\mathbf{a} + {}^{(i)}\Delta\Delta\mathbf{a}$

9. Check convergence criterion. If not converged :

$$i = i + 1, \text{ go to 6.}$$

10. Calculate new accelerations, velocities and displacements :

$$\ddot{\mathbf{a}}^{t+\Delta t} = c_0\Delta\mathbf{a} - c_1\dot{\mathbf{a}}^t - c_2\ddot{\mathbf{a}}^t$$

$$\dot{\mathbf{a}}^{t+\Delta t} = \dot{\mathbf{a}}^t + c_3\ddot{\mathbf{a}}^t + c_4\ddot{\mathbf{a}}^{t+\Delta t}$$

$$\mathbf{a}^{t+\Delta t} = \mathbf{a}^t + \Delta\mathbf{a}$$

11. Next step, go to 3.

$$\hat{\mathbf{K}} {}^{(i)}\Delta\Delta\mathbf{a} = \hat{\mathbf{f}},$$

(2.41)

where

$$\hat{\mathbf{K}} = {}^{(i-1)}\mathbf{K}^{t+\Delta t} + c_0\mathbf{M} \quad (2.42)$$

$$\hat{\mathbf{f}} = \mathbf{f}^{t+\Delta t} + \mathbf{M} {}^{(i-1)}\hat{\mathbf{a}}^{t+\Delta t} - {}^{(i-1)}\mathbf{f}_{int}^{t+\Delta t} . \quad (2.43)$$

This scheme corresponds to a full Newton-Raphson scheme, while a modified Newton iteration is obtained if  $\mathbf{K}^t$  is not updated during iteration. In Box 2.1 the algorithm for implicit integration of the semi-discrete equation of motion is outlined.

The Newmark method can be made unconditionally stable (Bathe 1982, Hughes 1987) if

$$\gamma \geq 1/2 \quad \text{and} \quad \beta \geq 1/4(\gamma + 1/2)^2 . \quad (2.44)$$

A most prominent member of the Newmark family that satisfies the abovementioned requirement is the constant or average acceleration method, which is obtained by setting  $\beta = 1/4$  and  $\gamma = 1/2$  (trapezoidal rule). This method will be used for the wave propagation analyses in this thesis. Other well-known members of the Newmark family are the linear acceleration method ( $\beta = 1/6$  and  $\gamma = 1/2$ ) and the Fox-Goodwin method ( $\beta = 1/12$  and  $\gamma = 1/2$ ), which are both conditionally stable. It may occur that higher-order frequencies are introduced by the semi-discretisation of the equation of motion, which are not present in the governing partial differential equations. Sometimes it may be necessary to have a form of algorithmic damping in the time integration scheme to exclude these artificial higher-order frequencies. By taking  $\gamma \geq 1/2$  (Hughes 1987) it is possible to filter out this spurious high-frequent response. However, by introducing numerical damping in the Newmark scheme the accuracy deteriorates.

For an unconditionally stable scheme there is no restriction to the size of the time step for reasons of stability. However, stability of the time integration does not ensure sufficient accuracy of the solution. To obtain an accurate solution  $\Delta t$  should be selected corresponding to the smallest period (highest frequency) in the loading pulse. Such a criterion is used for modal analyses but can hardly be used for a direct time integration analysis of a wave propagation problem, in which a large number of frequencies are excited. Instead, the time step can be adjusted to the size of the finite elements. If the size of the elements is chosen corresponding to the wave lengths present in the loading pulse a critical time step can be derived. For instance, for a linear two-noded line element under uniaxial tension or compression it can be derived (Hughes 1987) for the critical time step size that

$$\Delta t \leq \frac{l_m}{c_e} , \quad (2.45)$$

in which  $l_m$  is the element length and  $c_e = \sqrt{E/\rho}$  is the longitudinal wave velocity in the element. In fact, this is the time required to traverse one element. Hughes (1987) derived for some elements the critical time step size, depending on the size of the element, the mass distribution (lumped, consistent), and the interpolation polynomials. Finally, it is noted that, for linear systems, the solution becomes less accurate also when the time step is taken smaller than the critical time step, because we converge to the exact solution of the spatially discretised system (eq.(2.28)) instead of to the exact solution (Hughes 1987). So, for linear

calculations the most accurate solution is obtained if the time step is chosen equal to the critical time step, although in nonlinear calculations this critical value can be overruled by stronger requirements on the time step because of the dependence on the integration of the nonlinear constitutive equations.

With respect to the mass distribution in an element we consider a lumped and a consistent mass matrix, although higher-order mass matrices can also be used. Lumped and consistent matrices both represent approximations of the exact solution. By taking a consistent mass matrix a higher frequency with a smaller period is calculated in comparison with the exact solution. It turns out that the use of a consistent mass matrix yields an upper bound value for the frequency. A lumped mass matrix tends to behave in the opposite direction (Hughes 1987). Moreover, the time integration method also creates errors with respect to the exact solution. If we use an implicit (explicit) scheme we obtain a lower (upper) bound value for the frequency. This means that if we combine the implicit (explicit) time integrator with a consistent (lumped) mass matrix errors in the solution will be neutralised partially. This holds true for linear as well as for nonlinear analyses. To examine this we have used a lumped and a consistent mass matrix in a nonlinear problem solved with the Newmark time integrator ( $\beta = 1/4$ ,  $\gamma = 1/2$ ). We consider a shear layer, treated in section 7.4.1 (Figure 7.7), which is loaded at both sides of the layer. If the two shear waves meet in the middle of the layer, the elasticity limit is exceeded and a zone of highly localised deformations emerges. The development of the shear band, which is represented by a cosine-shaped shear strain profile, is simulated more accurately for the consistent mass matrix (Figure 2.1 - left) than for the lumped mass matrix (Figure 2.1 - right).

Finally, some promising numerical techniques are discussed which can be advantageous if they are used in analyses involving wave propagation and localisation, in which a large part of the structure behaves linearly elastic and only a small zone is responsible for the inelastic deformations. In many cases the small localisation zone puts a very severe restriction to the time step, which is not necessary for the rest of the structure. A technique to overcome this problem is subcycling, in which a part of the mesh is integrated with a smaller time step (Belytschko et al. 1984). Such an algorithm avoids the update of the entire mesh with a time step determined by the local nonlinearities. A second development is the use of implicit-explicit integration methods (Hughes 1983), which can be done for assemblies with a relatively stiff part (implicit integrator) and a relatively soft part (explicit integrator). In localisation calculations including softening the method can work in an opposite way. For the nonlinear soft part we require unconditionally stability (implicit integrator), which is not necessary for the remaining linear elastic hard part (explicit integrator). A third numerical tool is the use of a variable time step (Thomas and Gladwell 1988). When a structure is still linearly elastic larger time steps can be used than in the failure phase. Therefore, a time step control algorithm should be used which has similarities with the arc-length control method in static analyses (Riks 1979). Finally, advanced implicit time integration schemes have been developed, for instance the Hilber-Hughes-Taylor  $\alpha$ -method and the  $\Theta_1$ -method (Hoff, Hughes, Hulbert and

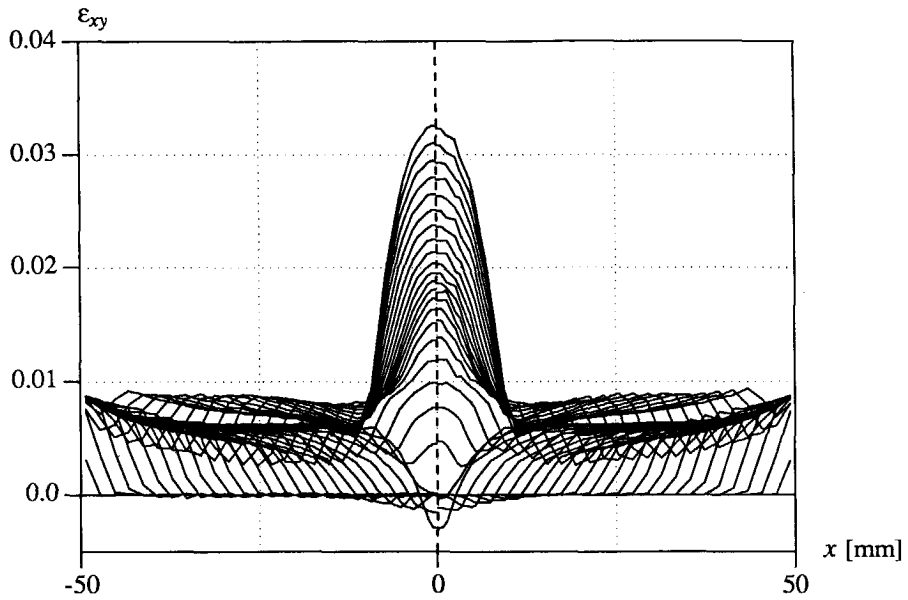


Figure 2.1 Stroboscopic development of a localisation band with consistent mass matrix (left) and lumped mass matrix (right).

Pahl 1989), which may result in more accurate nonlinear dynamic analyses.

### 3. STRAIN SOFTENING AND LOCALISATION OF DEFORMATION - PROBLEM STATEMENT

In this chapter the essential problems of the incorporation of strain softening in conventional continuum models will be discussed. For boundary value problems the numerical simulation of failure, initiated by strain softening, exhibits an excessive mesh dependence, which has been discussed by a number of authors including Bažant (1976), Crisfield (1982) and de Borst (1986). Here, it will be shown that this deficiency not only appears under static loading conditions but also under dynamic loading conditions. The character of the solution for wave propagation in softening solids will be investigated in a mathematical, mechanical and numerical sense.

The chapter is organised as follows. First, the translation of the discontinuous softening behaviour observed in experiments to a continuous strain-softening model will be discussed. Attention is paid to the necessity to model the contribution due to the softening effect and to the question whether softening originates from material or structural behaviour. Next, the mathematical consequences of the inclusion of strain softening are treated. In contrast to the boundary value problem, that loses ellipticity, the initial value problem loses hyperbolicity when the descending softening branch in the stress-strain diagram is entered. As a consequence of strain softening wave speeds become imaginary which leads to a physically non realistic solution for a wave propagation problem. This will be demonstrated by means of an analytical solution of a one-dimensional strain-softening bar. The absence of an internal length scale, for the setting of the width of the localisation zone, and the non-dispersive behaviour of waves are the basic deficiencies of classical strain-softening models. The observed pathological mesh dependence is a consequence thereof. Strain-softening models will be treated for mode-I and mode-II localisation processes : crack models for brittle mode-I dominated processes under tension and plasticity models for ductile (metals) or brittle (concrete, rock) mode-II dominated processes under compressive principal stresses. The strain-softening models are used for three wave propagation problems : the simple one-dimensional bar in pure tension (Example 1), the impact tensile test on a double-notched specimen (Example 2) and the impact biaxial test (Example 3).

#### 3.1 SOFTENING AND A TRANSLATION TO STRAIN SOFTENING

Tensile tests on concrete show that the specimen does not collapse abruptly when the maximum stress is reached but show a gradual decline of stress at increasing deformation. This phenomenon is called softening and can be observed under deformation controlled loading (see Figure 3.1). First the load increases approximately linearly with the displacement up to about 60 % of the maximum attainable load. Then cracks arise at the interface between aggregate and mortar (bond cracks) and the displacement starts to increase more than proportionally

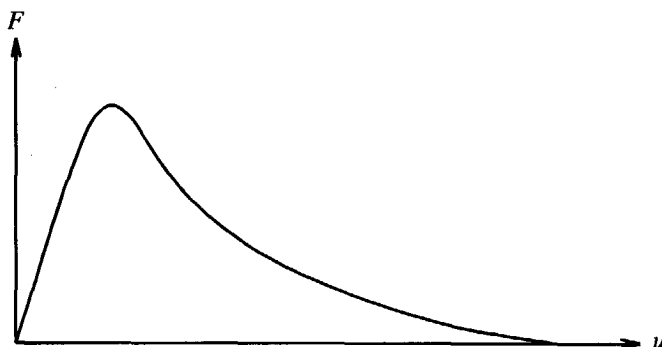


Figure 3.1 Characteristic load-displacement curve for a softening material.

with respect to the load. At a higher load level also cracks in the mortar (mortar cracks) arise. When the load reaches the maximum both types of cracks start to interact and microcracks develop in the concrete. A steep drop in load occurs with increasing displacement and a descending branch in the diagram appears. In fact, micro-cracking typically leads to a local reduction in the effective cross-sectional area available for transmitting the force. If softening occurs it is a precursor to failure and all deformation localises in small fracture zones (mode-I localisation). Fracture under tension with a post-peak softening behaviour is not only observed for concrete but also in other materials as rocks, alloys and plastics. Although the mechanisms at a micro-level, which drive the softening behaviour, may differ in these materials a comparable softening characteristic is measured at a macro-level. Softening not only occurs under tensile loadings but is also observed under compressive loadings, e.g. in geological materials as soils and rocks and in concrete. Moreover, in ductile materials as structural steels softening is observed in the final stage of failure independent of the loading conditions. However, the failure mode may differ. In case of mode-I localisation the cohesive properties of the material are more critical than the frictional properties, however, in the opposite case localisation becomes manifest along shear bands (mode-II localisation).

Mode-I and mode-II localisation of deformation are subject to an intense debate. For instance, at a micro-level the materials scientists study the micro-structural internal damage processes taking place in the cracked zone or in the shear band. In this thesis we follow a phenomenological approach in order to deal with localisation of deformation. The macroscopically observed softening behaviour will be described by a macroscopic set of parameters.

An important experimental result is that localisation regions at a macro-scale have a finite size. The width of the localisation zone  $w$  is determined experimentally, for instance for concrete  $w \approx 2.7 d_a$ , in which  $d_a$  is the maximum aggregate size (Bažant and Pijaudier-Cabot 1989) and for sands  $w \approx 10 d_g - 20 d_g$ , in which  $d_g$  is the mean grain size diameter (Mühlhaus



and Vardoulakis 1987). The scale of the localisation phenomenon may differ by some order of magnitude. In metals the localisation band width is less than a millimeter, while in rocks it can be several meters. Not only the width of the localisation zone has a finite value, but also the consumption of energy in the softening zones is finite. Moreover, in wave propagation problems a partial reflection and a partial transmission of waves on softening or localisation zones can be observed. It is essential that these features are recovered in numerical simulations of the localisation processes.

Softening occurs under static as well as under dynamic loading conditions. Under transient loading conditions inertia carries a part of the load and therefore the load of initiation of softening increases. A number of researchers have observed the dependence of the dynamic tensile strength on the stress rate (see Körmeling 1986 for a summary). Interpretation of experimental data must be done very carefully because the contribution of inertia effects in the structure should not be attributed to the material properties. Therefore the numerical simulation is an important tool to separate the true contribution of the changed material parameters and the inertia effects in the structure. About the influence of transient conditions on the softening behaviour not much experimental data is yet known. For concrete fracture Körmeling (1986) observed an increase of the fracture energy  $G_f$  related to the area under the load-displacement curve, when a total specimen is considered in which multiple crack zones occur. However, Weerheijm (1991), considering only one crack zone, observed a different shape of the softening curve but similarity between the static and dynamic value for the fracture energy in his test series on double-notched concrete specimens. So, more experimental research is necessary for a determination of the influence of rate effects on the softening response. Research should focus not only on the determination of the fracture energy but also on the number of crack planes in a specimen and the width of the localised crack zones. Not only the global response but also the local response gives useful information for the derivation of a phenomenological model for softening.

Under tension in brittle materials the occurrence of softening is an experimentally established fact and it is interesting from an economical viewpoint to make use of the redistribution of forces caused by softening. Under compression, however, in ductile materials softening may occur after an excursion in the plastic range and may be a precursor to progressive failure, which is not predicted by an elasto-plastic modelling of a material. So, under tension as well as under compression softening plays a dominating role in the failure process. Moreover, sometimes information about the failure mode of a structure is needed which is only possible when the softening effect is taken into account. The influence on the maximum load, the maximum attainable deformation and the failure mode of a structure show the significant role that softening plays. With the aid of accurate numerical schemes and more powerful computers the nonlinear static or dynamic analysis of softening materials is no longer impossible. For this reason a proper modelling of softening becomes more and more important.

There is no consensus (Read and Hegemier 1984, Sandler 1984) on the question whether strain softening is a true material property and can thus be used in the stress-strain relations.

For application in the finite element method softening is always attributed to the material and has been incorporated in the constitutive equations (strain-softening model). However, the descending branch in the stress-deformation curve in Figure 3.1 is a result of non-homogeneous deformation on a smaller scale and is also dependent on geometry and boundary conditions of the structure. Softening cannot simply be attributed to a continuum and is both dependent on structure and material. Nonlinear finite element software enables us to quantify the influence of the experimental set-up and the geometry of a specimen on the response. Therefore, semi-inverse modelling techniques should be used to derive a proper material model with reliable parameters for strain softening. In this way Rots (1988) studied softening with a numerical simulation of a specimen in pure tension. With a proper set of strain-softening material parameters he obtained a proper description of the non-homogeneous deformation. However, usually the strain-softening parameters are not derived from a semi-inverse technique but from a straightforward mapping of measured load-displacement data onto stress-strain relations. The stress-strain relation is obtained by means of

$$\epsilon = u/L \quad (3.1)$$

and

$$\sigma = F/A , \quad (3.2)$$

in which  $A$  and  $L$  are the original undeformed cross-sectional area and length of the specimen.  $F$  is the load and  $u$  is the deformation of the specimen. This translation leads to a negative slope in the stress-strain curve. The deformations are considered to be distributed homogeneously over the specimen. In section 3.5.2 this homogenisation technique will be used for the material modelling of the impact tensile test.

### 3.2 MATHEMATICS OF STRAIN-SOFTENING CONTINUUM

Recent studies (Read and Hegemier 1984, Sandler 1984, Lasry and Belytschko 1988) have treated the mathematical consequences of the inclusion of strain softening. If the initial value problem is considered in one spatial direction the governing equations for motion (cf. eq.(2.1)) and continuity (cf. eq.(2.2)) can be stated in a rate format as

$$\frac{\partial \dot{\sigma}}{\partial x} = \rho \frac{\partial^2 v}{\partial t^2} \quad (3.3)$$

and

$$\dot{\epsilon} = \frac{\partial v}{\partial x} , \quad (3.4)$$

in which velocity  $v = \dot{u}$ . In addition to these equations the constitutive equations must be specified. A classical strain-softening model with strain decomposition of the total strain  $\epsilon$  in

an elastic strain  $\epsilon_e$  and an inelastic strain  $\epsilon_i$ , as used in the strain-softening models in section 3.4, is of a general form

$$\sigma = f(\epsilon_i), \quad (3.5)$$

or in a rate form

$$\dot{\sigma} = f' \dot{\epsilon}_i. \quad (3.6)$$

Softening occurs if  $f' < 0$ , in which the superimposed prime denote differentiation with respect to the inelastic strain  $\epsilon_i$ . Combination of eq.(3.4) and (3.6), taking  $\dot{\epsilon}_i = \dot{\epsilon} - \dot{\epsilon}_e$  and  $\dot{\epsilon}_e = \dot{\sigma}/E$  and differentiation of the result with respect to  $x$  yields

$$\frac{\partial \dot{\sigma}}{\partial x} = \frac{f' E}{E + f'} \frac{\partial^2 v}{\partial x^2}. \quad (3.7)$$

If we substitute eq.(3.7) in (3.3) we obtain the wave equation for a one-dimensional strain-softening element

$$\frac{E + f'}{c_e^2} \frac{\partial^2 v}{\partial t^2} - f' \frac{\partial^2 v}{\partial x^2} = 0, \quad (3.8)$$

in which  $c_e = \sqrt{E/\rho}$  is the linear elastic, longitudinal wave velocity (so-called bar wave velocity). This second-order partial differential equation is linear if  $f'$  is constant (linear strain softening) and quasi-linear if  $f'$  is a function of  $\epsilon_i$  (nonlinear strain softening). The type of solution of eq.(3.8) can be investigated by means of the characteristics. Characteristics represent the directions along which the solution develops. In case of the wave equation these directions lie in the  $x-t$  plane. For a linear or a quasi-linear differential equation we can calculate the characteristics as follows. We consider the variation of the first derivatives of velocity  $v$  with respect to  $t$  and  $x$

$$d \left( \frac{\partial v}{\partial t} \right) = \frac{\partial^2 v}{\partial t^2} dt + \frac{\partial^2 v}{\partial x \partial t} dx \quad (3.9)$$

$$d \left( \frac{\partial v}{\partial x} \right) = \frac{\partial^2 v}{\partial x \partial t} dt + \frac{\partial^2 v}{\partial x^2} dx. \quad (3.10)$$

Combination of eq.(3.9) and (3.10) with the wave equation for the classical strain-softening bar (eq.(3.8)) yields a system of three second-order differential equations with the characteristic determinant

$$D = \begin{bmatrix} (E+f')/c_e^2 & 0 & -f' \\ dt & dx & 0 \\ 0 & dt & dx \end{bmatrix} = (E+f')/c_e^2 dx^2 - f' dt^2. \quad (3.11)$$

If  $D \neq 0$  a unique solution in the  $u-x-t$  space can be determined. However, if  $D = 0$  the system of equations is dependent and a curve in the  $u-x-t$  plane coincides with the characteristic directions

$$\frac{dx}{dt} = \pm c_e \sqrt{\frac{f'}{E+f'}}. \quad (3.12)$$

For a wave equation the characteristics ( $\pm dx/dt$ ) coincide with the wave speeds ( $\pm c$ ). If we have softening ( $f' < 0$ ) and consider the case of snap-through ( $f' > -E$ ) the characteristics and therefore the wave speeds will be imaginary. So, the wave equation loses hyperbolicity and becomes elliptic whenever strain softening is introduced. In fact, a domain is split up into an elliptic part, in which waves do not have the ability to propagate (standing waves), and into an hyperbolic part with propagating waves. Spatial interaction between the two domains is impossible. The loss of hyperbolicity means that the problem becomes ill-posed as an initial value problem. An ill-posed problem can no longer be a successful description of the underlying physical problem.

The concept of well-posedness has been discussed thoroughly by Benallal et al. (1991). The hyperbolicity of the field equations is one of the three conditions that are necessary for the well-posedness of the initial value problem. The boundary complementing condition, governing instabilities at the boundary due to the emergence of stationary surface waves (Rayleigh waves), and the interfacial complementing condition, governing instabilities at interfaces due to the emergence of stationary interfacial waves (Stoney waves), are the other two conditions.

The occurrence of strain softening causes the violation of the local stability criterion (Hill 1958)

$$\dot{\mathbf{e}}^T \dot{\boldsymbol{\sigma}} > 0. \quad (3.13)$$

A negative inner product of stress rate  $\dot{\boldsymbol{\sigma}}$  and strain rate  $\dot{\mathbf{e}}$  implies a material instability, which is the driving force behind localisation of deformation. In classical rate-independent continua, as shown above via  $\dot{\mathbf{e}}^T f' \dot{\mathbf{e}}_i < 0$ , this material instability can cause loss of hyperbolicity and thus loss of well-posedness. However, if a proper continuum description for strain softening is used a material instability may not imply the loss of hyperbolicity.

A material instability can lead to a structural instability. In that case the second-order work  $\delta^2 W$  (which is related to the second derivative of the potential energy  $U$  with respect to  $t$ ) is negative, which can be written as

$$\delta^2 W = \frac{1}{2} \int_V \dot{\mathbf{\epsilon}}^T \dot{\mathbf{\sigma}} dV < 0. \quad (3.14)$$

This corresponds with the loss of positive-definiteness of the structural tangential stiffness matrix  $\mathbf{K}$  (eq.(2.25)) (see de Borst et al. (1992)).

Dispersion is the observation that harmonic waves, with a different frequency, propagate with different velocities. Because a travelling wave is composed of harmonic waves the shape of a travelling wave is altered when the components have mutually different wave speeds. The ability to transform the shape of waves seems a necessary condition for continua to capture localisation phenomena. Waves that propagate through a classical strain-softening medium are not dispersive, i.e. the continuum is not able to transform waves into stationary localisation waves. For a dispersion investigation we assume a single linear harmonic wave propagating through a one-dimensional continuum with a velocity field of the form

$$v(x,t) = A e^{i(kx - \omega t)}, \quad (3.15)$$

in which  $\omega$  is the angular frequency and  $k$  is the wave number counting the number of wave lengths  $\lambda$  in the bar over  $2\pi$

$$k = \frac{2\pi}{\lambda}. \quad (3.16)$$

A dispersion relation can be obtained if eq.(3.15) is substituted in the wave equation (eq.(3.8)), which yields

$$\omega = c_e \sqrt{\frac{f'}{E + f'}} k. \quad (3.17)$$

Waves are called dispersive if the phase velocity  $c_f = \omega/k$  is a function of wave number  $k$ . For the classical strain-softening bar from eq.(3.17) it becomes clear that  $c_f$  is independent of  $k$  and therefore waves are non-dispersive (Whitham 1974). For this reason a classical strain-softening bar is not able to change the shape of an arbitrary loading wave into a stationary wave representing the localisation zone. It is noted that in a dispersive continuum a difference can exist between the phase velocity  $c_f$ , which is the velocity of propagation of a single harmonic wave and the group velocity  $c$ , which is the velocity at which the energy travels. For the classical strain-softening medium the phase velocity equals the group velocity and are both imaginary. However, in the treatment of the non-classical strain-softening models in the Chapters 4, 5, 6 and 7 a difference between phase and group velocity arises and will be discussed in more detail.

### 3.3 ANALYTICAL SOLUTION OF A CLASSICAL STRAIN-SOFTENING BAR

To investigate the consequences in a mechanical sense of the mathematical statements of ill-posedness and imaginary wave speeds, we will derive the analytical solution of a bar which is

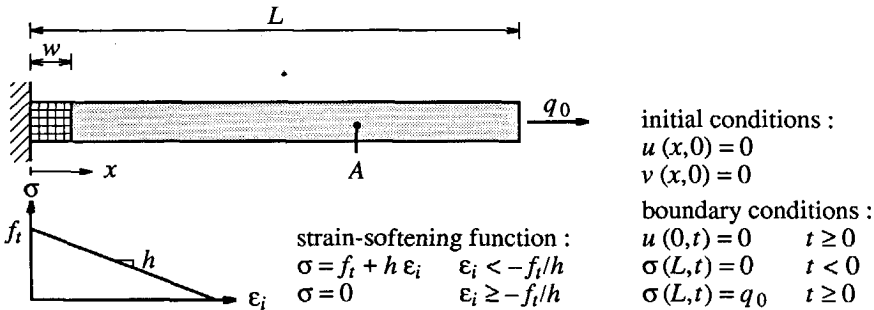


Figure 3.2 One-dimensional bar problem in tension (analytical problem).

fixed at one side and is loaded by a dynamic tensile force at the other side (cf. Bažant and Belytschko (1985), who found an exact analytical solution for a one-dimensional strain-softening bar with prescribed velocity at both sides of the bar). This longitudinal wave propagation problem is given in Figure 3.2 and will be investigated numerically in section 3.5. We use a linear strain-softening model and a step load, which does not narrow the results of this analysis. The transient wave propagates through the bar and reflects at the left boundary. If  $\frac{1}{2}f_t < q_0 < f_t$ , with  $f_t$  the tensile strength, the tensile strength is exceeded after reflection and a localised softening zone  $w$  emerges.

First, we assume that the bar behaves in a linearly elastic manner. The classical one-dimensional wave equation (cf. eq.(3.8)) reads

$$\frac{1}{c_e^2} \frac{\partial^2 u}{\partial t^2} - \frac{\partial^2 u}{\partial x^2} = 0. \tag{3.18}$$

A solution of this equation, the d'Alembert solution, consists of two waves  $f$  and  $g$  propagating in the characteristic directions

$$u(x,t) = f(x - c_e t) + g(x + c_e t). \tag{3.19}$$

For the problem under consideration we use, after a change of variables,

$$u(x,t) = f(t - (L-x)/c_e) + g(t - (L+x)/c_e), \tag{3.20}$$

in which  $f$  is the wave propagating to the left and  $g$  is the reflected wave. The solution for  $f$  for the given initial and boundary conditions reads

$$f(t - (L-x)/c_e) = \frac{H(t - (L-x)/c_e)}{\rho c_e} \frac{1}{A} \int_0^{t - (L-x)/c_e} F(\tau) d\tau = \tag{3.21}$$

$$\frac{H(t-(L-x)/c_e)}{\rho c_e} q_0(t-(L-x)/c_e),$$

in which  $H$  is the Heaviside step function, which is equal to 1 if  $H > 0$  and equal to 0 if  $H \leq 0$ . A similar solution for  $g$  completes the solution for the displacement field

$$u(x,t) = \frac{H(t-(L-x)/c_e)}{\rho c_e} q_0(t-(L-x)/c_e) - \frac{H(t-(L+x)/c_e)}{\rho c_e} q_0(t-(L+x)/c_e). \quad (3.22)$$

The strain field via  $\epsilon = \partial u / \partial x$  becomes

$$\epsilon(x,t) = \frac{q_0 H(t-(L-x)/c_e)}{E} + \frac{q_0 H(t-(L+x)/c_e)}{E}. \quad (3.23)$$

When the stress field  $\sigma(x,t) = E \epsilon(x,t)$  is determined the energy consumption (potential energy) in the elastic bar can be calculated via

$$U(t) = \frac{1}{2} A \int_0^L \sigma \epsilon dx = \frac{q_0^2 A}{2E} \int_0^L (H(t-(L-x)/c_e) + 3H(t-(L+x)/c_e)) dx \quad (3.24)$$

which after integration leads to

$$U(t) = \frac{q_0^2 A c_e}{2E} (t + 2(t-L/c_e)H(t-L/c_e)) \text{ for } 0 < t < 2L/c_e. \quad (3.25)$$

If strain softening occurs after reflection of the wave the inelastic behaviour of the strain-softening zone  $w$  is determined by eq.(3.8) with  $f' = h$  (linear strain softening). Eq.(3.8) becomes elliptic, which means that interaction over finite distances is immediate. This means that the localisation zone does not extend and remains infinitely small ( $w \rightarrow 0$ ). Therefore we postulate a solution and verify that it is a solution to the initial value problem and we claim no uniqueness. We define a constant strain field  $\epsilon_{loc}$  in an infinitely small localisation zone

$$u(x,t) = \epsilon_{loc} x \quad \text{for } 0 < x < w, \quad (3.26)$$

and for the remaining elastic part of the bar we have

$$u(x,t) = \frac{H(t-(L-x)/c_e)}{\rho c_e} q_0(t-(L-x)/c_e) + g(t-(L+x)/c_e) \quad \text{for } w < x < L, \quad (3.27)$$

in which the reflected wave  $g$  is unknown yet. Then the strain field becomes

$$\epsilon(x,t) = \frac{q_0 H(t-(L-x)/c_e)}{E} - \frac{1}{c_e} \frac{dg}{d(t-(L+x)/c_e)} \quad \text{for } w < x < L. \quad (3.28)$$

Now the displacement field and the strain field are defined inside as well as outside the localisation zone. Interface conditions must be used to solve the system of equations. First, using eqs.(3.26) and (3.27) and assuming displacement continuity at the interface ( $x = w$ ) yields an

expression for the strain in the localisation zone

$$\varepsilon_{loc} = \frac{1}{w} \left( \frac{q_0}{\rho c_e} (t - (L-x)/c_e) + g (t - (L+x)/c_e) \right). \quad (3.29)$$

Because  $w \rightarrow 0$  the strain in the localisation zone  $\varepsilon_{loc}$  becomes infinite. It is now proved, following Bažant and Belytschko (1985), that the velocity of the interface  $v_i$  is zero. If the interface would move to the right the stress outside the zone  $\sigma_2(w)$  would be equal to  $f_t$ , whereas the stress inside the zone  $\sigma_1(w)$  must be smaller than  $f_t$ . At the same time the strain inside the zone  $\varepsilon_1(w)$  is larger ( $> f_t/E$ ) than the strain outside the zone  $\varepsilon_2(w)$  ( $< f_t/E$ ). Thus the jump equation over the interface, derived from the rate of linear momentum,

$$[[\sigma]] = \rho v_i [[\varepsilon]] \quad \text{or} \quad \sigma_2 - \sigma_1 = \rho v_i (\varepsilon_2 - \varepsilon_1), \quad (3.30)$$

in which the brackets denote difference, can only be satisfied if  $v_i = 0$  and consequently  $\sigma_1 = \sigma_2$  and stress continuity over the interface is guaranteed. If we use the softening function  $\sigma = f_t + h\varepsilon_i$  for the inelastic part of the bar and  $\sigma = E\varepsilon$  for the elastic part, the continuity of stresses can be given by means of eq.(3.28)

$$q_0 - \frac{E}{c_e} \frac{dg}{d(t - (L+x)/c_e)} = f_t + h\varepsilon_{loc}. \quad (3.31)$$

Because  $\varepsilon_{loc} \rightarrow \infty$  the stress in the localisation zone and consequently the right-hand-side of eq.(3.31) vanishes because  $\sigma = 0$  if  $\varepsilon_{loc} \geq -f_t/h$  (see Figure 3.2). We can derive the expression for the reflected wave  $g$  by integration of eq.(3.31)

$$g = \frac{q_0}{\rho c_e} (t - (L+x)/c_e), \quad (3.32)$$

which can be substituted in eq.(3.27) to complete the solution

$$u(x,t) = \frac{H(t - (L-x)/c_e)}{\rho c_e} q_0 (t - (L-x)/c_e) + \frac{H(t - (L+x)/c_e)}{\rho c_e} q_0 (t - (L+x)/c_e). \quad (3.33)$$

A discontinuity appears at  $x = 0$ , at which a jump of displacement, equal to  $(2q_0/\rho c_e)(t - L/c_e)$  occurs after reflection at  $t = L/c_e$ . For this reason the strain in the localisation zone can be expressed by means of a Dirac delta function  $\delta(x)$ , namely

$$\varepsilon = \frac{2q_0}{\rho c_e} (t - L/c_e) \delta(x) \quad \text{if} \quad \int_0^w \varepsilon dx = \frac{2q_0}{\rho c_e} (t - L/c_e). \quad (3.34)$$

The complete strain field is obtained if we differentiate the displacement (eq.(3.33)) with respect to  $x$  and superpose the solution for the localisation zone



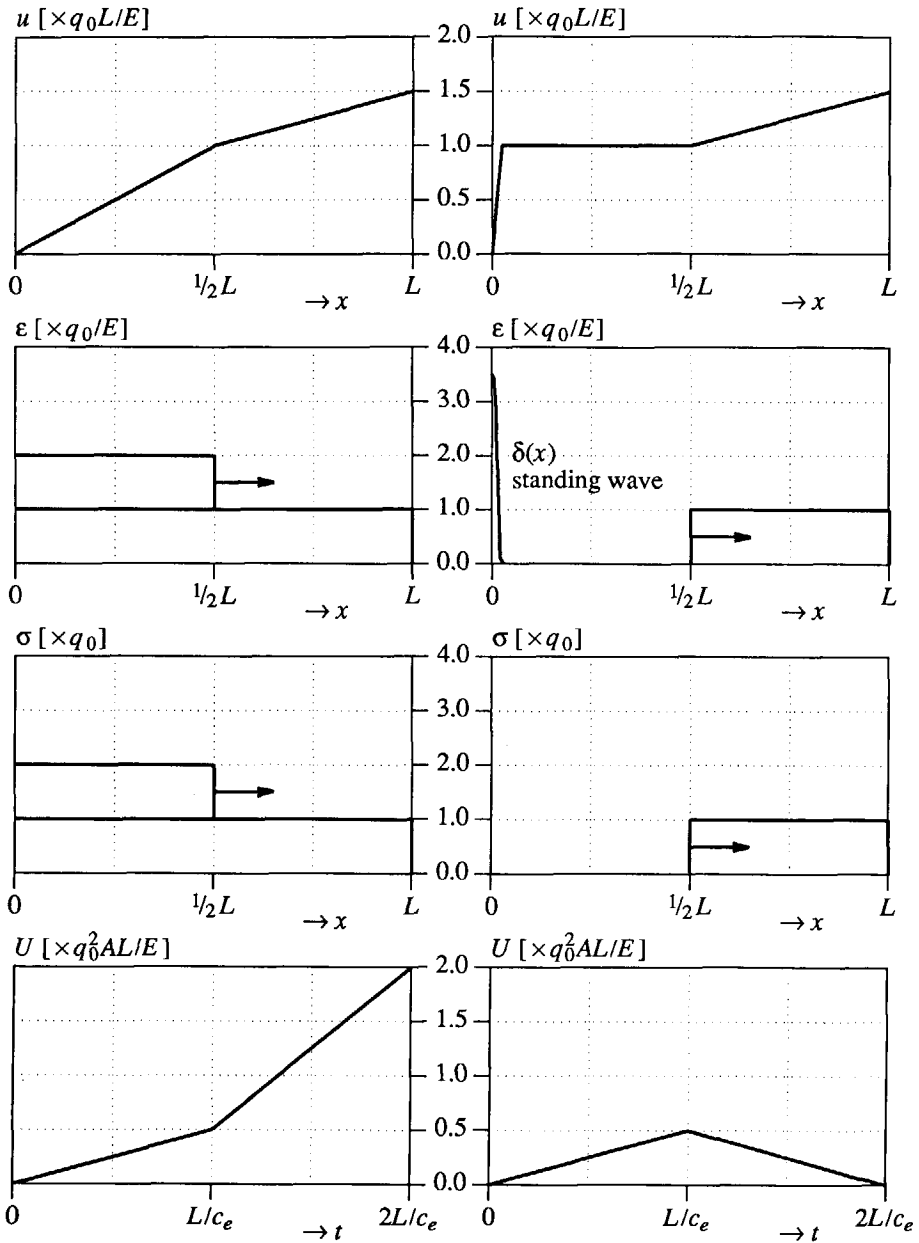


Figure 3.3 Analytical solution for elastic bar (left) and strain-softening bar (right) for displacements, strains, stresses (at  $t = \frac{3}{2}L/c_e$ ) and consumption of energy.

$$\varepsilon(x, t) = \frac{q_0}{E} (H(t - (L - x)/c_e) - H(t - (L + x)/c_e)) + \frac{2q_0}{\rho c_e} (t - L/c_e) \delta(x), \quad (3.35)$$

and the stress field becomes

$$\sigma(x, t) = q_0 (H(t - (L - x)/c_e) - H(t - (L + x)/c_e)). \quad (3.36)$$

If stresses and strains are known the energy consumption in the bar can be calculated with

$$U(t) = \frac{q_0^2 A}{2E} \int_0^L (H(t - (L - x)/c_e) - H(t - (L + x)/c_e)) dx \quad (3.37)$$

and integration of eq.(3.37) yields

$$U(t) = \frac{q_0^2 A c_e}{2E} (t - 2(t - L/c_e)H(t - L/c_e)) \text{ for } 0 < t < 2L/c_e. \quad (3.38)$$

The solution of this longitudinal wave propagation problem is fully determined via eqs.(3.33), (3.35), (3.36) and (3.38) for the displacements, strains, stresses and energy, respectively. The results of the analytical solution of the strain-softening bar have been plotted in Figure 3.3, in which a comparison is made with a purely elastic bar. The spurious character of the solution is obvious, the strain reaches infinity after reflection in a localisation zone of zero length. In fact, the solution of the elliptic equation is a standing wave, described by a Dirac delta function, which does not have the ability to extend. The stress drops to zero instantly and the wave reflects on the softening zone as on a free boundary. As already stated in the previous section spatial interaction between the elliptic and the hyperbolic system is no longer possible. The tensile wave returns as a pressure wave instead of a superposition of tensile waves which is usual after reflection on a fixed boundary. Furthermore, it is obvious that from  $t = L/c_e$  after reflection the bar is unable to consume a further amount of energy.

A remarkable result is that the solution is independent of the slope of the softening function  $h$ . So the restriction to a linear strain-softening function is no limitation. A discontinuity arises when  $h = 0$ . When  $h$  is slightly smaller than zero the abovementioned solution is valid, however, if  $h = 0$  (perfect plasticity) an entirely different solution of the problem is found.

### 3.4 CONSTITUTIVE EQUATIONS FOR STRAIN SOFTENING

As mentioned in section 3.1, softening can be modelled using a phenomenological approach or a micromechanical approach. For the micromechanical approach exact knowledge about the microstructural changes in the softening zone is necessary. For instance, for concrete fracture data about particles, matrix and interface should be described in force-displacement relations. A big disadvantage of the microstructural simulation of softening is the extreme demand for computer time. Especially for large scale structures there is a need for models at a macro level and for this reason the phenomenological approach is followed here. Because stresses and

strains are averaged quantities constitutive relations must be formulated empirically and if necessary via semi-inverse modelling techniques. Examples of phenomenological strain-softening models are crack models, based on a total or a decomposed strain concept, plasticity models with yield limit degradation and continuous damage models, based on a degradation of the stiffness determined by a damage parameter. Here, we will first treat the smeared crack model and next a softening plasticity model.

### 3.4.1 Smeared crack model

For the continuum approach of fracture a crack model can be defined in the framework of the fixed smeared crack concept (de Borst and Nauta 1985, Rots 1988). In this concept a cracked zone is conceived to be a continuum which permits a description in terms of stress-strain relations. We apply a decomposition of total strain rate into the elastic strain rate  $\dot{\mathbf{e}}_e$  and the crack strain rate  $\dot{\mathbf{e}}_{cr}$

$$\dot{\mathbf{e}} = \dot{\mathbf{e}}_e + \dot{\mathbf{e}}_{cr} . \quad (3.39)$$

When incorporating crack stress - crack strain laws it is convenient to set up a local  $n,t$ -coordinate system in a two-dimensional configuration, which is aligned with the crack. This necessitates a transformation between the crack strain rate  $\dot{\mathbf{e}}_{cr}$  in the global  $x,y,z$ -coordinates and the crack strain rate  $\dot{e}_{cr}$  in the local coordinates. The crack strain rate in the local coordinate system is defined as

$$\dot{e}_{cr} = [ \dot{e}_{nn} , 2\dot{e}_{nt} ]^T , \quad (3.40)$$

where  $\dot{e}_{nn}$  is the mode-I crack normal strain rate and  $\dot{e}_{nt}$  is the mode-II crack shear strain rate. The relation between local and global strain rates reads

$$\dot{\mathbf{e}}_{cr} = \mathbf{N}\dot{e}_{cr} \quad (3.41)$$

where  $\mathbf{N}$  is the transformation matrix given by

$$\mathbf{N} = \begin{bmatrix} \cos^2\alpha_i & -\sin\alpha_i \cos\alpha_i \\ \sin^2\alpha_i & \sin\alpha_i \cos\alpha_i \\ 2\sin\alpha_i \cos\alpha_i & \cos^2\alpha_i - \sin^2\alpha_i \end{bmatrix} , \quad (3.42)$$

with  $\alpha_i$  the inclination angle of the normal of the crack  $n$  with the  $x$ -axis. The angle is determined by the principal stress direction at the onset of cracking. An essential feature of the model is that  $\mathbf{N}$  is fixed upon crack formation so that the concept belongs to the class of fixed crack concepts.

In a similar way we can define a crack stress rate vector

$$\dot{\mathbf{t}}_{cr} = [\dot{t}_{nn}, \dot{t}_{nt}]^T, \quad (3.43)$$

in which  $\dot{t}_{nn}$  is the mode-I normal crack stress rate and  $\dot{t}_{nt}$  is the mode-II shear crack stress rate. The relation between the stress rate in the global coordinate system and the local stress rate can be derived to be

$$\dot{\mathbf{t}}_{cr} = \mathbf{N}^T \dot{\boldsymbol{\sigma}}. \quad (3.44)$$

To complete the system of equations we need a constitutive model for the intact concrete and for the smeared cracks. For the concrete between the cracks it is assumed that

$$\dot{\boldsymbol{\sigma}} = \mathbf{D}_e \dot{\boldsymbol{\epsilon}}_e. \quad (3.45)$$

The relation between the local crack strain rate and the local crack stress rate is

$$\dot{\mathbf{t}}_{cr} = \mathbf{D}_{cr} \dot{\boldsymbol{\epsilon}}_{cr}. \quad (3.46)$$

with  $\mathbf{D}_{cr} = \text{diag}[h, \beta_s \mu]$ , in which  $h$  is the mode-I softening modulus ( $h < 0$ ), which has been assumed to be a constant for the sake of simplicity. The shear stiffness in the crack is obtained by a multiplication of the elastic shear stiffness  $\mu$  with a shear reduction factor  $\beta_s$ . Coupling effects between the two modes are not considered. In this model fracture is assumed to be initiated in mode-I and mode-II effects enter upon rotation of the principal stresses.

Now, the overall stress-strain relation of the model with respect to the global coordinate system can be developed. Combining eqs.(3.39) and (3.45) and subsequent substitution of eq.(3.41) yields

$$\dot{\boldsymbol{\sigma}} = \mathbf{D}_e [\dot{\boldsymbol{\epsilon}} - \mathbf{N} \dot{\boldsymbol{\epsilon}}_{cr}]. \quad (3.47)$$

Premultiplying this equation by  $\mathbf{N}^T$  and substituting eqs.(3.44) and (3.46) yields the relation between the local crack strain rate and the global strain rate

$$\dot{\boldsymbol{\epsilon}}_{cr} = [\mathbf{D}_{cr} + \mathbf{N}^T \mathbf{D}_e \mathbf{N}]^{-1} \mathbf{N}^T \mathbf{D}_e \dot{\boldsymbol{\epsilon}}. \quad (3.48)$$

The overall relation between global stress rate and global strain rate is obtained by substituting eq.(3.48) into (3.47)

$$\dot{\boldsymbol{\sigma}} = [\mathbf{D}_e - \mathbf{D}_e \mathbf{N} [\mathbf{D}_{cr} + \mathbf{N}^T \mathbf{D}_e \mathbf{N}]^{-1} \mathbf{N}^T \mathbf{D}_e] \dot{\boldsymbol{\epsilon}}. \quad (3.49)$$

In this derivation only one crack is considered, but it is possible that due to the rotation of principal stresses new cracks arise. The crack strain is then decomposed into separate contributions from the multi-directional cracks (de Borst and Nauta 1985, Rots 1988).

The integration of eq.(3.49) can be done by a one-step forward scheme which is exact if the matrices  $\mathbf{D}_e$  and  $\mathbf{D}_{cr}$  remain constant during the time step. When, for instance,  $\mathbf{D}_{cr}$  is non-constant a predictor-corrector method can be used in a inner iteration loop to determine the incremental stresses (Rots 1988).

### 3.4.2 Softening plasticity model

The plastic response of a material becomes manifest as soon as a combination of the stress components reaches a characteristic value. For isotropic hardening or softening plasticity this characteristic value is governed by a yield function of the form

$$f(\boldsymbol{\sigma}, \kappa) = 0, \quad (3.50)$$

in which  $\kappa$  is a scalar valued hardening or softening parameter which is dependent on the strain history. In rate-independent plasticity inelastic deformations occur if the stress point is on the yield surface. Stress states outside the yield contour are not possible. For this reason, the stress point must remain on the yield contour during plastic flow. This leads to a second condition for plastic deformation

$$\dot{f}(\boldsymbol{\sigma}, \kappa) = 0, \quad (3.51)$$

which is commonly referred to as Prager's consistency condition. In plasticity theory the strain rate vector is decomposed into an elastic  $\dot{\boldsymbol{\epsilon}}_e$  and a plastic  $\dot{\boldsymbol{\epsilon}}_p$  part according to

$$\dot{\boldsymbol{\epsilon}} = \dot{\boldsymbol{\epsilon}}_e + \dot{\boldsymbol{\epsilon}}_p. \quad (3.52)$$

Therefore the stress-strain relation can be written in a rate form as

$$\dot{\boldsymbol{\sigma}} = \mathbf{D}_e(\dot{\boldsymbol{\epsilon}} - \dot{\boldsymbol{\epsilon}}_p). \quad (3.53)$$

The plastic strain rate vector is written as the product of a non-negative scalar  $\dot{\lambda}$  and a vector  $\mathbf{m}$ , representing the magnitude and the direction of the plastic flow, respectively

$$\dot{\boldsymbol{\epsilon}}_p = \dot{\lambda} \mathbf{m}. \quad (3.54)$$

The vector  $\mathbf{m}$  is often assumed to be the gradient of the plastic potential function  $g_p$

$$\mathbf{m} = \frac{\partial g_p}{\partial \boldsymbol{\sigma}}. \quad (3.55)$$

The plastic potential function  $g_p$  is equal to the the yield function  $f$  in case of associative flow.

The consistency equation can be elaborated as

$$\mathbf{n}^T \dot{\boldsymbol{\sigma}} + \frac{\partial f}{\partial \kappa} \dot{\kappa} = 0, \quad (3.56)$$

in which the vector  $\mathbf{n}$  is the gradient to the yield surface

$$\mathbf{n} = \frac{\partial f}{\partial \boldsymbol{\sigma}}. \quad (3.57)$$

If we define the softening modulus  $h$  as

$$h = -\frac{1}{\lambda} \frac{\partial f}{\partial \kappa} \dot{\kappa} \quad (3.58)$$

an explicit expression for the magnitude of the plastic flow can be derived by premultiplying eq.(3.53) by  $\mathbf{n}^T$ . Combination with eqs.(3.54), (3.56) and (3.58) then yields

$$\dot{\lambda} = \frac{\mathbf{n}^T \mathbf{D}_e \dot{\boldsymbol{\varepsilon}}}{h + \mathbf{n}^T \mathbf{D}_e \mathbf{m}} \quad (3.59)$$

We can now obtain the relation between stress rate and strain rate by substitution of eq.(3.59) in eq.(3.53)

$$\dot{\boldsymbol{\sigma}} = \left[ \mathbf{D}_e - \frac{\mathbf{D}_e \mathbf{m} \mathbf{n}^T \mathbf{D}_e}{h + \mathbf{n}^T \mathbf{D}_e \mathbf{m}} \right] \dot{\boldsymbol{\varepsilon}} \quad (3.60)$$

The expression between brackets is called the continuum tangent stiffness matrix. The integration of this rate equation can be done explicitly via an Euler forward scheme. Then the quantities  $\mathbf{m}$ ,  $\mathbf{n}$  and  $h$  are evaluated at the beginning of the time step. A more accurate scheme can be obtained by evaluating  $\mathbf{m}$ ,  $\mathbf{n}$  and  $h$  at time  $t + \Delta t$ , which is referred to as an Euler backward scheme. Therefore an iterative procedure must be set up at integration point level. Explicit as well as implicit schemes for the integration of eq.(3.60) are commonly called return mapping schemes. First a trial stress is calculated as an elastic predictor after which the trial stress is mapped back on the yield surface via a plastic corrector. Two return mapping algorithms are used in this thesis, namely the tangent cutting plane method (Chapter 5) and the Euler backward method (Chapter 3, 6 and 7) (Ortiz and Simo 1986, de Borst and Feenstra 1990). It is noted that with the use of a return mapping algorithm we obtain a total stress-strain relation within a finite time step as in deformation plasticity theories. From this relation another tangential matrix can be derived, the so-called consistent tangent stiffness matrix, which ensures a quadratic convergence when the nonlinear set of equations is solved by the Newton-Raphson iteration scheme.

The hardening/softening parameter  $\kappa$  is typically dependent on the strain history. In the calculations in this thesis we assume strain-hardening/softening in which the evolution of the hardening/softening parameter is postulated to be equal to

$$\dot{\kappa} = \sqrt{2/3} (\dot{\boldsymbol{\varepsilon}}_p)^T \dot{\boldsymbol{\varepsilon}}_p \quad (3.61)$$

which is basically the second invariant of the plastic strain vector (Note that  $\boldsymbol{\varepsilon}_p = (\varepsilon_{p_{xx}}, \varepsilon_{p_{yy}}, \varepsilon_{p_{zz}}, \varepsilon_{p_{xy}}, \varepsilon_{p_{yz}}, \varepsilon_{p_{zx}})$ ). The hardening/softening parameter can be integrated in time via

$$\kappa = \int \dot{\kappa} dt \quad (3.62)$$

Because the yield function  $f$  is dependent on a scalar  $\kappa$ , the yield surface can only expand

(hardening) or shrink (softening), which means that the theory is limited to isotropic type of hardening/softening.

The abovementioned derivation is general and can be elaborated for a specific choice of the yield function  $f(\sigma, \kappa)$ . In this thesis we will treat three different yield functions. Firstly, we shall use the pressure-independent criterion of von Mises

$$f(\sigma, \kappa) = \sqrt{3J_2} - \bar{\sigma}(\kappa), \quad (3.63)$$

in which

$$J_2 = 1/2 (s_1^2 + s_2^2 + s_3^2) \quad (3.64)$$

is the second invariant of the deviatoric stresses  $s_i = \sigma_i - p$ , with  $p = 1/3 (\sigma_1 + \sigma_2 + \sigma_3)$  the hydrostatic pressure.  $\bar{\sigma}$  is the yield stress which is a function of the softening parameter. Typically, metals and normally-consolidated clays under relatively rapid loading conditions (undrained behaviour) satisfy the pressure-insensitive criterion of von Mises. The second criterion which we shall use is the Drucker-Prager yield function which includes a dependence on the hydrostatic pressure  $p$ . The Drucker-Prager yield function is defined by

$$f(\sigma, \kappa) = \sqrt{3J_2} + \alpha p - k, \quad (3.65)$$

with  $\alpha$  and  $k$  constants given by

$$\alpha = \frac{6\sin\phi}{3 - \sin\phi} \left( \alpha_\psi = \frac{6\sin\psi}{3 - \sin\psi} \right) \quad (3.66)$$

and

$$k = \frac{6c(\kappa)\cos\phi}{3 - \sin\phi}, \quad (3.67)$$

in which  $\phi$  signifies the internal friction angle and  $c$  the cohesion of a material. In our calculations the cohesion  $c$  is made a function of the softening parameter. We can invoke the concept of non-associative flow by defining the plastic potential function  $g_p$  equal to  $f$  but with the dilatancy angle  $\psi$  substituted for the friction angle  $\phi$ . The Drucker-Prager criterion is well suited to describe the inelastic behaviour of sands, drained clays, rocks and concrete under compressive loading. The yield functions of von Mises and Drucker-Prager can be used for a mode-II dominated failure pattern. On the other hand, the principal stress yield criterion of Rankine is suited to predict a mode-I failure pattern. The yield function according to Rankine is defined as

$$f(\sigma, \kappa) = \sigma_i - \bar{\sigma}(\kappa), \quad (3.68)$$

in which  $\sigma_i = \max(\sigma_1, \sigma_2, \sigma_3)$ . This model can be used to model fracture of brittle materials with a plasticity model instead of a smeared crack, discrete crack or damage model.

### 3.5 NUMERICAL ANALYSES

For an investigation of the dynamic response in localisation problems the conventional strain-softening models are used first. In section 3.3 the mechanical consequences of the loss of hyperbolicity of the field equations has been discussed. Here, the numerical consequence of the ill-posedness of problem is demonstrated by a mesh-sensitivity analysis. With Example 1 we treat the uniaxial bar problem in tension for which the analytical solution has been given in section 3.3. Examples 2 and 3 are two-dimensional localisation problems. The analysis of the impact tensile test (Example 2) is focused on mode-I localisation and the analysis of the impact biaxial test (Example 3) shows a mode-II localisation process. The three examples will also be used in the following chapters for assessment of the strain-softening model under consideration. The time integration of the field equations in the three example calculations has been done with the Newmark scheme ( $\beta = 1/4$ ,  $\gamma = 1/2$ , see section 2.3). For the time step we take  $\Delta t = 5 \cdot 10^{-7}$  s for Example 1,  $\Delta t = 1 \cdot 10^{-6}$  s for Example 2 and  $\Delta t = 1.5 \cdot 10^{-6}$  s for Example 3. A consistent mass matrix has been used for all analyses with the conventional models.

#### 3.5.1 Example 1 : One-dimensional bar problem in tension

The problem of mesh-sensitivity can be demonstrated clearly by means of the one-dimensional case. The same problem of a bar under uniaxial dynamic tension, which has been considered analytically in section 3.3, will be investigated numerically. For the softening material of the bar the smeared crack model from section 3.4.1 is used. Attention is focused on the influence of mesh spacing on the strain localisation in the bar, the wave reflection on cracked zones and the consumption of energy in the cracked bar. The bar problem is sketched in Figure 3.4, including geometry, loading and material data. Use of these parameters yields a linear elastic wave speed  $c_e = 1000$  m/s. We consider a block wave with a vertical stress front which

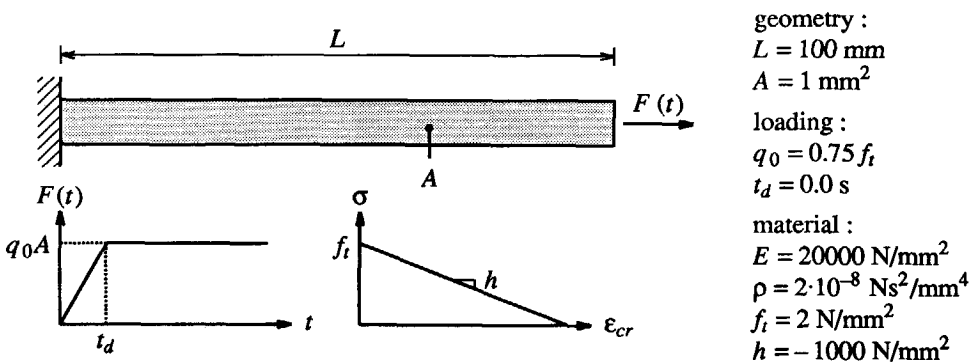


Figure 3.4 Example 1 : One-dimensional bar problem in tension.



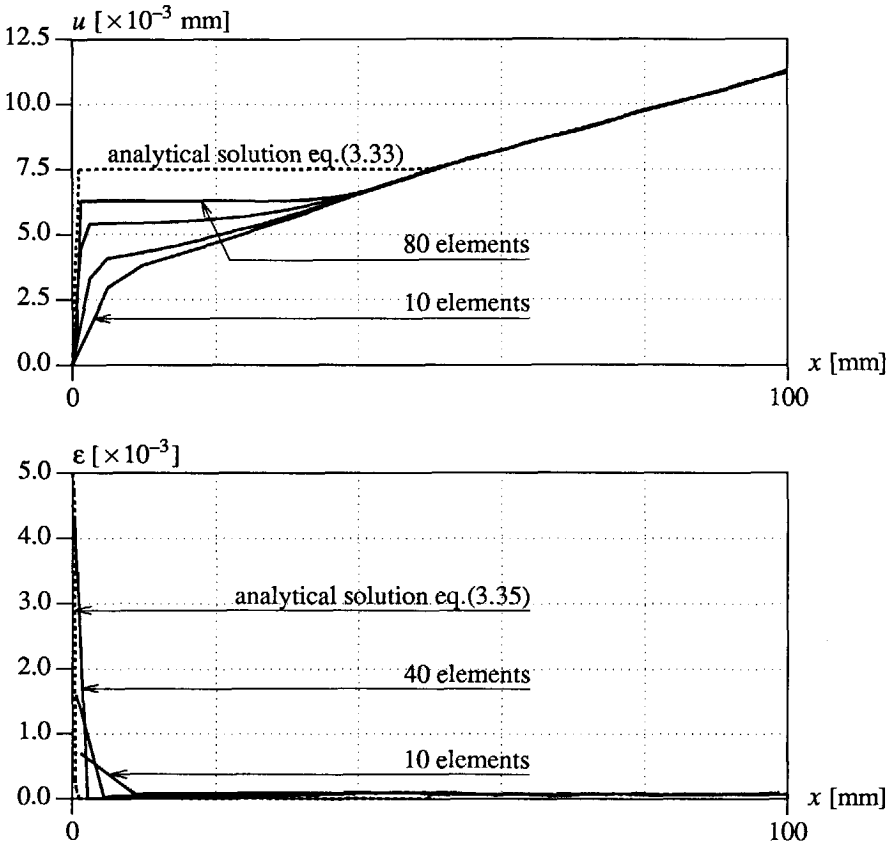


Figure 3.5 Mesh-dependent results with classical strain-softening model :  
 Top : Displacements along the bar at  $t = \frac{3}{2}L/c_e = 0.15 \cdot 10^{-3}$  s.  
 Bottom : Strain localisation along the bar at  $t = \frac{3}{2}L/c_e = 0.15 \cdot 10^{-3}$  s.

corresponds to  $t_d = 0$  s. The bar is divided into 10, 20, 40 and 80 elements, respectively. Use has been made of eight-noded elements with a nine-point Gauss integration scheme. The response of the bar is linearly elastic until the loading wave reaches the left boundary. The doubling in stress ( $2q_0 = \frac{3}{2}f_t$ ) due to reflection of the tensile wave causes the initiation of cracking. The material enters the softening regime and a localisation zone of intense straining emerges.

In Figure 3.5 the displacements and the strains for the different meshes are plotted at  $t = \frac{3}{2}L/c_e = 0.15 \cdot 10^{-3}$  s, that is when the wave has reflected at the left boundary and has returned to  $x = \frac{1}{2}L$ . Mesh sensitivity is obvious : strain localisation and, consequently, the jump in displacement occur in only one vertical row of three integration points which is the

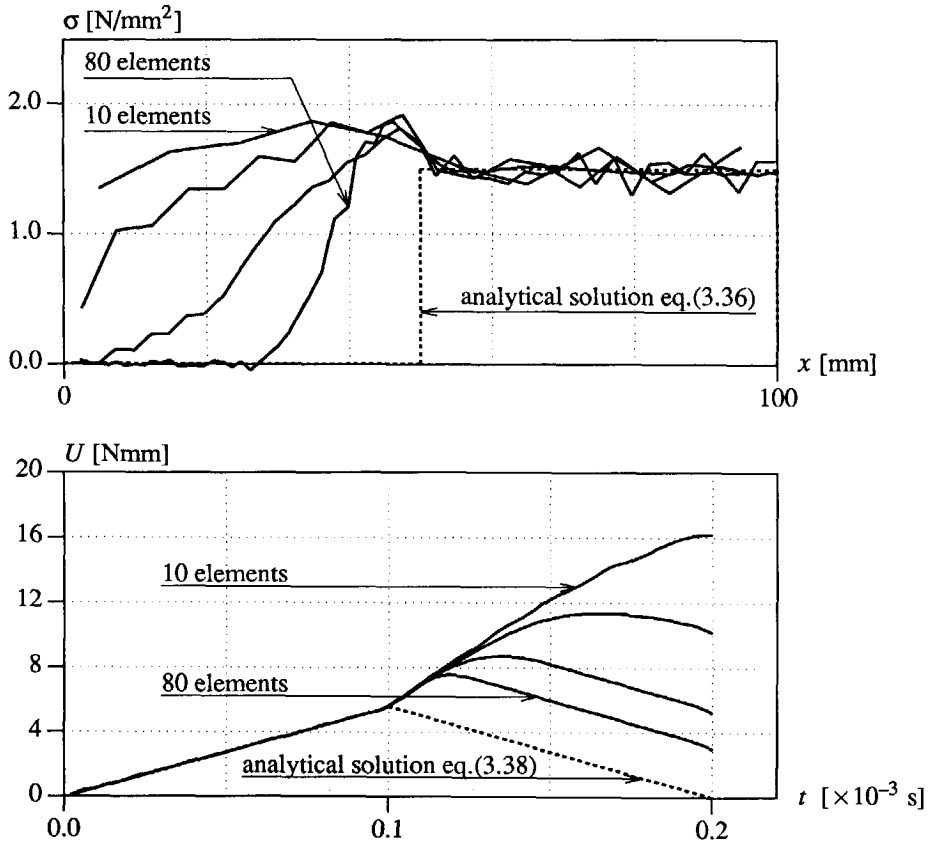


Figure 3.6 Mesh-dependent results with classical strain-softening model :  
 Top : Stress profiles along the bar at  $t = \frac{3}{2}L/c_e = 0.15 \cdot 10^{-3} \text{ s}$ .  
 Bottom : Energy consumption of the bar.

smallest possible zone. Hence, the width of the localisation zone  $w$  decreases when more elements are used. After reflection the strain localises in one vertical row of integration points at the left boundary and extension of the zone is not possible. This is in agreement with the analytical findings in section 3.2. It is obvious that the analytical solution from section 3.3 is approached when the mesh is refined. The results for the discretisation with 80 elements has not been plotted because at  $t = 0.15 \cdot 10^{-3} \text{ s}$  the bar has already failed. In Figure 3.6 the stress profiles after reflection show that the amount of wave reflection depends on the mesh : for more elements there is a larger reduction in stress of the reflected wave. When the mesh is finer the stress in the softening zone drops to zero more rapidly which determines the amount of reflection. As soon as the stress has become zero one vertical row of integration points start

to act as a free boundary on which the tensile wave reflects as a pressure wave. Summation of a tensile wave propagating to the left and a pressure wave propagating to the right yields a zero stress situation. Moreover, the development of the consumption of energy  $U$  in the bar depends on the number of elements in the mesh as can be seen from Figure 3.6. The increase of the sum of elastic and inelastic energy after reflection ( $t > L/c_e$ ) is smaller when the localisation zone is smaller. In the limiting analytical case failure occurs at  $t = L/c_e$  without any further energy consumption in the strain-softening zone of the bar. The stress drops to zero instantly and the wave reflects as a pressure wave. The elastic energy gradually vanishes in the bar with the returning pressure wave.

It turns out that under mesh refinement the spurious analytical solution treated in section 3.3 is recovered. The strain in the localisation zone approaches an infinite value, the jump in displacements at the boundary becomes discontinuous, the stress drops to zero in an infinitesimal time interval and the consumption of energy becomes zero because the volume of the strain-softening zone becomes zero.

The same one-dimensional analysis can be carried out for a mode-II localisation problem considering the propagation of a shear wave instead of a longitudinal wave. If we consider a shear layer the use of a softening plasticity model (von Mises) leads to a shear band failure pattern at the left boundary. The width of the shear band, the shear stress reflection on the shear band and the consumption of energy in the shear banding zone are identically dependent on the mesh as in the uniaxial case under tension.

### 3.5.2 Example 2 : Impact tensile test on a double-notched specimen

In the Stevin Laboratory of Delft University of Technology impact tensile tests have been carried out on double-notched, prismatic concrete specimens (Figure 3.7). A specimen with notches makes it possible to predetermine the failure zone and to measure the deformation inside as well as outside the fracture zone. The tests have been performed with a Split-Hopkinson bar apparatus by Weerheijm (Weerheijm and Reinhardt 1989, Weerheijm 1991). The specimen is kept between an upper bar (6.7 m) and a lower bar (3.5 m) and the tensile pulse is applied at the bottom of the experimental set-up. The main observations that have been reported are : the ultimate strength and the deformations inside and outside the fracture zone. The loading rate has been measured after the pulse had passed the specimen and is affected by the failure process and the geometry of the specimen.

The response measured in the experiments is influenced by structural effects as the geometry of the specimen and the stiffness of the experimental set-up. For this reason material parameters which determine the post-peak response cannot be derived directly from the experiment. However, the combination of experimental and numerical data, as discussed in section 3.1, makes it possible to separate the structural from the material response, provided that a proper material model is used and that the geometry and boundary conditions have been modelled correctly. Because the classical model for softening results in mesh sensitivity, this

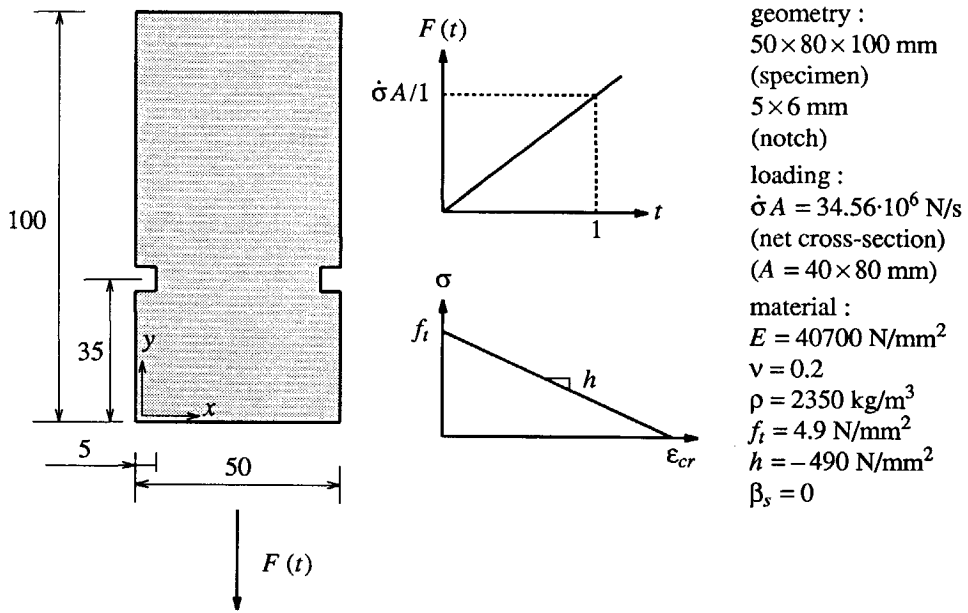


Figure 3.7 Example 2 : Impact tensile test on a double-notched specimen.

model is not appropriate for a semi-inverse determination of the material parameters. Here, the numerical description of the impact tensile test is only given to show the mesh dependence of the results.

For the numerical modelling of the specimen and the Split-Hopkinson bar we assume a plane-stress condition. The upper and lower bar of the Split-Hopkinson bar are very long to avoid reflections of stress waves, which would result in a disturbed response. So, in the numerical simulation the set-up cannot be omitted but must be modelled for a proper calculation of the response without undesirable reflections. However, the element size in the numerical modelling of the set-up is limited to the length traversed in one time step by the longitudinal elastic wave. Use of a larger element size would disturb the shape of the impact loading wave. A straightforward discretisation of the total Split-Hopkinson bar is therefore too expensive. A configuration with less elements can be obtained if we make use of the acoustic impedance

$$Z = A \sqrt{E\rho} \tag{3.69}$$

of the material, in which  $A$  is the cross-sectional area of the adapter. If  $Z$  is kept constant no reflections occur on an interface of materials with different properties. In this way the wave

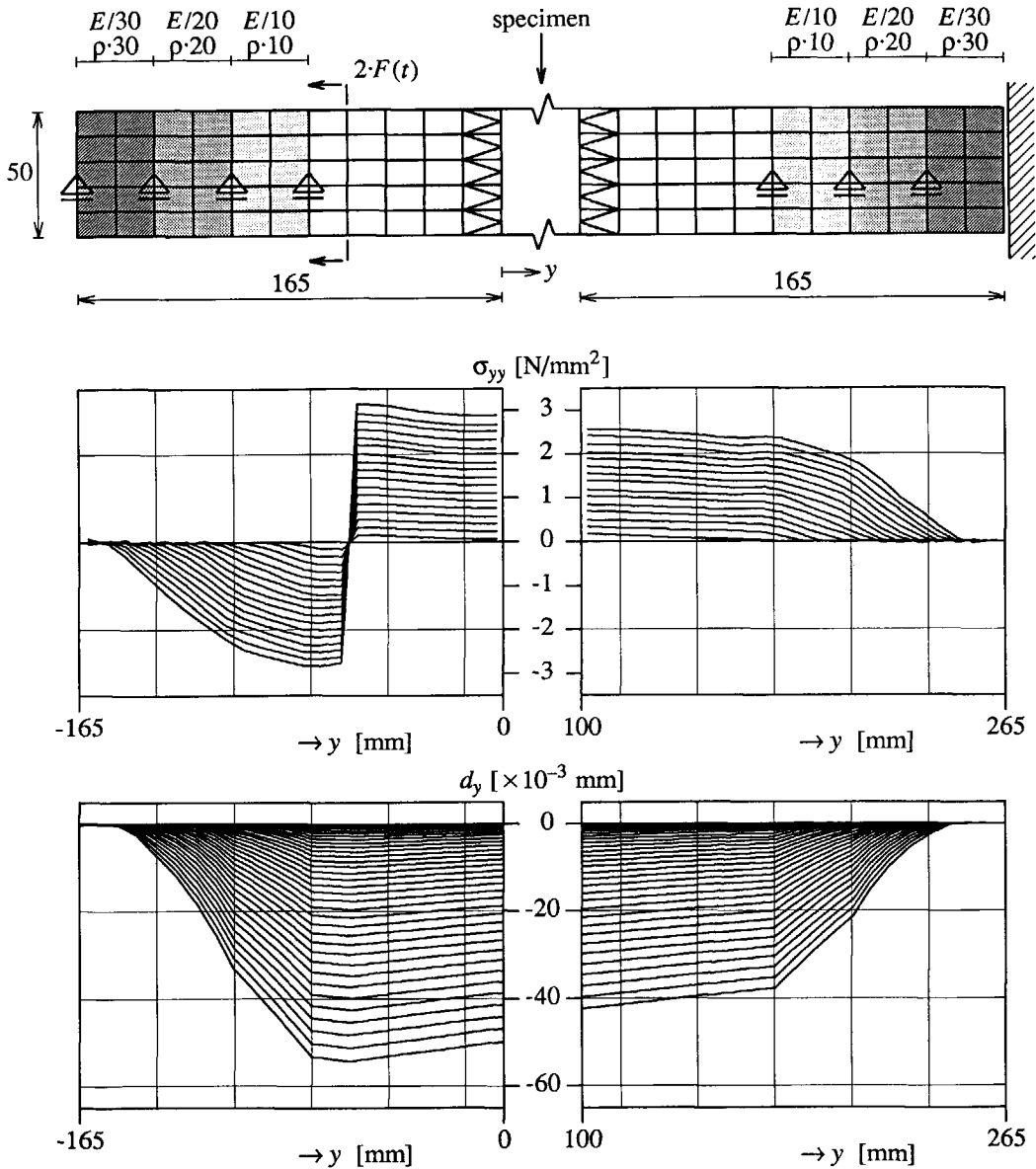


Figure 3.8 Numerical model of experimental set-up (top) with stress (centre) and displacement response (bottom) in upper (right) and lower (left) adapter.

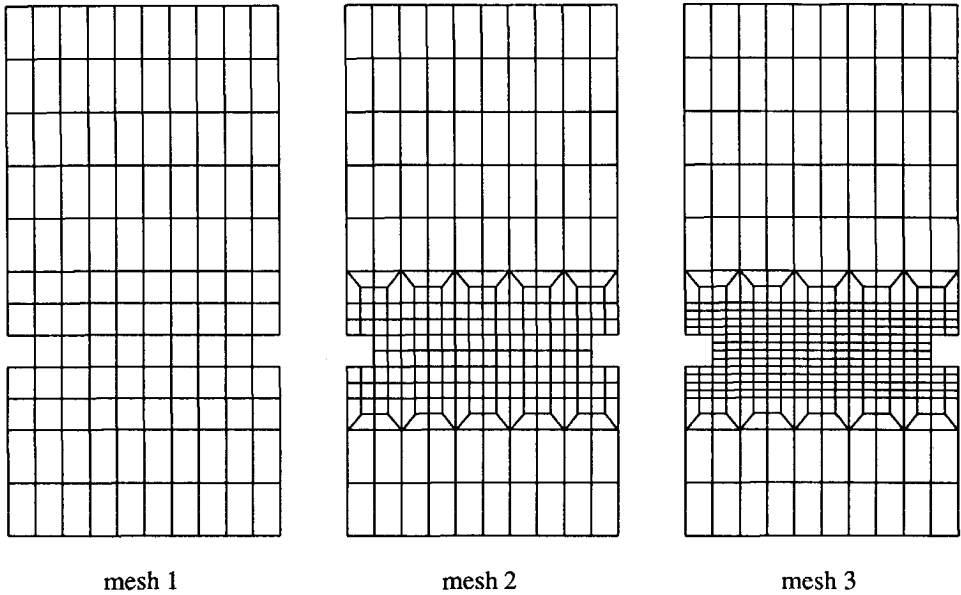


Figure 3.9 Finite element configurations for notched specimen.

speed can be slowed down by an increase of the density  $\rho$  and a decrease of Young's modulus  $E$ . Several zones are applied to gradually slow down the wave speed. The numerical model with the boundary elements is given in Figure 3.8. The strain and the displacement response in the upper and the lower adapter show the slowing down of the loading wave in the boundary elements.

The applied load is doubled because half of the load propagates to the specimen as a tensile wave and the other half propagates to the boundary elements as a pressure wave, which is clearly shown from the stress response in Figure 3.8. The numerical model of the set-up leads to different boundary conditions than the conditions in the test. The upper and lower bar of the set-up have been modelled with quadrilateral eight-noded elements with a four points Gauss integration and with triangular six-noded elements with a three points Gauss integration. To avoid reflections at the transition of the specimen and the set-up the same material parameters for the test set-up are chosen as for the specimen.

For the specimen three finite element discretisations have been used (Figure 3.9). For the different meshes we use one, two and four rows of elements in the notched section, respectively. The elements are eight-noded quadrilaterals but with a nine-point Gauss integration. The elastic and inelastic properties are given in Figure 3.7. The parameters are derived by a straightforward translation of experimental data. Because a notched specimen yields a lower value for the impact tensile strength the dynamic value for  $f_i$  is taken from empirical relations

derived in former programmes (Zielinski 1982). A simple linear strain-softening model is used and in a classical way, using a homogenisation technique, the constant softening modulus  $h$  was derived from the ultimate deformation measured in the experiment according to

$$\epsilon_u = \frac{\delta_u}{d_{notch}} = \frac{0.06}{6} = 0.01 \quad \text{and} \quad h = -\frac{f_t}{\epsilon_u} = -\frac{4.9}{0.01} = -490 \text{ N/mm}^2, \quad (3.70)$$

in which  $\epsilon_u$  is the ultimate crack strain and  $d_{notch}$  is the notch height. In the numerical analyses a section of 5×6 mm in front of the left notch was given a material imperfection in the sense that the tensile strength was reduced by 20 %. By inserting an imperfection the possibility is offered of computing an asymmetric component of the solution.

The results of the analyses show again mesh dependence as a consequence of an ill-posed continuum description for softening. Cracks start to propagate in one row of elements from the two notches to the centre of the specimen. In Figure 3.10 it is shown that the deformation (plotted with a multiplication factor FA = 500) localises along the crack in one single row of integration points for each of the three meshes. Here, a second problem appears which is caused by the ill-posedness of the problem, namely the mesh alignment of the results, i.e. the cracks or the localisation of deformation have a preferential direction of propagation which is aligned with the mesh lines. Mesh alignment is related to multiple equilibrium states which exist after the passing of spurious bifurcation points (de Borst 1986). During crack propagation the lowest equilibrium path is followed which often belongs to a propagation in the direction of the mesh lines. However, for finer meshes equilibrium states belonging to a propagation of cracks in directions not aligned with the mesh can be accessed more easily. This occurs in the mesh 3 analysis, in which the localisation band jumps between different rows of elements. In the impact tensile test the problem of mesh alignment has only a minor influence on the overall response because the crack propagation length is small and the mesh lines almost coincide with the direction of propagation of the cracks. A more convincing example of mesh alignment will be discussed in the next section.

The mesh dependence is shown for the total displacements in Figure 3.10 and for the axial strains in a vertical cross-section in Figure 3.11. Not only the classical strain-softening modelling of the material but also the singularity in the geometry of the specimen causes mesh dependence. The singularity at the notch forces the initiation of cracks at an earlier time stage for mesh 3 than for mesh 1. If a material is brittle this effect cannot be smoothed out and crack propagation occurs more rapidly and failure is accelerated. Already from the one-dimensional analysis it is observed that, using a classical strain-softening model, a finer mesh is equivalent to a more brittle material model (a faster stress drop after the initiation of softening). Hence, mesh sensitivity due to a stress singularity in the elastic solution and due to a classical strain-softening modelling amplify each other and at  $t = 0.50 \cdot 10^{-3}$  s the total displacements are much larger for the mesh 3 calculation than for the mesh 2 calculation, in which the stress peak at the notch is smoothed out partially by a redistribution of stresses.

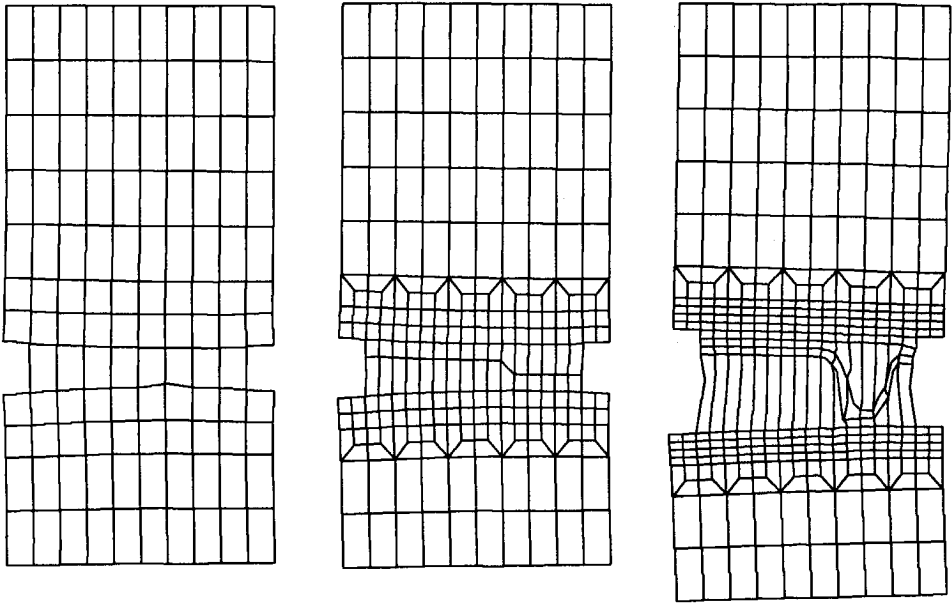


Figure 3.10 Displacement patterns at  $t = 0.50 \cdot 10^{-3}$  s (FA = 500).

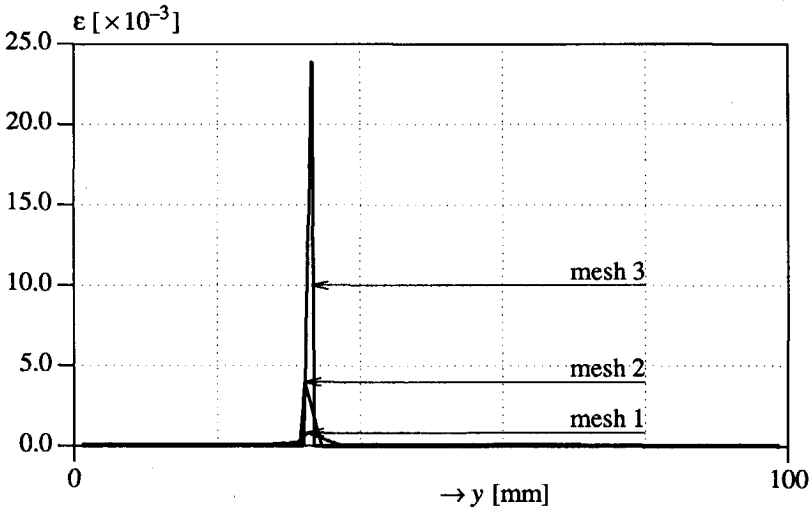


Figure 3.11 Total axial strains in centre section ( $x = 25$  mm) of the specimen ( $t = 0.50 \cdot 10^{-3}$  s).



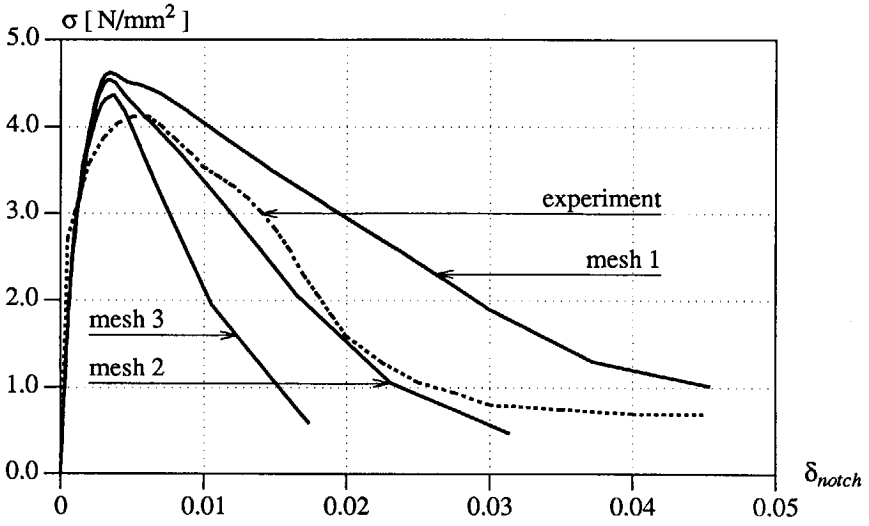


Figure 3.12 Stress-deformation curve inside the fracture zone.

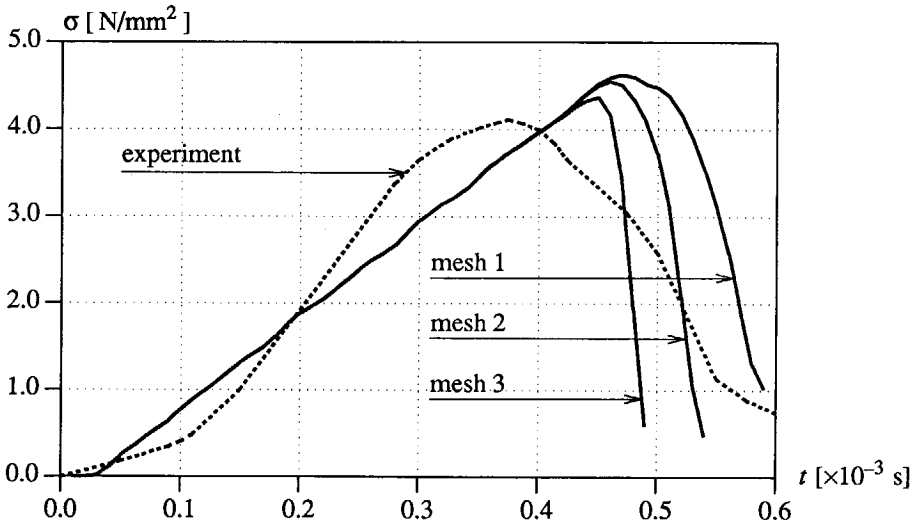


Figure 3.13 Stress-time curve of the transmitted loading pulse.

The numerical results can be compared with experimental data (Weerheijm 1991). The stress-deformation curves for the numerical analyses as well as for the experiment are plotted in Figure 3.12 in which  $\delta_{notch}$  represents the mean deformation over the left and the right notch and  $\sigma$  represents the vertical stress at the top of the specimen. Upon mesh refinement the behaviour becomes more brittle and the area under the curve is not an objective measure for the fracture energy. Mesh dependence starts already in the pre-peak regime, when the cracks propagate from the notch to the centre of the specimen. This results in a lower peak stress for the finest mesh. In Figure 3.13 the transmitted loading pulse is plotted as a function of time. Once again the influence of the mesh spacing results in a meaningless analysis. Experimental data can be fitted by an adaptation of the mesh.

The stress rate is measured in the test after the passing of the failure zone. These data have been used as input for the numerical analysis, which results in a difference between experimentally and numerically observed stress rates. The geometry of the specimen as well as the failure process influence the loading rate to such an extent that, in fact, a semi-inverse determination of the applied loading rate should have been used.

The imperfection forces asymmetric crack propagation before reaching the peak load. When the two cracks have met, which occurs roughly at peak load, the deformation patterns are mainly symmetric. It is noted that for the finer (i.e. more brittle) mesh more rotation of the specimen is observed.

### 3.5.3 Example 3 : Impact biaxial test

The third example of an impact biaxial test is a mode-II localisation problem. A sample is subjected to a dynamic pressure load, which forces a shear band failure pattern for a von Mises softening plasticity model. The biaxial test problem is sketched in Figure 3.14, including geometry, material and loading data. At the top of the sample a dynamic pressure load is applied. In addition a small horizontal load, which is 10% of the maximum vertical load, has been applied at the upper edge of the specimen. This load is static and forces the emergence of an asymmetric failure mode. The boundary conditions along the vertical sides are traction-free, while the bottom of the sample is rigid ( $u_x = 0$  and  $u_y = 0$ ). To ensure that all vertical displacements at the top of the sample displaced the same amount linear constraint equations have been used. The material parameter set is used in combination with a von Mises softening plasticity model (eq.(3.63)), as given in Figure 3.14 with  $\bar{\sigma}_0$  the uniaxial yield stress. Figure 3.15 shows that three discretisations have been used, namely a 3×6-mesh, a 6×12-mesh and a 12×24-mesh, where for the mesh-sensitivity analysis with a classical strain-softening model each quadrilateral is composed of four quadratic, crossed triangular elements. This element lay-out has been used because of the satisfaction of the incompressibility constraint in isochoric plasticity and because of the alignment of the element boundaries with the expected direction of the shear band on the basis of analytical expressions (see Appendix 3A). Here, it is recalled that mesh dependence is not only observed for the width of the shear band but also

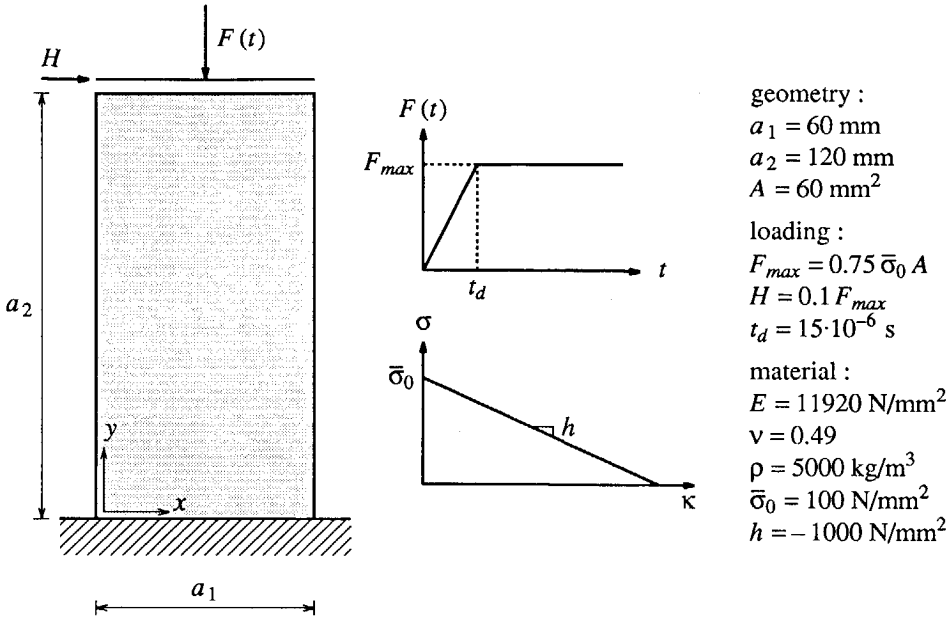


Figure 3.14 Example 3 : Impact biaxial test.

with respect to the orientation of the mesh lines (mesh alignment). For the plane-strain condition of the sample with a von Mises yield function and  $\nu = 0.49$  a shear band occurs with an inclination angle of  $45.0^\circ$  (eq.(3A.21)), so that the intrinsic bias of these element meshes is minimised and mesh-alignment problems are avoided. However, if the plane-stress condition is considered for the same meshes a spurious numerical result will be obtained because the inclination angle of the shear band is then  $35.3^\circ$  (eq.(3A.20)) which is not aligned with the mesh. To avoid mesh-alignment problems for classical strain-softening models a search algorithm, based on the characteristic tangent matrix  $Q_c$  from Appendix 3A (Larsson 1990), should be implemented to determine the inclination angle of the shear band. Next, mesh adaptation techniques are necessary to minimise the intrinsic bias of the mesh. This issue will be taken up again in the Chapters 5, 6 and 7.

The longitudinal pressure wave propagates in a linear-elastic manner through the specimen. After reflection at the lower boundary the returning wave causes softening over the total width of the specimen. The specimen starts to bulge for a short time after reflection. Next, a gradual development of the shear band occurs and all deformation is trapped in the shear band.

Again, for the classical continuum model the width of the shear band is determined by the element size as can be seen from the displacements in Figure 3.16. All deformation is

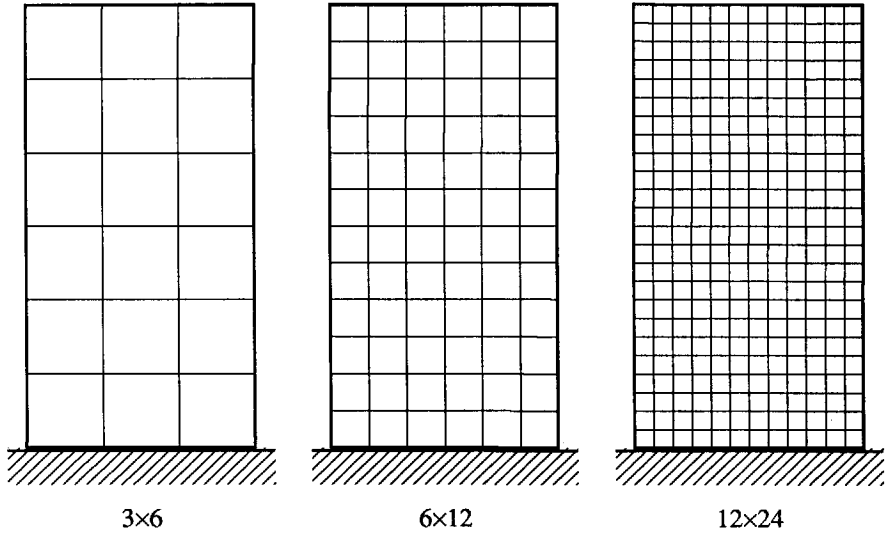


Figure 3.15 Finite element configurations for biaxial test.

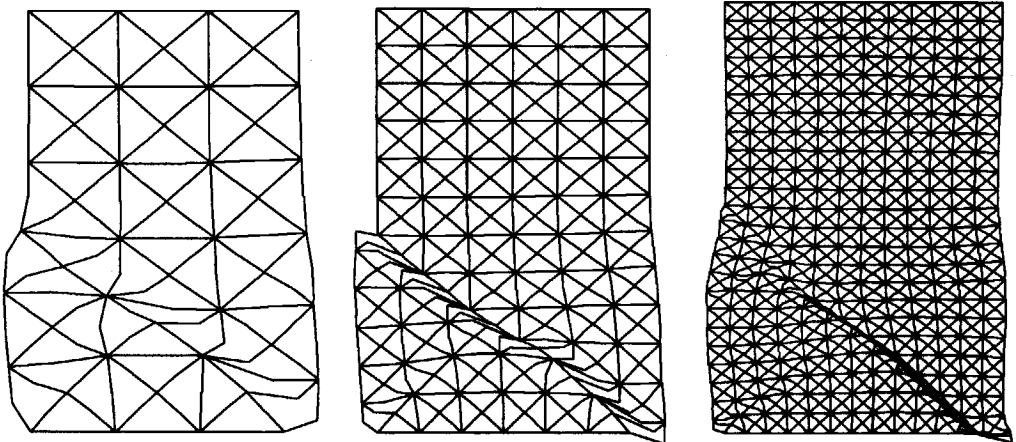


Figure 3.16 Total displacement patterns ( $3 \times 6$ -mesh:  $t = 0.165 \cdot 10^{-3} s$ ;  $6 \times 12$ -mesh :  $t = 0.150 \cdot 10^{-3} s$ ;  $12 \times 24$ -mesh :  $t = 0.1275 \cdot 10^{-3} s$ , FA = 15).

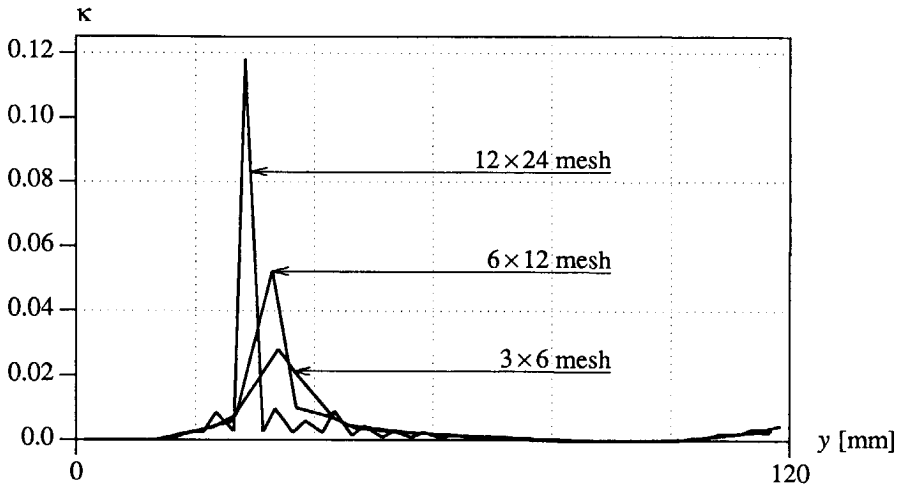


Figure 3.17 Equivalent plastic strain  $\kappa$  in centre section ( $x = 30$  mm) of the sample ( $t = 0.1275 \cdot 10^{-3}$  s).

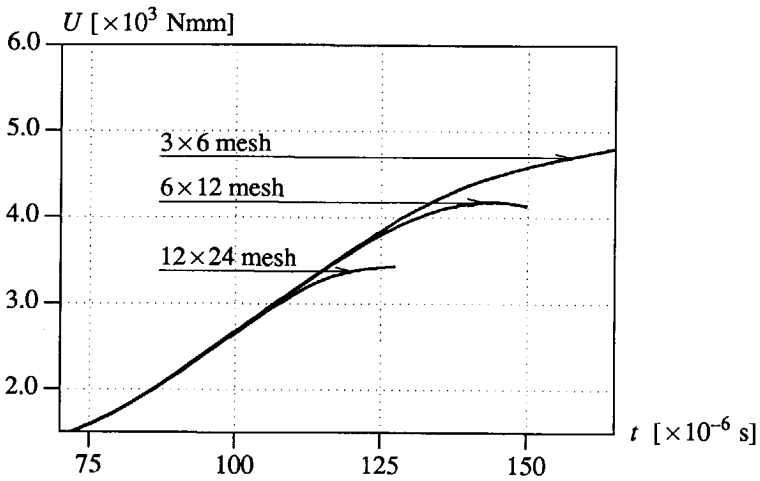


Figure 3.18 Energy consumption in the sample.

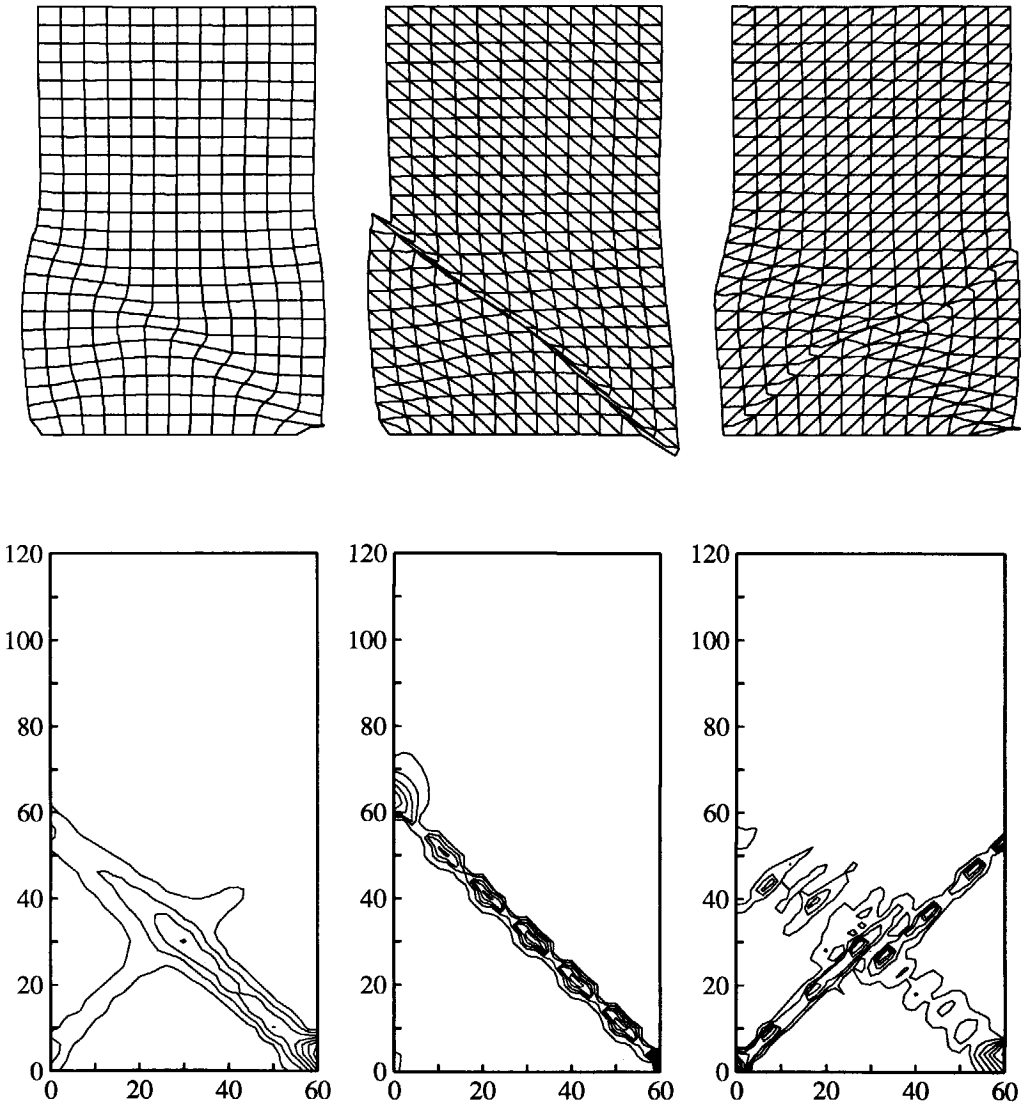


Figure 3.19 Displacements (top - FA = 15) and equivalent plastic strains (bottom)  
 - plane strain  $t = 0.15 \cdot 10^{-3}$  s :  
 Left : 288 quadrilateral elements  
 Centre : 576 triangular elements with diagonals aligned to shear band  
 Right : 576 triangular elements with diagonals perpendicular to shear band

localised along a line of integration points with an orientation angle of  $45^\circ$ . Mesh dependence is also obvious from the equivalent plastic strain profiles plotted in Figure 3.17 for the vertical centre cross-section of the specimen. In one integration point almost the total deformation of the cross-section is consumed. The behaviour becomes more brittle upon mesh refinement, which can also be observed from Figure 3.18 in which the energy consumption in the sample is plotted as a function of time. The energy consumption approaches zero (purely brittle) when the number of elements increases. So, the results for a mode-II localisation problem show the same mesh-sensitive behaviour as the mode-I localisation problems (Examples 1 and 2).

For the mesh-sensitivity analyses in the Figures 3.16 to 3.18 we have taken biased meshes with quadrilaterals, subdivided into four triangular elements. To investigate the influence of the direction of the mesh lines on the results we have discretised the sample into a mesh with 288 quadratic quadrilaterals ( $3 \times 3$  integration), a biased mesh with 576 quadratic triangular elements and an unbiased mesh with the same number of elements, of which the mesh lines lie in a direction perpendicular to the forced shear band. For the mesh-refinement analyses we observed that an increase of the number of integration points reduces the width of the shear band and causes the difference in the results. While the number of integration points for the three meshes, used to assess the influence of the orientation of the mesh lines, is almost the same (2592,2304,2304) the response is completely different. In Figure 3.19 the problem of mesh alignment is demonstrated by means of the deformed meshes and the contour plots of the equivalent plastic strains. For the mesh with quadrilateral elements the integration points lie on a line under  $45^\circ$  and a reasonable response is obtained. On the other hand, the analysis with the biased mesh show a much smaller localisation band because of the "cooperation" of the mesh lines with the shear band. The third analysis with the unbiased mesh offers results which are in contradiction with a physically realistic solution, namely driven by the mesh lines a dominant shear band develops perpendicular to the expected one. So, in conclusion, a proper solution technique must not only be aimed on an objective prediction of the width of the localisation zone, but must also yields results which are invariant to the direction of the mesh lines.

### 3.6 SOLUTION TECHNIQUES

As the classical continuum framework does not recognise any characteristic dimensions, it is impossible to capture the localisation phenomenon properly. The absence of such a length scale parameter leaves the width of the localisation band unspecified. Furthermore, in section 3.2 from a dynamic point of view propagating waves have been proven to be non-dispersive, i.e. the classical continuum is not able to transform arbitrarily shaped waves into stationary localisation waves as observed in experiments. To introduce an internal length scale, and accordingly, to make wave propagation dispersive, extra terms are necessary in the continuum formulation. At the same time the inclusion of these terms can cause the field equations to

remain well-posed after the onset of localisation. In the literature a few solution techniques have been suggested. Here, four methods will be discussed. The first method is a heuristic approach, while the methods two, three and four are rooted in a firm fundamental mathematical basis.

### 1) Fracture energy model

This solution technique is developed for mode-I fracture but can also be used for a mode-II shear band problem. The model is based on the assumption that the area under the softening curve can be regarded as a material parameter (Bažant and Oh 1983, Willam 1984). This area represents the fracture energy defined per unit area as

$$G_f = \int \sigma du = \int \sigma \epsilon ds . \quad (3.71)$$

In the Examples 1 to 3 we have seen that localisation occurs in one row of integration points (for quadratic elements). To guarantee a mesh-objective consumption of energy the softening modulus should be made a function of the element size. If we have linear strain softening and integrate eq.(3.71) under the assumption that the strain is constant in the localisation zone the softening modulus is given by

$$h = - \frac{w f_t^2}{2G_f} , \quad (3.72)$$

in which  $w$  is a function of the element size. Rots (1988) has given an overview for the crack band  $w$  for different types of elements.

A disadvantage of the fracture energy approach is that the numerical description of the strain-softening material is changed while the mathematical description is left unchanged. So, the underlying continuum description is still ill-posed, so that a dependence of the results on the finite element discretisation is still present. With the fracture energy model we can obtain mesh-objective results with regard to the energy consumption but we are not able to exclude the influence through mesh alignment. In fact, the method should be used in combination with a search algorithm to determine the orientation of localisation bands. By means of mesh adaptation the influence of mesh alignment can be minimised. Of course, this procedure is only possible when analytical solutions for the orientation of localisation bands can be found, or at least the failure mode can be predicted.

Another problem is the occurrence of multiple localisation zones (e.g. multiple cracking), which cannot be analysed properly with the fracture energy model. Moreover, the dependence of  $w$  on the element size limits the maximum size of the element in order to prevent snap back behaviour at a local, integration point level.



## 2) *Rate-dependent model*

An entirely different approach is the inclusion of rate dependence in the constitutive equations (Wu and Freund 1984, Needleman 1988, Lorent and Prevost 1990). Extra higher-order time derivative terms prevent the field equations from becoming elliptic and keep the problem well-posed. Dispersive waves and an implicit length scale enables the rate-dependent continuum to capture localisation of deformation. For mode-I fracture this method is discussed in Chapter 4, while mode-II shear banding is analysed by means of viscoplastic models in Chapter 6.

## 3) *Gradient model*

The continuum description can also be enriched by inclusion of higher-order gradient terms. Spatial derivatives of the inelastic state variables enter the constitutive equations. This can be done by means of integral expressions of the inelastic state variables. Bažant et al. (1984) have proposed a non-local strain model and recently Pijaudier-Cabot and Bažant (1987) have reported about a non-local damage model. Here, we do not use the integral expression but we define a dependence of the yield function on the second-order gradient of the equivalent plastic strain (Mühlhaus and Aifantis 1991, de Borst and Mühlhaus 1992). The system of equations remains well-posed with real wave speeds. In Chapter 5 this model is used for mode-I as well as for mode-II localisation problems.

## 4) *Cosserat continuum model*

The micro-polar (Cosserat) continuum model is based on the idea of a macro-structure subdivided into micro-elements (Cosserat and Cosserat 1909, Günther 1958, Schaefer 1962, Mindlin 1963 and 1964, Mühlhaus and Vardoulakis 1987). This model closely connects to the heterogeneous character of softening materials as sands, rock and concrete. A length scale is introduced by a finite size of the micro-elements. The regularisation effect comes from the introduction of couple-stresses and micro-rotations, so that extra rotational degrees-of-freedom are defined. The Cosserat continuum model will be discussed in Chapter 7 and it will be shown that mode-II localisation problems can be analysed properly.

### APPENDIX 3A : SHEAR BAND INCLINATION IN BIAxIAL TEST

Analytical results for the inclination of the shear band have been obtained by a number of authors, including Rudnicki and Rice (1975), Larsson (1990) and Runesson et al. (1991). For the classical continuum modelling of strain softening information about the orientation angle of the shear band is very important in order to align the element mesh along the shear band. For continuum models with extra or higher-order terms mesh alignment may not affect the results and analytical data are used for validation of the models.

In classical rate-independent continua the shear band is considered as a surface discontinuity. When the material model includes strain softening and/or non-associated plastic flow a continuous field  $\mathbf{v}_1$  can abruptly change in a discontinuous solution with the primary field  $\mathbf{v}_1$  and a bifurcated field  $\mathbf{v}_2$ . Across the characteristic surface  $C$  the velocity field is discontinuous. However, the difference  $[[\mathbf{v}]] = \mathbf{v}_2 - \mathbf{v}_1$  is constant along  $C$  which may be expressed as

$$d[[\mathbf{v}]] = \frac{\partial [[\mathbf{v}]]}{\partial \mathbf{x}} d\mathbf{x} = 0, \quad (3A.1)$$

where  $\mathbf{x}$  is the position vector and  $d\mathbf{x}$  is the tangent vector of  $C$ . If we define the unit vector  $\bar{\mathbf{n}}$  normal to  $C$  in the  $xy$ -plane we have  $\bar{\mathbf{n}} d\mathbf{x} = 0$ . The general solution of eq.(3A.1) is (Rice 1976, Runesson et al. 1991)

$$\frac{\partial [[\mathbf{v}]]}{\partial \mathbf{x}} = \xi \bar{\mathbf{n}}, \quad (3A.2)$$

in which  $\xi$  is an arbitrary vector. If we write eq.(2.2) in rate and tensor format we obtain

$$[[\dot{\epsilon}_{ij}]] = 1/2 ([[ \dot{v}_{i,j} ]] + [[ \dot{v}_{j,i} ]]). \quad (3A.3)$$

The jump of strain rate across  $C$  is obtained by combination of eq.(3A.2) and (3A.3) as

$$[[\dot{\epsilon}]] = 1/2 (\xi \bar{\mathbf{n}} + \bar{\mathbf{n}} \xi). \quad (3A.4)$$

Balance of linear momentum across the surface discontinuity  $C$  requires (see also section 3.3)

$$[[\dot{\sigma}]] \bar{\mathbf{n}} = 0, \quad (3A.5)$$

which may be combined with eq.(2.4) to give

$$[[\mathbf{D}_c \dot{\epsilon}]] \bar{\mathbf{n}} = 0, \quad (3A.6)$$

in which the assumption of a plastic response at both sides of  $C$  is made. Combination of eq.(3A.4) and (3A.6) leads to

$$\mathbf{Q}_c \xi = 0, \quad (3A.7)$$

in which  $\mathbf{Q}_c$  is the characteristic tangent stiffness matrix that is defined as

$$\mathbf{Q}_c = \bar{\mathbf{n}} \mathbf{D}_c \bar{\mathbf{n}} . \quad (3A.8)$$

Eq.(3A.7) is Hill's bifurcation criterion (Hill 1962) for a discontinuous velocity field with a velocity gradient. A non-trivial solution of eq.(3A.7) is possible when  $\mathbf{Q}_c$  is singular which implies

$$\det(\mathbf{Q}_c) = 0 . \quad (3A.9)$$

The elasto-plastic tangent stiffness matrix  $\mathbf{D}_c$  follows from eq.(3.60)

$$\mathbf{D}_c = \mathbf{D}_e - \frac{\mathbf{D}_e \mathbf{m} \mathbf{n}^T \mathbf{D}_e}{h + \mathbf{n}^T \mathbf{D}_e \mathbf{m}} . \quad (3A.10)$$

The characteristic tangent stiffness matrix  $\mathbf{Q}_c$  differs for the plane-strain and the plane-stress condition because the elastic stiffness matrix  $\mathbf{D}_e$  differs and the vectors  $\mathbf{m}$  and  $\mathbf{n}$  differ in the number of components.

It is noted that for this analysis the extra or higher-order terms in the constitutive model, which are necessary to regularise the mesh-dependence problem as described in the Chapters 4-6, have been neglected. This seems reasonable because at the onset of softening and initiation of the shear band these terms have no contribution yet. The higher-order terms act as a singular perturbation of the conventional plasticity model. Only the micro-polar effects in the Cosserat model (Chapter 7) are present in the elastic phase, which results in a different elastic stiffness matrix  $\mathbf{D}_e$  (eq.(7.12)).

We consider the orientation of the shear band in the interior of the specimen and neglect the change of shear band orientation at free surfaces, due to stationary Rayleigh waves, and at interfaces, due to stationary Stonely waves (Benallal et al. 1991, Needleman and Ortiz 1991). If we elaborate eq.(3A.9) according to Runesson et al. (1991) expressions for the critical hardening/softening modulus  $h_{cri}$  are obtained of the following format

$$\frac{h_{cri}}{2\mu} = f(\bar{\mathbf{n}}, \mathbf{n}, \mathbf{m}, \mathbf{v}) . \quad (3A.11)$$

If we introduce the constraint  $\bar{n}_2^2 = 1 - \bar{n}_1^2$  for the unit normal vector, an extreme value for  $h_{cri}$  can be obtained by differentiating eq.(3A.11) to the direction component  $\bar{n}_1$

$$\frac{d(h_{cri}/2\mu)}{d(\bar{n}_1^2)} = 0 . \quad (3A.12)$$

Because  $d^2(h_{cri}/2\mu)/d(\bar{n}_1^2)^2 < 0$  a maximum value for  $h_{cri}$  is obtained. From eq.(3A.12) we solve  $\bar{n}_1^2$  and because

$$\tan^2 \Theta = \frac{\bar{n}_1^2}{\bar{n}_2^2} , \quad (3A.13)$$

in which  $\Theta$  is the angle between y-axis and the normal vector  $\bar{n}$ , general expressions for the inclination angle can be derived for plane-stress conditions as

$$\tan^2 \Theta = -\frac{n_1(m_1 - m_2) + m_1(n_1 - n_2)}{n_2(m_1 - m_2) + m_2(n_1 - n_2)} \quad (3A.14)$$

and for plane-strain conditions as

$$\tan^2 \Theta = -\frac{n_1(m_1 - m_2) + m_1(n_1 - n_2) + \nu(n_3(m_1 - m_2) + m_3(n_1 - n_2))}{n_2(m_1 - m_2) + m_2(n_1 - n_2) + \nu(n_3(m_1 - m_2) + m_3(n_1 - n_2))} \quad (3A.15)$$

The von Mises yield criterion is given by the eqs.(3.63) and (3.64) and because of associative flow we have  $n_i = m_i$ . For a plane-stress condition we derive from eq.(3A.14)

$$\tan^2 \Theta = -\frac{s_1}{s_2}, \quad (3A.16)$$

and similar for a plane-strain condition we obtain from eq.(3A.15)

$$\tan^2 \Theta = -\frac{(1 - \nu)s_1 - \nu s_2}{\nu s_1 - (1 - \nu)s_2} \quad (3A.17)$$

The Drucker-Prager yield criterion is defined by the eqs.(3.65)-(3.67). Substitution of  $n_i$  and  $m_i$  into the eqs.(3A.14) and (3A.15) yields for plane-stress conditions

$$\tan^2 \Theta = -\frac{9s_1 + \sqrt{3J_2}(\alpha + \alpha_\psi)}{9s_2 + \sqrt{3J_2}(\alpha + \alpha_\psi)} \quad (3A.18)$$

and for plane-strain conditions

$$\tan^2 \Theta = -\frac{9(s_1 + \nu s_3) + (1 + \nu)\sqrt{3J_2}(\alpha + \alpha_\psi)}{9(s_2 + \nu s_3) + (1 + \nu)\sqrt{3J_2}(\alpha + \alpha_\psi)} \quad (3A.19)$$

Two cases have been treated in this thesis in which proper numerical results, i.e. in accordance with the analytical solutions for the orientation of the material instability, have been obtained because of the use of enriched continuum models for strain softening.

#### *Case 1 : Biaxial test with von Mises model (configuration in section 3.5.3)*

In Figure 3.14 the biaxial test problem is given with a vertical pressure load and a small horizontal load, which forces the occurrence of one shear band, starting in the bottom right corner of the specimen. With Poisson's ratio  $\nu = 0.49$  and a vertical stress  $\sigma_2 = -\sigma$  we obtain

plane stress :

$$\sigma_1 = 0; \sigma_2 = -\sigma \rightarrow s_1 = 0.333\sigma; s_2 = -0.667\sigma :$$

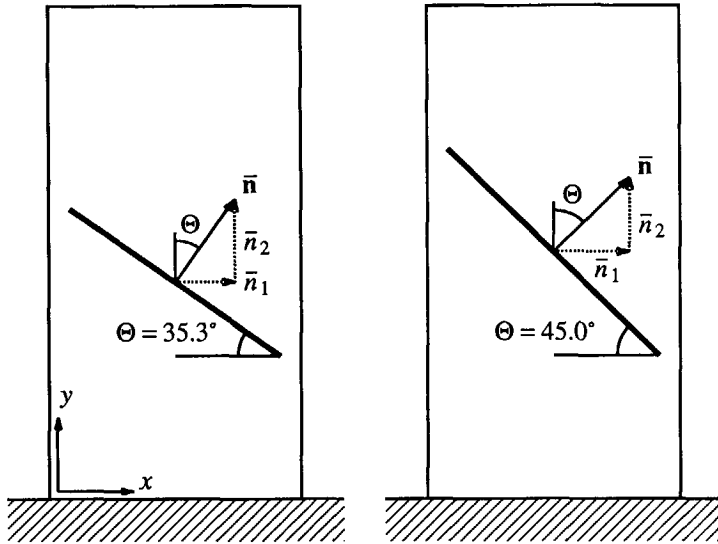


Figure 3A.1 Shear band inclination for plane-stress (left) and plane-strain (right) with a von Mises yield criterion.

$$\tan^2 \Theta = 0.5 \rightarrow \Theta = 35.3^\circ. \tag{3A.20}$$

plane strain :

$$\sigma_1 = 0 ; \sigma_2 = -\sigma ; \sigma_3 = \nu(\sigma_1 + \sigma_2) = -0.49 \sigma \rightarrow s_1 = 0.497 \sigma ; s_2 = -0.503 \sigma :$$

$$\tan^2 \Theta = 1.0 \rightarrow \Theta = 45.0^\circ. \tag{3A.21}$$

The analytical values for  $\Theta$  have been plotted in Figure 3A.1.

*Case 2 : Biaxial test with Drucker-Prager model (configuration in section 5.4.3)*

A different configuration has been used for the analysis with the Drucker-Prager model, in which asymmetry is not incorporated via the loads but via the boundary conditions. The orientation of the shear band depends on the stress state in the specimen and the material properties. From the numerical simulations we observe that for  $\phi = 20^\circ$  the shear band initiates in the bottom right corner because  $h_{cri}/2\mu$  is larger and therefore more critical for this shear band, while for  $\phi = 30^\circ$  the situation is the other way round. We consider the plane-strain situation and with  $\nu = 0.2$  and  $\psi = 0^\circ$  ( $\alpha_{\psi} = 0$ ) we obtain

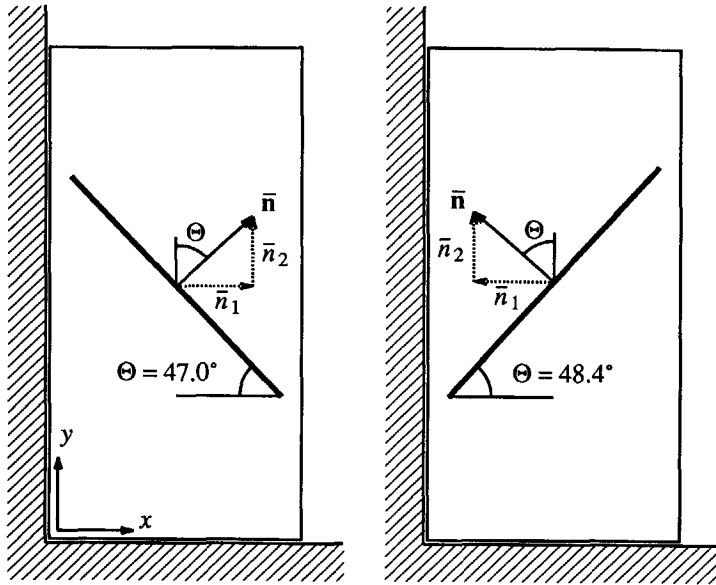


Figure 3A.2 Shear band inclination for friction angle  $\phi = 20^\circ$  (left) and  $\phi = 30^\circ$  (right) with a Drucker-Prager yield criterion.

$\phi = 20^\circ$  (initiation bottom right) :

$$\sigma_1 = 0; \sigma_2 = -\sigma; \sigma_3 = -\nu\sigma \rightarrow s_1 = 0.4\sigma; s_2 = -0.6\sigma; s_3 = 0.2\sigma; \sqrt{3J_2} = 0.92\sigma :$$

$$\tan^2 \Theta = 1.15 \rightarrow \Theta = 47.0^\circ. \quad (3A.22)$$

$\phi = 30^\circ$  (initiation bottom left) :

$$\sigma_1 = -\nu\sigma; \sigma_2 = -\sigma; \sigma_3 = -\nu\sigma \rightarrow s_1 = 0.267\sigma; s_2 = -0.533\sigma; s_3 = 0.267\sigma; \sqrt{3J_2} = 0.8\sigma :$$

$$\tan^2 \Theta = 1.27 \rightarrow \Theta = 48.4^\circ. \quad (3A.23)$$

The analytical values for  $\Theta$  have been plotted in Figure 3A.2.

## 4. RATE-DEPENDENT CRACK MODEL

The inclusion of strain rate dependence in the constitutive modelling of materials seems natural under transient loading conditions. However, also under quasi-static conditions final failure is accompanied by high strain rates. So, from a physical point of view the inclusion of rate effects is an important feature for a proper modelling of fracture. However, in this chapter we will pay more attention to the mathematical arguments for the inclusion of viscous or higher-order time derivative terms. The use of rate-dependent models in the context of mesh sensitivity has been reported earlier by Wu and Freund (1984), Needleman (1988), Loret and Prevost (1990) and Sluys and de Borst (1991,1992).

Rate dependence is introduced to prevent the character of the set of equations that describes the dynamic motion of the softening solid from becoming elliptic. In the rate-dependent, strain-softening continuum we obtain a wave-like solution with real wave speeds. Well-posedness of the initial value problem is preserved and meaningful results can be obtained for localised zones of intense straining. It is essential for the solution of the mesh-sensitivity problem that rate dependence naturally introduces an internal length scale into the initial value problem, although the constitutive equations do not explicitly contain a parameter with the dimension of length.

In this chapter a rate-dependent smeared crack model will be treated, including the algorithmic aspects necessary for numerical application. The existence of the length scale is proven from an analysis of dispersive waves. The one-dimensional bar in tension (Example 1) and the impact tensile test on a double-notched specimen (Example 2), treated in Chapter 3, will be analysed for the rate-dependent model to assess the performance with respect to mesh refinement. Finally, a comparison is made with a rate-dependent power law model, which has been used by Needleman (1988).

### 4.1 FORMULATION OF A RATE-DEPENDENT CRACK MODEL

The strain-softening model of section 3.2 only shows a dependence of the stress on the inelastic strain ( $\sigma = f(\epsilon_i)$ ). Here, we propose an enhanced model that exhibits a dependence of the stress on the inelastic or crack strain as well as on the crack strain rate, written in the rate format

$$\dot{\sigma} = f' \dot{\epsilon}_{cr} + m \frac{\partial \dot{\epsilon}_{cr}}{\partial t}, \quad (4.1)$$

where  $\dot{\epsilon}_{cr}$  denotes the crack strain rate and  $m$  is a rate-sensitivity parameter. Note that rate dependence is chosen as a function of the crack strain  $\epsilon_{cr}$  and not of the total strain. When a linear strain-softening function is utilised as in this study

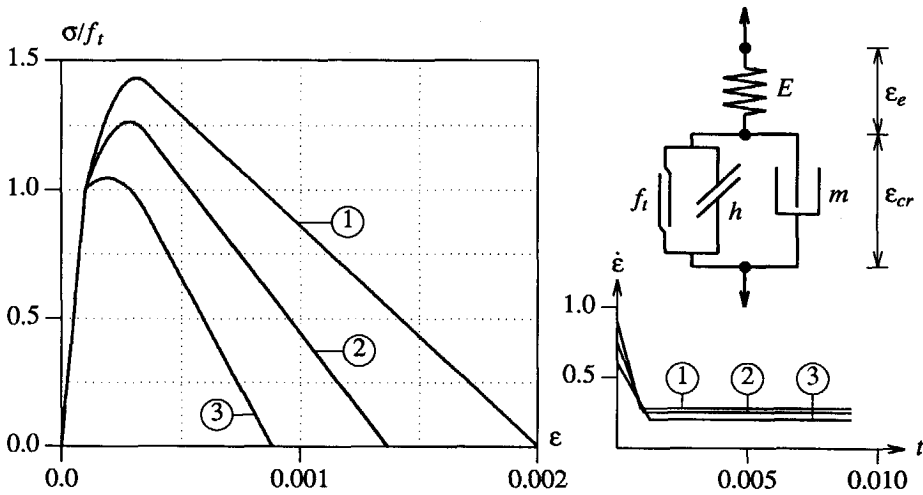


Figure 4.1 Rate-dependent crack model :  
 Left : Stress-strain curves for different imposed strain rates.  
 Top right : Schematic representation of the model.  
 Bottom right : Imposed strain rates.

$$f(\epsilon_{cr}) = f_t + h\epsilon_{cr} \quad \text{for } 0 < \epsilon_{cr} < -f_t/h \tag{4.2}$$

then eq.(4.1) becomes

$$\dot{\sigma} = h \dot{\epsilon}_{cr} + m \frac{\partial \dot{\epsilon}_{cr}}{\partial t} . \tag{4.3}$$

In eqs.(4.2) and (4.3)  $f_t$  is the initial tensile strength under static loading conditions. For unloading a secant modulus without rate dependence is used.

In Figure 4.1 computed stress-strain curves are shown for various imposed strain rates. For these curves the material data set from Figure 3.4 for the one-dimensional bar in tension (Example 1) is used with  $h = -5000 \text{ N/mm}^2$  and  $m = 0.2 \text{ Ns/mm}^2$ . The curves show an increase of the tensile strength under dynamic loading, which is also observed in several experiments summarised by Körmeling (1986). In these experiments the increase of tensile strength is measured as a function of a constant strain rate. However, these test series and the numerical simulations described in the subsequent section show that the strain rate not only varies in time but also displays large gradients along the localisation zone. It is therefore difficult to derive the material rate sensitivity parameter  $m$  from experimental data and semi-inverse modelling techniques are needed. As regards the increase of fracture energy per unit area and the ultimate strain less experimental support exists at present (cf. section 3.1).



The rate-dependent model has been implemented in the fixed smeared crack concept discussed in section 3.4.1. Now, in the crack not only a crack stress  $\mathbf{t}_{cr}$  but also a rate-dependent stress  $\mathbf{t}_{rd}$  is transmitted in the crack. We define the rate-dependent stress rate as

$$\dot{\mathbf{t}}_{rd} = \mathbf{M} \ddot{\mathbf{e}}_{cr}, \quad (4.4)$$

in which  $\mathbf{M} = \text{diag} [m, 0]$ , so that only mode-I rate effects are considered. The relation between local and global stress rate now becomes (cf. eq.(3.44))

$$\dot{\mathbf{t}}_{cr} + \dot{\mathbf{t}}_{rd} = \mathbf{N}^T \dot{\boldsymbol{\sigma}}. \quad (4.5)$$

If we substitute the eqs.(3.46) and (4.4) into eq.(4.5) we obtain

$$\mathbf{D}_{cr} \dot{\mathbf{e}}_{cr} + \mathbf{M} \ddot{\mathbf{e}}_{cr} = \mathbf{N}^T \dot{\boldsymbol{\sigma}}. \quad (4.6)$$

Again, premultiplying eq.(3.47) by  $\mathbf{N}^T$  and combining the result with eq.(4.6) yields the relation between the local crack strain rate and the global strain rate

$$\dot{\mathbf{e}}_{cr} = (\mathbf{N}^T \mathbf{D}_e \mathbf{N} + \mathbf{D}_{cr})^{-1} [\mathbf{N}^T \mathbf{D}_e \dot{\boldsymbol{\epsilon}} - \mathbf{M} \ddot{\mathbf{e}}_{cr}]. \quad (4.7)$$

This equation can be substituted in eq.(3.47), which gives the global constitutive equation

$$\dot{\boldsymbol{\sigma}} = \mathbf{D}_e [\mathbf{I} - \mathbf{N} (\mathbf{N}^T \mathbf{D}_e \mathbf{N} + \mathbf{D}_{cr})^{-1} \mathbf{N}^T \mathbf{D}_e] \dot{\boldsymbol{\epsilon}} + \mathbf{D}_e \mathbf{N} [\mathbf{N}^T \mathbf{D}_e \mathbf{N} + \mathbf{D}_{cr}]^{-1} \mathbf{M} \ddot{\mathbf{e}}_{cr}. \quad (4.8)$$

For sake of simplicity only one crack has been considered in this derivation, but it is possible that due to the rotation of principal stresses new cracks arise. The rate-dependent crack strain is then decomposed into separate contributions from the multi-directional cracks.

## 4.2 WAVE PROPAGATION IN A RATE-DEPENDENT BAR

We investigate wave propagation by considering the set of equations for a one-dimensional rate-dependent bar. If we combine the constitutive equation, given by eq.(4.3), with the kinematic equation eq.(3.4), take  $\dot{\mathbf{e}}_{cr} = \dot{\boldsymbol{\epsilon}} - \dot{\mathbf{e}}_e$  and  $\dot{\mathbf{e}}_e = \dot{\boldsymbol{\sigma}}/E$  and differentiate the results with respect to  $x$  we obtain

$$\frac{\partial}{\partial x} \left( \frac{m}{E} \frac{\partial \dot{\boldsymbol{\sigma}}}{\partial t} + \frac{E+h}{E} \dot{\boldsymbol{\sigma}} \right) = \frac{\partial^2}{\partial x^2} \left( h v + m \frac{\partial v}{\partial t} \right). \quad (4.9)$$

If we use the equation of motion eq.(3.3) we obtain the third-order differential equation for the one-dimensional rate-dependent strain-softening bar

$$m \left( \frac{1}{c_e^2} \frac{\partial^3 v}{\partial t^3} - \frac{\partial^3 v}{\partial x^2 \partial t} \right) + \frac{E+h}{c_e^2} \frac{\partial^2 v}{\partial t^2} - h \frac{\partial^2 v}{\partial x^2} = 0. \quad (4.10)$$

If  $m \rightarrow 0$  the classical rate-independent wave equation (3.8) is recovered with imaginary

characteristics and imaginary wave speeds (cf. section 3.2). We can investigate the type of the wave equation by means of its characteristics. Therefore we consider the variation of two second-order derivative terms of  $v$

$$d\left(\frac{\partial^2 v}{\partial t^2}\right) = \frac{\partial^3 v}{\partial t^3} dt + \frac{\partial^3 v}{\partial x \partial t^2} dx \quad (4.11)$$

$$d\left(\frac{\partial^2 v}{\partial x \partial t}\right) = \frac{\partial^3 v}{\partial x \partial t^2} dt + \frac{\partial^3 v}{\partial x^2 \partial t} dx. \quad (4.12)$$

Combination of eq.(4.11) and (4.12) and the wave equation for the rate-dependent bar eq.(4.10) yields a system of three third-order differential equations with a characteristic determinant

$$D = \begin{bmatrix} m/c_e^2 & 0 & -m \\ dt & dx & 0 \\ 0 & dt & dx \end{bmatrix} = m((1/c_e^2)dx^2 - dt^2). \quad (4.13)$$

With  $D = 0$  the characteristics are equal to the elastic bar velocity  $\pm c_e$  and remain real when strain softening occurs. This means that the wave equation remains hyperbolic and the initial value problem is well-posed. The characteristics no longer equal the physical wave speed in the rate-dependent bar. This is only the case if the second-order terms in eq.(4.10) are absent ( $m \rightarrow \infty$ ). Then the wave speed exactly equals the elastic wave velocity  $c_e$  as will be proved below by a dispersion analysis. So, the suggestion in literature (Needleman 1988, Loret and Prevost 1990) that in a rate-dependent continuum disturbances due to inelastic effects travel with the elastic wave speed is correct for the limiting case.

To investigate the dispersive character of wave propagation in the rate-dependent, softening continuum a general solution for a single linear harmonic wave with angular frequency  $\omega$  and wave number  $k$  is assumed to be of a form given by eq.(3.15). The dispersion relation in a non-explicit notation can be obtained by substitution of eq.(3.15) into eq.(4.10)

$$(\rho m \omega^3 - m E k^2 \omega) i - \rho(E + h)\omega^2 + h E k^2 = 0. \quad (4.14)$$

If we consider  $\omega$  and  $k$  to be real no solution is possible. Eq.(4.14) can only be satisfied if  $k$  is complex and therefore  $k$  is set equal to  $k_r + \alpha i$ . This complex value for  $k$  means that the harmonic wave is attenuated exponentially as it proceeds through the bar and the expression for  $v(x, t)$  may now be written as

$$v(x, t) = A e^{-\alpha x} e^{i(k_r x - \omega t)}. \quad (4.15)$$

If we equate real and imaginary parts of eq.(4.14) we obtain respectively

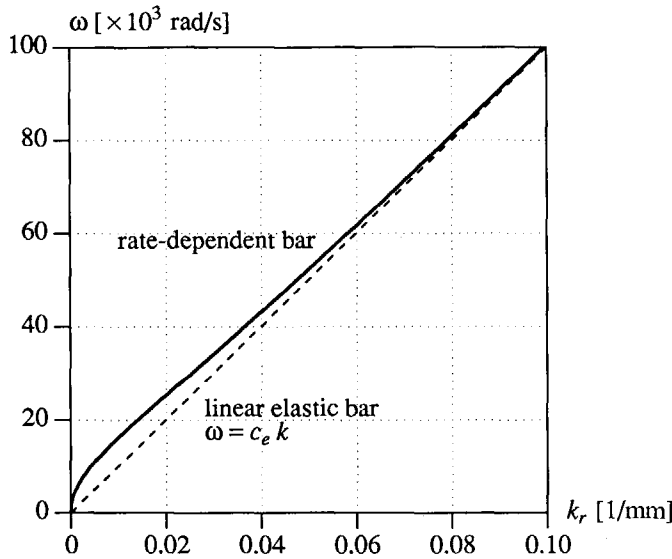


Figure 4.2 Dispersion relation  $\omega - k_r$  for a rate-dependent bar.

$$k_r^2 = \frac{\rho\omega^2}{2E} \left( \frac{-(m^2\omega^2 + h^2 + Eh) + ((m^2\omega^2 + h^2 + Eh)^2 + (mE\omega)^2)^{1/2}}{m^2\omega^2 + h^2} \right) \quad (4.16)$$

and

$$\alpha^2 = \frac{\rho\omega^2}{2E} \left( \frac{+(m^2\omega^2 + h^2 + Eh) + ((m^2\omega^2 + h^2 + Eh)^2 + (mE\omega)^2)^{1/2}}{m^2\omega^2 + h^2} \right). \quad (4.17)$$

In the Figures 4.2, 4.3 and 4.4 the results for the dispersive wave propagation are plotted for the parameter set of Example 1 in section 4.4.1. In Figure 4.2 the dispersion relation  $\omega = f(k_r)$  shows that waves in a rate-dependent softening continuum behave nearly similar to waves in a linear elastic continuum. If  $k_r$  approaches zero, i.e. for waves of a very low frequency, the slope of the dispersion curve becomes infinite for softening ( $h < 0$ ). This means that the quotient  $\omega/k_r \rightarrow \infty$  for a static response. In the rate-dependent, strain-softening bar wave propagation is dispersive because the phase velocity  $c_f = \omega/k_r$  is a function of  $\omega$  (Figure 4.3), in contrast to the classical strain-softening bar in which  $c_f$  is independent of  $k$  (cf. section 3.2). The dispersion property implies that the rate-dependent strain-softening continuum is able to transform the shape of travelling waves because the harmonic components have different phase velocities. In localisation analyses this has the advantageous effect that arbitrarily shaped waves can be transformed in the localisation zone.

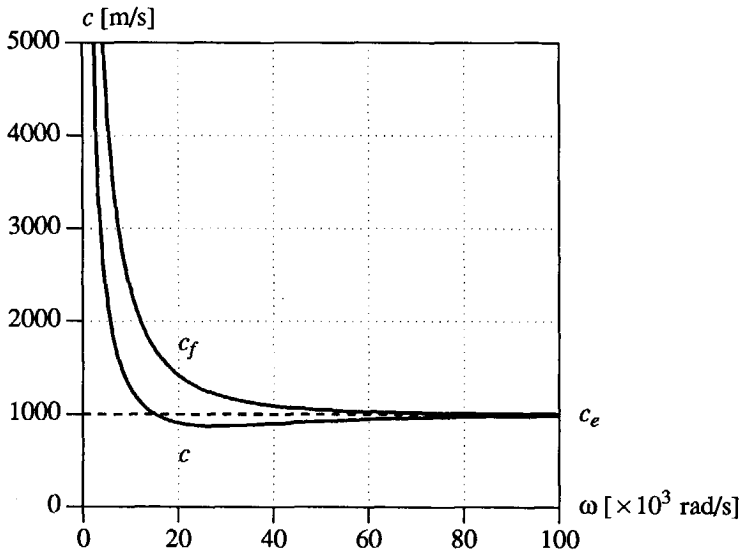


Figure 4.3 Phase and group velocity as a function of  $\omega$  for a rate-dependent bar.

The physical velocity of propagation of a pulse is not determined by the phase velocity  $c_f$  of an individual wave but by a superposition of harmonic waves. The speed of a group of harmonic waves is called the group velocity and can be determined by considering two harmonic waves with a mutual difference in wave number  $\Delta k$  and in angular frequency  $\Delta\omega$ . Superposition of the two waves produces an envelope wave which travels with velocity  $\Delta\omega/\Delta k$  (Achenbach 1973, Eringen and Suhubi 1975). The limiting value of the quotient is then the group velocity  $c$

$$c = \lim_{\Delta k \rightarrow 0} \frac{\Delta\omega}{\Delta k} = \frac{\partial\omega}{\partial k}. \quad (4.18)$$

In Figure 4.3 the phase and group velocity are plotted as a function of  $\omega$  and it can be seen that the velocities become infinite for  $\omega \rightarrow 0$ . In this case the damper element plays no role any more and a non-physical situation arises in which the energy travels with an infinite velocity. Thus for very low frequencies, i.e. quasi-static loading conditions, the regularisation effect by the viscous terms vanishes. For higher frequencies a positive wave speed is obtained which approaches the linear elastic velocity  $c_e$  if  $\omega \rightarrow \infty$ .

In Figure 4.4 the damping coefficient  $\alpha$  is plotted as a function of  $\omega$  according to eq.(4.17). The limit of  $\alpha$  with respect to  $\omega$  reads

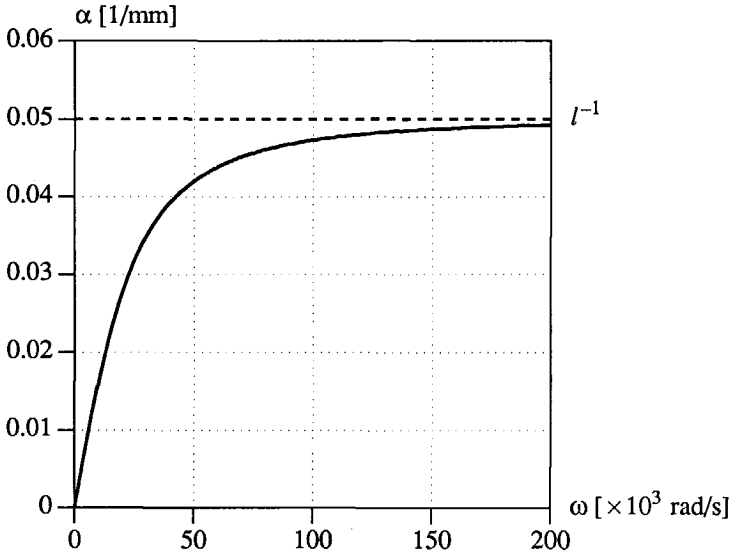


Figure 4.4 Damping coefficient  $\alpha$  as a function of  $\omega$  for a rate-dependent bar.

$$\lim_{\omega \rightarrow \infty} \alpha(\omega) = l^{-1}, \quad \text{with } l = \frac{2mc_e}{E}. \quad (4.19)$$

The parameter  $l$  sets the internal length scale of this rate-dependent crack model. High frequencies are attenuated exponentially in the space domain to an extent which is determined by the length scale  $l$ . The implicit presence of an internal length scale is essential for the solution of the mesh-sensitivity problem.

In case of nonlinear softening ( $h \neq \text{const.}$ ) or nonlinear damping ( $m \neq \text{const.}$ ) an initial perturbation of the velocity field  $\delta v(x, t)$  provides the same results for dispersion in the rate-dependent, strain-softening bar.

A complete analytical solution of a rate-dependent, strain-softening bar is not known and the analytical treatment here is limited to the derivation of the dispersion relationships for a single mode. For the total solution of a one-dimensional bar problem we have to rely entirely on numerical techniques.

### 4.3 ALGORITHMIC ASPECTS

Using the rate equations for the rate-dependent crack model we can develop an algorithm that determines the stress increment in a finite time step  $\Delta t$ . Therefore we consider the stress-strain equation (3.47) in its incremental form

$$\Delta\sigma = \mathbf{D}_e (\Delta\epsilon - \mathbf{N}\Delta\epsilon_{cr}), \quad (4.20)$$

in which we define  $\Delta\sigma$ ,  $\Delta\epsilon$  and  $\Delta\epsilon_{cr}$  as the increments in a time interval  $t \leq \tau \leq t + \Delta t$ . Denoting the crack strain rate at the beginning of the time step by  $\dot{\epsilon}_{cr}^t$  and that at the end of the time step by  $\dot{\epsilon}_{cr}^{t+\Delta t}$  the incremental crack strain is chosen according to

$$\Delta\epsilon_{cr} = ((1 - \Theta)\dot{\epsilon}_{cr}^t + \Theta\dot{\epsilon}_{cr}^{t+\Delta t})\Delta t, \quad (4.21)$$

where  $\Theta$  is an interpolation parameter,  $0 \leq \Theta \leq 1$ . For  $\Theta = 0$  we obtain the fully explicit Euler scheme. On the other hand  $\Theta = 1$  gives a scheme that is fully implicit and the case in which  $\Theta = 1/2$  represents an implicit scheme according to the trapezoidal rule. At the beginning of the time interval the crack strain rate reads

$$\dot{\epsilon}_{cr}^t = [\mathbf{M}]^{-1} (\mathbf{t}^t - \mathbf{t}_{cr}^t), \quad (4.22)$$

in which  $\mathbf{t}_{cr}^t = \mathbf{D}_{cr}\mathbf{e}_{cr}^t$  and  $\mathbf{t}^t$  is the sum of rate-dependent stress  $\mathbf{t}_{rd}^t$  and crack stress  $\mathbf{t}_{cr}^t$ . The crack strain rate at the end of the time interval is expressed in a limited Taylor series expansion as

$$\dot{\epsilon}_{cr}^{t+\Delta t} = \dot{\epsilon}_{cr}^t + \left[ \frac{\partial \dot{\epsilon}_{cr}}{\partial t} \right]^t \Delta t + \left[ \frac{\partial \dot{\epsilon}_{cr}}{\partial \mathbf{t}_{cr}} \right]^t \left[ \frac{\partial \mathbf{t}_{cr}}{\partial \mathbf{e}_{cr}} \right]^t \Delta \mathbf{e}_{cr}, \quad (4.23)$$

which can be rewritten in

$$\dot{\epsilon}_{cr}^{t+\Delta t} = \dot{\epsilon}_{cr}^t + [\mathbf{M}]^{-1} (\Delta \mathbf{t} - \mathbf{D}_{cr}\Delta \mathbf{e}_{cr}). \quad (4.24)$$

By substitution of  $\Delta \mathbf{t} = \mathbf{N}^T \Delta \sigma$  into eq.(4.24) and combination of the eqs.(4.20), (4.21) and (4.24) we obtain an explicit relation for the incremental crack strain

$$\Delta \mathbf{e}_{cr} = (\mathbf{N}^T \mathbf{D}_e \mathbf{N} + \mathbf{D}_{cr} + (1/(\Theta \Delta t)) \mathbf{M})^{-1} [\mathbf{N}^T \mathbf{D}_e \Delta \epsilon + (1/\Theta) \mathbf{M} \dot{\epsilon}_{cr}^t]. \quad (4.25)$$

This equation can be substituted in eq.(4.20) to obtain the incremental constitutive relation at time  $t + \Delta t$

$$\Delta \sigma = \mathbf{D}_c \Delta \epsilon - \Delta \mathbf{q}, \quad (4.26)$$

where

$$\mathbf{D}_c = \mathbf{D}_e [\mathbf{I} - \mathbf{N} (\mathbf{N}^T \mathbf{D}_e \mathbf{N} + \mathbf{D}_{cr} + (1/(\Theta \Delta t)) \mathbf{M})^{-1} \mathbf{N}^T \mathbf{D}_e] \quad (4.27)$$

and

$$\Delta \mathbf{q} = (1/\Theta) \mathbf{D}_e \mathbf{N} [\mathbf{N}^T \mathbf{D}_e \mathbf{N} + \mathbf{D}_{cr} + (1/(\Theta \Delta t)) \mathbf{M}]^{-1} \mathbf{M} \dot{\epsilon}_{cr}^t. \quad (4.28)$$

Matrix  $\mathbf{D}_c$  is determined not only by material parameters since the time integration parameters  $\Delta t$  and  $\Theta$  also enter the expression. The stress-strain relation can be substituted in the virtual work expression eq.(2.15) in section 2.2. The spatial discretisation of the initial value problem (see section 2.3) leads to a modified set of discretised equations of motion

$$\mathbf{M}\ddot{\mathbf{a}}^{t+\Delta t} + \mathbf{K}^t \Delta \mathbf{a} = \mathbf{f}^{t+\Delta t} + \Delta \mathbf{f}_{rd} - \mathbf{f}_{int}^t, \quad (4.29)$$

in which the extra pseudo-nodal force vector is

$$\Delta \mathbf{f}_{rd} = \int_V \mathbf{B}^T \Delta \mathbf{q} dV. \quad (4.30)$$

#### 4.4 NUMERICAL ANALYSES

To investigate the performance of the rate-dependent crack model numerical simulations have been carried out for the one-dimensional bar in tension (Example 1) and the impact tensile test on a double-notched specimen (Example 2). For the time integration of the field equations we again use the Newmark scheme ( $\beta = 1/4$ ,  $\gamma = 1/2$ , see section 2.3). For the coarse meshes in Example 1 we use a time step  $\Delta t = 5 \cdot 10^{-7}$  s and for the 80 elements mesh  $\Delta t = 2.5 \cdot 10^{-7}$  s. For the impact tests a time step  $\Delta t = 5 \cdot 10^{-7}$  s has been taken. For all analyses  $\Theta = 1/2$  and a consistent mass matrix has been used.

##### 4.4.1 Example 1 : One-dimensional bar problem in tension

The one-dimensional bar problem has been discussed in section 3.5.1 and has been outlined in Figure 3.4. A slight modification of the parameter set is applied by taking a steeper softening branch  $h = -5000$  N/mm<sup>2</sup>. This modification does not necessarily increase the brittleness of the material because the viscosity of the material also "carries" a part of the load. The material rate-sensitivity parameter  $m = 0.2$  Ns/mm<sup>2</sup>, which results in a length scale parameter  $l = 20$  mm (eq.(4.19)).

In the first analysis the same loading pulse as in the rate-independent analysis in section 3.5.1 with  $t_d = 0$  is applied. In Figure 4.6 a comparison between different meshes is made, at a time that the loading pulse has returned at the point of loading. The exponential decrease in strain after reflection as derived in the analytical consideration in section 4.2 comes out nicely. The strain pattern of the coarse mesh (10 elements) still deviates somewhat but the finer meshes give identical results. So, for the rate-dependent bar a localisation zone emerges that converges to a finite, constant band width upon mesh refinement. In Figure 4.6 also the stroboscopic development of the total strain along the bar is plotted with a time interval of  $1 \cdot 10^{-5}$  s for the case of 80 elements. It is observed that the width of the localisation zone remains constant whereas the loading wave propagates. Mesh independence is not only obtained in the sense that the band width is constant upon mesh refinement but also that the wave reflection pattern is objective with respect to the mesh as can be seen from the stress profiles (Figure 4.7 - top) of the reflected wave. We observe a partial reflection on the localisation zone, which is constant upon mesh refinement. In the bottom picture of Figure 4.7 the energy in the bar is plotted as a function of time. After reflection ( $t = 0.1 \cdot 10^{-3}$  s) we observe a

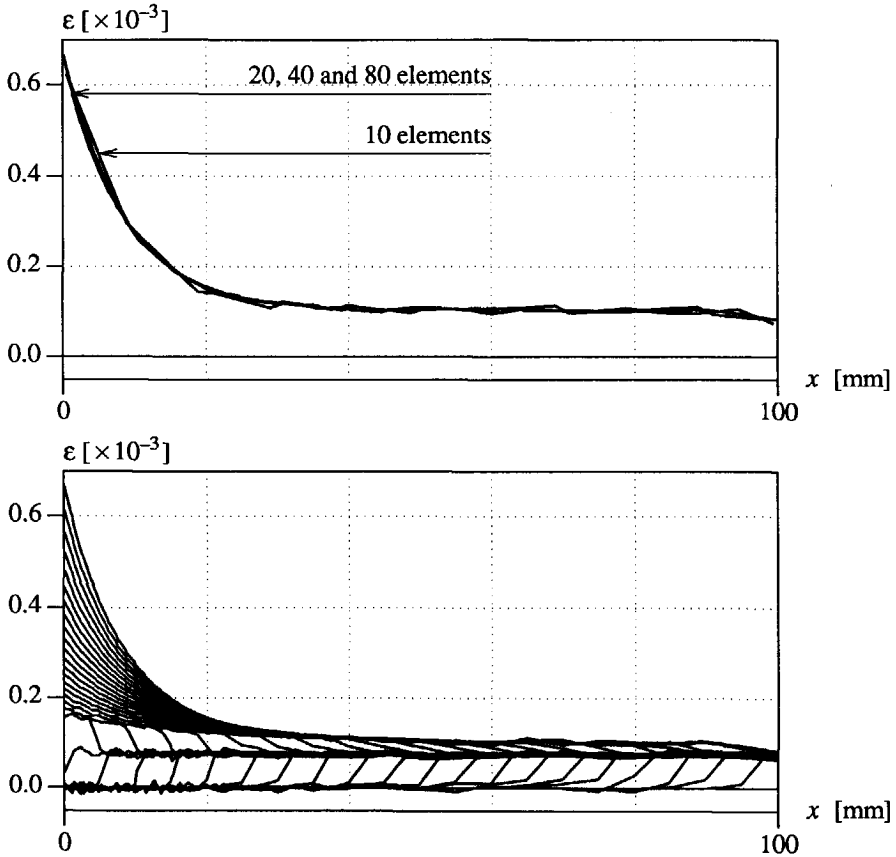


Figure 4.6 Rate-dependent crack model with  $t_d = 0$ . s :  
 Top : Strain localisation along the bar at  $t = 0.2 \cdot 10^{-3}$  s.  
 Bottom : Development of the localisation band (80 elements).

positive first derivative term ( $dU/dt > 0$ ) but a negative second derivative term ( $d^2U/dt^2 < 0$ ), which corresponds with a structural instability (see section 3.2. eq.(3.14)). Despite this, the energy consumption remains finite during the loading cycle.

A second analysis has been carried out for a different loading pulse. In the time-load diagram the time span  $t_d$  is now chosen as  $50 \cdot 10^{-6}$  s. So, the loading pulse firstly increases linearly in time before it becomes constant. Again the effect of the inclusion of the length scale can be observed from the strain localisation plots for different meshes (Figure 4.8 - top) and at different times (Figure 4.8 - bottom). Convergence to a solution with a finite width of the localisation zone characterises the mesh independence. It is noted that the strain distribution



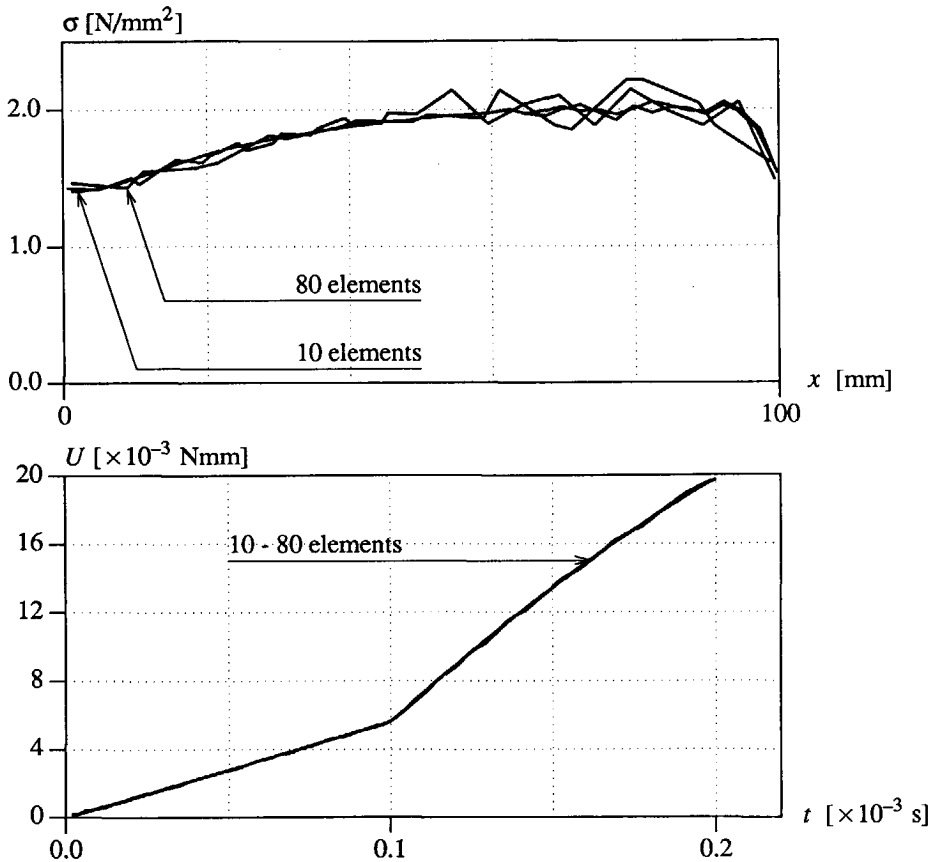


Figure 4.7 Rate-dependent crack model with  $t_d = 0. \text{ s}$  :  
 Top : Stress profiles along the bar at  $t = 0.2 \cdot 10^{-3} \text{ s}$ .  
 Bottom : Energy consumption of the bar.

in the localisation zone has a different shape for this loading case. In the previous analysis a sharp peak in the strain occurs at the left boundary, whereas in this analysis the strain profile is more uniformly distributed and has a lower peak value. This is due to the strain rate profiles in the bar at the moment of cracking. In the previous analysis cracking is initiated in one point at the left boundary from which the exponential decay started. In this analysis the static tensile strength is exceeded over a zone with a fixed length (16.7 mm). At the edge of this zone ( $x = 16.7 \text{ mm}$ ) the attenuation of the loading wave starts exponentially and at this point a bending point in the strain profile occurs (see Figure 4.8).

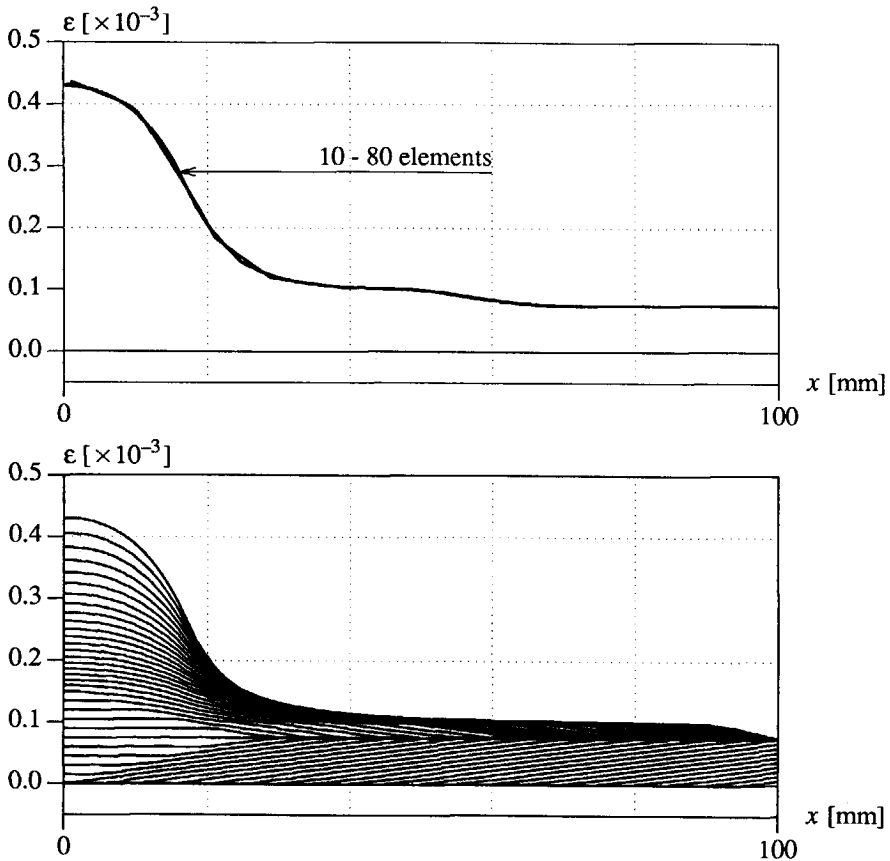


Figure 4.8 Rate-dependent model with  $t_d = 50 \cdot 10^{-6}$  s :  
 Top : Strain localisation along the bar at  $t = 0.25 \cdot 10^{-3}$  s.  
 Bottom : Development of the localisation band (80 elements).

Finally, the width of the localisation band has been analysed. Firstly, the influence of the length scale parameter on the observed localisation width was investigated in an analysis with  $t_d = 0$  by using three different values for  $l$ , namely 15, 20 and 25 mm. From the upper plot of Figure 4.9 it appears that the width of the localised zone is a function of the length scale parameter. These results agree with the observation that the localisation zone should vanish when the length scale parameter approaches zero. A comparison of the results shown in the Figures 4.6 and 4.8 had already made it clear that the shape of the loading wave influences the strain rate distribution in the localisation zone and therefore also the localisation band width. This effect is shown more clearly in the bottom plot of Figure 4.9 by taking three different values for the time span  $t_d$  in which the load is increased from zero to its maximum value.

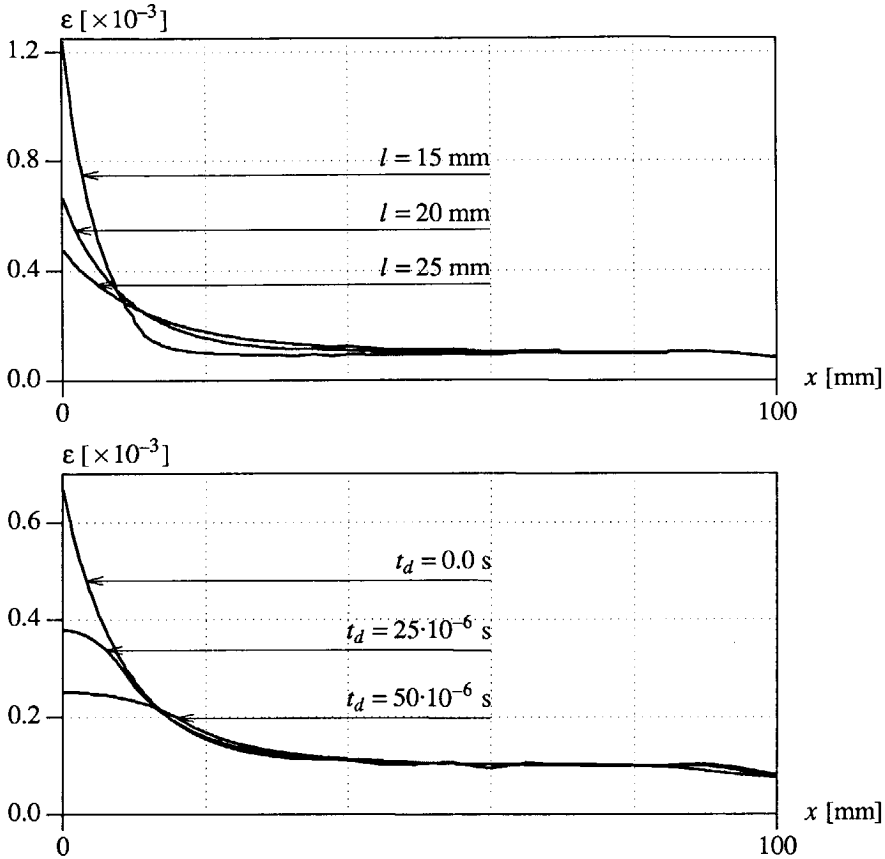


Figure 4.9 Top : Variation of the length scale parameter ( $t = 0.2 \cdot 10^{-3}$  s).  
Bottom : Variation of the loading rate ( $t = 0.2 \cdot 10^{-3}$  s).

#### 4.4.2 Example 2 : Impact tensile test on a double-notched specimen

The numerical simulations of the impact tensile tests with the Split-Hopkinson bar, discussed in section 3.5.2, show the poor performance of a classical rate-independent fracture model. A similarity for the global response between experiment and numerical calculation can be obtained by an adaptation of the mesh. Of course, such a result reduces the predictable value of a numerical simulation to zero.

The impact tensile test has also been analysed using a fracture energy model (solution technique 1 in section 3.6). This model guarantees a mesh-objective fracture energy dissipation if one crack is considered. Indeed, these analyses for the impact tensile test provide a

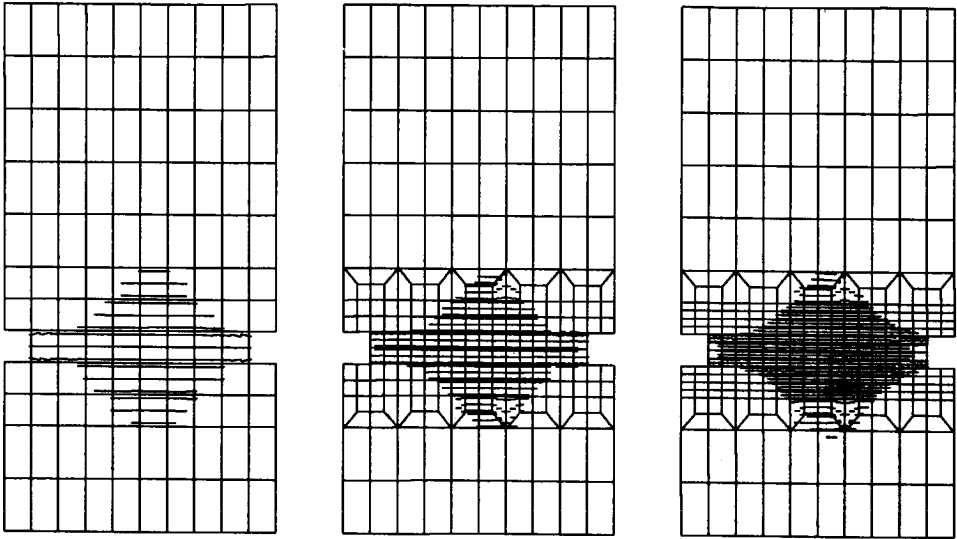


Figure 4.10 Crack patterns at  $t = 0.45 \cdot 10^{-3}$  s for the rate-dependent model.

reasonable prediction of the ultimate load and the post-peak behaviour (Sluys 1989). However, because of the disadvantages of a fracture energy model with respect to multiple cracking and mesh-alignment problems, discussed in section 3.6, this solution technique is considered to be inferior and will not be discussed here.

For the analyses with the rate-dependent crack model we apply a slight modification of the parameter set from Figure 3.7. In the classical strain-softening model the increase of tensile strength due to dynamic effects must be incorporated entirely in the strain-softening function, whereas in the rate-dependent crack model strain softening can occur before the ultimate stress is reached (see Figure 4.1). Already in the pre-peak regime we model at a constitutive level some damage through strain softening while viscous effects cause the further increase of the stress. For this reason a redistribution of stresses is possible already in the pre-peak regime. In this analysis we assume that the stress at which strain softening starts is 80 % of the dynamic tensile strength of the concrete ( $4.9 \text{ N/mm}^2$ ). In experiments it is observed that at this stress level micro-cracks start to develop. Furthermore, we take the strain-softening modulus  $h = -2500 \text{ N/mm}^2$  and the material rate sensitivity  $m = 0.1 \text{ Ns/mm}^2$ . In combination with the parameter set from Figure 3.7 this results in a length scale parameter  $l = 20.5 \text{ mm}$  (eq.(4.19)).

The computational results differ markedly from the results obtained with the rate-independent crack model. Now, a localisation band occurs that is independent of the choice of the finite element discretisation. At the notches the very local stress concentrations keep the band

small but the width of the localisation band increases when the crack propagates to the centre of the specimen. This can be seen from the crack patterns in Figure 4.10 for the three meshes at a time when the failure zone has developed completely. The deformation patterns for the three meshes, plotted in Figure 4.11, not only show the mesh independence but also the misalignment of the localised deformations with the mesh. In contrast to the calculations with the rate-independent model in which the deformation localises along the horizontal mesh lines, the cracks branch off and the deformation band becomes wider independent of the alignment of the mesh. In Figure 4.12 the total axial strains are plotted for a vertical cross-section in the centre of the specimen. The strain profiles coincide more or less and show the division of the strain localisation band into two separate zones. The development of the localisation band can be investigated in more detail if we consider the axial strains in a relevant part of the specimen, shown as the zone enclosed by the dashed lines in Figure 4.13. Cracking starts in the singular points at the upper and lower corner of the two notches. Both cracks at the left notch first join and at a later stage split up into two separate localisation bands. So there remains an almost unstretched zone in the middle of the specimen. The same crack propagation process occurs at the right notch. A small mesh dependence appears in the results due to the presence of singularities in the elastic solution at the notches of the specimen. The inclusion of rate dependence apparently solves the problems caused by the singularity in the constitutive equation but does not affect the singularities in the geometry.

Again, the numerical results have been compared with the experimental data (Weerheijm 1991). The stress-deformation curves for the numerical analyses as well as for the experiment are plotted in Figure 4.14. We observe not only mesh independence, but also a reasonable similarity between numerical analysis and experiment. The calculated maximum tensile stress is slightly smaller and the application of a linear strain-softening model prevents the proper simulation of a nonlinear softening branch, which is measured in the experiment. Another comparison between experiment and calculation is made in Figure 4.15 for the loading pulse which is transmitted by the fracture zone. The results for the three meshes are identical but differ slightly from the measured pulse which shows a different loading rate for reasons as discussed in section 3.5.2. The rate-dependent crack model is a very simple model and it was not the prime aim of this study to exactly simulate the experiments. Rather it was meant to provide a solution technique for mesh sensitivity. The second step is now to calibrate the model to experiments, for instance these impact tensile tests. It is expected that numerical results can be obtained which are in a better agreement with the experimental data. If we use a nonlinear strain-softening function the response will be steeper immediately after cracking and more flat in the final softening stage. Also, a nonlinear function for the material rate sensitivity can improve the numerical results with respect to the experiment. If we take a larger value for  $m$  only in the first regime of the strain-softening function a larger value for the ultimate stress can be calculated.

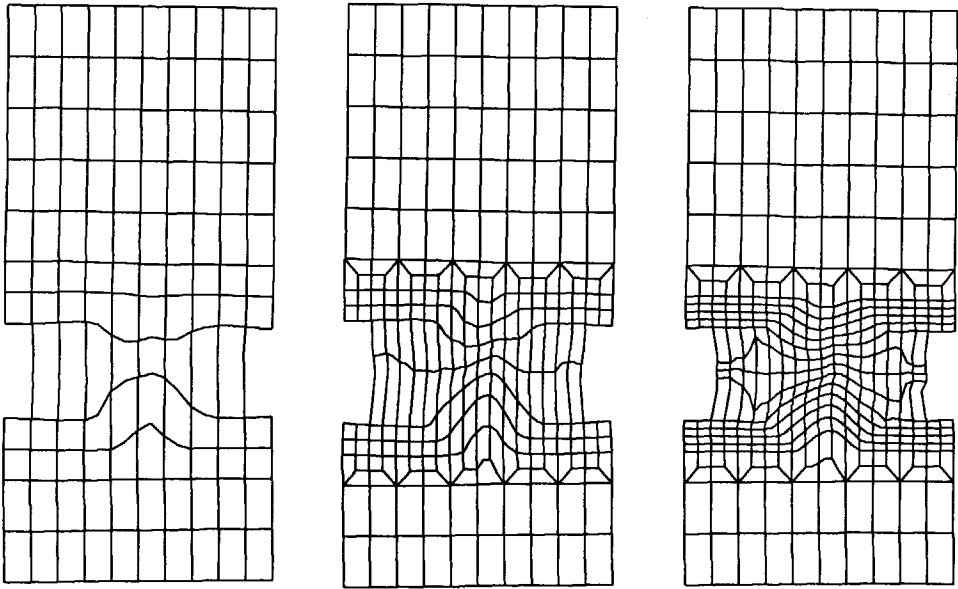


Figure 4.11 Incremental displacement patterns at  $t = 0.45 \cdot 10^{-3}$  s.

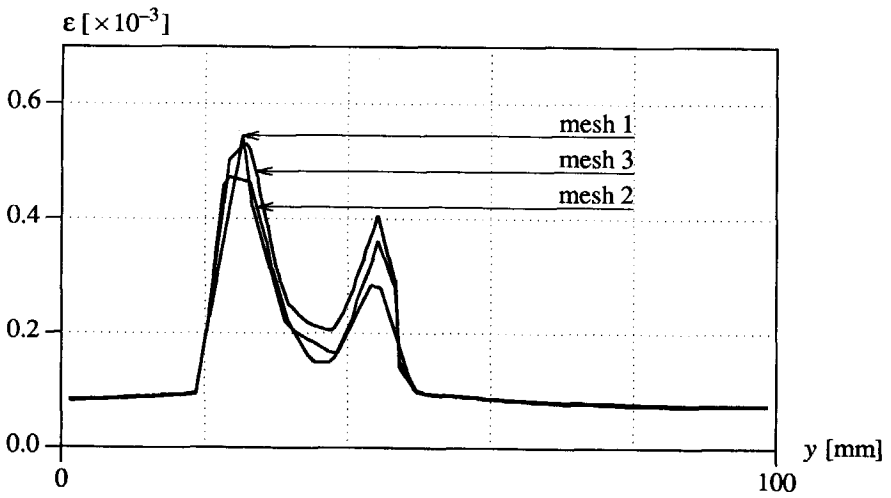


Figure 4.12 Total axial strains in centre section ( $x = 25$  mm) of the specimen ( $t = 0.45 \cdot 10^{-3}$  s).

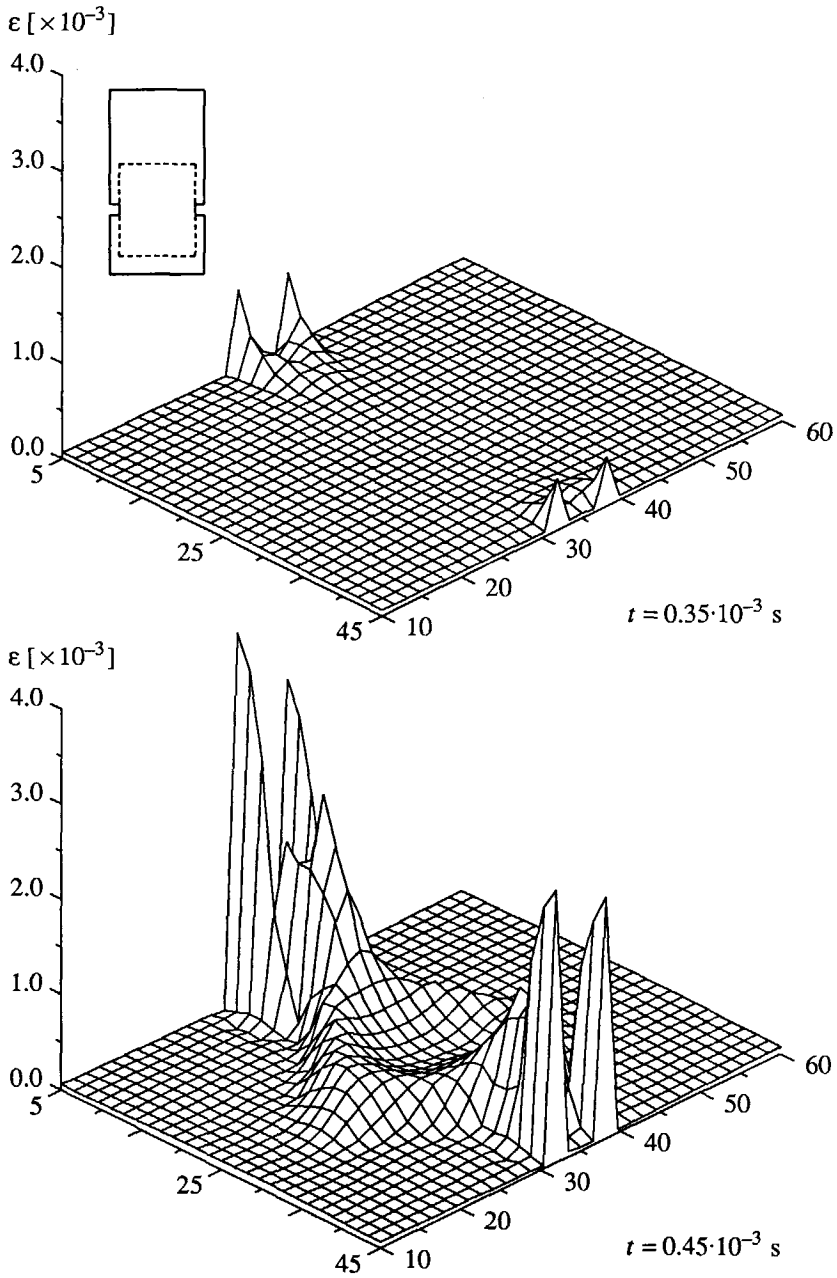


Figure 4.13 Development of the localisation zone (axial strains - Mesh 3).

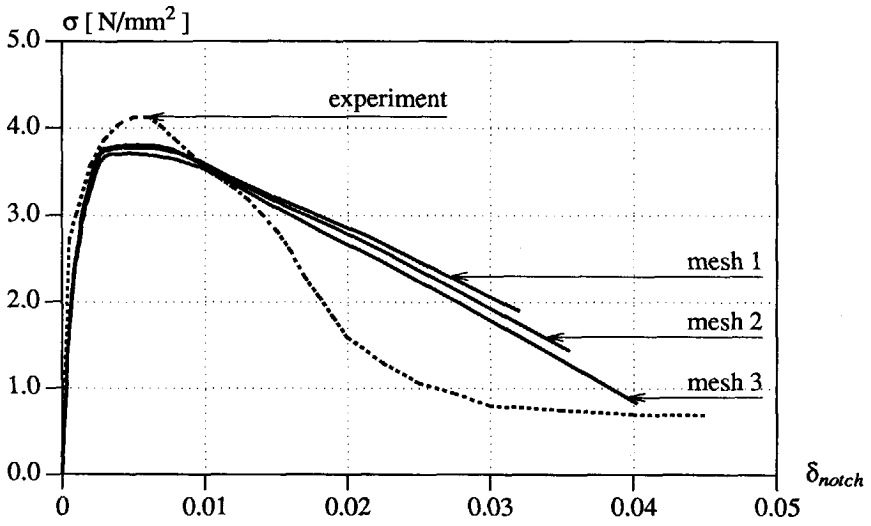


Figure 4.14 Stress-deformation curve inside the fracture zone.

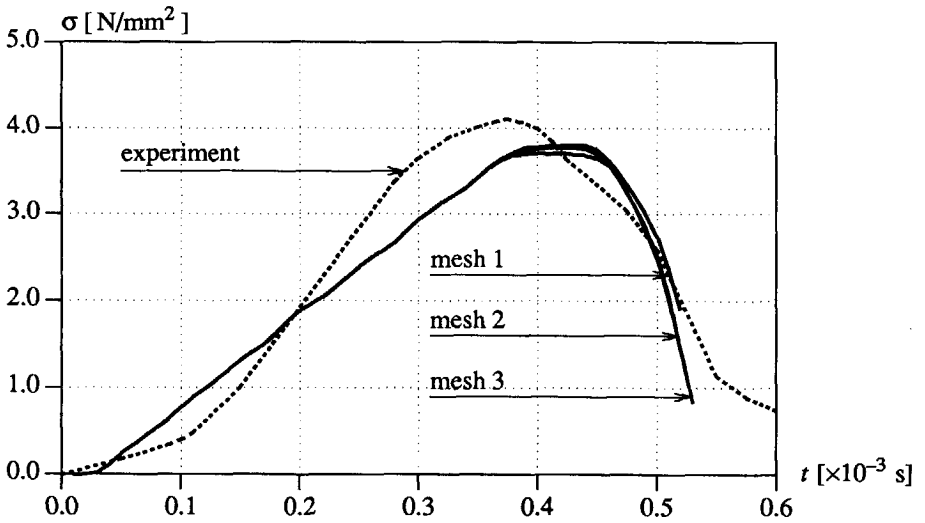


Figure 4.15 Stress-time curve of the transmitted loading pulse.



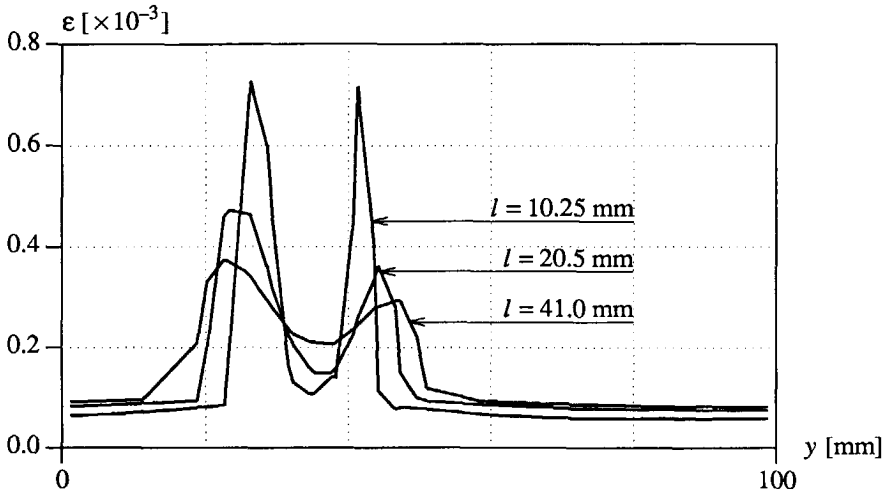


Figure 4.16 Comparison of axial strain for different values for  $l$  - ( $l = 10.25$  mm -  $t = 0.41 \cdot 10^{-3}$  s,  $l = 20.5$  mm -  $t = 0.45 \cdot 10^{-3}$  s,  $l = 41.0$  mm -  $t = 0.48 \cdot 10^{-3}$  s).

Finally, the length scale parameter  $l$  has been varied through a variation of the material rate-sensitivity parameter  $m$ . In Figure 4.16 the axial strain profiles in the centre section of the specimen show the dependence of the localisation zone on  $l$ . An increase of  $l$  by a factor 2 provides a wider and smoother localisation zone, whereas a division of  $l$  by 2 yields sharper peaks in a smaller localisation zone for the strain response. In the stress-deformation curve in Figure 4.17 the influence of the parameter  $l$  is also clear : a smaller value for  $l$  leads to a steeper drop in the curve and to a more brittle behaviour, whereas an increase of  $l$  yields a more ductile response, although the maximum stress is predicted more accurately. Hence,  $l$  is a parameter which has an influence similar to that of the fracture energy  $G_f$ . Because the length scale parameter also determines the width of the band, brittleness of a material and the width of the localisation zone are related phenomena. In Figure 4.18 the influence of  $l$  on the shape of the loading pulse, which passes the crack plane, is also shown. A larger value for  $l$  slows down the failure process and enables the cross-section to redistribute the stress, which leads to a larger maximum stress value. It turns out that the behaviour close to the peak load is very important and determines the crack propagation speed and the extent of redistribution of stresses.

Now the role of the imperfection adjacent to the left notch, which has been applied in order to trigger an asymmetric failure mode, will be discussed. The rotation during failure which is observed in the test is found to be less pronounced in the numerical simulations. The

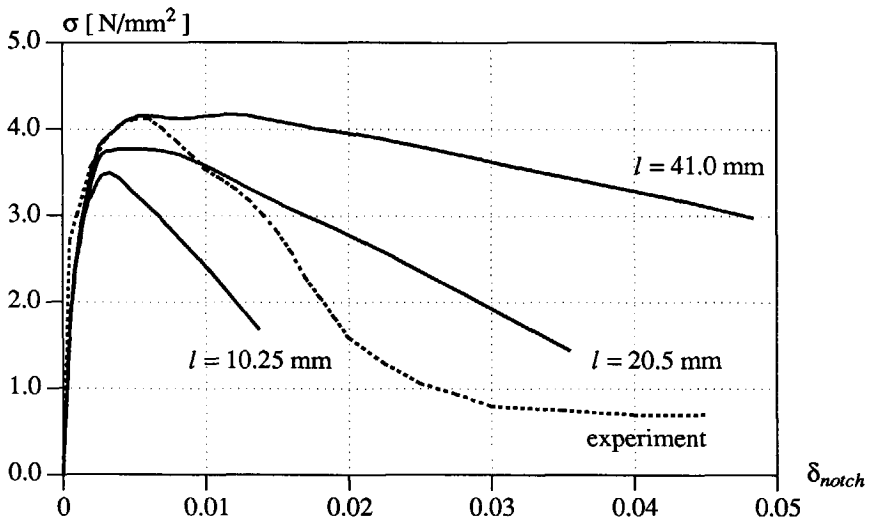


Figure 4.17 Stress-deformation curve inside the fracture zone for different values for  $l$ .

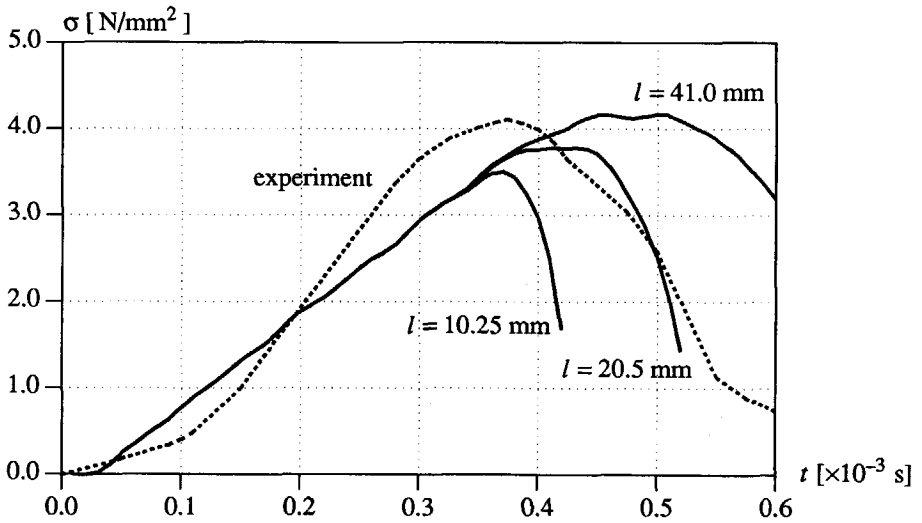


Figure 4.18 Stress-time curve of the transmitted loading pulse for different values for the length scale parameter  $l$ .

analysis with  $l = 41.0$  mm shows a purely symmetric response,  $l = 20.5$  mm leads to a slight rotation of the specimen and only  $l = 10.25$  mm offers the possibility to simulate rotation of the crack plane. However, the latter analysis gives a worse prediction of the global response as observed in the Figures 4.17 and 4.18. A remarkable result is that in the experiment as well as in the numerical simulation ( $l = 10.25$  mm) the entire rotation occurs in the pre-peak regime. Rotation starts when the first cracks appear at the left notch and reaches its maximum when the crack pattern is complete and the ultimate stress is reached. As discussed earlier the response is influenced not only by material behaviour but also by structural effects. It is plausible that the experimental set-up has an influence on at least a part of the rotation of the specimen. In the numerical simulation the set-up differs from the real set-up as has been described in section 3.5.2, which can be a cause of the poor prediction of the rotation of the specimen. A second point of consideration is the plane-stress modelling of an experiment in which three-dimensional effects are present. This can also contribute to an asymmetric response. A third possible cause for the discrepancy is the linear softening branch that has been utilised.

## 4.5 POWER LAW MODEL

### 4.5.1 Model formulation

Another rate-dependent model has been used by Needleman (1988) and Asaro (1983). Needleman has used the power law formulation in a plasticity model for the investigation of shear band formation in structural metals. Here, we use it within the framework of a principal stress criterion model for the description of fracture zones in brittle materials. In the one-dimensional formulation of the model the crack strain rate is chosen according to a power law function

$$\frac{\partial \epsilon_{cr}}{\partial t} = \dot{a} (\sigma/g)^N \quad (4.31)$$

where  $\dot{a}$  is a material parameter of dimension 1/s and  $g$  is a hardness parameter which depends on the crack strain. The parameter  $N$  depends on the strain rate sensitivity of the material. The distinction between this model and the rate-dependent crack model of section 4.1 is that the strain rate is a function of the total stress ( $\sigma$ ) and not of a part of the stress ( $\sigma - \sigma_{cr}$ ). Instead of a parallel softening-damper element (see Figure 4.1) now we only have a nonlinear damper element with a power law characteristic (see Figure 4.19 -  $N = 1$ ).

For the parameter  $g$  a bilinear diagram is used with an evolution law according to

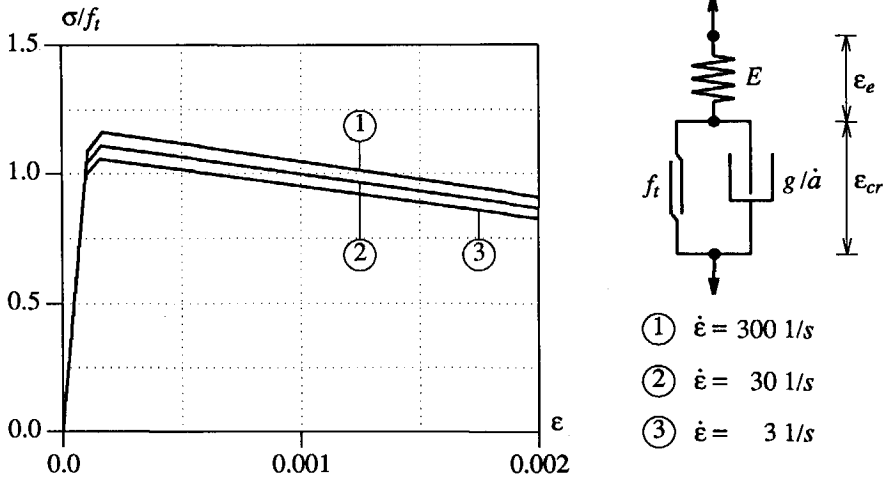


Figure 4.19 Power law model for different strain rates.

$$\frac{\partial g}{\partial t} = \begin{cases} h_1 \frac{\partial \epsilon_{cr}}{\partial t} & \text{for } \epsilon_{cr} \leq \epsilon_{crm} \\ h_2 \frac{\partial \epsilon_{cr}}{\partial t} & \text{for } \epsilon_{cr} > \epsilon_{crm} \end{cases} \quad (4.32)$$

with  $g(0) = f_i$  and  $\epsilon_{crm}$  the transition strain between hardening ( $\epsilon_{cr} < \epsilon_{crm}$ ) and softening ( $\epsilon_{cr} > \epsilon_{crm}$ ). In Figure 4.19 computed stress-strain curves are plotted for different strain rates. Additional to the parameters used in Figure 4.1 we have chosen :  $\dot{a} = 4.0 \text{ 1/s}$ ,  $N = 50$ ,  $\epsilon_{crm} = 1/2 f_i/E$ ,  $h_1 = 2500 \text{ N/mm}^2$  and  $h_2 = -250 \text{ N/mm}^2$ . It is difficult to give a physical explanation for the choice of parameters because, so far, application of the model has only been done for structural metals. The implicit length scale parameter  $l$  is defined by (Needleman 1988)

$$l = \frac{c_e}{\dot{a}}, \quad (4.33)$$

which can be considered as the distance an elastic wave travels in a characteristic time  $1/\dot{a}$ .

If we take  $N = 1$  and consider the case of softening ( $h_2 < 0$ ) the wave equation for the power law model reads

$$\frac{g}{\dot{a}} \left( \frac{1}{c_\varepsilon^2} \frac{\partial^3 v}{\partial t^3} - \frac{\partial^3 v}{\partial x^2 \partial t} \right) + \rho \frac{\partial^2 v}{\partial t^2} = \frac{h_2}{\dot{a}} \frac{\partial \dot{\varepsilon}_{cr}}{\partial t} \left( \frac{\partial^2 v}{\partial x^2} - \frac{1}{c_\varepsilon^2} \frac{\partial^2 v}{\partial t^2} \right). \quad (4.34)$$

The same third-order terms as in the wave equation for the rate-dependent bar (eq.4.10) appear, multiplied with a softening term  $g/\dot{a}$ . These third-order terms, which determine the well-posedness of the solution (cf. section 4.2) gradually vanish when strain softening occurs ( $g(\varepsilon_{cr}) \rightarrow 0$ ). Therefore, the solution approaches the solution of the classical rate-independent problem from Chapter 3 and if  $g = 0$  mesh dependence is obtained again. It is obvious that the initial value problem quickly becomes ill-posed for steep softening branches, as, for instance, in concrete. This means that proper results can only be obtained for ductile strain-softening models, as will be shown in section 4.5.3.

#### 4.5.2 Algorithmic aspects

For the one-dimensional case a simple algorithm is used. Again, we use the incremental stress-strain equation

$$\Delta \sigma = E(\Delta \varepsilon - \Delta \varepsilon_{cr}). \quad (4.35)$$

The incremental crack strain  $\Delta \varepsilon_{cr}$  can be estimated via an Euler forward scheme

$$\Delta \varepsilon_{cr} = \frac{\partial \varepsilon_{cr}^t}{\partial t} \Delta t = \dot{a} \left( \frac{\sigma^t}{g^t} \right)^N \Delta t. \quad (4.36)$$

Substitution of (4.36) in eq.(4.35) offers a first approximation for the stress  $\sigma$  and the hardness  $g$  at time  $t + \Delta t$ . It is now possible to estimate the crack strain rate at  $t + \Delta t$  and with the linear interpolation formula (cf. eq.(4.21)) we are able to calculate an improved approximation for the incremental crack strain. This completes the data set required for the incremental constitutive equation

$$\Delta \sigma = E \Delta \varepsilon - \Delta q, \quad (4.37)$$

with

$$\Delta q = \dot{a} E \left[ (1 - \Theta) \left( \frac{\sigma^t}{g^t} \right)^N + \Theta \left( \frac{\sigma^{t+\Delta t}}{g^{t+\Delta t}} \right)^N \right] \Delta t. \quad (4.38)$$

When choosing  $\Theta = 1/2$  this procedure corresponds to an implicit Heun integration scheme. The total inelastic response is transferred via the  $\Delta q$ , from which the pseudo-nodal force  $\Delta f_{rd}$  can be deduced.

### 4.5.3 Numerical results

We have also used the one-dimensional bar problem in tension (Example 1) for a mesh-sensitivity analysis of the power law model with the parameters used in Figure 4.19. Mesh independence has been obtained only for an analysis with a rather small negative slope ( $h_2 = -250 \text{ N/mm}^2$ ) and a small loading rate corresponding to a time span  $t_d = 50 \cdot 10^{-6} \text{ s}$ . In Figure 4.20 it is shown that the width of the localisation zone at  $t = 0.25 \cdot 10^{-3} \text{ s}$  is more or less constant, independent of the discretisation of the bar. However, it appeared that at a higher

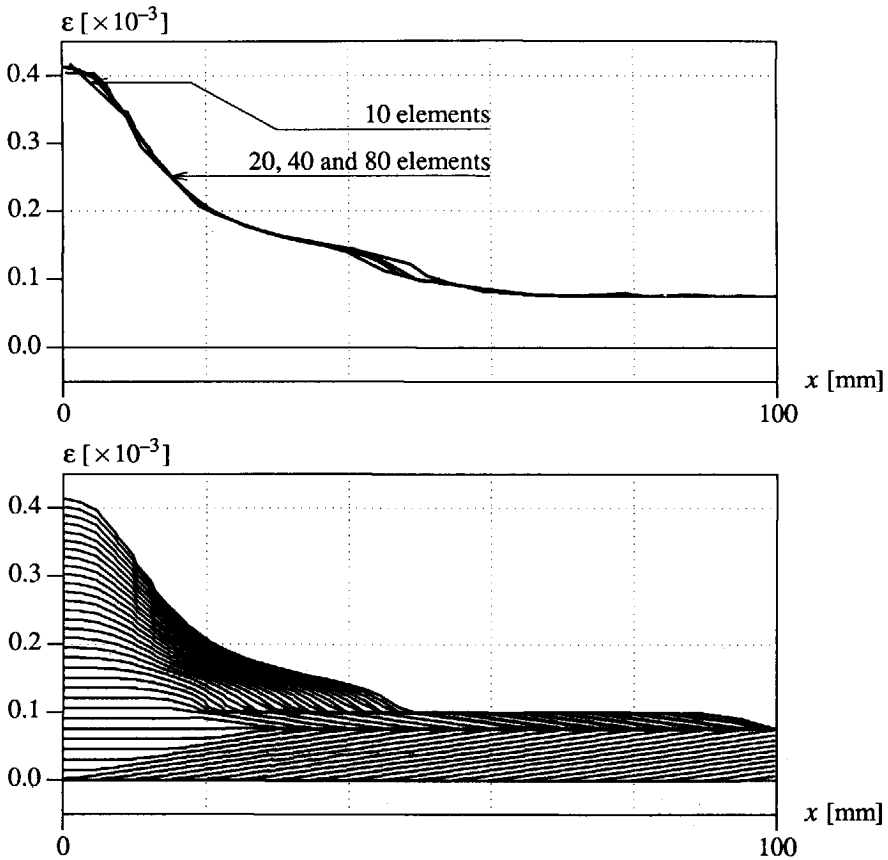


Figure 4.20 Power law model with  $t_d = 50 \cdot 10^{-6} \text{ s}$  :  
 Top : Strain localisation along the bar at  $t = 0.25 \cdot 10^{-3} \text{ s}$ .  
 Bottom : Development of the localisation band (40 elements).

strain level, when the stabilising viscous effect gradually disappears, localisation again becomes mesh dependent. This type of behaviour becomes worse when a strain-softening model with a steeper branch is used or when the loading rate is increased. This is in agreement with the observations made in section 4.5.1 with respect to the role of the factor  $g/\dot{a}$  in the differential equation that governs the response of the bar using the power law model. In brittle materials we deal with strain-softening models that show a relatively rapid stress drop after cracking which suggests that viscous regularisation via the power law model is less appropriate for modelling of brittle materials. From the bottom picture of Figure 4.20 we observe that the localisation zone increases in thickness in the course of time due to the small hardening region in the model.





## 5. GRADIENT-DEPENDENT MODEL

From Chapter 3 it appeared that micro-structural modifications, which occur in a localisation zone, cause discontinuous deformation processes which cannot be described with classical continuum models. Therefore, enrichment of the continuum has been proposed to avoid a spurious solution for the localisation zone. In Chapter 4 a higher-order time derivative term was included in the material description to overcome the problems. Another type of regularisation methods is based on the inclusion of higher-order spatial derivatives in the constitutive equations (Schreyer and Chen 1986, Lasry and Belytschko 1988, Zbib and Aifantis 1988, Mühlhaus and Aifantis 1991, de Borst and Mühlhaus 1991 and 1992) or the averaging of strains, the so-called non-local models (Bažant et al. 1984, Pijaudier-Cabot and Bažant 1987). In the approach followed in this chapter we assume the presence of second-order strain gradient terms in the stress-strain law. Mühlhaus and Aifantis (1991) and de Borst and Mühlhaus (1991) have shown that such a gradient-dependent model can be derived from non-local models. Gradient models as well as non-local models reflect the fact that the interaction between micro-structural deformations in the localisation zone is non-local.

The use of a higher-order gradient model can result in a well-posed set of partial differential equations. Furthermore, the gradient model explicitly incorporates an internal length scale. From a dispersion analysis it becomes clear that the wave speeds remain real under strain-softening conditions and that the continuum is capable of transforming a travelling wave into a stationary localisation wave. As a consequence of the well-posedness of the mathematical problem numerical results do not suffer from the pathological mesh dependence.

This chapter is organised as follows. First, a description is given of the gradient model, in which the yield function not only depends on the stress and a hardening/softening parameter but also on the Laplacian of the latter quantity. We investigate wave propagation in a bar of gradient-dependent material by means of a dispersion analysis. This study leads to an exact prediction of the width of the localisation zone. Next, the algorithmic difficulties caused by the incorporation of the gradient effect are discussed. Results of numerical analyses are presented for the uniaxial bar problem in tension (Example 1) and the impact biaxial test (Example 3). Using a gradient model convergence of the results upon refinement of the discretisation can be obtained for mode-I and mode-II localisation problems.

### 5.1 FORMULATION OF A GRADIENT-DEPENDENT PLASTICITY MODEL

In the gradient-plasticity model the yield strength does not only depend upon the equivalent plastic strain  $\kappa$ , but also upon the Laplacian thereof. So, we consider the following yield condition

$$f(\sigma, \kappa, \nabla^2 \kappa) = 0. \quad (5.1)$$

As in classical plasticity (see section 3.4.2) the stress point must remain on the yield surface during plastic deformation, which yields for the consistency condition for continuing plastic flow

$$\frac{\partial f^T}{\partial \boldsymbol{\sigma}} \dot{\boldsymbol{\sigma}} + \frac{\partial f}{\partial \kappa} \dot{\kappa} + \frac{\partial f}{\partial \nabla^2 \kappa} \nabla^2 \dot{\kappa} = 0. \quad (5.2)$$

If we use the gradient to the yield surface  $\mathbf{n}$  and the hardening/softening modulus  $h$  as defined in the eqs.(3.57) and (3.58) and assume the dependence of  $f$  upon  $\nabla^2 \kappa$  to be a constant

$$\bar{c} = \frac{\partial f}{\partial \nabla^2 \kappa}, \quad (5.3)$$

the consistency equation can be rewritten in

$$\mathbf{n}^T \dot{\boldsymbol{\sigma}} - h \dot{\lambda} + \bar{c} \nabla^2 \dot{\kappa} = 0. \quad (5.4)$$

A further assumption is made that the relationship between the plastic multiplier  $\dot{\lambda}$  and the hardening/softening rate  $\dot{\kappa}$  can be established of the form

$$\dot{\kappa} = \eta \dot{\lambda}, \quad (5.5)$$

with  $\eta$  a constant. This assumption seems a limitation of the model but large classes of hardening/softening hypotheses and yield functions satisfy eq.(5.5). In this thesis we apply the strain-hardening/softening hypothesis (eq.(3.61)). In combination with the used yield criteria we obtain

$$\eta = 1 \quad \text{for von Mises and Rankine} \quad (5.6)$$

and

$$\eta = \sqrt{1 + 2/9 \alpha^2} \quad \text{for Drucker-Prager}, \quad (5.7)$$

if we assume the cohesion parameter  $c$  dependent on the hardening/softening parameter in the Drucker-Prager yield function. If we use  $\bar{c}_\eta = \eta \bar{c}$  eq.(5.4) can be written as

$$\mathbf{n}^T \dot{\boldsymbol{\sigma}} - h \dot{\lambda} + \bar{c}_\eta \nabla^2 \dot{\lambda} = 0. \quad (5.8)$$

So, for gradient-dependent plasticity the consistency condition results in a differential equation for  $\dot{\lambda}$  and an explicit expression for  $\dot{\lambda}$  at a local (integration point) level (cf. eq.(3.59)) cannot be obtained.

## 5.2 WAVE PROPAGATION IN A ONE-DIMENSIONAL GRADIENT-DEPENDENT BAR

In a one-dimensional analysis the equivalent plastic strain (cf. eq.(3.54)) equals the axial plastic strain, so that for a stress point on the yield surface ( $f = 0$ ) we obtain the one-dimensional

form of eq.(5.1), written in rate format

$$\dot{\sigma} = h \dot{\epsilon}_p - \bar{c} \frac{\partial^2 \dot{\epsilon}_p}{\partial x^2}, \quad (5.9)$$

in which a linear softening function is utilised ( $h = \text{const.}$ ). Combining the constitutive equation (5.9) with the kinematic equation (3.4), taking  $\dot{\epsilon}_p = \dot{\epsilon} - \dot{\epsilon}_e$  and  $\dot{\epsilon}_e = \dot{\sigma}/E$  and differentiating the result with respect to  $x$  yields

$$\frac{\partial}{\partial x} \left( -\frac{\bar{c}}{E} \frac{\partial^2 \dot{\sigma}}{\partial x^2} + \frac{E+h}{E} \dot{\sigma} \right) = \frac{\partial^2}{\partial x^2} \left( h v - \bar{c} \frac{\partial^2 v}{\partial x^2} \right). \quad (5.10)$$

If we use the equation of motion eq.(3.3) we obtain a fourth-order differential equation for the one-dimensional gradient-dependent, strain-softening bar

$$\bar{c} \left( \frac{\partial^4 v}{\partial x^4} - \frac{1}{c_e^2} \frac{\partial^4 v}{\partial x^2 \partial t^2} \right) + \frac{E+h}{c_e^2} \frac{\partial^2 v}{\partial t^2} - h \frac{\partial^2 v}{\partial x^2} = 0. \quad (5.11)$$

If  $\bar{c} \rightarrow 0$ , again, the wave equation for the classical strain-softening bar (eq.(3.8)) is recovered with imaginary characteristics and imaginary wave speeds. The condition of eq.(5.11) can be investigated by means of its characteristics. To this end we consider the variation of two third-order derivative terms of  $v$

$$d \left( \frac{\partial^3 v}{\partial x^3} \right) = \frac{\partial^4 v}{\partial x^3 \partial t} dt + \frac{\partial^4 v}{\partial x^4} dx \quad (5.12)$$

$$d \left( \frac{\partial^3 v}{\partial x^2 \partial t} \right) = \frac{\partial^4 v}{\partial x^2 \partial t^2} dt + \frac{\partial^4 v}{\partial x^3 \partial t} dx. \quad (5.13)$$

Combination of eq.(5.12) and (5.13) and the wave equation for the gradient-dependent bar eq.(5.11) yields a system of three fourth-order differential equations with a characteristic determinant

$$D = \begin{bmatrix} \bar{c} & 0 & -\bar{c}/c_e^2 \\ dx & dt & 0 \\ 0 & dx & dt \end{bmatrix} = \bar{c}(dt^2 - (1/c_e^2) dx^2). \quad (5.14)$$

With  $D = 0$  the characteristics are equal to the elastic bar velocity  $\pm c_e$  and remain real when strain softening occurs. So, the wave equation remains hyperbolic and the initial value problem is well-posed.

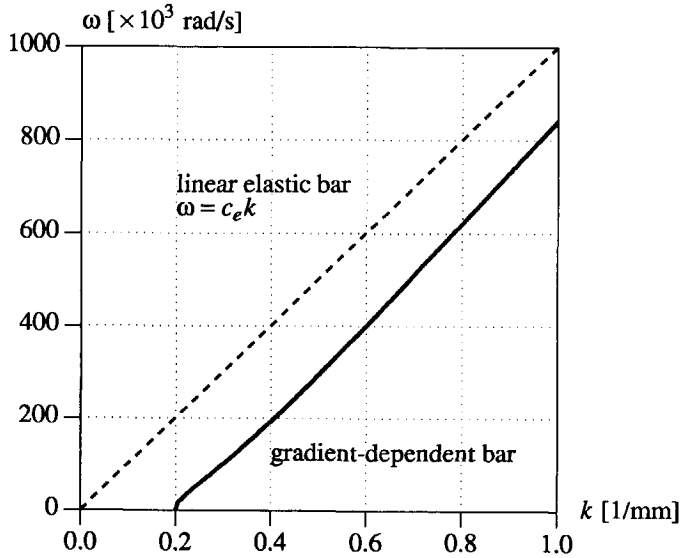


Figure 5.1 Dispersion relation for the gradient-dependent bar.

We now carry out a dispersion analysis for the gradient-dependent bar. Substitution of the general solution (3.15) for a single harmonic wave into the wave equation (5.11) gives the dispersion relation for the gradient-dependent bar

$$\bar{c}k^4 - \bar{c}/c_e^2 k^2 \omega^2 - (E+h)/c_e^2 \omega^2 + hk^2 = 0. \quad (5.15)$$

Considering the positive root for  $\omega$

$$\omega = c_e \sqrt{\frac{h + \bar{c}k^2}{E + h + \bar{c}k^2}} k, \quad (5.16)$$

it becomes clear that the classical non-dispersive equation (3.17) is recovered when  $\bar{c} \rightarrow 0$ . The dispersion relation is plotted in Figure 5.1 for the one-dimensional reference problem (Example 1), treated in section 5.4.1. The phase velocity  $c_f = \omega/k$  of the harmonic wave reads

$$c_f = c_e \sqrt{\frac{h + \bar{c}k^2}{E + h + \bar{c}k^2}}. \quad (5.17)$$

Equation (5.17) is plotted in Figure 5.2. The phase speed  $c_f$  depends on the wave number  $k$  and, consequently, wave propagation is dispersive for the gradient-dependent bar (Whitham 1974). Owing to the fact that different harmonic waves propagate with different velocities the

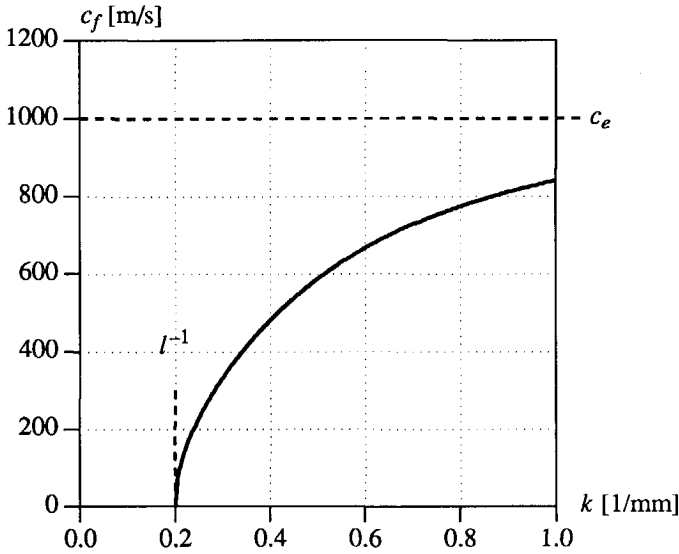


Figure 5.2 Phase velocity - wave number curve for gradient-dependent model.

shape of a pulse is altered and, similar to the rate-dependent medium in Chapter 4, a loading wave can be transformed into a stationary localisation wave in the gradient-dependent medium. For a gradient-dependent model it turns out that the phase speed not necessarily becomes imaginary at the onset of softening as in a classical model. From eq.(5.17) it follows that the phase velocity remains real if

$$k \geq \sqrt{-\frac{h}{\bar{c}}} \quad \text{and thus} \quad \lambda \leq 2\pi l, \quad \text{with} \quad l = \sqrt{-\frac{\bar{c}}{h}}. \quad (5.18)$$

The parameter  $l$  is now the internal length scale in the gradient-dependent model. If  $k < l^{-1}$  or wave length  $\lambda > 2\pi l$  we recover the situation in which a disturbance  $\delta v$  is unbounded and stability in the sense of Lyapunov is lost (i.e. a small disturbance of boundary data results in large changes of the response). However, strain-softening regions remain small and no wave lengths larger than  $2\pi l$  can occur because they do not fit within the strain-softening region. Consequently, all phase velocities remain real because the first-order wave with the lowest wave number (largest wave length) has a wave number which is larger than the critical value in eq.(5.18). In the numerical analyses in the next paragraph we will see that all higher frequencies which are present in a loading wave vanish under the influence of nonlinear material behaviour and we obtain a stationary harmonic localisation wave with a width equal to the maximum wave length  $\lambda = w = 2\pi l$ .

### 5.3 ALGORITHMIC ASPECTS

In Chapter 3 we have derived a weak form of the initial value problem at  $t + \Delta t$  according to

$$\int_V \delta \mathbf{u}^T [\mathbf{R}\ddot{\mathbf{u}}^{t+\Delta t}] dV + \int_V \delta \boldsymbol{\varepsilon}^T \int_t^{t+\Delta t} \dot{\boldsymbol{\sigma}} d\tau dV = \int_S \delta \mathbf{u}^T \mathbf{t}^{t+\Delta t} dS - \int_V \delta \boldsymbol{\varepsilon}^T \boldsymbol{\sigma}^t dV, \quad (5.19)$$

in which the body forces  $\mathbf{p}$  have been neglected. Because we cannot satisfy the yield function at a local level we assume satisfaction in a distributed sense. A weak form of eq.(5.1) is given by

$$\int_V \delta \lambda f(\boldsymbol{\sigma}^{t+\Delta t}, \boldsymbol{\kappa}^{t+\Delta t}, \nabla^2 \boldsymbol{\kappa}^{t+\Delta t}) dV = 0. \quad (5.20)$$

The yield function at  $t + \Delta t$  can be written as

$$f(\boldsymbol{\sigma}^{t+\Delta t}, \boldsymbol{\kappa}^{t+\Delta t}, \nabla^2 \boldsymbol{\kappa}^{t+\Delta t}) = f(\boldsymbol{\sigma}^t, \boldsymbol{\kappa}^t, \nabla^2 \boldsymbol{\kappa}^t) + \int_t^{t+\Delta t} \dot{f}(\boldsymbol{\sigma}, \boldsymbol{\kappa}, \nabla^2 \boldsymbol{\kappa}) d\tau. \quad (5.21)$$

With the consistency equation (5.8), eq.(5.20) can now be modified to

$$\int_V \delta \lambda \int_t^{t+\Delta t} [\mathbf{n}^T \dot{\boldsymbol{\sigma}} - h \dot{\lambda} + \bar{c}_\eta \nabla^2 \dot{\lambda}] d\tau dV = - \int_V \delta \lambda f(\boldsymbol{\sigma}^t, \boldsymbol{\kappa}^t, \nabla^2 \boldsymbol{\kappa}^t) dV. \quad (5.22)$$

Substitution of  $\boldsymbol{\varepsilon}_p = \dot{\lambda} \mathbf{m}$  into the stress rate-strain rate equation (3.53) leads to

$$\dot{\boldsymbol{\sigma}} = \mathbf{D}_e (\dot{\boldsymbol{\varepsilon}} - \dot{\lambda} \mathbf{m}) \quad (5.23)$$

If we substitute this relationship in the eqs.(5.19) and (5.22) we obtain

$$\int_V \delta \mathbf{u}^T [\mathbf{R}\ddot{\mathbf{u}}^{t+\Delta t}] dV + \int_V \delta \boldsymbol{\varepsilon}^T \int_t^{t+\Delta t} \mathbf{D}_e (\dot{\boldsymbol{\varepsilon}} - \dot{\lambda} \mathbf{m}) d\tau dV = \int_S \delta \mathbf{u}^T \mathbf{t}^{t+\Delta t} dS - \int_V \delta \boldsymbol{\varepsilon}^T \boldsymbol{\sigma}^t dV = 0, \quad (5.24)$$

and

$$\int_V \delta \lambda \int_t^{t+\Delta t} [\mathbf{n}^T \mathbf{D}_e \dot{\boldsymbol{\varepsilon}} - (h + \mathbf{n}^T \mathbf{D}_e \mathbf{m}) \dot{\lambda} + \bar{c}_\eta \nabla^2 \dot{\lambda}] d\tau dV = - \int_V \delta \lambda f(\boldsymbol{\sigma}^t, \boldsymbol{\kappa}^t, \nabla^2 \boldsymbol{\kappa}^t) dV. \quad (5.25)$$

It is emphasized that in contrast to the conventional approach in computational plasticity, the plastic multiplier is taken as an independent variable. While this approach is, in principle, also possible in gradient-independent plasticity it does not seem to entail major advantages when compared with the return-mapping algorithms (Ortiz and Simo 1986, de Borst and Feenstra 1990). For gradient plasticity, i.e. when  $\bar{c}_\eta \neq 0$  in eq.(5.25), however the discretisation of  $\dot{\lambda}$  seems natural and automatically gives satisfaction of the consistency condition in a distributed sense (Simo 1989). Other alternatives of dealing with the extra partial differential equation have been discussed by de Borst and Mühlhaus (1991).

The discretisation of strain and displacement field has already been discussed in Chapter 2. We can discretise the plastic multiplier  $\dot{\lambda}$  in a similar fashion by

$$\lambda = \mathbf{h}^T \mathbf{A}, \quad (5.26)$$

with vector  $\mathbf{h}$  containing the shape functions  $h_1, \dots, h_n$  for the interpolation of the plastic multiplier and  $\mathbf{A}$  denoting the vector of additional nodal degrees-of-freedom. Eq.(5.26) in a rate form yields

$$\dot{\lambda} = \mathbf{h}^T \dot{\mathbf{A}}. \quad (5.27)$$

Since the Laplacian operator of  $\dot{\lambda}$  must also be computed, the differential operator vector  $\mathbf{p}$  is introduced

$$\nabla^2 \dot{\lambda} = \mathbf{p}^T \dot{\mathbf{A}}, \quad (5.28)$$

in which  $\mathbf{p}$  is defined by

$$\mathbf{p} = [\nabla^2 h_1, \dots, \nabla^2 h_n]^T. \quad (5.29)$$

Generally, the vector  $\mathbf{h}$  will not contain the same interpolation polynomials as  $\mathbf{H}$ . While the interpolation of the displacement degrees-of-freedom requires only  $C^0$ -continuity, the fact that second derivatives of  $\dot{\lambda}$  enter the weak form of the consistency condition makes it necessary to select  $C^1$ -continuous shape functions for the interpolation of  $\dot{\lambda}$ . For instance, for the one-dimensional examples that will be treated in a subsequent section, a Hermitian interpolation is employed for  $\dot{\lambda}$  and linear interpolation is used for  $u_x$ , quite similar to beam-column elements where the interpolation of the transverse displacements is usually also achieved through Hermitian shape functions and the axial displacements are interpolated linearly.

Next we substitute eqs.(2.16), (2.17), (2.19), (2.20), (5.26) and (5.27) in eqs.(5.24) and (5.25). The result is

$$\begin{aligned} \delta \mathbf{a}^T \int_V \mathbf{H}^T \mathbf{R} \mathbf{H} \dot{\mathbf{a}}^{t+\Delta t} + \delta \mathbf{a}^T \int_V \int_t^{t+\Delta t} [\mathbf{B}^T \mathbf{D}_e \mathbf{B} \dot{\mathbf{a}} - \mathbf{B}^T \mathbf{D}_e \mathbf{m} \mathbf{h}^T \dot{\lambda}] d\tau dV = \\ \delta \mathbf{a}^T \int_S \mathbf{H}^T \mathbf{t}^{t+\Delta t} dS - \delta \mathbf{a}^T \int_V \mathbf{B}^T \boldsymbol{\sigma}^t dV, \end{aligned} \quad (5.30)$$

and

$$\begin{aligned} \delta \Lambda^T \int_V \int_t^{t+\Delta t} [-\mathbf{h} \mathbf{n}^T \mathbf{D}_e \mathbf{B} \dot{\mathbf{a}} + (\mathbf{h} + \mathbf{n}^T \mathbf{D}_e \mathbf{m}) \mathbf{h} \mathbf{h}^T \dot{\lambda} - \bar{c}_\eta \mathbf{h} \mathbf{p}^T \dot{\lambda}] d\tau dV = \\ \delta \Lambda^T \int_V f(\boldsymbol{\sigma}^t, \boldsymbol{\kappa}^t, \nabla^2 \boldsymbol{\kappa}^t) \mathbf{h} dV. \end{aligned} \quad (5.31)$$

As in Chapter 2 we assume Euler forward predictions for the time integrals in eqs.(5.30) and (5.31). Therefore in the zero-th iteration of a Newton-Raphson scheme we take  $\mathbf{n}$ ,  $\mathbf{m}$  and  $h$  at

time  $t$ . Furthermore, similar to the definition of  $\Delta \mathbf{a}$  in Chapter 2 we define

$$\Delta \Lambda = \int_t^{t+\Delta t} \dot{\Lambda} d\tau. \quad (5.32)$$

Since the identities (5.30) and (5.31) must hold for any admissible  $\delta \mathbf{a}$  and  $\delta \Lambda$  the following set of algebraic equations ensues

$$\int_V [\mathbf{H}^T \mathbf{R} \mathbf{H} \dot{\mathbf{a}}^{t+\Delta t} dV + \int_V [\mathbf{B}^T \mathbf{D}_e \mathbf{B} \Delta \mathbf{a} - \mathbf{B}^T \mathbf{D}_e \mathbf{m}^t \mathbf{h}^T \Delta \Lambda] dV = \int_S \mathbf{H}^T \mathbf{t}^{t+\Delta t} dS - \int_V \mathbf{B}^T \boldsymbol{\sigma}^t dV, \quad (5.33)$$

and

$$\int_V [-\mathbf{h}(\mathbf{n}^t)^T \mathbf{D}_e \mathbf{B} \Delta \mathbf{a} + (\mathbf{h}^t + (\mathbf{n}^t)^T \mathbf{D}_e \mathbf{m}^t) \mathbf{h} \mathbf{h}^T \Delta \Lambda - \bar{c}_\eta \mathbf{h} \mathbf{p}^T \Delta \Lambda] dV = \int_V f(\boldsymbol{\sigma}^t, \boldsymbol{\kappa}^t, \nabla^2 \boldsymbol{\kappa}^t) \mathbf{h} dV. \quad (5.34)$$

Eqs.(5.33) and (5.34) can be written in a compact fashion as

$$\begin{bmatrix} \mathbf{M}_{aa} & 0 \\ 0 & 0 \end{bmatrix} \begin{bmatrix} \dot{\mathbf{a}}^{t+\Delta t} \\ \dot{\Lambda}^{t+\Delta t} \end{bmatrix} + \begin{bmatrix} \mathbf{K}_{aa} & \mathbf{K}_{a\lambda} \\ \mathbf{K}_{\lambda a} & \mathbf{K}_{\lambda\lambda} \end{bmatrix} \begin{bmatrix} \Delta \mathbf{a} \\ \Delta \Lambda \end{bmatrix} = \begin{bmatrix} \mathbf{f}^{t+\Delta t} - \mathbf{f}_{int}^t \\ \mathbf{f}_\lambda^t \end{bmatrix}, \quad (5.35)$$

where

$$\mathbf{M}_{aa} = \int_V \mathbf{H}^T \mathbf{R} \mathbf{H} dV, \quad (5.36)$$

$$\mathbf{K}_{aa} = \int_V \mathbf{B}^T \mathbf{D}_e \mathbf{B} dV, \quad (5.37)$$

$$\mathbf{K}_{a\lambda} = - \int_V \mathbf{B}^T \mathbf{D}_e \mathbf{m}^t \mathbf{h}^T dV, \quad (5.38)$$

$$\mathbf{K}_{\lambda a} = - \int_V \mathbf{h}(\mathbf{n}^t)^T \mathbf{D}_e \mathbf{B} dV, \quad (5.39)$$

$$\mathbf{K}_{\lambda\lambda} = \int_V [(\mathbf{h}^t + (\mathbf{n}^t)^T \mathbf{D}_e \mathbf{m}^t) \mathbf{h} \mathbf{h}^T - \bar{c}_\eta \mathbf{h} \mathbf{p}^T] dV, \quad (5.40)$$

and

$$\mathbf{f}_\lambda^t = \int_V f(\boldsymbol{\sigma}^t, \boldsymbol{\kappa}^t, \nabla^2 \boldsymbol{\kappa}^t) \mathbf{h} dV, \quad (5.41)$$

while  $\mathbf{f}^{t+\Delta t}$  and  $\mathbf{f}_{int}^t$  satisfy the definitions in Chapter 2. In the Newton-Raphson iteration scheme, which is used to solve the nonlinear set of algebraic equations, the values at time  $t$  are replaced by the values at time  $t+\Delta t$  for the last iteration (see section 2.3). The time integration procedure of Chapter 2 has also been adopted for eq.(5.35). Evidently the tangent stiffness matrix as defined in eqs.(5.35)-(5.40) is non-symmetric because of the gradient terms and the use of a non-associative flow rule. If we assume associative plasticity ( $\mathbf{m} = \mathbf{n}$  and thus



$\mathbf{K}_{a\lambda} = \mathbf{K}_{\lambda a}$ ) the non-symmetry in eq.(5.40) disappears if  $\bar{c}_\eta = 0$ . We retrieve a symmetric operator as one would expect in classical plasticity with an associated flow rule.

For the pure rate problem the non-symmetric tangent operator defined in eqs.(5.35)-(5.40) can be symmetrised. However, when we consider finite loading steps, this is not possible and symmetrisation of eq.(5.40) therefore does not seem to offer much practical advantage. The main significance is that a formulation, which sets out from a weak formulation of the evolution equation for the inelastic state variables (de Borst and Mühlhaus 1991 and 1992), can be shown to be identical to the formulation that arises upon application of the variational principle for gradient plasticity, recently proposed by Mühlhaus and Aifantis (1991). The other advantage is that the role of the additional boundary condition on  $\dot{\lambda}$  is elucidated. For this discussion it is sufficient to only consider the last term of eq.(5.40) in a rate format, or, more conveniently, eq.(5.25). Application of Green's theorem to this term yields

$$\int_V \bar{c}_\eta \delta \dot{\lambda} \nabla^2 \dot{\lambda} dV = - \int_V \bar{c}_\eta (\nabla \delta \dot{\lambda})^T (\nabla \dot{\lambda}) dV + \int_{S_\lambda} \bar{c}_\eta \delta \dot{\lambda} (\nabla \dot{\lambda})^T \mathbf{n}_\lambda dS_\lambda, \quad (5.42)$$

with  $\mathbf{n}_\lambda$  the outward normal at the elastic-plastic boundary  $S_\lambda$ . From eq.(5.42) it follows that the condition on  $\dot{\lambda}$  at the boundary of the plastically deforming part of the body must either be

$$\delta \dot{\lambda} = 0 \quad \text{or} \quad (\nabla \dot{\lambda})^T \mathbf{n}_\lambda = 0. \quad (5.43)$$

Eq.(5.43.1) is automatically satisfied at each point of the (internal) elastic-plastic boundary in the interior of the body. When the spread of the plastic zone extends to an external boundary of the body either of conditions (5.43) may be imposed.

With eq.(5.42) and assuming that the appropriate boundary conditions are satisfied  $\mathbf{K}_{\lambda\lambda}$  can be rewritten as

$$\mathbf{K}_{\lambda\lambda} = \int_V [(\mathbf{h} + \mathbf{n}^T \mathbf{Dn}) \mathbf{h} \mathbf{h}^T + \bar{c}_\eta \mathbf{q} \mathbf{q}^T] dV, \quad (5.44)$$

where

$$\mathbf{q} = [\nabla h_1, \dots, \nabla h_n]^T. \quad (5.45)$$

Comparing eq.(5.35) with  $\mathbf{M}_{aa}$ ,  $\mathbf{K}_{aa}$ ,  $\mathbf{K}_{a\lambda}$ ,  $\mathbf{K}_{\lambda a}$  and  $\mathbf{K}_{\lambda\lambda}$  as defined by eqs.(5.36), (5.37), (5.38), (5.39) and (5.44), with the tangent stiffness operator that follows from the variational principle of Mühlhaus and Aifantis (1991), shows that both formulations yield the same result for infinitesimally small load increments. When finitely sized loading steps are used this is no longer the case and the non-symmetric definition of eq.(5.40) must be utilised to obtain proper convergence characteristics in an incremental-iterative procedure.

## 5.4 NUMERICAL ANALYSES

To investigate the dispersive character of the gradient-dependent model and the performance

with respect to mesh refinement dynamic analyses have been carried out for the one-dimensional bar in tension (Example 1) and the impact biaxial test (Example 3). All calculations in this chapter have been carried out with the Newmark time integration scheme ( $\beta = 1/4$ ,  $\gamma = 1/2$ , see section 2.3). For the time step we take  $\Delta t = 5 \cdot 10^{-7}$  for Example 1 and  $\Delta t = 1.5 \cdot 10^{-6}$  s for Example 3. A constant mass matrix has been used in all analyses with the gradient model.

#### 5.4.1 Example 1 : One-dimensional bar problem in tension

First, we have investigated the gradient model by means of the one-dimensional bar problem in pure tension. This problem was already used as a reference problem in Chapters 3 and 4 for an analytical and numerical treatment of the classical strain-softening model and a rate-dependent crack model. The geometrical, material and loading data for the bar have been given in Figure 3.4. Instead of a crack model, as used for the bar in the Chapters 3 and 4, a softening plasticity model according to the Rankine yield function is now used. A minor difference in the response occurs because of the different unloading behaviour between a crack model and a plasticity model. We apply a slight modification of the parameter set by taking a steeper softening branch compared with the classical case :  $h = -2000 \text{ N/mm}^2$ . This does not necessarily increase the brittleness of the material because the gradient effect "carries" a part of the load, in the same fashion as the viscous effect does in the rate-dependent models. The extra gradient constant  $\bar{c}_\eta = 50000 \text{ N}$ . The values for  $h$  and  $\bar{c}_\eta$  imply an internal length scale parameter  $l = 5 \text{ mm}$  (eq.(5.18)). For the bar we use 20, 40, 80 and 160 line elements, respectively, with  $C^0$ -continuous shape functions for the displacement degree-of-freedom  $u_x$  and  $C^1$ -continuous shape functions for the interpolation of  $\hat{\lambda}$ . Again, we consider a block wave  $t_d = 0$  travelling linearly elastic through the bar until reflection occurs and the localisation process is initiated. Extra boundary conditions (cf. eq.(5.43)) have been applied ( $\partial \hat{\lambda} / \partial x = 0$ ) at both sides of the bar.

For the gradient model a localisation zone emerges the width of which converges to a finite, constant value upon mesh refinement. In Figure 5.3 the strain profile is plotted for different meshes to demonstrate the uniqueness of the solution. The coarser meshes with 20 and 40 elements still deviate somewhat but the fine meshes give almost identical results. In the same figure the development of the localisation band has been plotted at several time steps. First, the width of the zone increases after reflection but later, the speed of extension of the zone vanishes and a localisation band of constant width arises ( $1/2 w \approx 16 \text{ mm}$ ). Due to material damping the higher-order waves are attenuated. Owing to dispersion and material damping the shape of the loading wave changes into a first-order harmonic wave with velocity  $c_f$  equal to zero. This corresponds to a wave number  $k = 0.2 \text{ 1/mm}$  and a harmonic wave length  $\lambda = 2 \pi l = 31.4 \text{ mm}$  (cf. eqs.(5.17) and (5.18)). So, the numerical localisation band width  $w$  equals the first order wave length  $\lambda$  belonging to a phase velocity  $c_f = 0 \text{ m/s}$  under the condition that the localisation band has developed completely. So, the localisation zone is represented by a stationary harmonic wave. In Figure 5.4 it is shown that mesh independence is not

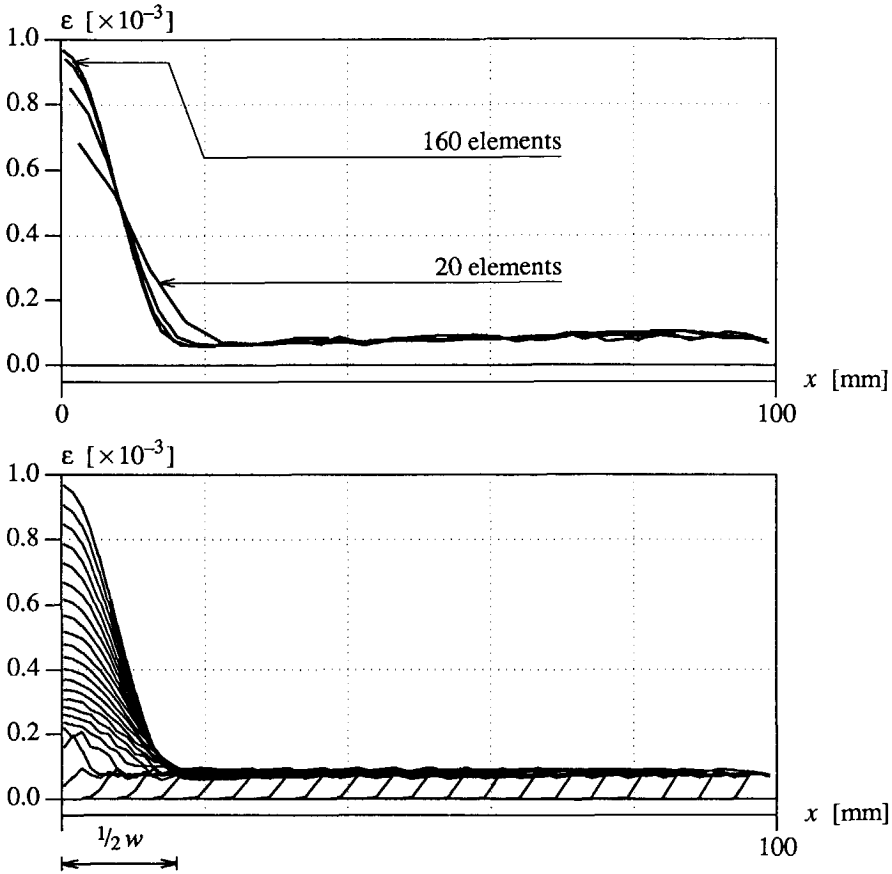


Figure 5.3 Gradient-dependent model with  $t_d = 0. s$  :  
 Top : Strain localisation along the bar at  $t = 0.2 \cdot 10^{-3} s$ .  
 Bottom : Development of the localisation band (160 elements).

only obtained for the width of the localisation zone but also for the wave reflection patterns and the energy consumption. The stress profiles (Figure 5.4 - top) are a superposition of the loading wave travelling to the left and the reflected wave travelling to the right. The patterns are more or less identical for the four meshes and it appears that wave reflection in a gradient-dependent bar is not determined by the number of elements. In the bottom picture of Figure 5.4 we observe, at increasing consumption of energy  $U$  in the bar, a negative value of the second derivative  $d^2U/dt^2$  after reflection ( $t = 0.1 \cdot 10^{-3} s$ ). As discussed in section 3.2 this corresponds with the occurrence of a structural instability, which for the gradient model does not result in loss of hyperbolicity. So, we can compare the results for the gradient-dependent bar

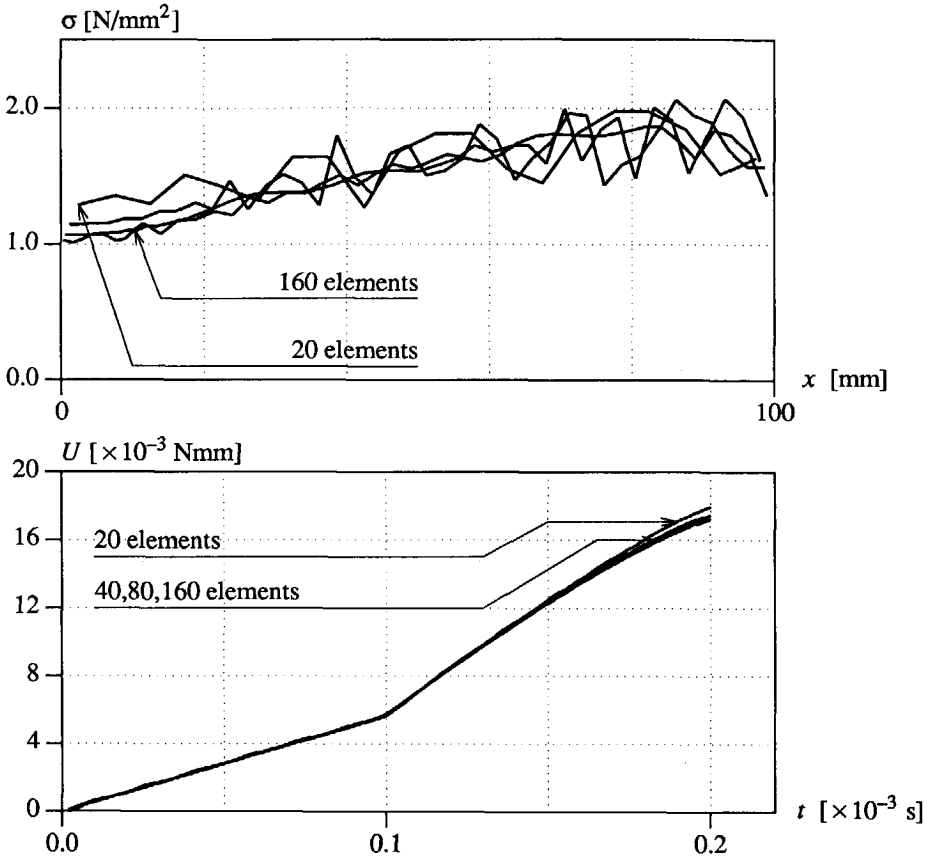


Figure 5.4 Gradient-dependent crack model with  $t_d = 0$ . s ;  
 Top : Stress profiles along the bar at  $t = 0.2 \cdot 10^{-3}$  s.  
 Bottom : Energy consumption of the bar.

in the Figures 5.3 and 5.4 with the results for the classical strain-softening bar in the Figures 3.5 and 3.6. For the gradient model, in contrast to the classical modelling, the localisation zone converges to a non-zero width and to physically realistic responses for the wave reflection on the zone and the energy consumption in the zone.

The internal length scale parameter of the gradient model has been varied by taking  $l = 2.5 \text{ mm}$ ,  $l = 5.0 \text{ mm}$  and  $l = 7.5 \text{ mm}$ . The results in Figure 5.5 prove the analytical equation for the localisation band width (for this problem :  $\frac{1}{2} w = \pi l$ ). Applying  $\dot{\lambda} = 0$  as boundary condition at both sides of the bar instead of  $\partial \dot{\lambda} / \partial x = 0$  affects the localisation process. In Figure 5.6 it is shown that the localisation band develops over the total zone  $w = 2 \pi l$  because

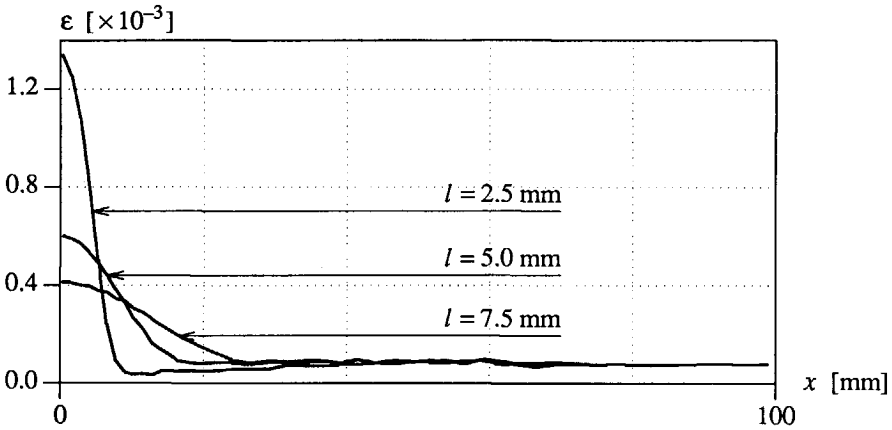


Figure 5.5 Variation of the length scale parameter (160 elements -  $t = 0.17 \cdot 10^{-3}$  s).

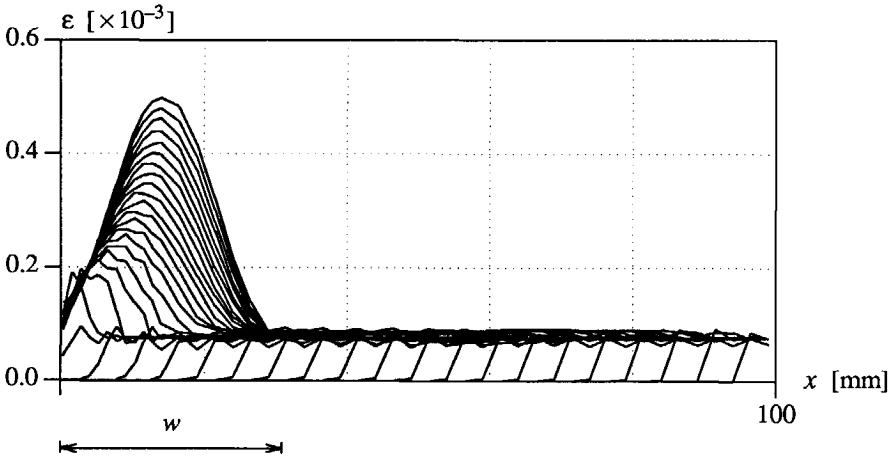


Figure 5.6 Application of boundary condition  $\dot{\lambda} = 0$  at both sides of the bar.

the plastic strain is kept zero at  $x = 0$ . A new stage in the localisation process is entered when in some part of the localisation zone the strength contribution due to local softening has vanished, so that the load-carrying capacity is only due to gradient effects. From eq.(5.17) and (5.18) it appears that the wave length  $\lambda$  then starts to increase, the wave speed becomes positive and the localisation zone is no longer stationary, which in turn causes an extension of the localisation zone. This phenomenon is plotted in the picture of Figure 5.7 for an analysis with a slightly different parameter set :  $\bar{c}_\eta = 100000$  N and  $h = -4000$  N/mm<sup>2</sup> ( $\kappa_\mu = \bar{\sigma}_0/h = 0.5 \cdot 10^{-3}$ ).

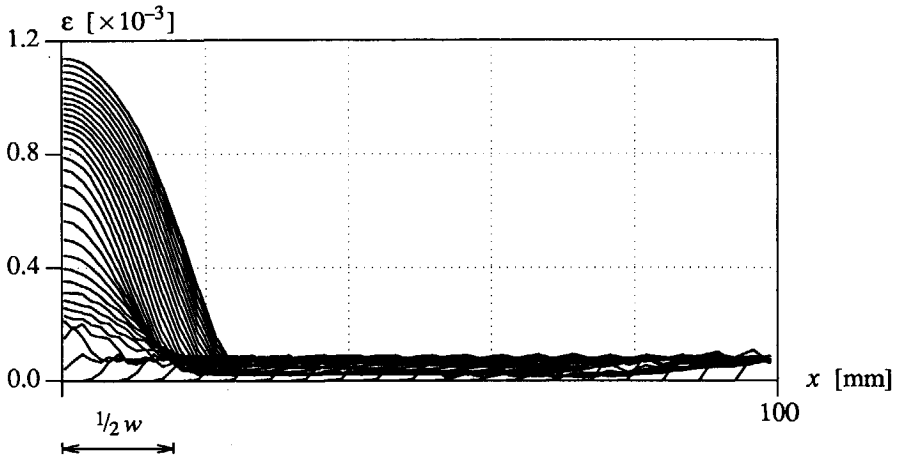


Figure 5.7 Extension of the localisation zone after the termination of softening.

The width of the localisation band does not depend on the loading rate. Such a dependence was found for the rate-dependent softening model in the previous chapter. For the gradient model a higher loading rate influences the development of the localisation zone but it does not affect the band width. The use of an impact loading wave with a vertical stress front ( $t_d = 0$ ) implies a high stress rate and the presence of higher-order waves in the loading pulse. Due to dissipation of energy these higher-order waves attenuate and the vertical stress front changes into a harmonic cosine shape. When, for instance, a linearly increasing load in time ( $t_d \neq 0$ ) is used the loading rate is smaller and higher-order waves are hardly present which cause a more gradual development of the localisation zone, but the width of and the ultimate strain profile in the localisation band are not affected (Sluys et al. 1991).

#### 5.4.2 Example 3 : Impact biaxial test

For a strain-softening model without rate or gradient effects a search algorithm should be used to determine the orientation of the shear band after which a mesh-adaptation strategy is necessary to minimise the intrinsic bias. For the gradient model mesh adaptation is not necessary. A full treatment of the mesh-alignment problem, with biased and unbiased meshes (cf. Figure 3.19), cannot yet be carried out because, at this moment, only a rectangular element with linear interpolation of the displacements and cubic interpolation of the plastic multiplier (Pamin and de Borst 1992) is available that incorporates the gradient effect. By considering the plane-strain and plane-stress condition for a von Mises type material and the plane-strain condition for a Drucker-Prager material it will be shown that the direction of propagation of the shear band complies with the analytical predicted direction and is not influenced by the mesh lines.

The finite element configurations of Figure 3.15 have been changed somewhat, i.e. each quadrilateral is now composed of four four-noded quadrilateral elements. As for the one-dimensional bar extra boundary conditions should be used for the sample (cf. eq.(5.43)). At the vertical sides of the sample  $\partial\dot{\lambda}/\partial x$  (and consequently  $\partial^2\dot{\lambda}/\partial x\partial y$ ) is kept zero, while at the top and bottom of the sample  $\partial\dot{\lambda}/\partial y$  (and consequently  $\partial^2\dot{\lambda}/\partial x\partial y$ ) is zero.

*- biaxial test with von Mises material (plane-strain)*

For the analysis with the von Mises plasticity model the material and loading data from Figure 3.14 have been used. The additional constant employed is  $\bar{c}_\eta = 6250$  N. With a softening modulus  $h = -1000$  N/mm<sup>2</sup> we obtain for the length scale parameter  $l = 2.5$  mm (eq.(5.18)). Again, one loading cycle is considered in which the pressure wave reflects at the bottom of the sample and the returning wave causes bulging and finally shear banding.

In Figure 5.8 the displacement patterns are plotted with the corresponding contour plots of the equivalent plastic strains. The inclination angle of the shear band is  $45^\circ$  (eq.(3A.21)) and the width of the band is constant for the three meshes. We obtain a unique solution for the properties of the localisation band. Due to dispersion and material damping the shear band transforms into a stationary harmonic wave. This can be seen from a plot of the cosine-shaped equivalent plastic strains in a vertical cross-section of the sample in Figure 5.9. A comparison of the consumption of energy for the meshes in Figure 5.10 once again demonstrates the insensitiveness of the solution for the finite element discretisation. The Figures 5.8 to 5.10 should be compared to the Figures 3.16 to 3.18 to see the differences between a strain-softening modelling with and without gradient incorporation.

*- biaxial test with von Mises material (plane-stress)*

The problem has also been analysed for a plane-stress condition. The parameter set is modified by taking the gradient constant  $\bar{c}_\eta = 2500$  N and the softening modulus  $h = -400$  N/mm<sup>2</sup>. These values result in the same length scale parameter  $l = 2.5$  mm. It is important to demonstrate that the inclination angle of the shear band can vary without influence of the mesh lines. The analytical prediction of the inclination angle  $\Theta = 35.3^\circ$  (eq.(3A.20)) comes out nicely. This is demonstrated by means of a plot of the displacements and the equivalent plastic strains in Figure 5.11. Also, the solution for the width of the localisation zone remains finite upon mesh refinement for the plane-stress case.

*- biaxial test with Drucker-Prager material (plane-strain)*

The performance of the gradient model in combination with a Drucker-Prager yield criterion has been investigated for a specimen of which the configuration has been changed somewhat with respect to the specimen in Figure 3.14. We consider a quadrant of a specimen and

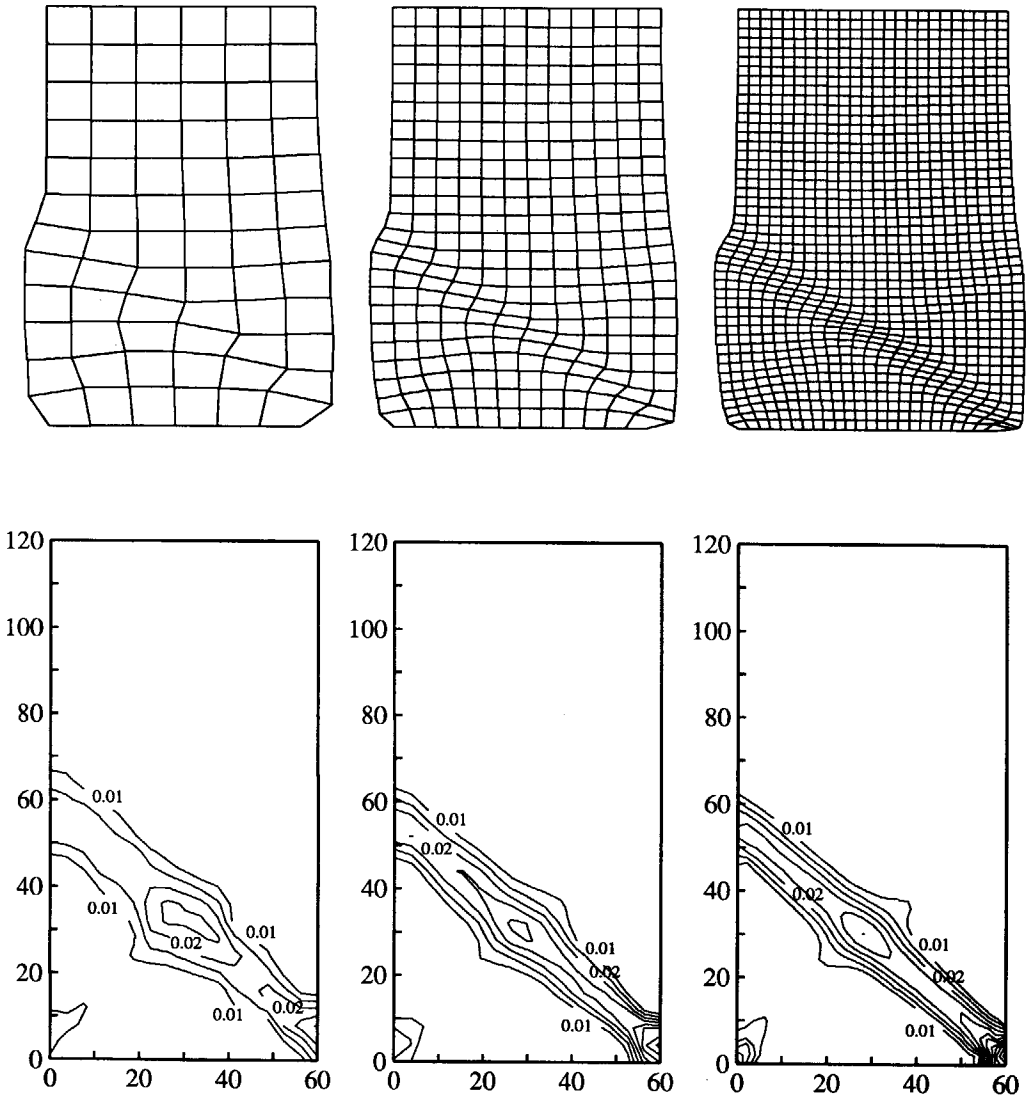


Figure 5.8 Gradient model (Von Mises) with plane-strain elements :  
Top : Total displacement patterns ( $t=0.165 \cdot 10^{-3}$  s, FA = 15).  
Bottom : Contour plots of the equivalent plastic strains.



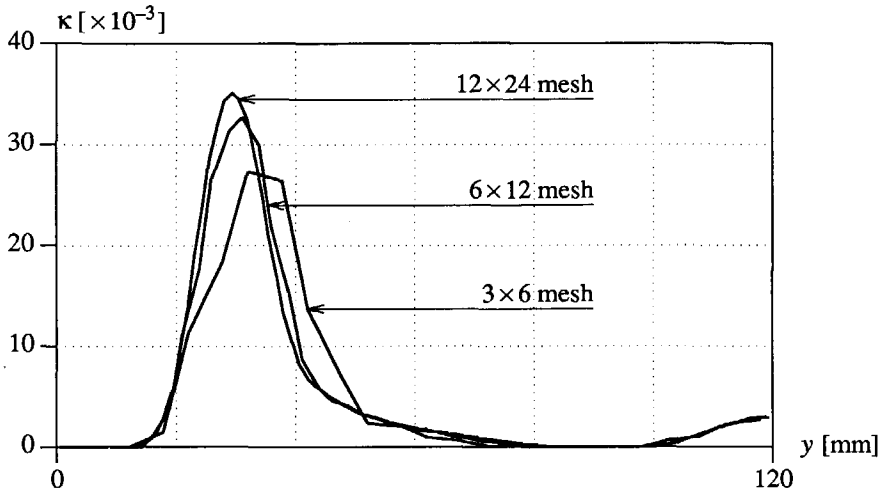


Figure 5.9 Equivalent plastic strains  $\kappa$  in centre section ( $x = 30$  mm) of the sample ( $t = 0.165 \cdot 10^{-3}$  s).

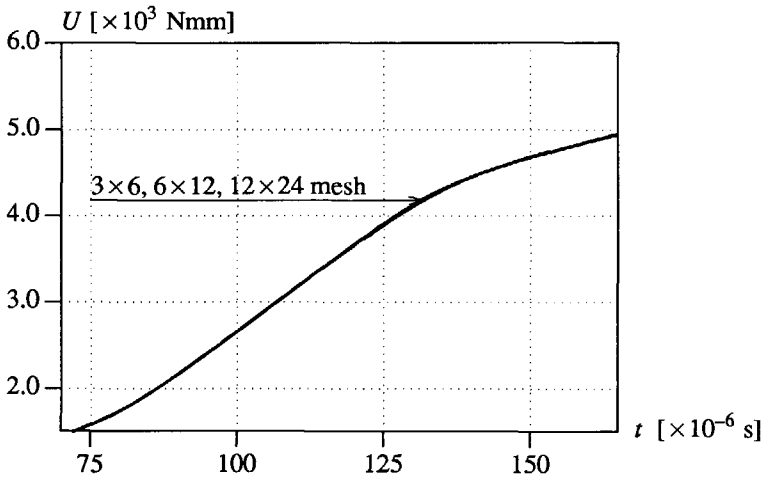


Figure 5.10 Energy consumption in the sample.

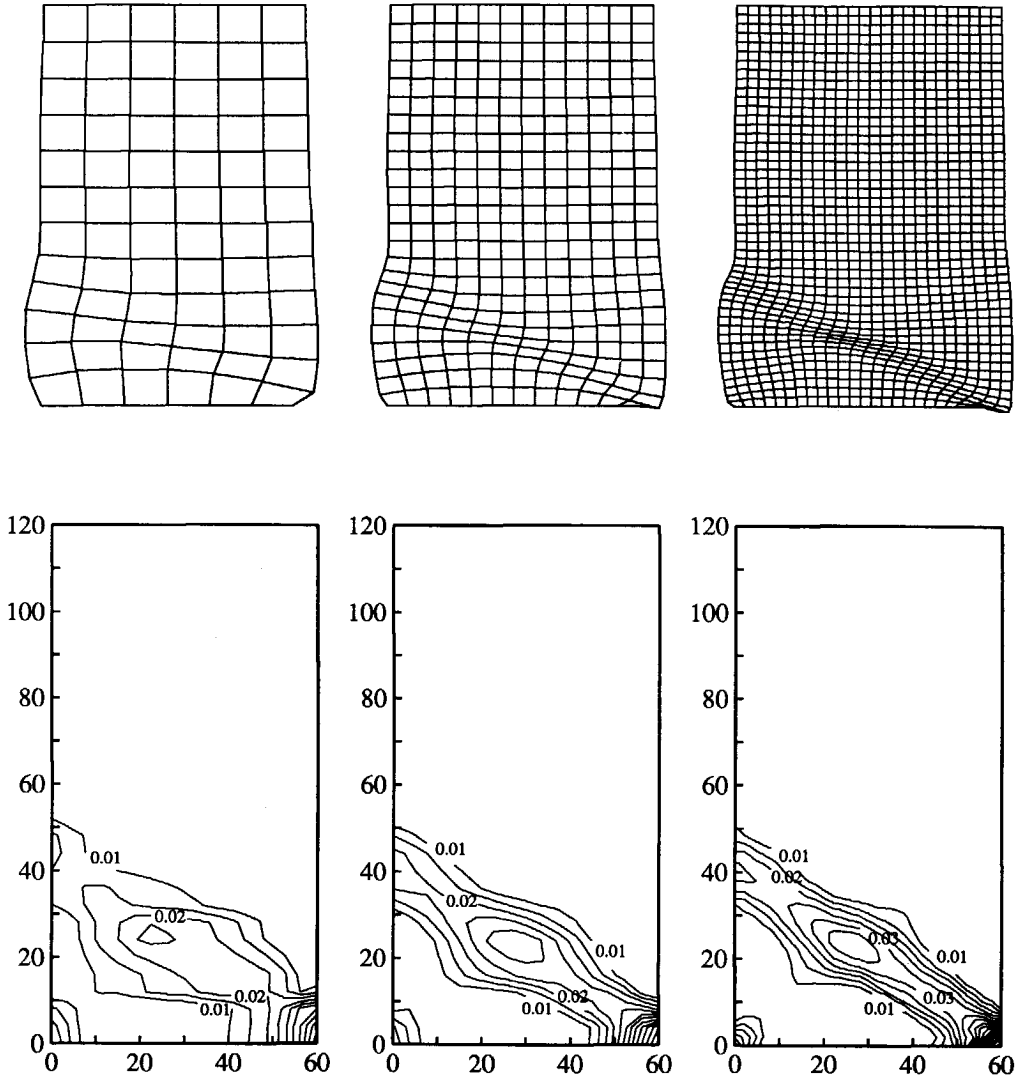


Figure 5.11 Gradient model (Von Mises) with plane-stress elements :  
 Top : Total displacement patterns ( $t = 0.165 \cdot 10^{-3}$  s, FA = 15).  
 Bottom : Contour plots of the equivalent plastic strains.

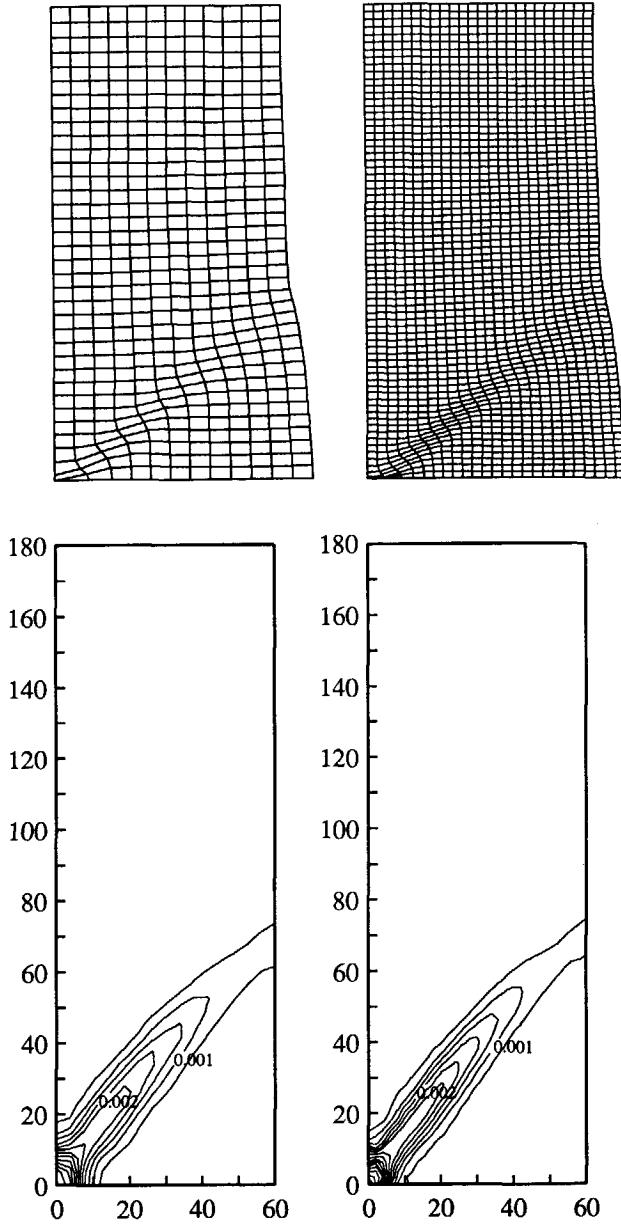


Figure 5.12 Gradient model (Drucker-Prager) with plane-strain elements :  
Top : Total displacement patterns ( $t = 0.24 \cdot 10^{-3}$  s, FA = 150).  
Bottom : Contour plots of the equivalent plastic strains.

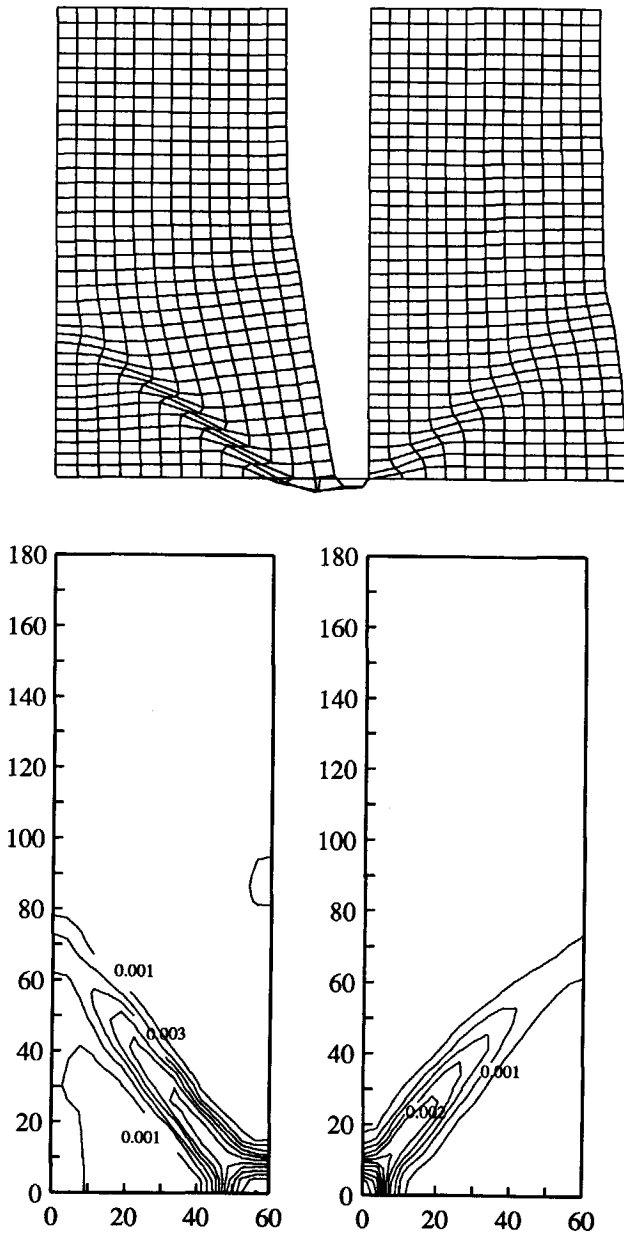


Figure 5.13 Gradient model (Drucker-Prager) with plane-strain elements using friction angle  $\phi = 20^\circ$  (left) and  $\phi = 30^\circ$  (right).

therefore the horizontal displacement is kept zero at the left vertical side ( $u_x = 0, u_y \neq 0$ ) and the bottom of the sample is rigid and smooth ( $u_x \neq 0, u_y = 0$ ). Furthermore, a longer specimen has been selected so as to admit the emergence of a shear band which now runs steeper (according to the analytical solution in Appendix 3A). The horizontal force is omitted because asymmetry in the boundary conditions already forces an asymmetric failure pattern. The data set now reads (cf. Figure 3.14) : length  $a_2 = 180$  mm, pressure load  $F_{max} = 150$  kN, Young's modulus  $E = 2400$  N/mm<sup>2</sup>, Poisson's ratio  $\nu = 0.2$  and density  $\rho = 1250$  kg/m<sup>3</sup>. For the Drucker-Prager model the following parameters have been chosen : friction angle  $\phi = 30^\circ$ , dilatancy angle  $\psi = 0^\circ$  and cohesion  $c = 1$  N/mm<sup>2</sup>, linearly dependent on the equivalent plastic strain with an ultimate strain  $\kappa_u = 0.005$ . For the gradient model we take  $\bar{c}_\eta = 1800$  N and if we set  $h$  in eq.(5.18) equal to  $dc/d\kappa$  we obtain a length scale parameter  $l = 3.0$  mm. The additional boundary conditions listed in the analysis for the von Mises model have also been used for this analysis.

The results of the plane-strain analysis after one cycle ( $t = 0.24 \cdot 10^{-3}$  s) of the pressure wave have been plotted in Figure 5.12. Again, we observe that refinement of the mesh has no influence on the size of the shear band. The shear band is initiated at the bottom left corner of the specimen with an inclination angle  $\Theta \approx 50^\circ$ , while analytically it was obtained that  $\Theta = 48.4^\circ$  (eq.(3A.23)). We observe a clear mismatch in orientation between the shear band in the interior and on the boundary of the specimen. Needleman and Ortiz (1991) have explained this phenomenon by means of an analytical treatment of the interaction between the shear band in the interior of the body and a stationary Rayleigh wave at the free boundary. A remarkable result is obtained if we take the internal friction angle  $\phi = 20^\circ$ . Figure 5.13 shows that the shear band now starts at the bottom right corner of the specimen. This change of orientation is due to the fact that a different stress state in the bottom corners of the specimen in combination with a different angle of internal friction leads to a different location of the critical state which drives the propagation of the shear band (related to  $h_{cri}/2\mu$  in Appendix 3A). This problem has been discussed in more detail in Appendix 3A. The numerically obtained inclination angle for  $\phi = 20^\circ$  equals  $\Theta \approx 49^\circ$ , which is in reasonable accordance with the analytical value  $\Theta = 47.0^\circ$  (eq.(3A.22)).



## 6. VISCOPLASTIC MODELS

The inclusion of rate effects as a regularisation method for localisation problems has been discussed before in Chapter 4. It was shown that softening during the fracture process leads to a mode-I dominated localisation process. This is typical for brittle softening materials as concrete and rock under low confining pressures. However, for softening materials as metals and soils the failure process at a macro-scale is dominated by mode-II effects and it is observed that at incipient failure all further deformation localises in shear bands. It appears that mode-II localisation (shear banding) prevails over mode-I localisation (fracture) when the frictional properties of the material are more critical than the cohesive properties. The occurrence of softening in shear bands is a ductile process and can be described by means of a softening plasticity model. Just as fracture, plastic deformation unambiguously is a process which is dependent on the time and time rate effects cannot be ignored when the loading conditions are transient. High strain rates mobilise viscous effects in a material which carry a part of the load, so that, from a physical point of view the extension of the plasticity relations with viscous terms (viscoplasticity) is evident.

As shown in Chapter 4 the inclusion of rate effects in the constitutive equations for a smeared crack model results in an implicit introduction of an internal length scale and in dispersive wave propagation in the rate-dependent medium. Just as the rate-dependent fracture theory, viscoplasticity offers the possibility to obtain mesh-objective results with respect to the size of the shear band, the wave reflection patterns and the dissipation of energy in shear failure zones.

Firstly, two approaches for viscoplastic modelling will be treated, namely the Perzyna theory (Perzyna 1966, Corneau 1975, Owen and Damjanić 1982) and the Duvaut-Lions theory (Duvaut and Lions 1972, Simo et al. 1988, Loret and Prevost 1990). Next, the viscoplastic models will be tested on their capability with respect to mesh sensitivity. This is done by means of a study on shear band formation in a one-dimensional shear layer (Example 1) and in the biaxial test (Example 3). Special attention is paid to the influence of the orientation of the mesh lines on the results. Finally, an overview of rate-dependent models will be given, in which the viscoplastic models have been compared to the rate-dependent crack models treated in Chapter 4.

### 6.1 CONSTITUTIVE EQUATIONS FOR VISCOPLASTICITY

In the viscoplastic theory an important distinction from the inviscid plasticity theory stems from the fact that stress states outside the yield surface are not illegal. If the external loading remains constant the stresses return to the yield surface as a function of time. Because of this feature viscoplastic theories are commonly called overstress laws. Similar to the rate-independent theory the strain rate is decomposed into an elastic and a viscoplastic strain rate

$$\dot{\boldsymbol{\epsilon}} = \dot{\boldsymbol{\epsilon}}_e + \dot{\boldsymbol{\epsilon}}_{vp} . \quad (6.1)$$

Eq.(2.6) then becomes

$$\dot{\boldsymbol{\sigma}} = \mathbf{D}_e(\dot{\boldsymbol{\epsilon}} - \dot{\boldsymbol{\epsilon}}_{vp}) . \quad (6.2)$$

The two different approaches in viscoplasticity treated here, namely the Perzyna viscoplasticity theory and the Duvaut-Lions viscoplasticity theory, are based on a different choice for the viscoplastic strain rate  $\dot{\boldsymbol{\epsilon}}_{vp}$ .

### 6.1.1 Perzyna viscoplasticity

In the theory proposed by Perzyna (1966) the viscoplastic strain rate is defined in a similar fashion as in the rate-independent plasticity theory

$$\dot{\boldsymbol{\epsilon}}_{vp} = \gamma \langle \phi(f) \rangle \mathbf{m} . \quad (6.3)$$

Now  $\mathbf{m}$  is defined as the gradient of the viscoplastic potential function  $g_{vp}$  (cf.eq.(3.55))

$$\mathbf{m} = \frac{\partial g_{vp}}{\partial \boldsymbol{\sigma}} . \quad (6.4)$$

Associative flow is invoked by  $g_{vp} = f$ . In eq.(6.3)  $\gamma$  is a fluidity parameter, which depends on the viscosity of the material and can be constant or a function of the stress or strain rate,  $\phi(f)$  is an arbitrary function of the flow function. The notation  $\langle \phi(f) \rangle$  implies that  $\langle \phi(f) \rangle = 0$  if  $f \leq 0$  and that  $\langle \phi(f) \rangle = \phi(f)$  if  $f > 0$ . Two choices for the function  $\phi(f)$  are

$$\phi(f) = \left[ \frac{f}{\bar{\sigma}_0} \right]^N \quad (6.5)$$

and

$$\phi(f) = \left[ \frac{f}{\bar{\sigma}} \right]^N , \quad (6.6)$$

in which  $N$  is a constant used to fit experimental data and  $\bar{\sigma} = \bar{\sigma}_0 + h\epsilon_{vp}$  is the strain-softening function.

In the left picture of Figure 6.1 a representation of the Perzyna model is given in the stress space. Stress states outside the yield surface are admissible and the value of the yield function  $f_{vp}$  determines the intensity of viscoplastic straining. If we apply eq.(6.5) with  $N = 1$  we are able to give a simple one-dimensional representation of the model (Figure 6.1 - centre) in which the softening element (left, active if  $\sigma > \bar{\sigma}_0$ ) is connected to the damper element in parallel (right). Summation of "softening stress rate"  $\dot{\bar{\sigma}}$  and "rate-dependent stress rate"  $\dot{\sigma}_{vp}$  gives



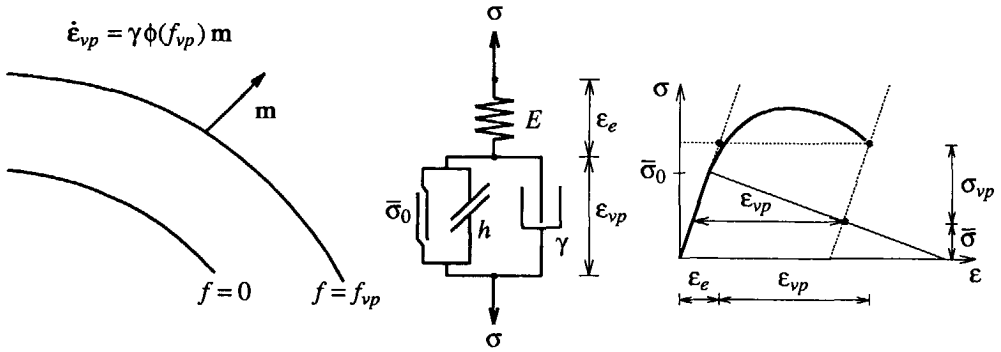


Figure 6.1 Representation of Perzyna type viscoplastic model.

$$\dot{\sigma} = \dot{\bar{\sigma}} + \dot{\sigma}_{vp} = h \dot{\epsilon}_{vp} + \frac{\bar{\sigma}_0}{\gamma} \frac{\partial \dot{\epsilon}_{vp}}{\partial t}. \tag{6.7}$$

The response of this one-dimensional Perzyna element is given in the diagram on the right of Figure 6.1. If we compare eq.(6.7) with eq.(4.3) of the rate-dependent crack model it is observed that the models coincide if  $\bar{\sigma}_0/\gamma = m$ . So, for the one-dimensional case the dispersion analysis, carried out in section 4.2 for the rate-dependent crack model, is also valid for the Perzyna viscoplastic model if  $\phi = f/\bar{\sigma}_0$ . Real characteristics of the initial value problem can be derived and wave propagation in the viscoplastic element is dispersive. In the Chapters 4 and 5 this feature has been shown to be a necessary condition for capturing localisation of deformation in a proper fashion. Along the same lines as followed in section 4.2 an internal length scale parameter can be derived for a mode-I localisation analysis

$$l = \frac{2\bar{\sigma}_0 c_e}{\gamma E}. \tag{6.8}$$

However, in two- and three-dimensional continuum analyses a pure mode-I analysis cannot be carried out. A property of almost all yield functions is that plastic straining occurs in the directions of intermediate principal stresses. Only if we take a purely one-dimensional shear problem (mode-II) the plastic volume change can be kept zero without spoiling the one-dimensional character of the problem. For a mode-II analysis we then obtain an internal length scale equal to

$$l = \frac{4\bar{\sigma}_0 c_g}{3\gamma E}, \tag{6.9}$$

in which  $c_g = \sqrt{\mu/\rho}$  is the linear elastic shear wave speed.

6.1.2 Duvaut-Lions viscoplasticity

A different approach, which in its elaboration connects more closely to the rate-independent plasticity theory, has been proposed by Duvaut and Lions (1972). The theory is based on the difference in response between the rate-independent material and the viscoplastic material. The viscoplastic strain rate is defined as

$$\dot{\epsilon}_{vp} = \frac{1}{\eta} [D_e]^{-1} (\sigma - \sigma_p) \tag{6.10}$$

and in a similar fashion the hardening rate is

$$\dot{\kappa} = -\frac{1}{\eta} (\kappa - \kappa_p) . \tag{6.11}$$

The vector  $\sigma_p$  can be viewed as the projection of the current stress on the yield surface and  $\kappa_p$  is determined by the rate-independent plastic strain history. The viscosity parameter  $\eta$  represents the relaxation time of the material. Eq.(6.10) and (6.11) are valid if  $f(\sigma, \kappa) > 0$  and if this condition is not met,  $\dot{\epsilon}_{vp}$  and  $\dot{\kappa}$  are both equal to zero. Combination of eq.(6.10) and (6.2) leads to the following first-order differential equation

$$\dot{\sigma} + \frac{1}{\eta} \sigma = D_e \dot{\epsilon} + \frac{1}{\eta} \sigma_p . \tag{6.12}$$

In Figure 6.2 (left picture) the model representation in the stress space is shown. The viscoplastic strain rate is determined by the difference between the total stress and the stress in the inviscid backbone model, which is in contrast to the Perzyna model in which the value of the dynamic yield surface  $f_{vp}$  determines the viscoplastic strain rate. This has the far-reaching consequence that the Duvaut-Lions model can be combined with a yield surface which has an

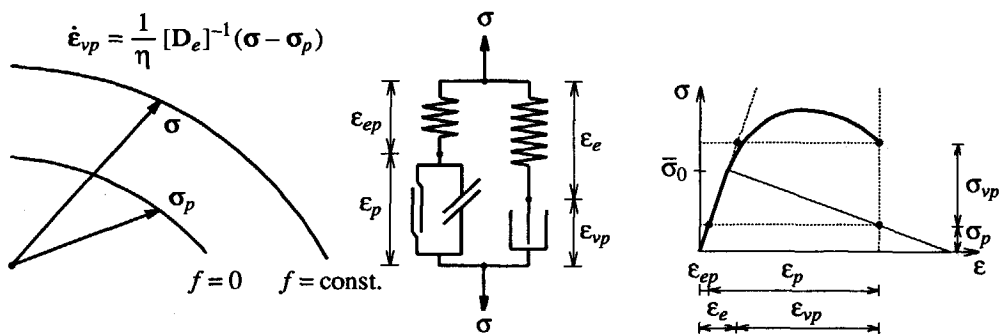


Figure 6.2 Representation of Duvaut-Lions type viscoplastic model.

apex (Drucker-Prager, Mohr-Coulomb) or a non-smooth surface (Mohr-Coulomb, Tresca), which is not possible for the Perzyna model. This will be explained in section 6.2.1. The one-dimensional discrete representation of the model (Figure 6.2 - centre) is more complicated than that of the Perzyna model. The rate-independent plastic response causes an elastic pre-training  $\epsilon_{ep}$ , only after which the damper element starts to contribute. The left chain of the model represents the rate-independent stress contribution  $\sigma_p$  and the right chain shows the rate-dependent contribution  $\sigma_{vp}$ . Summation of the stress rates now yields

$$\dot{\sigma} = \dot{\sigma}_p + \dot{\sigma}_{vp} = h \dot{\epsilon}_p + \eta E \frac{\partial \dot{\epsilon}_{vp}}{\partial t} . \quad (6.13)$$

Note that for the one-dimensional case  $\sigma_p = \bar{\sigma}$  (cf. eq.(6.7)). Since  $\epsilon_p \neq \epsilon_{vp}$  the stress is no longer an explicit function of the viscoplastic strain as it is in the Perzyna model. This implies that the wave equation for a one-dimensional Duvaut-Lions element (see eq.(6.50) in section 6.4) contains two state variables ( $v, \epsilon_{ep}$ ) and a dispersion analysis, along the same lines as in section 4.2, cannot be carried out. So, a length scale parameter cannot be derived from a dispersion analysis but is chosen equal to the expression for the Perzyna model (eq.(6.8) and (6.9)) with the constraint that the third-order terms in the wave equations of both models (see section 6.4) coincide, i.e.  $\eta E = \bar{\sigma}_0/\gamma$ . This yields

$$l = 2\eta c_e \text{ (mode-I)} \quad \text{and} \quad l = 4/3 \eta c_g \text{ (mode-II)} . \quad (6.14)$$

## 6.2. ALGORITHMIC ASPECTS

### 6.2.1 Perzyna model

From eq.(6.2) the incremental stress-strain relation can be written as

$$\Delta \sigma = D_e (\Delta \epsilon - \Delta \epsilon_{vp}) . \quad (6.15)$$

Again, we define the incremental values as the increment in time interval  $t \leq \tau \leq t + \Delta t$ . By utilising the viscoplastic strain rate at the beginning of the time step  $\dot{\epsilon}_{vp}^t$  and that at the end of the time step  $\dot{\epsilon}_{vp}^{t+\Delta t}$  the incremental viscoplastic strain is chosen according to

$$\Delta \epsilon_{vp} = ((1 - \Theta) \dot{\epsilon}_{vp}^t + \Theta \dot{\epsilon}_{vp}^{t+\Delta t}) \Delta t , \quad (6.16)$$

where  $\Theta$  is the interpolation parameter for which  $0 \leq \Theta \leq 1$ . For  $\Theta = 0$ ,  $\Theta = 1/2$  and  $\Theta = 1$  we obtain an explicit scheme, a scheme according to the trapezoidal rule and a fully implicit scheme, respectively. We anticipate on the use of an associative flow rule and therefore with  $\mathbf{m} = \mathbf{n}$  the viscoplastic strain rate at time  $t$  reads

$$\dot{\epsilon}_{vp}^t = \gamma \langle \phi^t(f) \rangle \mathbf{n}^t . \quad (6.17)$$

The viscoplastic strain rate at the end of the time interval is expressed in a limited Taylor series expansion as

$$\dot{\boldsymbol{\varepsilon}}_{vp}^{t+\Delta t} = \dot{\boldsymbol{\varepsilon}}_{vp}^t + \left[ \frac{\partial \dot{\boldsymbol{\varepsilon}}_{vp}}{\partial \boldsymbol{\sigma}} \right]^t \Delta \boldsymbol{\sigma} + \left[ \frac{\partial \dot{\boldsymbol{\varepsilon}}_{vp}}{\partial \bar{\sigma}} \right]^t \left( \frac{\partial \bar{\sigma}}{\partial \kappa} \right)^t \Delta \kappa. \quad (6.18)$$

We now define the matrix  $\mathbf{H}$  as

$$\mathbf{H} = \frac{\partial \dot{\boldsymbol{\varepsilon}}_{vp}}{\partial \boldsymbol{\sigma}}, \quad (6.19)$$

so that, under the assumption of a stress-independent fluidity parameter, substitution of eq.(6.3) with  $\mathbf{m} = \mathbf{n}$  gives

$$\mathbf{H} = \gamma \left[ \frac{\partial \phi}{\partial \mathbf{f}} \frac{\partial \mathbf{f}}{\partial \boldsymbol{\sigma}} \frac{\partial \mathbf{f}^T}{\partial \boldsymbol{\sigma}} + \phi \frac{\partial^2 \mathbf{f}}{\partial \boldsymbol{\sigma}^2} \right]. \quad (6.20)$$

Next, the last term of eq.(6.18) is considered. The term is zero for perfect plasticity, but is significant in hardening/softening plasticity with steep hardening/softening diagrams. It can be rewritten by using eq.(6.3)

$$\mathbf{h}^t = \left[ \frac{\partial \dot{\boldsymbol{\varepsilon}}_{vp}}{\partial \bar{\sigma}} \right]^t \left( \frac{\partial \bar{\sigma}}{\partial \kappa} \right)^t \Delta \kappa = \gamma \left[ \frac{\partial \phi}{\partial \bar{\sigma}} \mathbf{n} \right]^t \left( \frac{\partial \bar{\sigma}}{\partial \kappa} \right)^t \Delta \kappa, \quad (6.21)$$

in which the rate of hardening is assumed to be equal to

$$\dot{\kappa} = \sqrt{2/3} (\dot{\boldsymbol{\varepsilon}}_{vp})^T \dot{\boldsymbol{\varepsilon}}_{vp}, \quad (6.22)$$

and where the incremental growth of the hardening/softening parameter during the time interval  $\Delta t$  is approximated by an Euler forward prediction

$$\Delta \kappa = \dot{\kappa}^t \Delta t. \quad (6.23)$$

If we use the results of eqs.(6.18)-(6.23) for the determination of the incremental viscoplastic strain we obtain

$$\Delta \boldsymbol{\varepsilon}_{vp} = (\dot{\boldsymbol{\varepsilon}}_{vp}^t + \Theta \mathbf{H}^t \Delta \boldsymbol{\sigma} + \Theta \mathbf{h}^t) \Delta t. \quad (6.24)$$

This equation can be substituted in the incremental stress-strain relation (6.15), which yields

$$\Delta \boldsymbol{\sigma} = \mathbf{D}_c^t \Delta \boldsymbol{\varepsilon} - \Delta \mathbf{q} \quad (6.25)$$

in which

$$\mathbf{D}_c^t = \left[ \mathbf{D}_e^{-1} + \Theta \Delta t \mathbf{H}^t \right]^{-1} \quad (6.26)$$

$$\Delta \mathbf{q} = \left[ \mathbf{D}_e^{-1} + \Theta \Delta t \mathbf{H}^t \right]^{-1} (\dot{\epsilon}_{vp}^t \Delta t + \Theta \Delta t \mathbf{h}^t) \quad (6.27)$$

Matrix  $\mathbf{D}_e^t$  is not only determined by material parameters since the time integration parameters  $\Delta t$  and  $\Theta$  also enter. The format of the stress-strain law (6.25) is similar to the constitutive relation derived for the rate-dependent smeared crack model (eq.(4.26)). Again, a pseudonodal force vector can be deduced according to

$$\Delta \mathbf{f}_{vp} = \int_V \mathbf{B}^T \Delta \mathbf{q} dV, \quad (6.28)$$

which is used in the discretised equation of motion (cf. eq.(4.29)).

#### *Elaboration for the von Mises yield function*

For the calculation of the matrix  $\mathbf{H}$  a yield function must be chosen. It is noted that for the Perzyna viscoplastic theory the yield surface is required to be smooth with continuous derivatives with respect to the stress. Only then the direction of the viscoplastic strain rate can be defined uniquely. Moreover, combination of the Perzyna theory with the pressure-dependent, smooth plasticity criterion of Drucker-Prager leads to a non-correct value for  $\phi(f)$  beyond the apex. In this area the value  $\phi(f)$  should be calculated with respect to the apex, while, without special provisions, this is done with respect to the yield cone beyond the apex. For this reason the yield function should be redefined for a proper calculation of viscoplastic strains in the stress space beyond the apex. Because of these two considerations the yield criterion of von Mises (eq.(3.63)) with a smooth, pressure independent surface is considered here for the use in the Perzyna viscoplastic theory. Using the gradient  $\mathbf{n}$  to the von Mises yield surface the matrix  $\mathbf{H}$  becomes

$$\mathbf{H} = \gamma \frac{\partial \phi}{\partial f} \left[ \mathbf{nn}^T \right] + \frac{\gamma \phi}{\sqrt{3J_2}} \left[ \mathbf{M} - \mathbf{nn}^T \right], \quad (6.29)$$

where

$$\mathbf{M} = \begin{bmatrix} 1 & -1/2 & -1/2 & 0 & 0 & 0 \\ -1/2 & 1 & -1/2 & 0 & 0 & 0 \\ -1/2 & -1/2 & 1 & 0 & 0 & 0 \\ 0 & 0 & 0 & 3 & 0 & 0 \\ 0 & 0 & 0 & 0 & 3 & 0 \\ 0 & 0 & 0 & 0 & 0 & 3 \end{bmatrix}. \quad (6.30)$$

### Elaboration for a specific choice of $\phi$

The scalar values  $\partial\phi/\partial f$  in the matrix  $\mathbf{H}$  and  $\partial\phi/\partial\bar{\sigma}$  in the vector  $\mathbf{h}$  can be elaborated when a choice for the function  $\phi(f)$  is made. We assume a yield function of the format  $f(\boldsymbol{\sigma}, \kappa) = F(\boldsymbol{\sigma}) - \bar{\sigma}(\kappa)$  as the von Mises criterion. For the flow expressions (6.5) and (6.6) we obtain, respectively

$$\frac{\partial\phi}{\partial f} = \frac{N}{\bar{\sigma}_0} \left[ \frac{f}{\bar{\sigma}_0} \right]^{N-1} \quad (6.31)$$

and

$$\frac{\partial\phi}{\partial f} = \frac{N}{\bar{\sigma}} \left[ \frac{f - \bar{\sigma}}{\bar{\sigma}} \right]^{N-1} \quad (6.32)$$

For the derivative of  $\phi$  with respect to the uniaxial stress we obtain for either of the two functions

$$\frac{\partial\phi}{\partial\bar{\sigma}} = -\frac{N}{\bar{\sigma}_0} \left[ \frac{f}{\bar{\sigma}_0} \right]^{N-1} = -\frac{\partial\phi}{\partial f} \quad (6.33)$$

and

$$\frac{\partial\phi}{\partial\bar{\sigma}} = -\frac{Nf}{\bar{\sigma}^2} \left[ \frac{f - \bar{\sigma}}{\bar{\sigma}} \right]^{N-1} = -\frac{f}{\bar{\sigma}} \frac{\partial\phi}{\partial f} \quad (6.34)$$

Eqs.(6.31)-(6.34) should be substituted in eqs.(6.20) and (6.21).

### 6.2.2 Duvaut-Lions model

The procedure to integrate eq.(6.11) and (6.12) consists of two steps. In STEP 1 the quantities  $\sigma_p$  and  $\kappa_p$  of the rate-independent back-bone model are determined. With the outcome of STEP 1 the viscoplastic values for the stress and hardening can be derived in STEP 2.

STEP 1 : Determination of  $\sigma_p$  and  $\kappa_p$ .

The solutions for  $\sigma_p$  and  $\kappa_p$  can be obtained with the classical rate-independent theory of section 3.4.2. A general Euler backward algorithm (Ortiz and Simo 1986, de Borst and Feenstra 1990) is used for the return mapping of the stress on the yield surface. The return mapping algorithm is applied for the Von Mises yield criterion and the Drucker-Prager yield criterion. In contrast to the Perzyna theory, the Duvaut-Lions model can be combined with a linearly pressure-dependent yield criterion, because in stress situations beyond the apex a proper viscoplastic strain rate is calculated.

STEP 2 : Determination of  $\sigma$  and  $\kappa$ .

The viscoplastic response is determined by the first-order differential equations (6.11) and (6.12). A closed form solution of these equations is discussed by Simo et al. (1988). We do not use this solution for eq.(6.12) because it does not provide a stress-strain matrix  $D_c$ , which is needed for a use in the implicit time integration scheme of section 2.3.

Instead, we use the incremental stress-strain relation (6.15) and the incremental viscoplastic strain according to eq.(6.16). A limited Taylor series expansion for the viscoplastic strain rate now reads

$$\dot{\epsilon}_{vp}^{t+\Delta t} = \dot{\epsilon}_{vp}^t + \left[ \frac{\partial \dot{\epsilon}_{vp}}{\partial \sigma} \right]^t \Delta \sigma + \left[ \frac{\partial \dot{\epsilon}_{vp}}{\partial \sigma_p} \right]^t \Delta \sigma_p . \quad (6.35)$$

Substitution of eq.(6.10) into eq.(6.35) yields

$$\dot{\epsilon}_{vp}^{t+\Delta t} = \dot{\epsilon}_{vp}^t + \frac{1}{\eta} [D_e]^{-1} (\Delta \sigma - \Delta \sigma_p) . \quad (6.36)$$

With this approximated value for the viscoplastic strain rate at  $t + \Delta t$  we calculate the incremental viscoplastic strain

$$\Delta \epsilon_{vp} = [\dot{\epsilon}_{vp}^t + \frac{\Theta}{\eta} [D_e]^{-1} (\Delta \sigma - \Delta \sigma_p)] \Delta t , \quad (6.37)$$

which after substitution into eq.(6.15) yields

$$\Delta \sigma = D_c \Delta \epsilon - \Delta q \quad (6.38)$$

in which

$$D_c = (\eta / (\eta + \Theta \Delta t)) D_e \quad (6.39)$$

$$\Delta q = (\eta / (\eta + \Theta \Delta t)) [D_e \dot{\epsilon}_{vp}^t \Delta t - (\Theta \Delta t / \eta) \Delta \sigma_p] . \quad (6.40)$$

Similar to the Perzyna model and the rate-dependent models treated in Chapter 4 a pseudo-nodal force vector  $\Delta f_{vp}$  is deduced.

For eq.(6.11) the closed form solution of Simo et al. (1988) is used which takes the form

$$\kappa^{t+\Delta t} = \kappa^t e^{-\Delta t / \eta} + \int_t^{t+\Delta t} e^{-(t+\Delta t-\tau)/\eta} \frac{1}{\eta} \kappa_p d\tau , \quad (6.41)$$

in which  $\kappa_p$  is determined by the rate-independent plastic strain history at  $t + \Delta t$ . Using

$$\int_t^{t+\Delta t} e^{-(t+\Delta t-\tau)/\eta} \frac{1}{\eta} \kappa_p d\tau = (1 - e^{-\Delta t / \eta}) \kappa_p , \quad (6.42)$$

we obtain

$$\kappa^{t+\Delta t} = \kappa^t e^{-\Delta t/\eta} + (1 - e^{-\Delta t/\eta}) \kappa_p. \quad (6.43)$$

The elastic case is recovered if  $\Delta t/\eta \rightarrow 0$  and the rate-independent plastic case is recovered if  $\Delta t/\eta \rightarrow \infty$ . This is an important feature of the Duvaut-Lions model because the algorithm of the Perzyna model does not provide such a smooth return to the yield surface. If  $\gamma \Delta t \rightarrow \infty$  situations directly inside and outside the yield surface are calculated successively which yields an improperly converging solution.

## 6.3 NUMERICAL ANALYSES

With the rate-dependent smeared crack model in Chapter 4 the mode-I localisation problems (Example 1 and 2) have been analysed. Here, we will limit the attention to mode-II localisation problems. Therefore Example 1 is transformed into a one-dimensional shear problem and furthermore the impact biaxial test (Example 3) is considered. We use the Newmark time integration scheme ( $\beta = 1/4$ ,  $\gamma = 1/2$ , see section 2.3) with a time step  $\Delta t = 5 \cdot 10^{-7}$  s for Example 1 and  $\Delta t = 1.5 \cdot 10^{-6}$  s for Example 3. For the calculations the consistent mass matrix is used and the integration constant  $\Theta = 1/2$  in all calculations.

### 6.3.1. Example 1 : One-dimensional bar problem in shear

We depart from the data set given in Figure 3.4. For a comparison with the tensile bar problem in the sections 3.5.1, 4.4.1 and 5.4.1 the parameter set is modified to  $\mu = 20000$  N/mm<sup>2</sup>,  $\bar{\sigma}_0 = 2\sqrt{3}$  N/mm<sup>2</sup> and  $h = -15000$  N/mm<sup>2</sup>. We use the Perzyna model with  $\phi = f/\bar{\sigma}_0$  (eq.(6.5) with  $N = 1$ ) and the fluidity parameter  $\gamma = \bar{\sigma}_0/\sqrt{3}m = 10/\sqrt{3}$  1/s, to obtain the same amount of viscosity as in the rate-dependent crack model with  $m = 0.2$  Ns/mm<sup>2</sup> (section 4.4.1). Using this parameter set the elastic shear wave speed  $c_g = 1000$  m/s and the length scale parameter for the shear band  $l = 20$  mm (eq.(6.9)).

First, we consider a block-shaped ( $t_d = 0$  s) shear wave travelling through the shear layer. The shear band, developing after reflection, has a constant width for the four meshes as can be observed from the shear strain profiles in Figure 6.3. The exponential decrease in  $x$ -direction, analytically found in the dispersion analysis of viscous models (section 4.2), can be seen from the stroboscopic development of the shear band in the bottom picture of Figure 6.3. If we compare the shear strain in Figure 6.3 with the axial strain in Figure 4.6 we see the agreement between the Perzyna viscoplastic model and the rate-dependent crack model. The slight difference is due to the fact that the rate-dependent crack model unloads according to the secant stiffness and the viscoplastic model unloads elastically.

A second analysis has been carried out to obtain a more pronounced shear band. Taking  $\gamma = 15/\sqrt{3}$  1/s and  $t_d = 25 \cdot 10^{-6}$  s mesh objectivity is once again demonstrated by means of the displacements at time  $t = 0.25 \cdot 10^{-3}$  s. The development of the shear strain in the bottom picture shows a different shape of the strain field in the localisation zone due to a different



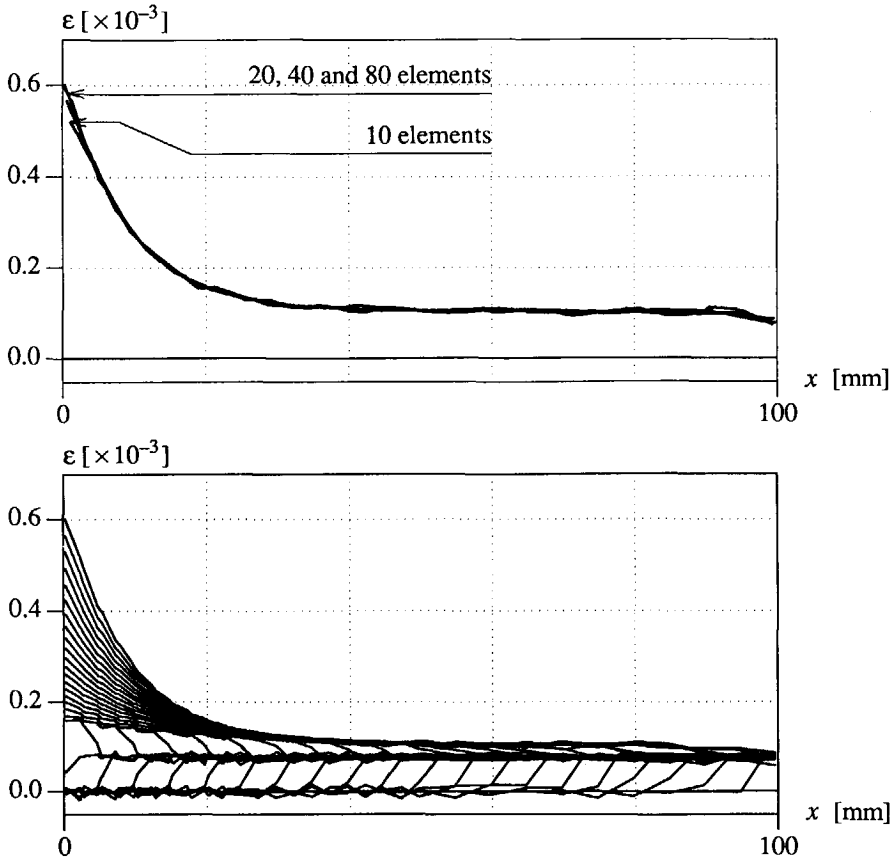


Figure 6.3 Perzyna viscoplastic model with  $t_d = 0$ . s :  
 Top : Shear strain localisation along the bar at  $t = 0.2 \cdot 10^{-3}$  s.  
 Bottom : Development of the shear band (40 elements).

loading as discussed in section 4.4.1.

A comparison between the models is made in Figure 6.5. For the Perzyna model with  $\gamma = 10/\sqrt{3}$  1/s the function  $\phi$  has been varied and the results have been compared to the Duvaut-Lions model with a relaxation time  $\eta = 1.5 \cdot 10^{-5}$  s ( $l = 20$  mm eq.(6.14.2)). The results for the Duvaut-Lions model and the Perzyna model with  $\phi = f/\bar{\sigma}_0$  are almost identical. We observe a slightly smaller peak strain in the shear band for the Perzyna model. By taking  $N = 2$  for  $\phi = (f/\bar{\sigma}_0)^N$  as well as for  $\phi = (f/\bar{\sigma})^N$  the strain profiles in the localisation zone become smoother. The shear band becomes wider and the peak strain decreases. Taking the function  $\phi = f/\bar{\sigma}$  instead of  $\phi/\bar{\sigma}_0$  leads to larger peak strains and a smaller localisation zone. Furthermore, the case  $\phi = (f/\bar{\sigma})^N$  demonstrates that mesh objectivity is not always guaranteed

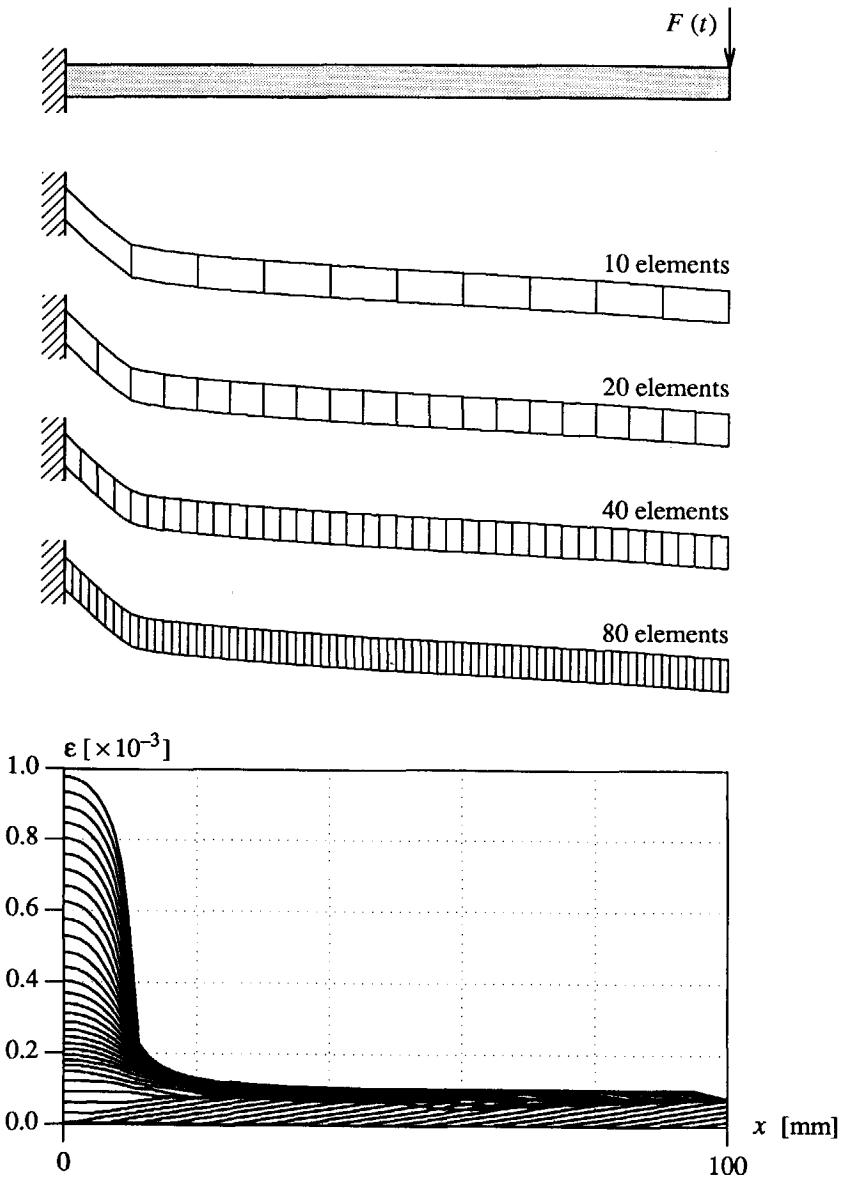


Figure 6.4 Perzyna viscoplastic model with  $t_d = 25 \cdot 10^{-6}$  s :  
 Top : Deformed meshes at  $t = 0.25 \cdot 10^{-3}$  s (FA = 1000).  
 Bottom : Development of the shear band (80 elements).

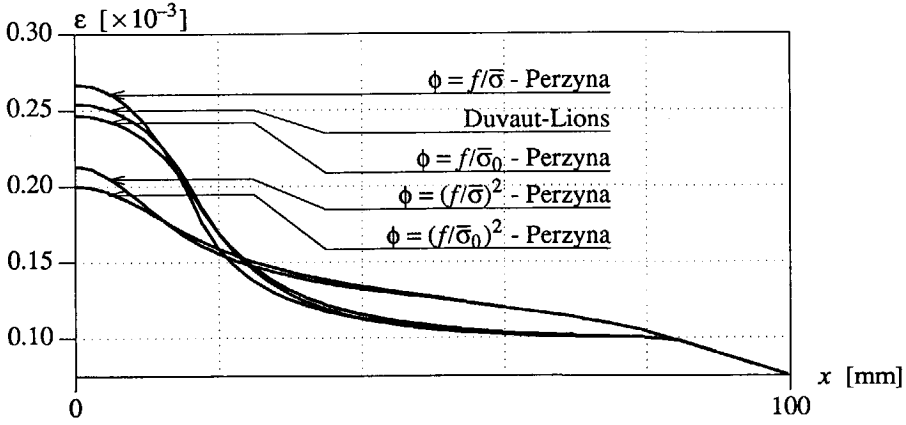


Figure 6.5 Comparison of viscoplastic models ( $t_d = 50 \cdot 10^{-6}$  s,  $t = 0.20 \cdot 10^{-3}$  s, 40 elements).

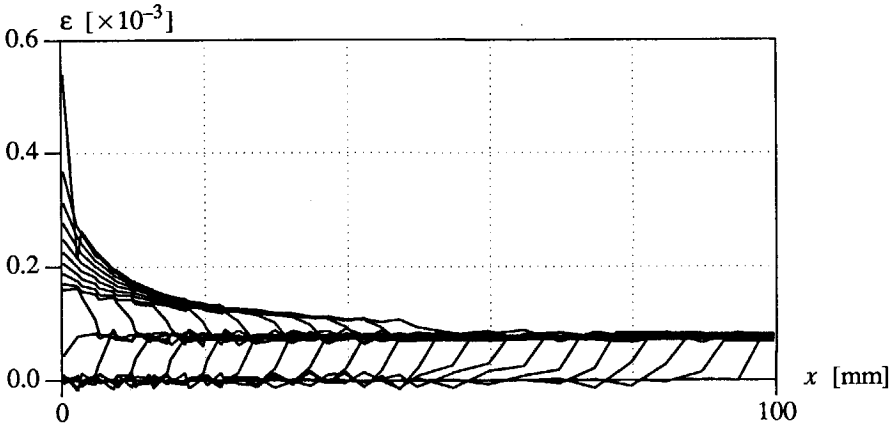


Figure 6.6 Mesh dependence for Perzyna viscoplastic model with  $\phi = (f/\bar{\sigma})^2$  ( $t_d = 0$  s,  $0 < t < 0.15 \cdot 10^{-3}$  s, 40 elements).

by a viscoplastic modelling of the layer. In fact, for this case the stabilising viscous effect gradually vanishes due to softening ( $\bar{\sigma} \rightarrow 0$ ). The cause is similar as that for the rate-dependent power law model in section 4.5 : the third-order terms in the wave equation vanish and well-posedness is lost. These effects are shown in Figure 6.6. In this calculation  $\phi = (f/\bar{\sigma})^2$  and we observe localisation in one row of integration points when  $\epsilon_{vp} > 0.0004$  and  $\bar{\sigma} = 0$ . The role of the damper element in Figure 6.1 becomes less important and when its

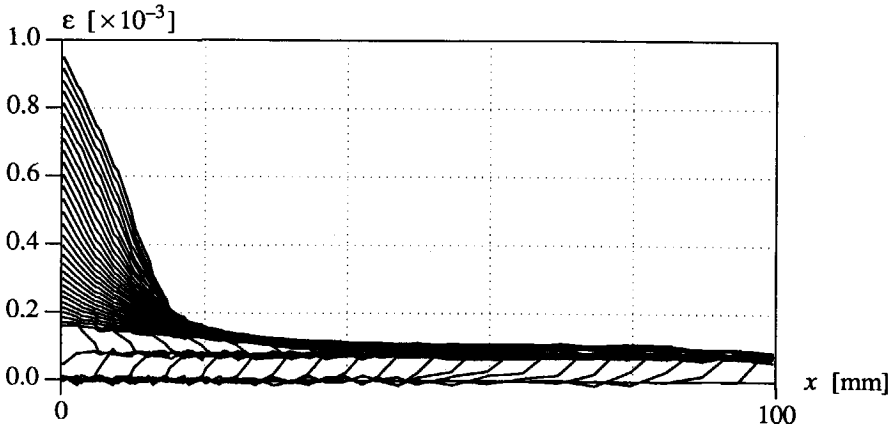


Figure 6.7 Extension of the localisation zone after the termination of softening ( $t_d = 0$  s,  $0 < t < 0.25 \cdot 10^{-3}$  s, 40 elements).

contribution is reduced to zero the classical rate-dependent problem is recovered. On the other hand, even when  $\bar{\sigma}$  becomes zero, use of  $\phi = (f/\bar{\sigma}_0)^N$ , ensures well-posedness and, just as in the gradient model, the localisation zone no longer behaves stationary but starts to propagate when the softening effect is no longer present. This is demonstrated in Figure 6.7 for an analysis with  $N = 1$ .

### 6.3.2. Example 3 : Impact biaxial test

After the treatment of the biaxial test for a classical strain-softening model in section 3.5.3 and the gradient strain-softening model in section 5.4.2 the viscoplastic models of Perzyna and Duvaut-Lions will be used here. Mesh sensitivity of the results with respect to the size and the orientation of the elements will be considered. The meshes from section 3.5.3 have been used for analyses under plane-strain and plane-stress conditions. First, the Perzyna model is analysed in combination with the von Mises yield function for the sample under a plane-strain condition. Next, we treat the von Mises model in combination with Duvaut-Lions viscoplasticity and plane-stress elements and, finally, the Drucker-Prager yield criterion is used for a plane-strain analysis of the sample with Duvaut-Lions viscoplasticity.

- *biaxial test with von Mises - Perzyna viscoplastic model (plane-strain)*

The input data set for the problem is given in Figure 3.14, in which the softening modulus  $h$  is  $-3333$  N/mm<sup>2</sup>. For the Perzyna model the function  $\phi = f/\bar{\sigma}_0$  is taken for reasons mentioned in

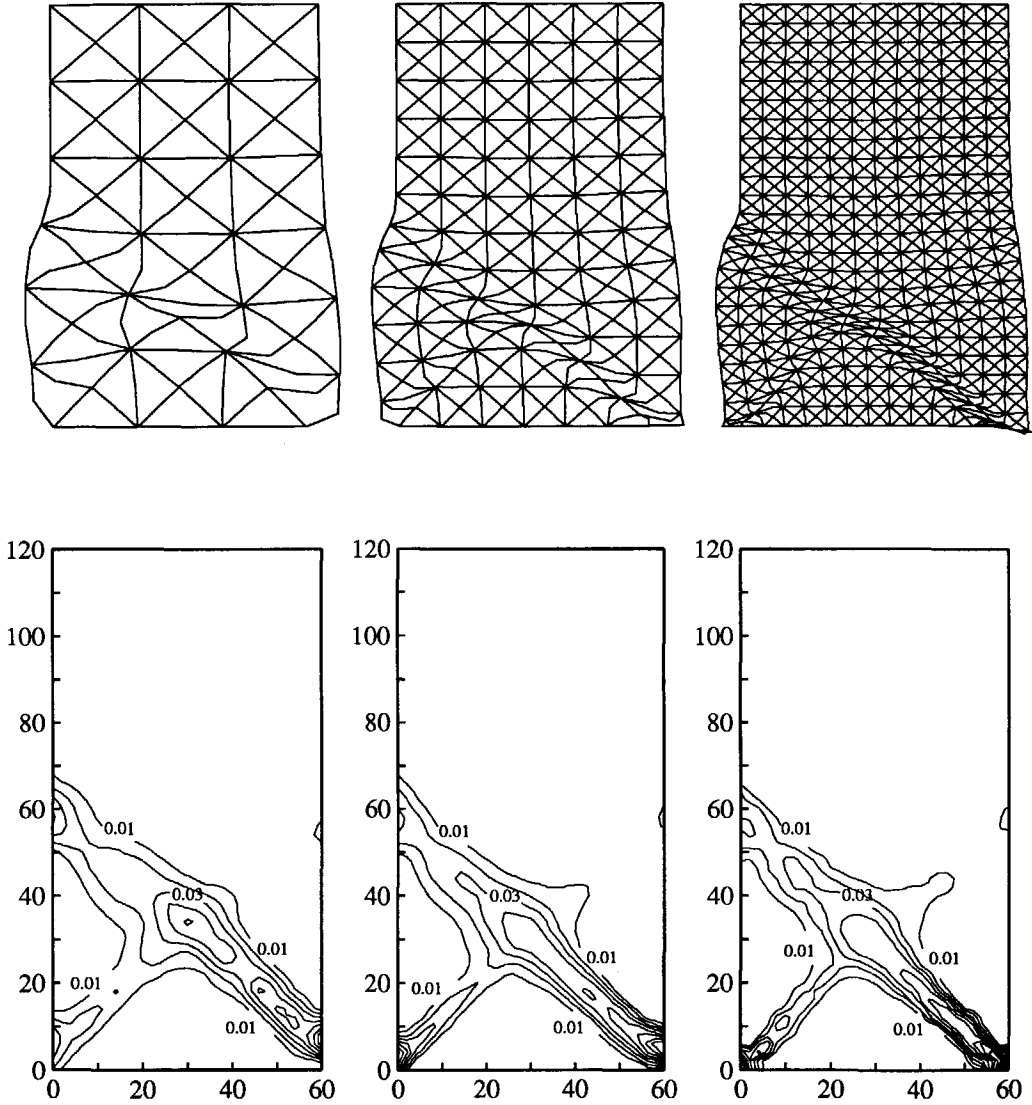


Figure 6.8 Von Mises - Perzyna viscoplastic model with plane-strain elements :  
 Top : Total displacement patterns ( $t = 0.165 \cdot 10^{-3}$  s, FA = 15).  
 Bottom : Contour plots of the equivalent plastic strains.

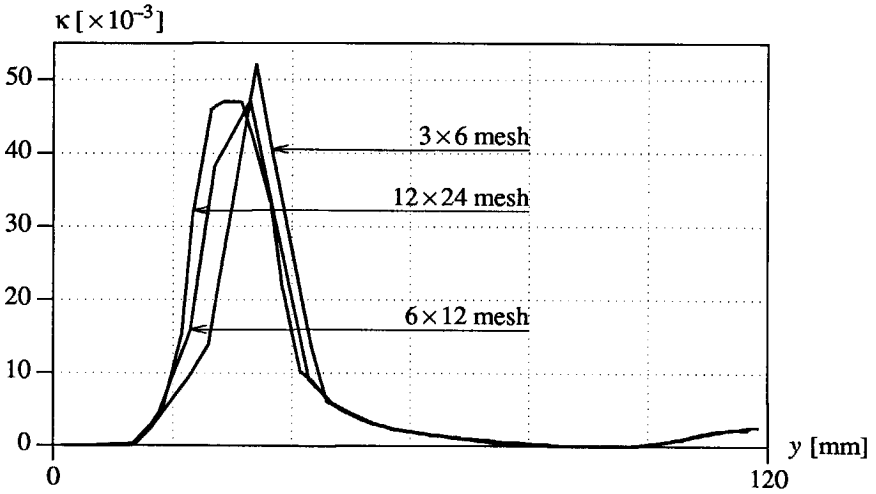


Figure 6.9 Equivalent plastic strains  $\kappa$  in centre section ( $x = 30$  mm) of the sample ( $t = 0.165 \cdot 10^{-3}$  s).

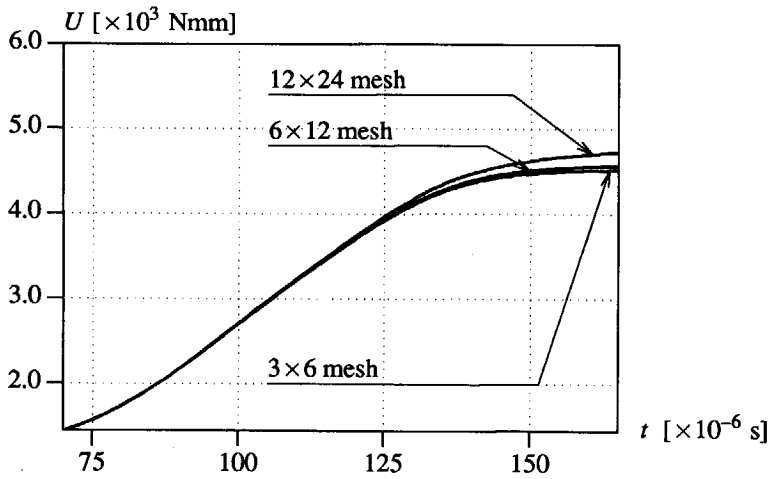


Figure 6.10 Energy consumption in the sample.

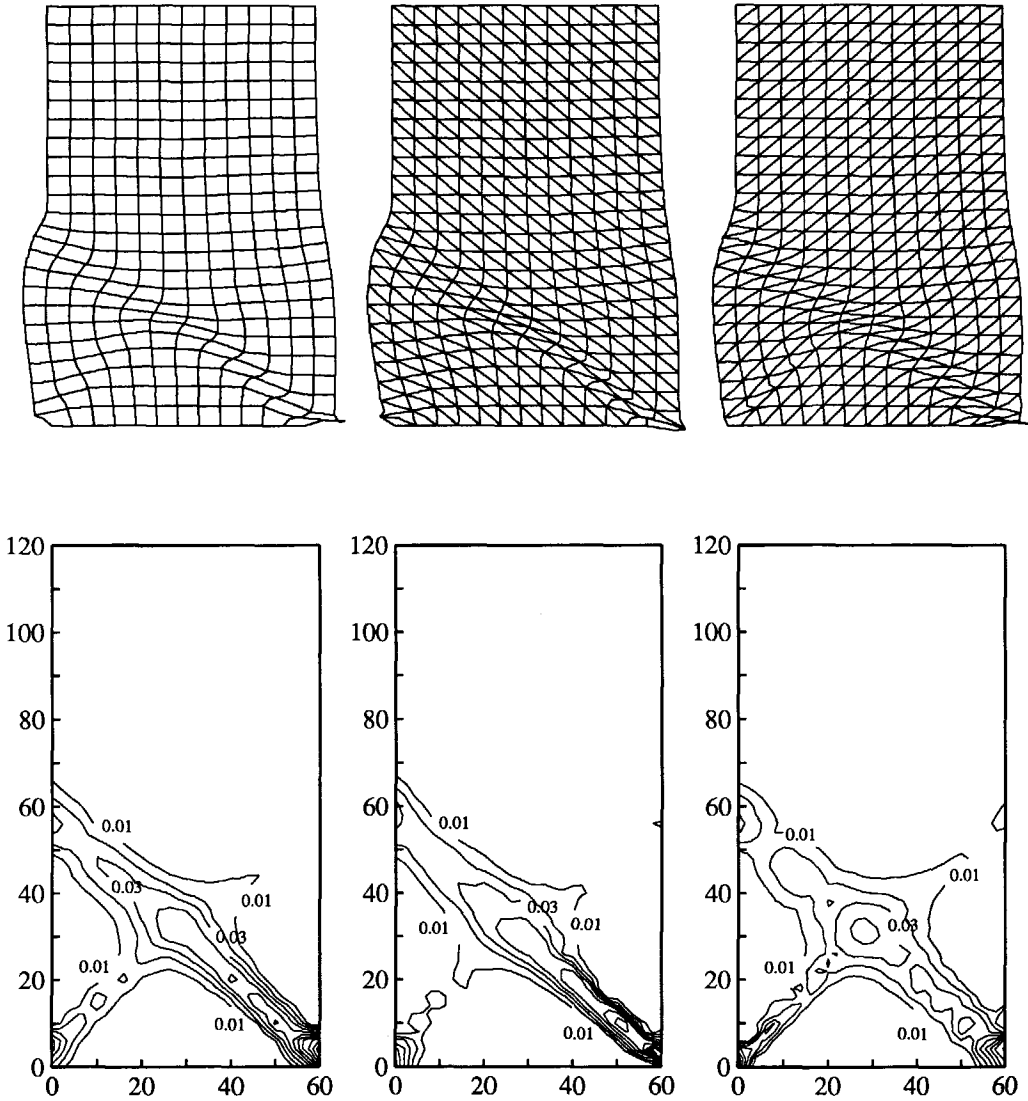


Figure 6.11 Von Mises - Perzyna viscoplastic model with plane-strain elements :  
 Top : Total displacement patterns ( $t = 0.165 \cdot 10^{-3}$  s,  $FA = 15$ ).  
 Bottom : Contour plots of the equivalent plastic strains.

the previous paragraph. The fluidity parameter  $\gamma = 2000$  1/s which results in an internal length scale  $l = 6.1$  mm (eq.(6.9)).

In Figure 6.8 the deformed meshes have been plotted with the corresponding contour plots of the equivalent plastic strains at a time at which the pressure wave has returned at the top of the sample. The shear band width with an inclination angle of  $45^\circ$  remains more or less constant upon mesh refinement. In comparison with the gradient model we observe a more pronounced development of the second shear band. Because of a singularity in the elastic solution in the corners of the sample a slight mesh dependence remains present close to the corners. The plot of the equivalent plastic strains in the centre section of the sample in Figure 6.9 shows a proper similarity between the meshes. A comparison of the energy consumption in the three analyses in Figure 6.10 shows a reasonable agreement with a slight deviation for the  $12 \times 24$  mesh which may be due to the corner singularity.

The influence of the mesh lines can be investigated by using the meshes of Figure 3.19, in which the direction of the mesh lines is varied. The analyses with the classical strain-softening model showed completely different failure modes (Figure 3.19). Using the viscoplastic regularisation, the situation is remedied as shown in Figure 6.11. For the mesh with quadrilateral elements (left) and the biased mesh (centre) the results coincide with the results in Figure 6.8. Only the third mesh (right) gives a slightly stiffer response and a small deviation from the results for the first two meshes. However, if we refine the third mesh the results become exactly similar to that from the first two analyses (Bolck 1992).

*- biaxial test with von Mises - Duvaut-Lions viscoplastic model (plane-stress)*

We take the relaxation time  $\eta = 8 \cdot 10^{-6}$  s for the Duvaut-Lions model. This implies an internal length scale  $l = 9.5$  mm (eq.(6.14.2)). Just as for the Perzyna model first we focus on the objectivity of the shear band width upon mesh refinement. Next, we investigate the impact of the presence of a bias in the discretisation on the results.

With the viscoplastic model we compute a shear band with an inclination angle of  $35^\circ$  which is similar for the three meshes (see Figure 6.12) and in agreement with the analytical expression (eq.(3A.20)). While the meshes have a bias of  $45^\circ$  the shear band develops in the direction of the analytically predicted shear band.

Mesh alignment is also investigated for the plane-stress condition of the biaxial test. The results, shown in Figure 6.13, are identical with the results of Figure 6.12 and entirely invariant to the influence of the mesh lines. Even for the third mesh a shear band with a similar size and inclination angle is obtained. So, the viscoplastic models are strong enough as a regularisation method to overcome mesh-alignment problems.

*- biaxial test with Drucker-Prager - Duvaut-Lions viscoplastic model (plane-strain)*

The Duvaut-Lions model can also be combined with the Drucker-Prager yield criterion. A



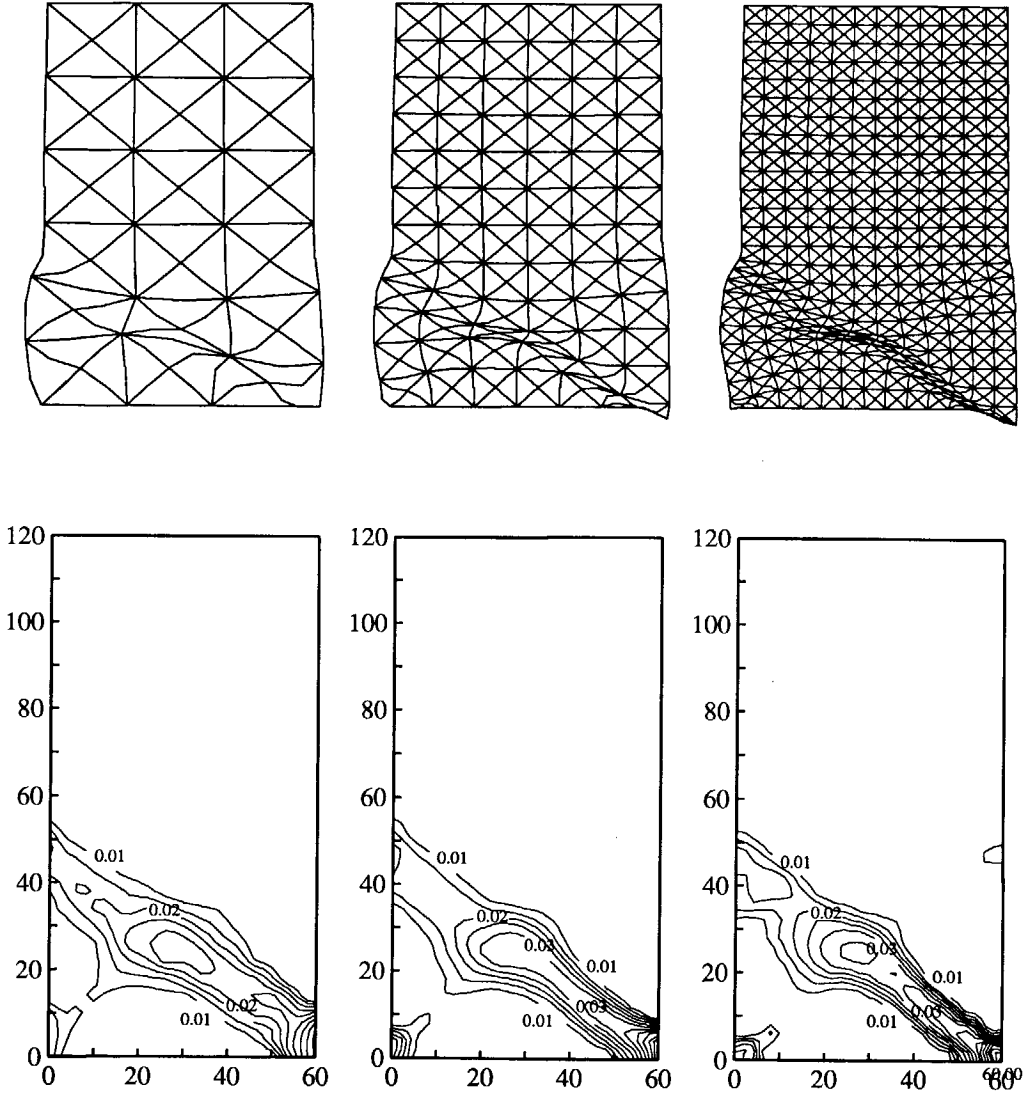


Figure 6.12 Von Mises - Duvaut-Lions viscoplastic model with plane-stress elements :  
Top : Total displacement patterns ( $t = 0.165 \cdot 10^{-3}$  s, FA = 15).  
Bottom : Contour plots of the equivalent plastic strains.

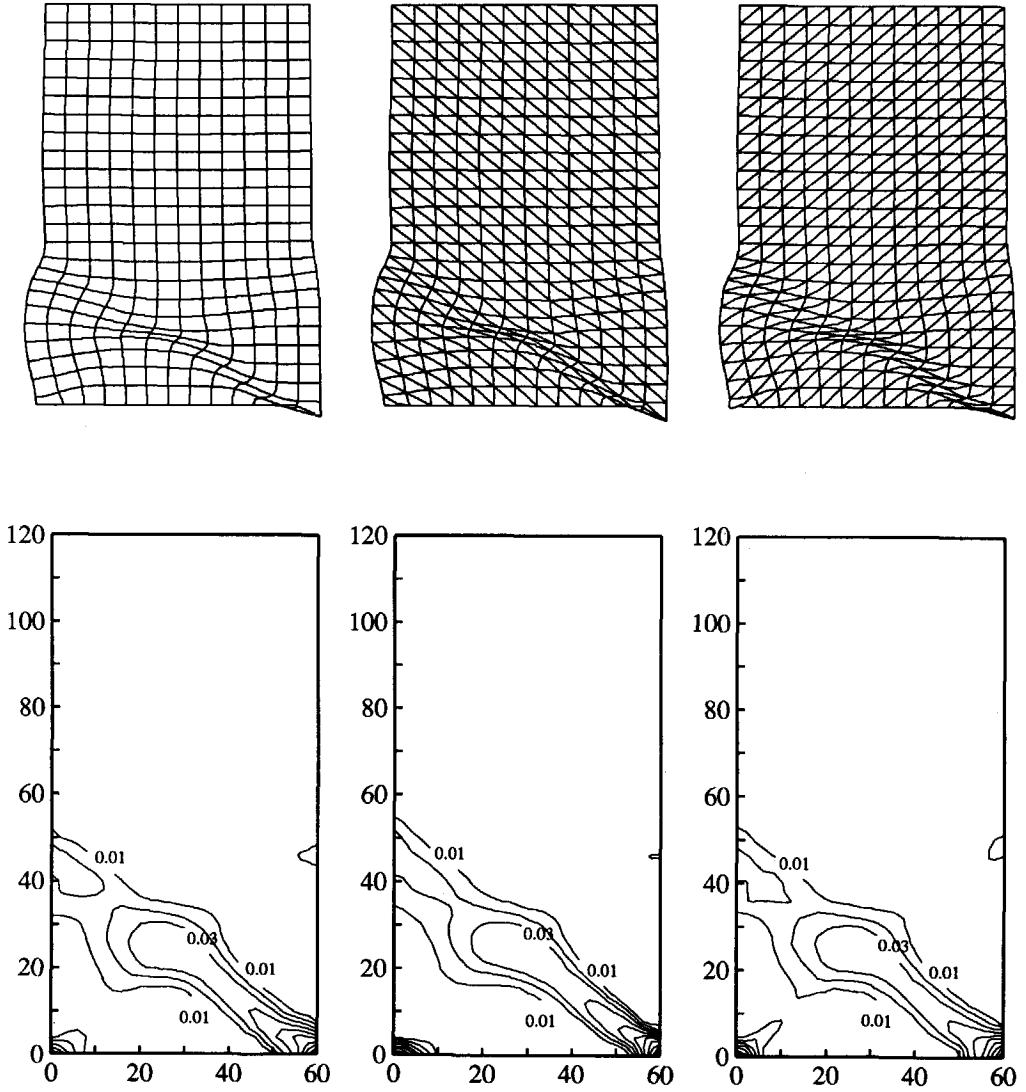


Figure 6.13 Von Mises - Duvaut-Lions viscoplastic model with plane-stress elements :  
Top : Total displacement patterns ( $t = 0.165 \cdot 10^{-3}$  s, FA = 15).  
Bottom : Contour plots of the equivalent plastic strains.

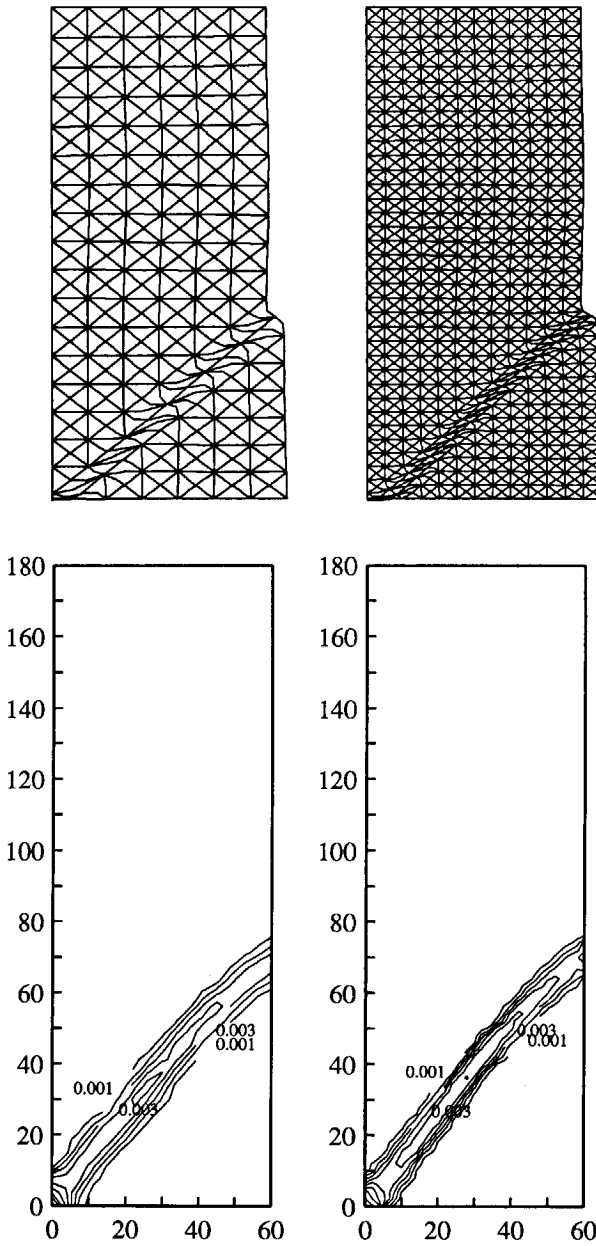


Figure 6.14 Duvaut-Lions (Drucker-Prager) viscoplastic model with plane-strain elements displacements (top - FA = 100) and contour plots (bottom) at  $t = 0.30 \cdot 10^{-3}$  s.

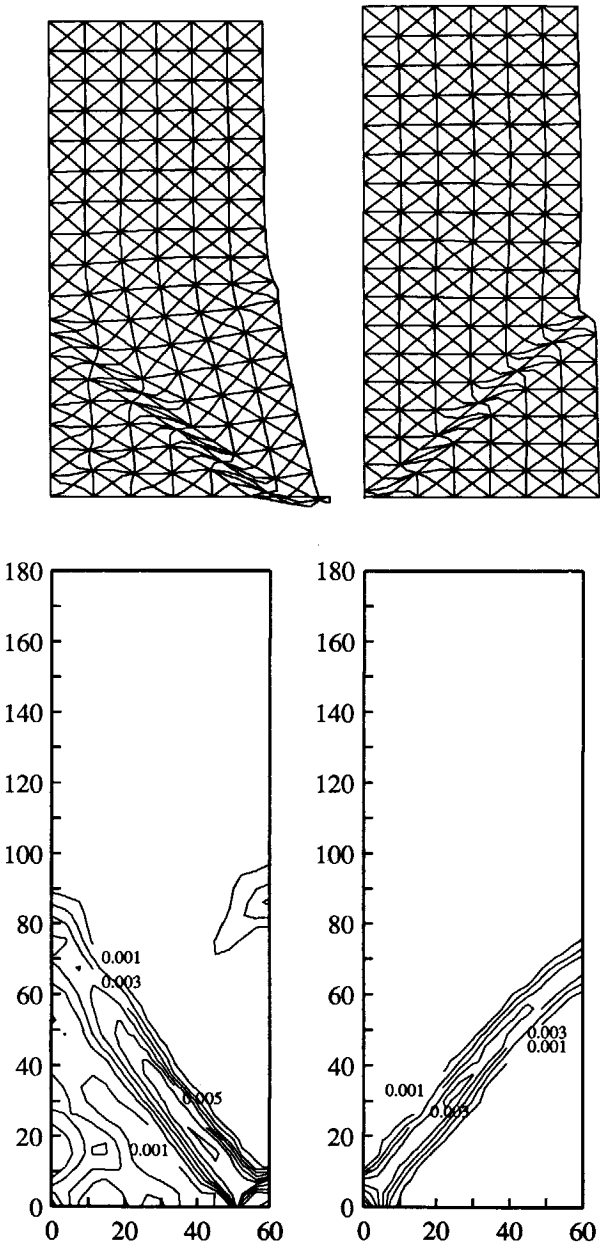


Figure 6.15 Duvaut-Lions (Drucker-Prager) viscoplastic model with plane-strain elements using friction angle  $\phi = 20^\circ$  (left) and  $\phi = 30^\circ$  (right).

symmetric quadrant of a specimen is considered as described in the Drucker-Prager analysis of the gradient model in section 5.4.2. The same data set is used as in section 5.4.2 with a modification for the ultimate equivalent plastic strain  $\kappa_u = 0.0025$ . The relaxation time  $\eta = 2.5 \cdot 10^{-6}$  s, which implies an internal length scale  $l = 3.0$  mm (eq.(6.14.2)).

The results for a mesh-sensitivity analysis with friction angle  $\phi = 30^\circ$  have been plotted in Figure 6.14. Just as for the gradient model we observe that the shear band is initiated at the bottom of the left corner and a change of orientation appears at the free boundary (Needleman and Ortiz 1991). It is shown that also for the Drucker-Prager model the viscoplastic regularising effect yields a mesh-objective solution for the shear band with respect to size and orientation. It should be said that a much smaller time step is needed ( $\Delta t/8$ ) than that is used for the von Mises calculations to obtain objectivity with respect to the time step. The results of an analysis in which the friction angle has been varied are plotted in Figure 6.15. The same change of orientation of the shear band is observed as we have seen for the gradient model (see discussion section 5.4.2). From the equivalent plastic strains it comes out that the shear band runs steeper than the mesh lines which are under  $45^\circ$ . For  $\phi = 30^\circ$  we obtain  $\Theta \approx 50^\circ$  with the analytical value  $\Theta = 48.4^\circ$  (eq.(3A.23)) and for  $\phi = 20^\circ$  we obtain  $\Theta \approx 51^\circ$  which deviates somewhat from the analytical value  $\Theta = 47.0^\circ$  (eq.(3A.22)).

#### 6.4 THE BIG PICTURE : A COMPARISON OF RATE-DEPENDENT MODELS

The rate-dependent models treated in Chapter 4 can be compared to the viscoplastic models of Perzyna and Duvaut-Lions. Therefore, we consider the one-dimensional case which makes it possible to compare a principal stress criterion, used for the crack models, with a yield criterion, used for the viscoplastic models.

The one-dimensional wave equation based on the rate-dependent crack model is given by eq.(4.10)

$$m \left( \frac{1}{c_e^2} \frac{\partial^3 v}{\partial t^3} - \frac{\partial^3 v}{\partial x^2 \partial t} \right) + \frac{E+h}{c_e^2} \frac{\partial^2 v}{\partial t^2} - h \frac{\partial^2 v}{\partial x^2} = 0. \quad (6.44)$$

The highest-order terms determine the character of the solution of the wave equation. From a dispersion analysis in section 4.2 it was proved that the wave speeds remain real which yields a normal wave-like solution, in contrast to the spurious standing wave type solution for the rate-independent medium. From the dispersion analysis we have also derived the internal length scale parameter

$$l = \frac{2mc_e}{E}. \quad (6.45)$$

The wave equation (eq.(4.34)) for the power law model ( $N=1$  and in case of softening ( $h_2$ )), used in Chapter 4 for the simulation of cracking, reads

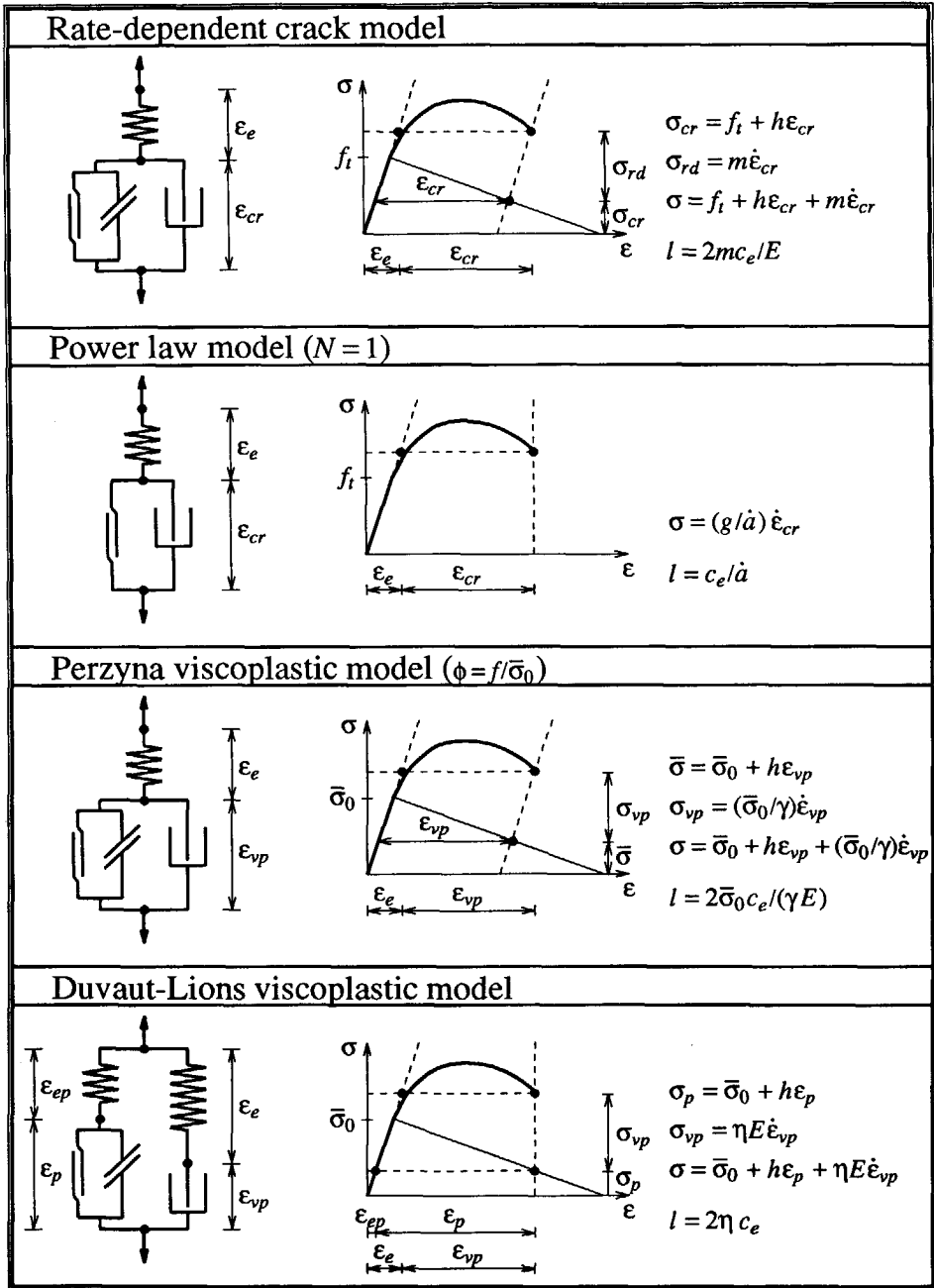


Figure 6.16 Overview of rate-dependent models.

$$\frac{g}{\dot{a}} \left( \frac{1}{c_e^2} \frac{\partial^3 v}{\partial t^3} - \frac{\partial^3 v}{\partial x^2 \partial t} \right) + \rho \frac{\partial^2 v}{\partial t^2} = \frac{h_2}{\dot{a}} \frac{\partial \dot{\epsilon}_{cr}}{\partial t} \left( \frac{\partial^2 v}{\partial x^2} - \frac{1}{c_e^2} \frac{\partial^2 v}{\partial t^2} \right). \quad (6.46)$$

The third-order terms gradually vanish when softening occurs. For this reason mesh sensitivity emerges when the power law model is used for brittle softening materials. The length scale is chosen according to

$$l = \frac{c_e}{\dot{a}}. \quad (6.47)$$

The Perzyna model is similar to the rate-dependent crack model if we set  $\phi = f/\bar{\sigma}_0$ . We obtain

$$\frac{\bar{\sigma}_0}{\gamma} \left( \frac{1}{c_e^2} \frac{\partial^3 v}{\partial t^3} - \frac{\partial^3 v}{\partial x^2 \partial t} \right) + \frac{E+h}{c_e^2} \frac{\partial^2 v}{\partial t^2} - h \frac{\partial^2 v}{\partial x^2} = 0, \quad (6.48)$$

representing the one-dimensional motion of the viscoplastic element. A dispersion analysis along the same lines as for the rate-dependent crack model leads to the internal length scale parameter

$$l = \frac{2\bar{\sigma}_0 c_e}{\gamma E}. \quad (6.49)$$

If we set  $\phi = f/\bar{\sigma}$  the stabilising effect of the third-order terms in eq.(6.51) gradually vanishes when softening occurs. If the softening contribution has reduced to zero mesh dependence of the results is obtained (see Figure 6.6).

The third-order wave equation for the Duvaut-Lions viscoplastic model reads

$$\eta E \left( \frac{1}{c_e^2} \frac{\partial^3 v}{\partial t^3} - \frac{\partial^3 v}{\partial x^2 \partial t} \right) + \rho \frac{\partial^2 v}{\partial t^2} - h \frac{\partial^2 v}{\partial x^2} = -h \frac{\partial \dot{\epsilon}_{ep}}{\partial x}. \quad (6.50)$$

Just as for the rate-dependent crack model, the stabilising third-order terms provide the regularisation effect irrespective of the extent of softening. The length scale parameter is defined as

$$l = 2\eta c_e. \quad (6.51)$$

If the third-order terms are considered it appears that the wave equations for the four treated models have the same character. In Figure 6.16 an overall picture of the models is given. The rheology of the models with the one-dimensional response show the mutual differences and similarities.

Rate-dependent crack models and viscoplastic models differ from each other with respect to unloading and reloading behaviour. The models have different criteria for unloading and reloading, which is shown in Figure 6.17 for the one-dimensional case. In the rate-dependent

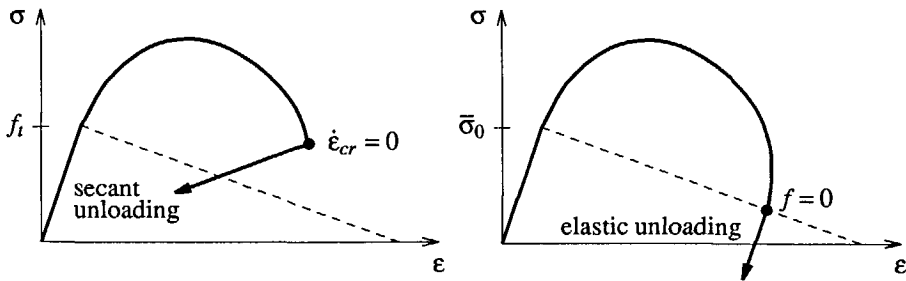


Figure 6.17 Unloading/reloading criteria for rate-dependent crack models (left) and viscoplastic models (right).

crack modelling unloading and reloading occur with a secant stiffness at the moment that the crack strain rate  $\dot{\epsilon}_{cr} < 0$ . The viscoplastic models, however, show elastic unloading and reloading when the stress state has returned inside the yield contour ( $f < 0$ ).



## 7. COSSERAT CONTINUUM MODEL

The results of the mesh-sensitivity study, carried out in Chapter 3 for a conventional continuum, have led to the unambiguous conclusion that an enriched continuum description of the strain-softening solid is necessary. In the Chapters 4, 5 and 6 higher-order terms have been included in the constitutive description of the strain-softening material to provide a regularisation of the governing field equations. In the Cosserat continuum theory, which is treated here, the enrichment of the continuum emanates from extra terms in the kinematics of the strain-softening material. In the eighty year old theory of the Cosserats (Cosserat and Cosserat 1909, Günther 1958, Schaefer 1962, Mindlin 1963 and 1964, Mühlhaus and Vardoulakis 1987, Mühlhaus and Triantafyllidis 1987, Mühlhaus 1988, 1989 and 1990) a macro-structure is assumed to consist of micro-elements with a finite length scale. The finite size of the micro-elements implies the inclusion of an internal length scale which prevents the continuum to suffer from the pathological mesh dependence. The Cosserat theory augments the three translational degrees-of-freedom in a continuum by three rotational degrees-of-freedom. Because of the existence of the rotational degrees-of-freedom additional micro-rotation wave types arise in the Cosserat medium and wave propagation becomes dispersive (Sluys 1990, de Borst and Sluys 1991).

To provide a proper setting we will first give a derivation of the governing equations of a Cosserat continuum. Then, the additional material parameters required in an elasto-plastic Cosserat medium are discussed. Assuming a cuboidal lattice structure with micro-elements of a finite size an explicit expression for the spin inertia is derived. Next, the additional wave types and the dispersive character of wave propagation in Cosserat continua is examined. For the one-dimensional problem of a purely elastic, infinitely long shear layer the governing equations can be reduced such that an analytical solution is possible. Analytical solutions do not seem to be possible for the softening Cosserat continuum, not even for a simple geometry as the above-mentioned shear layer and numerical techniques are then indispensable. It will be proven that the Cosserat theory is not a proper regularisation method for mode-I dominated localisation problems (e.g. Example 1 and 2). However, for the shear layer and the biaxial test (Example 3) the model warrants convergence to a unique, physically realistic solution upon mesh refinement.

### 7.1 COSSERAT THEORY

The derivation of the Cosserat theory, which forms part of the more general micro-polar theory, is given for two-dimensional, planar deformations, so that each material point in a Cosserat continuum is assigned two translational degrees-of-freedom, namely  $u_x$  and  $u_y$ , and a rotational degree-of-freedom  $\omega_z$ , the rotation axis of which is orthogonal to the  $x,y$ -plane. The introduction of the rotational degree-of-freedom stems from the micro-rotation of the

micro-element in the Cosserat medium. So, the displacement vector of the two-dimensional Cosserat medium becomes

$$\mathbf{u} = [ u_x , u_y , \omega_z ] . \tag{7.1}$$

As in a classical continuum (cf. eq.(2.2)) the normal strains are defined as

$$\epsilon_{xx} = \frac{\partial u_x}{\partial x} \tag{7.2a}$$

and

$$\epsilon_{yy} = \frac{\partial u_y}{\partial y} . \tag{7.2b}$$

The shear strains, however, are defined in a slightly different fashion

$$\epsilon_{xy} = \frac{\partial u_y}{\partial x} - \omega_z \tag{7.3a}$$

and

$$\epsilon_{yx} = \frac{\partial u_x}{\partial y} + \omega_z , \tag{7.3b}$$

in which  $\epsilon_{xy}$  and  $\epsilon_{yx}$  can be viewed as the relative deformation between the macro-displacement gradients  $\partial u_x/\partial y$  or  $\partial u_y/\partial x$  and the micro-rotation  $\omega_z$  (see Figure 7.1).

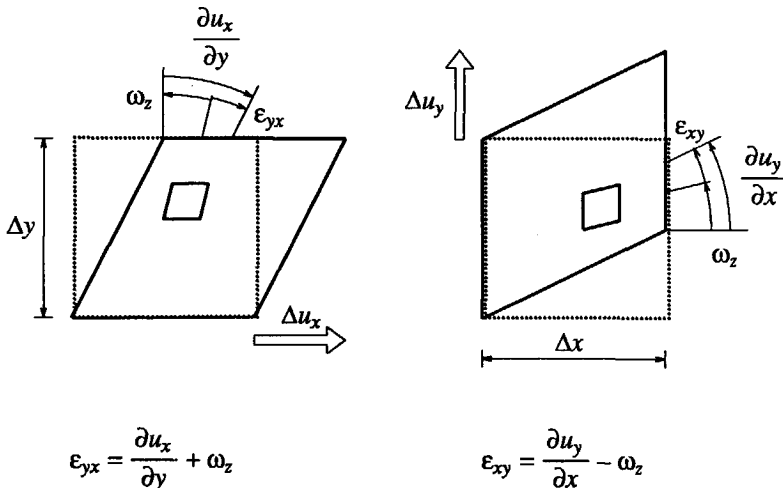


Figure 7.1 Kinematic relations for shear.

In addition to normal strains and shear strains, Cosserat theory also requires the introduction of curvatures

$$\kappa_{xz} = \frac{\partial \omega_z}{\partial x} \quad (7.4a)$$

and

$$\kappa_{yz} = \frac{\partial \omega_z}{\partial y} . \quad (7.4b)$$

Let us now consider the equations of motion for a Cosserat continuum. Conservation of linear momentum in a two-dimensional Cosserat medium results in a set of equations that are identical for a conventional (cf. eq.(2.1)) and for a Cosserat continuum

$$\frac{\partial \sigma_{xx}}{\partial x} + \frac{\partial \sigma_{yx}}{\partial y} = \rho \frac{\partial^2 u_x}{\partial t^2} \quad (7.5)$$

and

$$\frac{\partial \sigma_{xy}}{\partial x} + \frac{\partial \sigma_{yy}}{\partial y} = \rho \frac{\partial^2 u_y}{\partial t^2} , \quad (7.6)$$

in which  $\sigma_{xx}$  and  $\sigma_{yy}$  have the usual meaning of a normal stress in the  $x$  and  $y$ -directions respectively. But in contrast to a conventional continuum the shear stresses  $\sigma_{xy}$  and  $\sigma_{yx}$  (Figure 7.2) are not necessarily equal. Because of the presence of the couple-stresses  $m_{xz}$  and  $m_{yz}$  (Figure 7.2), which are energetically conjugate to the micro-curvatures  $\kappa_{xz}$  and  $\kappa_{yz}$ , and the inertia of micro-rotation per unit volume  $\Theta$ , conservation of angular momentum not necessarily results in a symmetric stress tensor

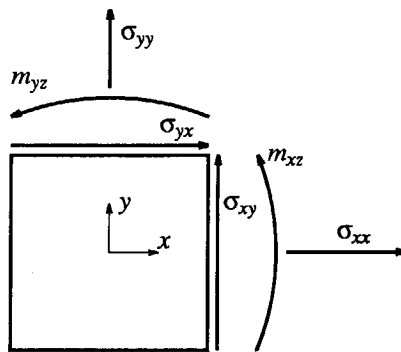


Figure 7.2 Stress and couple-stress in a two-dimensional Cosserat-continuum.

$$\frac{\partial m_{xz}}{\partial x} + \frac{\partial m_{yz}}{\partial y} - (\sigma_{yx} - \sigma_{xy}) = \Theta \frac{\partial^2 \omega_z}{\partial t^2}. \quad (7.7)$$

So, for two dimensions the density matrix  $\mathbf{R}$  can be redefined (cf. eq.(2.1)) as  $\mathbf{R} = \text{diag}(\rho, \rho, \Theta)$ . As will be explained in more detail in section 7.2 the value for  $\Theta$  depends on the size of the micro-elements and on the density  $\rho$ . Assembling the strain components in a vector  $\boldsymbol{\varepsilon}$

$$\boldsymbol{\varepsilon} = [\varepsilon_{xx}, \varepsilon_{yy}, \varepsilon_{zz}, \varepsilon_{xy}, \varepsilon_{yx}, \kappa_{xz}l, \kappa_{yz}l]^T, \quad (7.8)$$

and the stress components in a vector  $\boldsymbol{\sigma}$

$$\boldsymbol{\sigma} = [\sigma_{xx}, \sigma_{yy}, \sigma_{zz}, \sigma_{xy}, \sigma_{yx}, m_{xz}/l, m_{yz}/l]^T, \quad (7.9)$$

the differential operator matrix  $\mathbf{L}$  for two dimensions can be redefined (cf. eq.(2.3)) as

$$\mathbf{L} = \begin{bmatrix} \frac{\partial}{\partial x} & 0 & 0 \\ 0 & \frac{\partial}{\partial y} & 0 \\ 0 & 0 & 0 \\ 0 & \frac{\partial}{\partial x} & -1 \\ \frac{\partial}{\partial y} & 0 & +1 \\ 0 & 0 & l \frac{\partial}{\partial x} \\ 0 & 0 & l \frac{\partial}{\partial y} \end{bmatrix}. \quad (7.10)$$

The constitutive relation for an elastic Cosserat continuum is formulated as

$$\boldsymbol{\sigma} = \mathbf{D}_e \boldsymbol{\varepsilon}, \quad (7.11)$$

in which  $\mathbf{D}_e$  is the stiffness matrix that contains the elastic moduli (cf. eq.(2.7))

$$\mathbf{D}_e = \begin{bmatrix} 2\mu a_1 & 2\mu a_2 & 2\mu a_2 & 0 & 0 & 0 & 0 \\ 2\mu a_2 & 2\mu a_1 & 2\mu a_2 & 0 & 0 & 0 & 0 \\ 2\mu a_2 & 2\mu a_2 & 2\mu a_1 & 0 & 0 & 0 & 0 \\ 0 & 0 & 0 & \mu + \mu_c & \mu - \mu_c & 0 & 0 \\ 0 & 0 & 0 & \mu - \mu_c & \mu + \mu_c & 0 & 0 \\ 0 & 0 & 0 & 0 & 0 & 2\mu & 0 \\ 0 & 0 & 0 & 0 & 0 & 0 & 2\mu \end{bmatrix}, \quad (7.12)$$

with  $a_1$  and  $a_2$  as defined in eq.(2.7). The classical elastic stiffness matrix for a plane-strain medium is recovered if  $\mu_c = 0$  and if the couple stresses are not present. Apart from the usual material parameters  $\mu$  and  $\nu$  the two additional elastic constants  $\mu_c$  and  $l$  enter the constitutive relation. Especially the parameter  $l$  is important since it sets the length scale in the enhanced continuum description. To obtain a dimensional similitude of all entries in the vectors  $\sigma$ ,  $\epsilon$  and the matrix  $D_e$ ,  $l$  has been incorporated in the vectors  $\sigma$  and  $\epsilon$  via the generalised curvatures  $\kappa_{xz}l$ ,  $\kappa_{yz}l$  and the generalised couple-stresses  $m_{xz}/l$ ,  $m_{yz}/l$ . This also has advantages for an efficient numerical implementation (de Borst 1991). It is furthermore noted that the term  $2\mu l^2$  that sets the relation between the curvatures  $\kappa_{xz}$ ,  $\kappa_{yz}$  and the couple-stresses  $m_{xz}$ ,  $m_{yz}$  respectively, can be interpreted as a bending modulus (Schaefer 1962, Mindlin 1963). This interpretation becomes important in the next section when the expression for the spin inertia is derived.

For the formulation of an elasto-plastic Cosserat continuum the conventional hypothesis of small-strain plasticity is adopted that the strain can be decomposed into an elastic contribution  $\epsilon_e$  and a plastic contribution  $\epsilon_p$  (eq.(3.52)). So, the classical flow theory derived in section 3.4.2 can be used for the Cosserat continuum model. In the Cosserat model for the von Mises and the Drucker-Prager plasticity theories the second invariant of the deviatoric stresses  $J_2$  can be generalised as (Mühlhaus and Vardoulakis 1987, Mühlhaus 1988, de Borst 1991)

$$J_2 = g_1 s_{ij} s_{ij} + g_2 s_{ij} s_{ji} + g_3 m_{ij} m_{ij} / l^2, \quad (7.13)$$

with  $g_{1,2,3} = (1/4, 1/4, 1/2)$  and where the summation convention with respect to repeated indices has been adopted. An energetically conjugate expression for the hardening parameter is then (Mühlhaus and Vardoulakis 1987, Mühlhaus 1988, de Borst 1991)

$$\dot{\kappa} = [h_1 \dot{\epsilon}_{ij}^p \dot{\epsilon}_{ij}^p + h_2 \dot{\epsilon}_{ij}^p \dot{\epsilon}_{ji}^p + h_3 \dot{\kappa}_{ij}^p \dot{\kappa}_{ij}^p l^2]^{1/2}, \quad (7.14)$$

with  $h_{1,2,3} = (1/3, 1/3, 2/3)$  and  $\dot{\epsilon}_{ij}^p$  the plastic deviatoric strain-rate tensor. If other values are considered for  $g_{1,2,3}$  the set  $h_{1,2,3}$  must be changed as well in order to keep the expression for the hardening parameter energetically conjugate.

With the above definitions a plasticity theory (for von Mises and Drucker-Prager) can be constructed for a Cosserat medium in an elegant and straightforward fashion. The integration algorithm for this model is based on a return mapping scheme. The concept of a consistent tangent operator is used within the framework of Newton's method (de Borst 1991).

For the examination of the dispersive character of wave motions in Cosserat continua and the derivation of an analytical solution in a one-dimensional, linear-elastic Cosserat medium, which will be presented in a subsequent section, it is useful to state the governing field equations expressed in displacements and rotations of a two-dimensional, linear-elastic Cosserat medium. Combination of the kinematic relations (7.2)-(7.4), the equations of motion (7.5)-(7.7) and the constitutive law (7.11)-(7.12) results in

$$(2\mu a_1) \frac{\partial^2 u_x}{\partial x^2} + (\mu(1+2a_2) - \mu_c) \frac{\partial^2 u_y}{\partial x \partial y} + (\mu + \mu_c) \frac{\partial^2 u_x}{\partial y^2} + 2\mu_c \frac{\partial \omega_z}{\partial y} = \rho \frac{\partial^2 u_x}{\partial t^2}, \quad (7.15)$$

$$(2\mu a_1) \frac{\partial^2 u_y}{\partial y^2} + (\mu(1+2a_2) - \mu_c) \frac{\partial^2 u_x}{\partial x \partial y} + (\mu + \mu_c) \frac{\partial^2 u_y}{\partial x^2} - 2\mu_c \frac{\partial \omega_z}{\partial x} = \rho \frac{\partial^2 u_y}{\partial t^2}, \quad (7.16)$$

$$2\mu l^2 \left( \frac{\partial^2 \omega_z}{\partial x^2} + \frac{\partial^2 \omega_z}{\partial y^2} \right) + 2\mu_c \frac{\partial u_y}{\partial x} - 2\mu_c \frac{\partial u_x}{\partial y} - 4\mu_c \omega_z = \Theta \frac{\partial^2 \omega_z}{\partial t^2}. \quad (7.17)$$

## 7.2 ADDITIONAL MATERIAL PARAMETERS

Apart from the conventional, linear inertia term, also the rotational- or spin inertia is taken into account in a Cosserat continuum. The spin inertia is determined by the shape and the size of the micro-elements. In the calculations described in this thesis the micro-elements have been assumed to be cubes with edges of length  $2d_c$  (Figure 7.3). In two dimensions the spin inertia of such a cubic micro-element is

$$\Theta_c = \int_{-d_c}^{d_c} \int_{-d_c}^{d_c} \rho(x^2 + y^2) 2d_c \, dx \, dy. \quad (7.18)$$

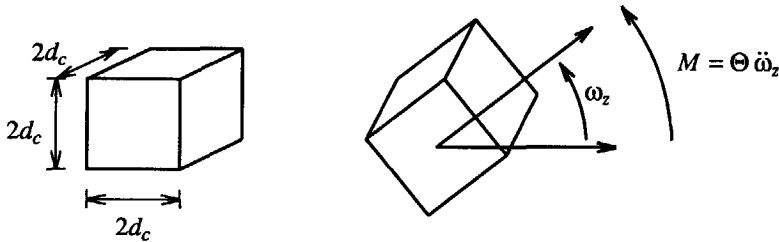


Figure 7.3 Micro-element (left) and momentum of spin inertia (right).

Carrying out the spatial integration with respect to  $x$  and to  $y$  results in

$$\Theta_c = \frac{16}{3} \rho d_c^5. \quad (7.19)$$

The spin inertia per unit volume is therefore given by

$$\Theta = \frac{2}{3} \rho d_c^2. \quad (7.20)$$

Shapes other than cubes may be physically more appealing, e.g., when the underlying material has a granular structure like sand. In the latter case an assumption of spherically shaped

micro-elements might be more plausible (Mühlhaus et al. 1991). However, with the latter assumption the material cannot be composed entirely of micro-elements.

The characteristic length  $l$  introduced in the preceding section depends on the shape and the size of the micro-elements. This will be shown for the simple case of a cube with edges of length  $2d_c$  parallel to the axes  $x$  and  $y$ . An elementary consideration shows that the discrete moment  $M_{xz}$  that acts on a single micro-element is given by

$$M_{xz} = \frac{\mu(1+\nu)}{6}(2d_c)^4 \kappa_{xz} . \quad (7.21)$$

For the couple stress  $m_{xz}$  we then find

$$m_{xz} = \frac{2\mu(1+\nu)d_c^2}{3} \kappa_{xz} . \quad (7.22)$$

In consideration of eqs.(7.11) and (7.12) the relation between  $d_c$  and  $l$  therefore reads

$$d_c^2 = \frac{3}{1+\nu} l^2 . \quad (7.23)$$

Substitution of this result in eq.(7.20) finally results in

$$\Theta = \frac{2\rho}{1+\nu} l^2 . \quad (7.24)$$

### 7.3 WAVE PROPAGATION IN A COSSERAT SHEAR LAYER

Before embarking on an analysis of wave propagation and localisation in an elasto-plastic Cosserat continuum it is instructive to first examine wave propagation in an elastic Cosserat medium. Because of the inclusion of the micro-rotation and the spin inertia micro-rotation waves arise, which are not found in a classical continuum. Due to the presence of micro-elements the shear wave and the micro-rotation wave behave in a dispersive manner and the shape of a pulse is altered as it propagates through a medium. To keep the presentation relatively simple the wave propagation analysis has been carried out for a one-dimensional shear layer. For a shear layer all derivatives with respect to  $y$  vanish and the displacements in the  $x$ -direction are zero ( $u_x=0$ ). These two observations effectively exclude longitudinal effects and the field equations (7.15)-(7.17) reduce to

$$(\mu+\mu_c) \frac{\partial^2 u_y}{\partial x^2} - 2\mu_c \frac{\partial \omega_z}{\partial x} = \rho \frac{\partial^2 u_y}{\partial t^2} \quad (7.25)$$

and

$$2\mu l^2 \frac{\partial^2 \omega_z}{\partial x^2} + 2\mu_c \frac{\partial u_y}{\partial x} - 4\mu_c \omega_z = \Theta \frac{\partial^2 \omega_z}{\partial t^2}. \quad (7.26)$$

Again, we consider waves which propagate in the  $x$ -direction with wave number  $k$  and angular frequency  $\omega$  (cf. eq.(3.15)). A general solution for  $u_y$  and  $\omega_z$  of the form

$$u_y = A e^{i(kx - \omega t)} \quad (7.27)$$

and

$$\omega_z = B e^{i(kx - \omega t)} \quad (7.28)$$

is assumed. Substitution of this solution in the set of equations (7.25) and (7.26) then gives the matrix-vector equation

$$\begin{bmatrix} -(\mu + \mu_c)k^2 + \rho\omega^2 & -2\mu_c ik \\ 2\mu_c ik & -2\mu l^2 k^2 - 4\mu_c + \Theta\omega^2 \end{bmatrix} \begin{bmatrix} A \\ B \end{bmatrix} = \mathbf{0}, \quad (7.29)$$

for which a non-trivial solution exists if and only if the determinant of the matrix is zero. This yields

$$\rho\Theta\omega^4 - [\Theta(\mu + \mu_c)k^2 + 2\mu l^2 \rho k^2 + 4\rho\mu_c] \omega^2 + 2\mu l^2 (\mu + \mu_c)k^4 + 4\mu\mu_c k^2 = 0. \quad (7.30)$$

The positive roots of this equation are

$$\omega_{1,2} = \sqrt{-(b/2a) \pm \sqrt{(b/2a)^2 - c/a}}, \quad (7.31)$$

where

$$a = \rho\Theta, \quad (7.32)$$

$$b = -[\Theta(\mu + \mu_c)k^2 + 2\mu l^2 \rho k^2 + 4\rho\mu_c], \quad (7.33)$$

$$c = 2\mu l^2 (\mu + \mu_c)k^4 + 4\mu\mu_c k^2. \quad (7.34)$$

Equation (7.31) is a dispersion relation where the plus sign represents a micro-rotation wave and the minus sign represents a shear wave. Hence, a dynamic transverse loading in a Cosserat medium (and also in other micro-polar continua) is composed of a shear mode and a micro-rotation mode. The two wave types are coupled and cannot exist without each other. The dispersion relation is plotted in Figure 7.4. For this curve the material data ( $\mu, \mu_c, \rho, \Theta, l$ ) of the shear layer from section 7.4.1 have been used. Clearly, for the same wave number the micro-rotation vibrations have higher frequencies than the shear vibrations. The eigenmodes  $(\omega, k)$  can be obtained when the geometry data and the boundary conditions of a structure are applied as will be demonstrated for the shear layer in section 7.4.1.

The dispersion relation (7.31) can be reformulated as a relation between the phase velocity  $c_f$  and the wave number  $k$ . The phase velocity is the velocity of propagation of one single



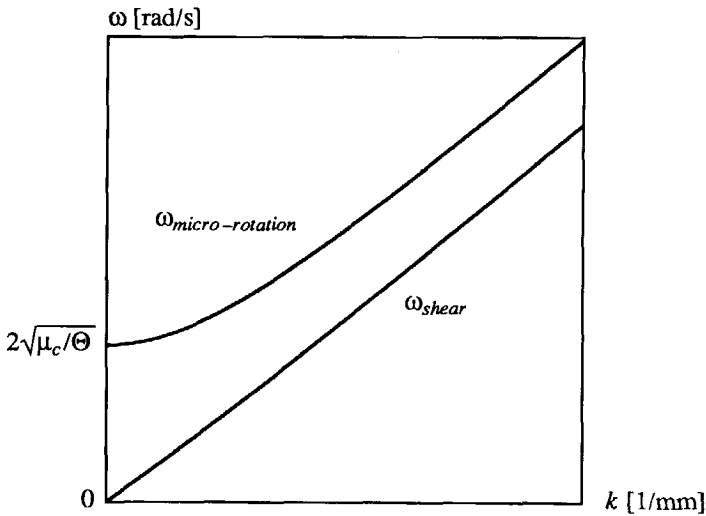


Figure 7.4 Dispersion relation between angular frequency  $\omega$  and wave number  $k$ .

harmonic wave with a constant phase  $kx - \omega t$ . By using  $\omega = k c_f$  the phase velocity can be expressed as

$$c_{f1,2} = \sqrt{-b/(2ak^2) \pm \sqrt{b^2/(2ak^2)^2 - c/(ak^4)}} \tag{7.35}$$

This relation is shown in Figure 7.5. The dependence of shear phase velocity and micro-rotation phase velocity on the wave number is evident. Indirectly the phase velocity is then also dependent on the wave length.

The parameters which determine the shear and the micro-rotation phase velocities cannot be chosen freely. If the curves in Figure 7.5 intersect, the discriminant in eq.(7.35) becomes negative which results in imaginary phase velocities for the harmonic shear wave as well as for the harmonic micro-rotation wave. Consequently, for the one-dimensional transverse wave propagation problem a consistent solution cannot be found if

$$\frac{l^2}{\Theta} < \frac{\mu + \mu_c}{2\mu\rho} \tag{7.36}$$

From the  $c_f - k$  curve it becomes clear that every harmonic constituent of an initial disturbance travels with a different phase velocity and therefore the shape of the pulse will be altered as it travels. As discussed in section 4.2, in a dispersive medium distinction exists between the phase velocity  $c_f$  of the single harmonic wave and the velocity at which the energy travels, the group velocity  $c = \partial\omega/\partial k$ . The group velocity is plotted as a function of the wave number  $k$  in

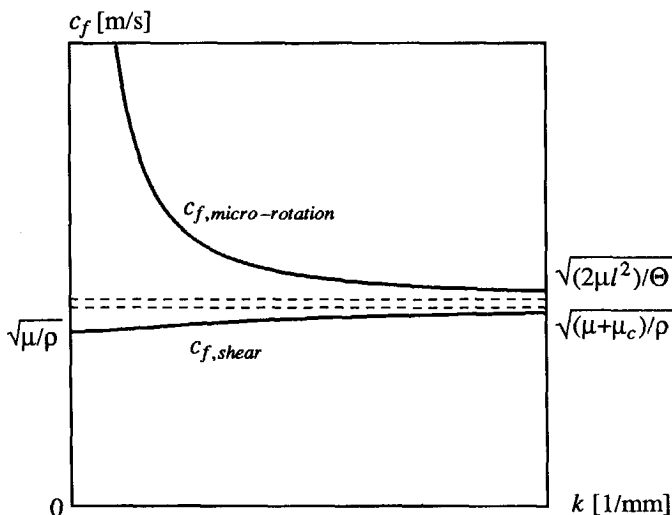


Figure 7.5 Dispersion relation between phase velocity  $c_f$  and wave number  $k$ .

Figure 7.6. The Figures 7.5 and 7.6 reveal that for the limiting case that the wave number approaches zero the shear group velocity as well as the shear phase velocity tends to the value that is computed for a classical continuum. Accordingly, for  $\lambda \rightarrow \infty$ , or equivalently for  $k \rightarrow 0$ , the classical wave propagation problem is recovered.

To analyse the propagation of a longitudinal wave in a one-dimensional micro-polar continuum the displacement  $u_y$  and the gradients in  $y$ -direction are kept zero, so that eq.(7.15) reduces to

$$2\mu a_1 \frac{\partial^2 u_x}{\partial x^2} = \rho \frac{\partial^2 u_x}{\partial t^2} . \tag{7.37}$$

Using the general solution

$$u_x = A e^{i(kx - \omega t)} , \tag{7.38}$$

it follows that the phase velocity  $c_f$  as well as the longitudinal wave velocity  $c$  is given by

$$c = \sqrt{2\mu a_1 / \rho} = \sqrt{E(1-\nu)/\rho(1+\nu)(1-2\nu)} , \tag{7.39}$$

which is not dispersive and equal to the longitudinal wave velocity in the classical continuum (Achenbach 1973, Eringen and Suhubi 1975). It is emphasized that this equation for the longitudinal wave speed is valid for an unbounded medium. In case of a one-dimensional stress situation, e.g. a thin bar, the solution for the longitudinal wave velocity reduces to  $c_e = \sqrt{E/\rho}$

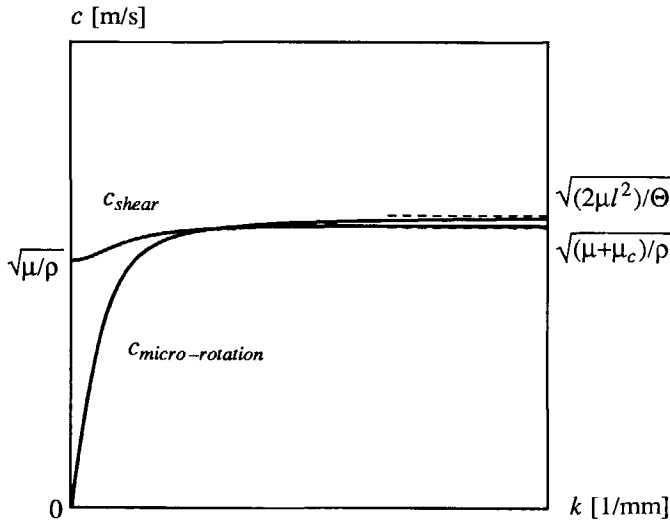


Figure 7.6 Dispersion relation between group velocity  $c$  and wave number  $k$ .

(bar velocity), which has been used in the previous chapters. In a two-dimensional bounded medium the wave velocity is between the "unbounded" velocity and the bar velocity.

It is finally noted that in a three-dimensional Cosserat medium six different waves can be distinguished. In addition to the longitudinal wave, the shear waves and micro-rotation waves already encountered in the two-dimensional Cosserat continuum a longitudinal micro-rotation wave, or micro-torsion wave, arises which acts in a plane perpendicular to its direction of propagation. The determination of the wave velocities can be done in a similar fashion as has been done for the one-dimensional cases.

So, the one-dimensional cases of shear and extension for the elastic Cosserat element can be analysed by means of a dispersion analysis. However, for the one-dimensional shear problem of a strain-softening Cosserat element a dispersion analysis cannot be carried out because the wave equations cannot be expressed in an explicit way. On the other hand, the one-dimensional extension problem for the strain softening element yields the classical wave equation eq.(3.8) derived in Chapter 3. So, the conclusions drawn from section 3.2 about mathematical ill-posedness unfortunately also apply to a Cosserat element under mode-I loading. In pure mode-I loading the rotational degrees-of-freedom do not become active and the micro-curvatures and couple stresses remain zero. Hence, if a problem is dominated by mode-I effects the Cosserat continuum modelling is an insufficient regularisation technique to obtain a convergence to a unique solution upon mesh refinement.

### 7.4 NUMERICAL ANALYSES

To investigate the performance of the micro-polar plasticity model two numerical simulations have been carried out in which mode-II failure is dominant. First, an analysis has been made of a one-dimensional shear layer, and next, shear banding in the biaxial plane-strain test (Example 3) has been simulated numerically. To investigate the characteristics of the micro-polar plasticity model a mesh-refinement study has been carried out. For the numerical calculations use has been made of a six-noded triangular plane-strain element with 18 degrees-of-freedom. The time integration of the field equations has been done with the Newmark scheme ( $\beta = 1/4$ ,  $\gamma = 1/2$ , see section 2.3). For the shear layer problem a time step  $\Delta t = 7.5 \cdot 10^{-8}$  s and for the biaxial test a time step  $\Delta t = 1.5 \cdot 10^{-6}$  s has been used.

#### 7.4.1 Shear layer problem

For the Cosserat continuum a somewhat different configuration has been investigated than the shear layer problem in Chapter 6, which is done for a comparison with the static results of the problem (de Borst 1990). The shear layer can be taken from a semi-infinite strip with a shear stress jump along its boundaries. The sketch of the problem is given in Figure 7.7. In the cen-

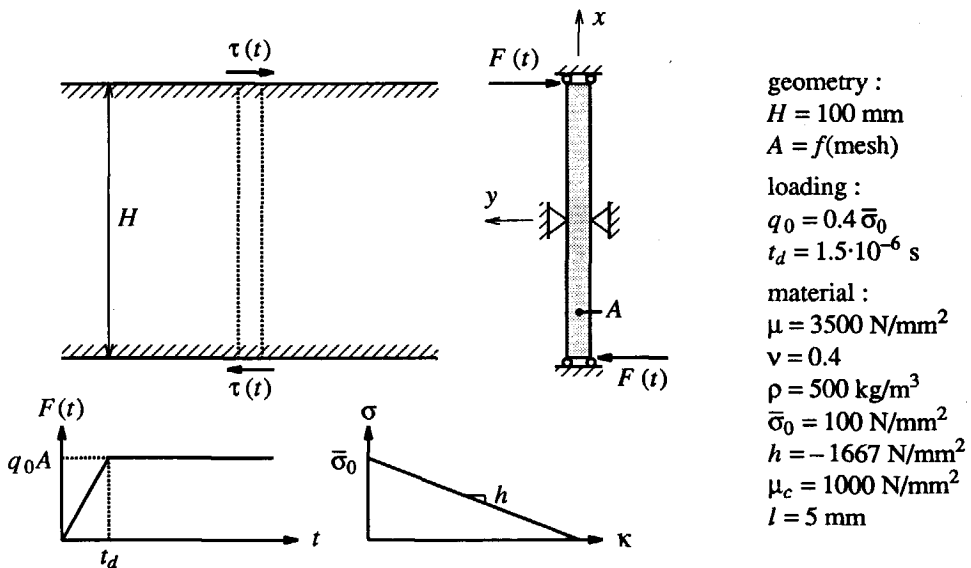


Figure 7.7 Shear layer problem.

tre of the layer the horizontal displacements are prevented ( $u_y = 0$ ) because of symmetry considerations, while essential boundary conditions  $\omega_z = 0$  have been applied at the upper and lower boundaries. The displacements in the  $x$ -direction are also constrained to zero. Basically, the problem is one-dimensional and the use of two-dimensional elements therefore requires the addition of linear constraint equations. For the conventional continuum model they only have to be applied to the displacements in the  $y$ -direction. The Cosserat continuum also requires that constraint equations are used for the rotational degrees-of-freedom. The elastic and inelastic material data set is given in Figure 7.7. A linear softening diagram in a von Mises plasticity model is used with an ultimate equivalent plastic strain  $\kappa_u = 0.06$  at which the yield strength has been reduced to zero. For the Cosserat continuum the additional material constants are :  $\mu_c = 1000 \text{ N/mm}^2$  and  $l = 5 \text{ mm}$ . With eq.(7.24) this results in a value for the spin inertia  $\Theta = 1.786 \cdot 10^{-8} \text{ N s}^2/\text{mm}^2$ . For the elastic solution of the shear layer we use a lumped mass matrix, while for the localised solution of the layer we use a consistent mass matrix in order to obtain a more accurate description of the localisation zone (see section 2.3).

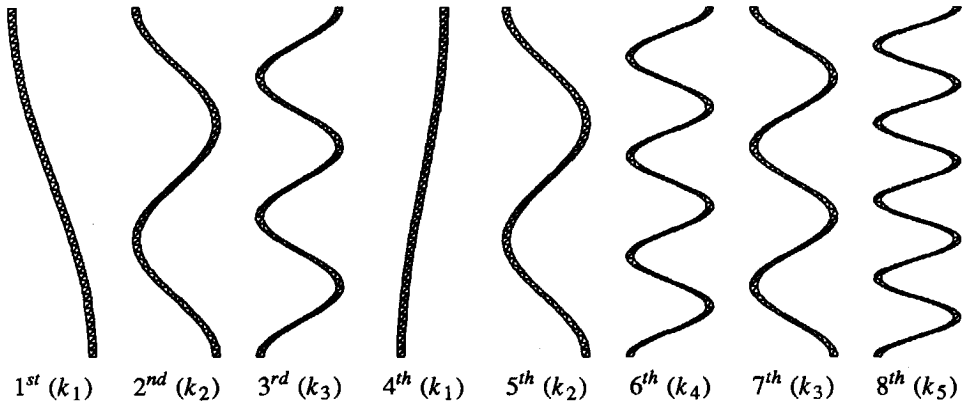
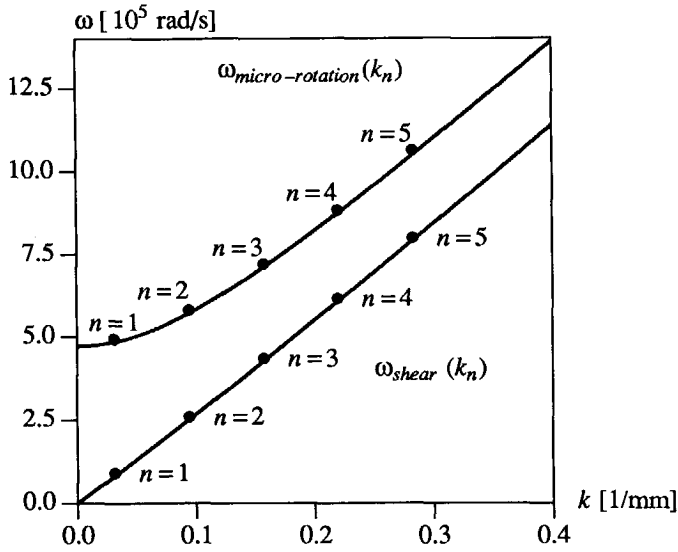
*- elastic solution of the shear layer*

First, the wave propagation will be discussed for an elastic Cosserat medium. The dispersion relations derived in section 7.3 and the above listed geometry data and boundary conditions of the layer can be used to calculate the exact analytical values for the wave numbers  $k$  and the angular frequencies  $\omega$ . A full derivation can be found in Appendix 7A (see also Sluys (1990)) and results in the relation

$$\frac{(2n-1)\pi}{H} = k_n \quad n = 1, 2, 3, \dots \quad (7.40)$$

for the shear wave and for the micro-rotation wave. Substitution of  $k_n$  in eq.(7.31)-(7.34) yields values for  $\omega_{1n}$  and  $\omega_{2n}$ , in which  $\omega_{1n}$  represents the  $n$ -th angular frequency of the shear wave and  $\omega_{2n}$  represents the  $n$ -th angular frequency of the micro-rotation wave. In Figure 7.8 these analytically derived shear modes and micro-rotation modes have been plotted in the  $\omega$ - $k$  plane. The analytical results have been verified numerically with a mesh with 100 elements. An eigenvalue analysis yields the eigenmodes and angular frequencies shown in the bottom picture of Figure 7.8. The numerical values for  $\omega$ , listed in the table, and for  $k$ , which follow from the wave lengths, are in exact agreement with the analytical values. The eigenmodes are plotted in ascending order with respect to  $\omega$ , the 1<sup>st</sup>, 2<sup>nd</sup>, 3<sup>rd</sup>, 6<sup>th</sup> and 8<sup>th</sup> mode are shear modes and the 4<sup>th</sup>, 5<sup>th</sup> and 7<sup>th</sup> mode are micro-rotation modes. These modes correspond to the modes  $n = 1$  to 5 for shear and  $n = 1$  to 3 for micro-rotation in the dispersion curve in Figure 7.8.

The dispersion phenomenon cannot only be shown from an analysis of harmonic waves but also from a study on travelling waves. We consider the propagation of one loading wave (applied at  $x = -1/2 H$ ) through the Cosserat shear layer. To avoid reflection at the centre of the layer the vertical displacement is kept zero at  $x = 1/2 H$  instead of at  $x = 0$ . The response is



no.	angular frequency	type of mode	no.	angular frequency	type of mode
1 <sup>st</sup>	$\omega = 83264$ rad/s	shear	5 <sup>th</sup>	$\omega = 573353$ rad/s	micro-rotation
2 <sup>nd</sup>	$\omega = 252715$ rad/s	shear	6 <sup>th</sup>	$\omega = 607938$ rad/s	shear
3 <sup>rd</sup>	$\omega = 427885$ rad/s	shear	7 <sup>th</sup>	$\omega = 712139$ rad/s	micro-rotation
4 <sup>th</sup>	$\omega = 486659$ rad/s	micro-rotation	8 <sup>th</sup>	$\omega = 791305$ rad/s	shear

Figure 7.8 Eigenmodes of the shear layer with analytical values  $(\omega_i, k_i)$  from dispersion analysis (top) and corresponding numerical eigenmodes  $k_i$  (bottom).

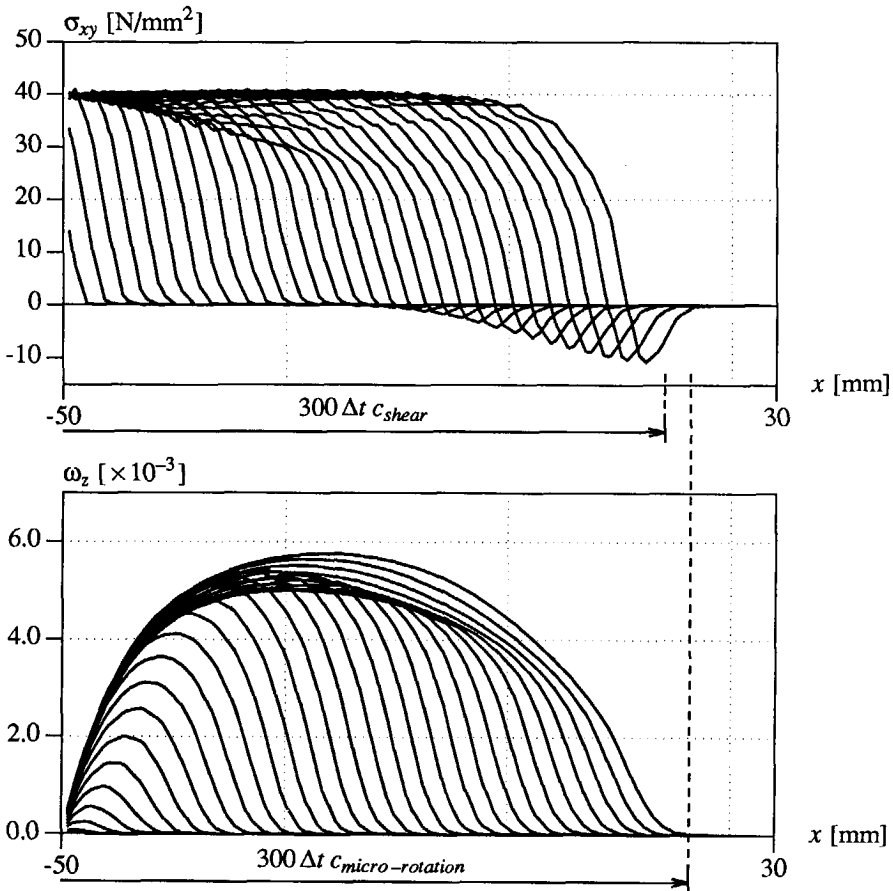


Figure 7.9 Wave propagation in the elastic Cosserat shear layer ( $0 < t < 300 \Delta t$ ): Shear stresses (top) and micr-rotations (bottom).

plotted in Figure 7.9 by means of the shear stress  $\sigma_{xy}$  and the rotation degree-of-freedom  $\omega_z$ . The response is a coupling of shear and micro-rotation effects, which can be seen from the shear stresses  $\sigma_{xy}$ . The small response travelling ahead of the main pulse is caused by the micro-rotation wave. This is obvious from a comparison of the maximum speed of the rotation wave ( $c_{micro-rotation} = (2\mu l^2/\Theta)^{1/2} = 3130 \text{ m/s}$ ) with the maximum speed of the shear wave ( $c_{shear} = ((\mu + \mu_c)/\rho)^{1/2} = 3000 \text{ m/s}$ ) which follow from the dispersion curve in Figure 7.6. Finally the influence of the spin inertia on the response has been investigated. The results plotted in Figure 7.10 show that putting  $\Theta = 0$  the micro-rotation wave speed goes to infinity (see also Figure 7.6). On the other hand, taking the spin inertia  $\Theta$  equal to the critical value  $\Theta_{cri}$  derived from the condition (7.36) the shear wave speed and the micro-rotation wave

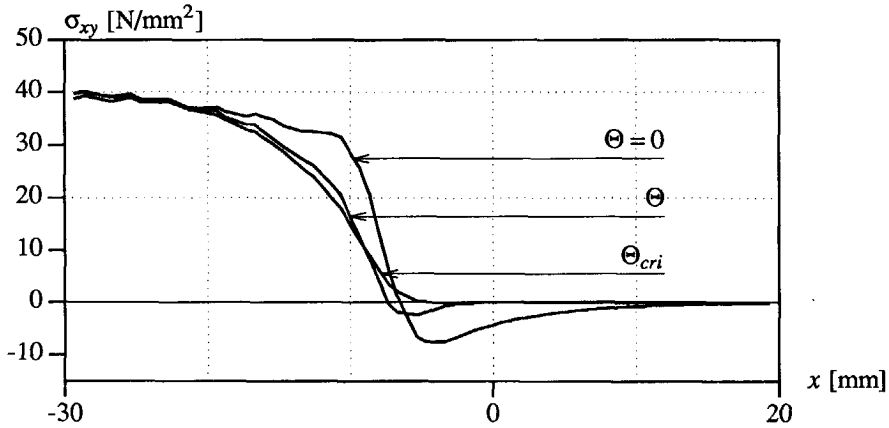


Figure 7.10 Wave propagation in the elastic Cosserat shear layer - variation of the spin inertia for the shear stresses.

speed coincide and the small micro-rotation wave which travels ahead of the shear wave is no longer present.

*- localised solution of the shear layer*

Now, the strain-softening behaviour of the shear layer of micro-polar material will be considered. A mesh-sensitivity study has been carried out with four different discretisations, namely with 10, 20, 100 and 200 elements. Analyses of the classical strain-softening layer for static (de Borst 1990) and dynamic (Sluys 1990) loading conditions prove the entire dependence of the localisation zone data on the mesh spacing. Softening is initiated when both shear waves meet at the centre of the layer and the shear stress intensity is doubled. Owing to the ensuing softening behaviour localisation occurs.

For the Cosserat layer a localisation zone emerges which converges to a finite, constant band width upon mesh refinement. This is shown in Figure 7.11 for the displacement patterns and in Figure 7.12 for the shear strain fields  $\epsilon_{xy}$  for the different meshes. While the band width of the localisation zone is still somewhat too wide for the coarsest meshes (10 and 20 elements) the finest meshes give identical results. Obviously the continuum is capable of transforming the loading wave into a stationary localisation wave. The internal length scale of the model is necessary to set the mesh-independent localisation band width. Mesh independence is also observed from the consumption of energy in the layer during the inelastic deformation. In Figure 7.13 the consumption of energy is plotted and although we have a structural instability because the second derivative is slightly negative ( $d^2U/dr^2 < 0$  see section 3.2) the layer consumes a finite amount of energy independently of the finite element discretisation. The development of the localisation zone is shown by means of the shear strains in Figure



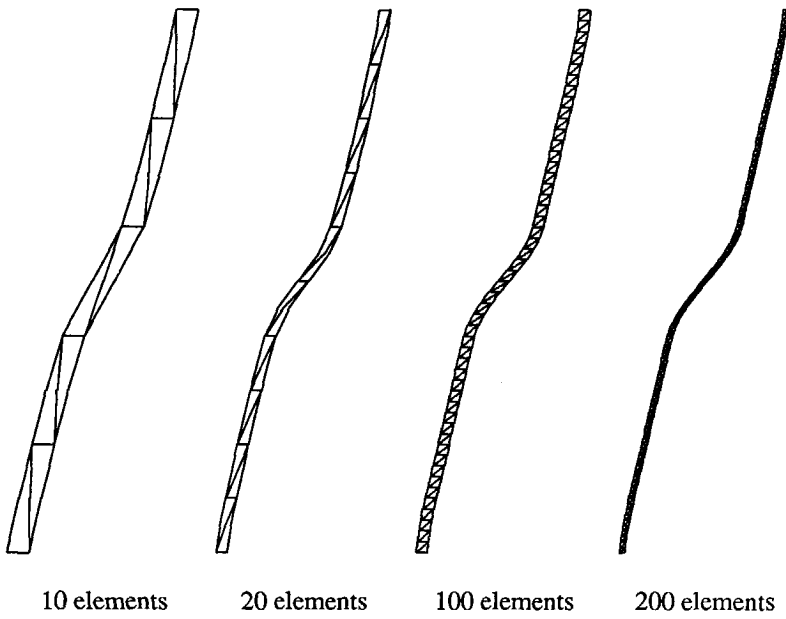


Figure 7.11 Displacement patterns at  $t = 33.75 \cdot 10^{-6}$  s (FA = 150).

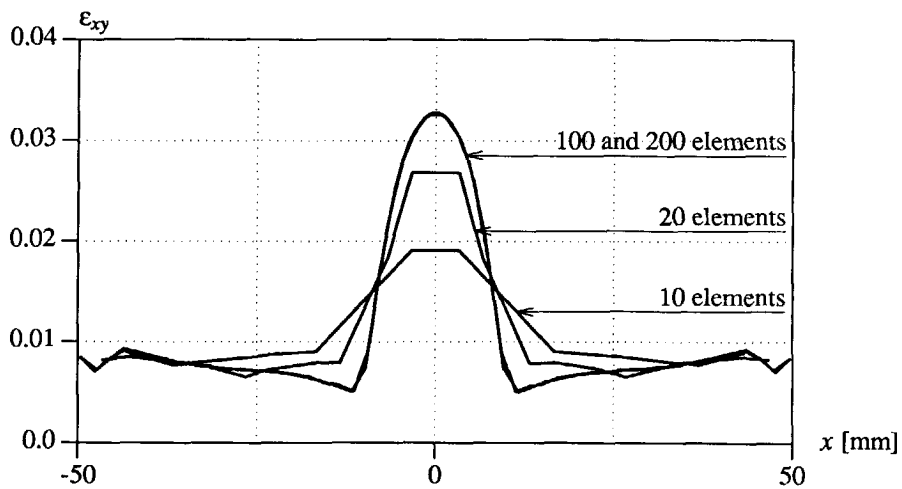


Figure 7.12 Strain distribution along the layer at  $t = 33.75 \cdot 10^{-6}$  s.

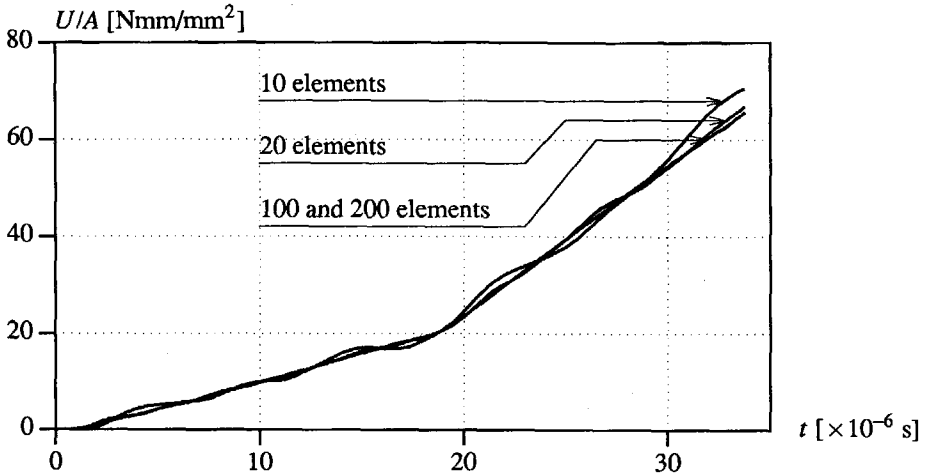


Figure 7.13 Energy consumption in the shear layer.

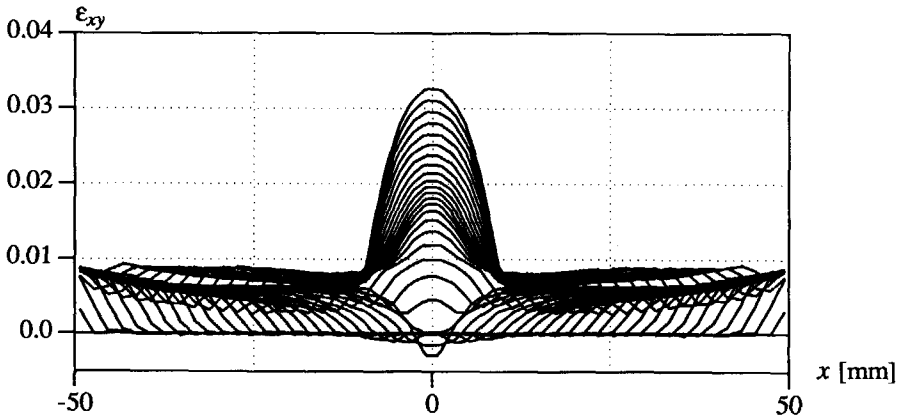


Figure 7.14 Stroboscopic development of the shear strains ( $0 \leq t \leq 33.75 \cdot 10^{-6}$  s).

7.14 and by means of the shear stresses in Figure 7.15. The formation of the localisation band occurs rapidly but after a full development the width of the shear band remains constant in time. The localisation zone is a cosine-shaped stationary shear wave. From the shear stresses it appears that at the interface of the shear band we have stress continuity as we have assumed earlier in section 3.3 and Appendix 3A.

The sensitivity of the solution to changes in the inelastic material data set is investigated. First, the influence of the  $l$ -parameter on the observed width of the localisation band was

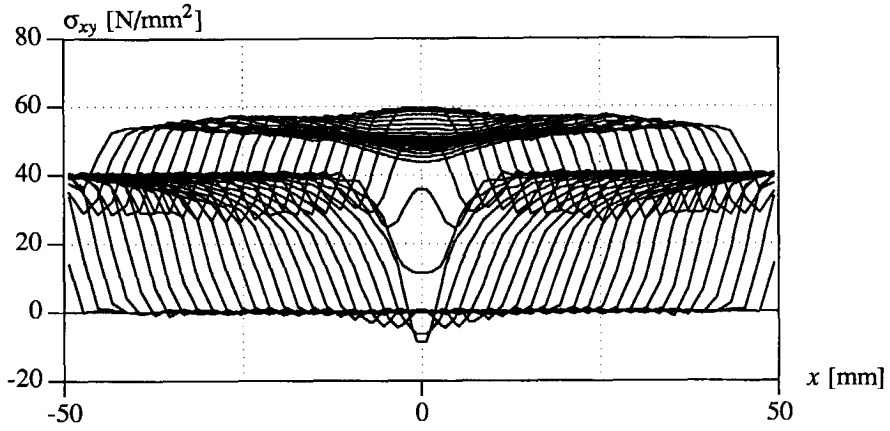


Figure 7.15 Stroboscopic development of the shear stresses ( $0 \leq t \leq 33.75 \cdot 10^{-6}$  s).

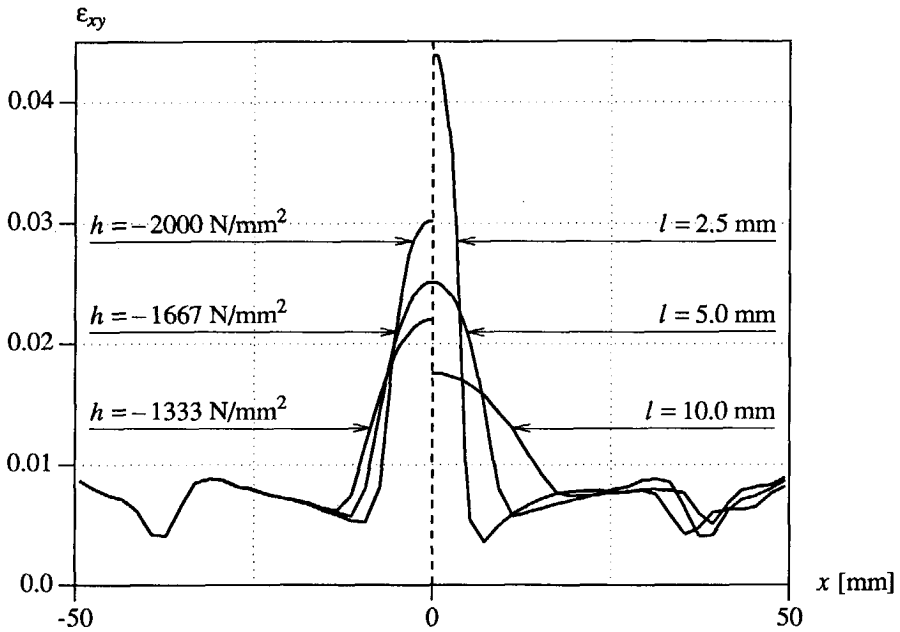


Figure 7.16 Variation of  $h$  (left) and  $l$  (right) for mesh with 100 elements ( $t = 30 \cdot 10^{-6}$  s).

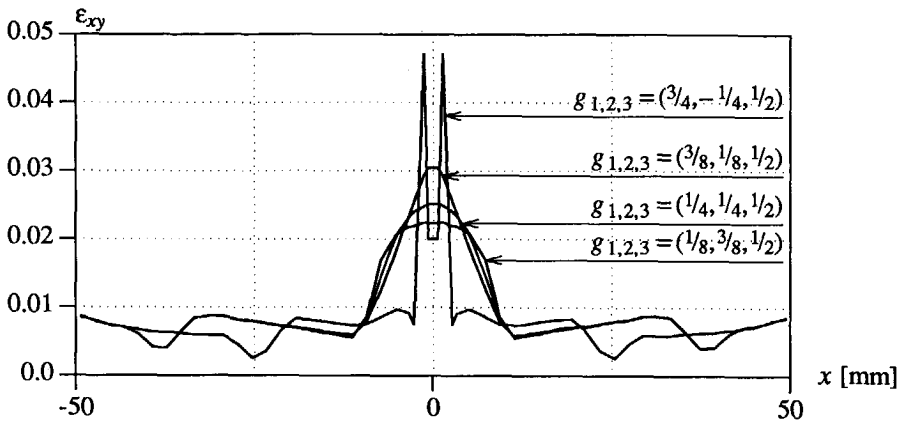


Figure 7.17 Variation of the second invariant of the deviatoric stresses  $J_2$  ( $t = 30.0 \cdot 10^{-6}$  s, except  $g_{1,2,3} = (3/4, -1/4, 1/2)$  at  $t = 25.5 \cdot 10^{-6}$  s).

investigated by using three different values for  $l$ , namely 2.5, 5.0 and 10.0 mm. Figure 7.16 (right plot) shows an almost linear dependence of the width of the localisation band on  $l$ . For a smaller  $l$  a more rapid failure and more brittle behaviour is obtained, while for a larger value of  $l$  the behaviour is more ductile. So, the value for  $l$  determines the size of the localisation band and governs the brittleness of a structure. The slope of the strain-softening curve  $h$  is a second important parameter which determines the behaviour in the localisation zone. Variation of  $h$  yields the same tendencies as obtained for variation of the length scale parameter (Figure 7.16 - left plot). A steeper strain-softening diagram shows a brittle response and localisation in a small localisation zone, whereas a more ductile strain-softening curve stabilises the failure process in a wider localisation band. Variation of the loading rate by changing the parameter  $t_d$  hardly has any effect on the formation of the band.

Finally, the plasticity model has been changed by means of a variation of  $J_2$  (cf. eq.(7.13)). If we set  $g_{1,2,3} = (1/8, 3/8, 1/2)$  we obtain more uniformly distributed and lower peak strains in the localisation zone (see Figure 7.17). On the other hand, the profile of the shear strains becomes smaller for  $g_{1,2,3} = (3/8, 1/8, 1/2)$  and even shows mesh dependence (localisation in two symmetric integration points) for  $g_{1,2,3} = (3/4, -1/4, 1/2)$ . The latter two models are known as the kinematic model and the static model, respectively (Vardoulakis 1989).

### 7.4.2 Example 3 : Impact biaxial test

Now, the micro-polar Cosserat model is used for an analysis of the biaxial test. A mesh-sensitivity analysis to the influence of fineness and distribution of the elements is carried out with the finite element discretisations as used in section 3.5.3. The problem has been analysed

using the von Mises softening plasticity model. In contrast to the analyses with the gradient model and the viscoplastic models only the plane-strain condition will be considered.

The impact biaxial test for the analysis of shear banding is a wave propagation problem in which the pressure longitudinal wave propagates in a linear-elastic manner through the specimen. The transverse system of shear and micro-rotation waves, which is present in a direction perpendicular to the direction of propagation, can hardly be observed (Sluys 1990).

*- biaxial test with von Mises material (plane-strain)*

For the first analysis with a von Mises softening plasticity model the material and loading data from Figure 3.14 have been used. The additional material constants for the Cosserat medium are :  $\mu_c = 2000 \text{ N/mm}^2$  and  $l = 1.25 \text{ mm}$ . The value for the internal length scale parameter  $l$  results in a spin inertia  $\Theta = 1.05 \cdot 10^{-8} \text{ N s}^2/\text{mm}^2$  (eq.(7.24)).

The effect of the inclusion of the internal length scale can be observed from the plot of the displacement fields and the equivalent plastic strains after one loading cycle in Figure 7.18. The width of the shear band shows a slight decrease upon mesh refinement. This is also observed in Figure 7.19 for the equivalent plastic strains in the centre section of the sample. We observe a larger peak strain in a smaller localisation band when we refine the mesh. Despite this result for the width of the zone, the consumption of energy in the sample shows a reasonable similarity for the three meshes (see Figure 7.20). The plane-strain analysis for the Cosserat medium shows a shear band with an inclination angle which is slightly smaller than  $45^\circ$  (eq.(3A.21)) which is due to the micro-polar description of the material already in the elastic stage (Steinmann and Willam 1991).

It is obvious that the results obtained with the Cosserat model remedies the spurious results for the classical analysis of the biaxial test in the Figures 3.16 to 3.18, but not to the same extent as obtained with the gradient model (Figures 5.8 to 5.10) and with the viscoplastic models (Figures 6.8 to 6.10). It becomes clear that, as already mentioned in section 7.3, the mode-I pressure component in the problem partially spoils the well-posedness of the problem. A complete insensitiveness of the solution on the discretisation can only be obtained for a pure mode-II problem as the shear layer in the previous section. Mesh dependence gradually returns when mode-I components become more and more active.

Furthermore, it has been investigated to which extent the numerically observed localisation band width is influenced by the length scale parameter  $l$  and by the slope of the strain-softening curve. If the length scale parameter is multiplied by a factor 1.5 the band width also increases by approximately a factor 1.5. A similar increase of the width of the localisation band is obtained by enlarging the ultimate equivalent plastic strain by a factor 1.5 (i.e.  $h = -666 \text{ N/mm}^2$ ). In Figure 7.21 the total displacements and the equivalent plastic strains for these two calculations are compared with the results obtained for the reference analysis.

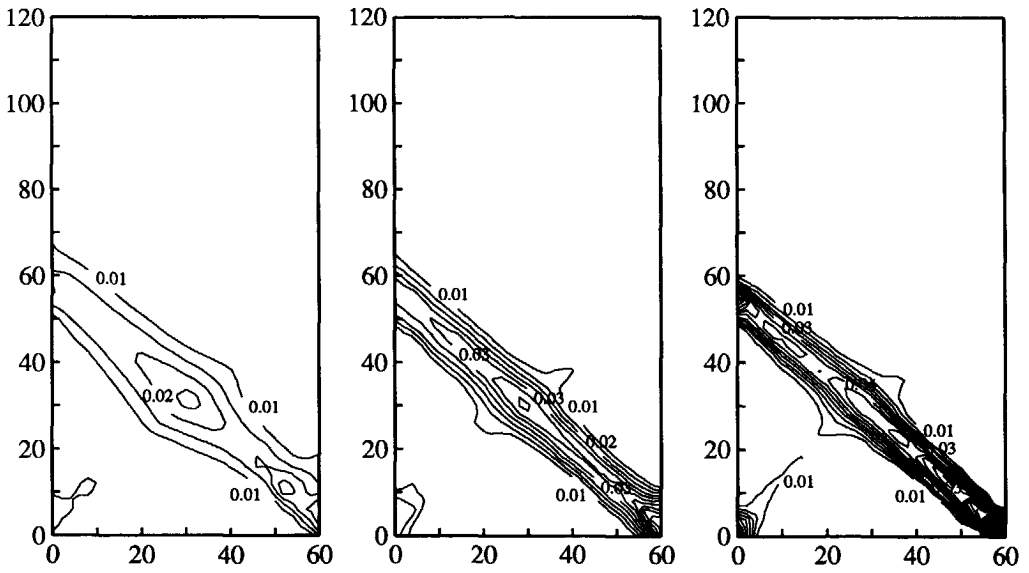
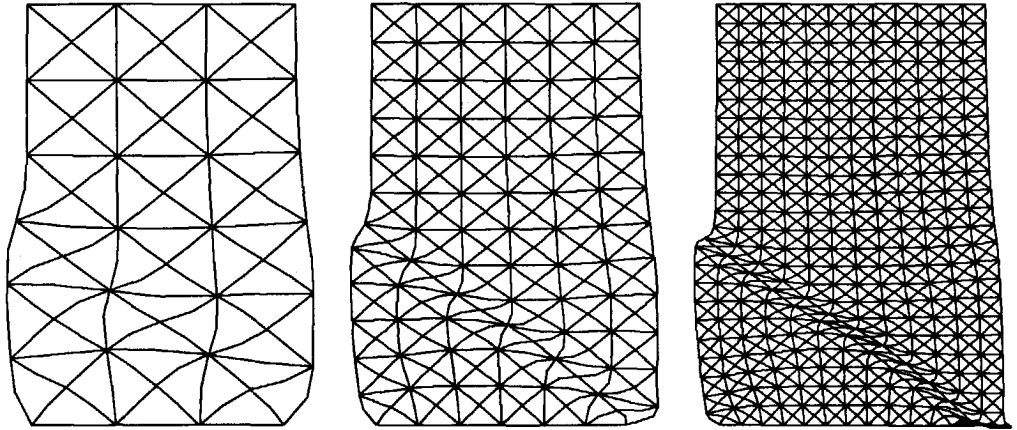


Figure 7.18 Cossierat continuum model with plane-strain elements :  
 Top : Total displacement patterns ( $t = 0.165 \cdot 10^{-3}$  s,  $FA = 15$ ).  
 Bottom : Contour plots of the equivalent plastic strains.

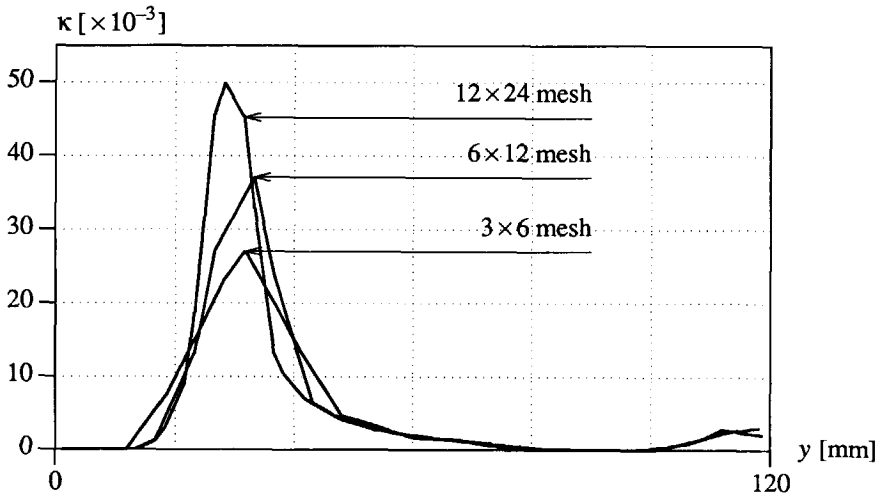


Figure 7.19 Equivalent plastic strains  $\kappa$  in centre section ( $x = 30$  mm) of the sample ( $t = 0.165 \cdot 10^{-3}$  s).

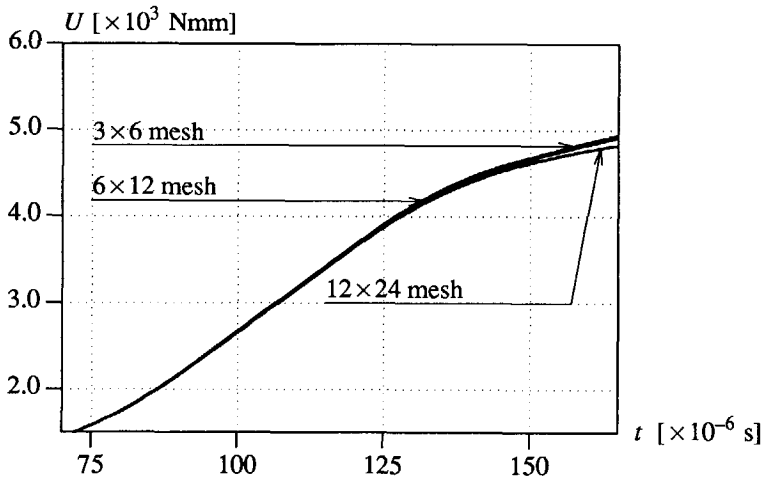


Figure 7.20 Energy consumption in the sample.

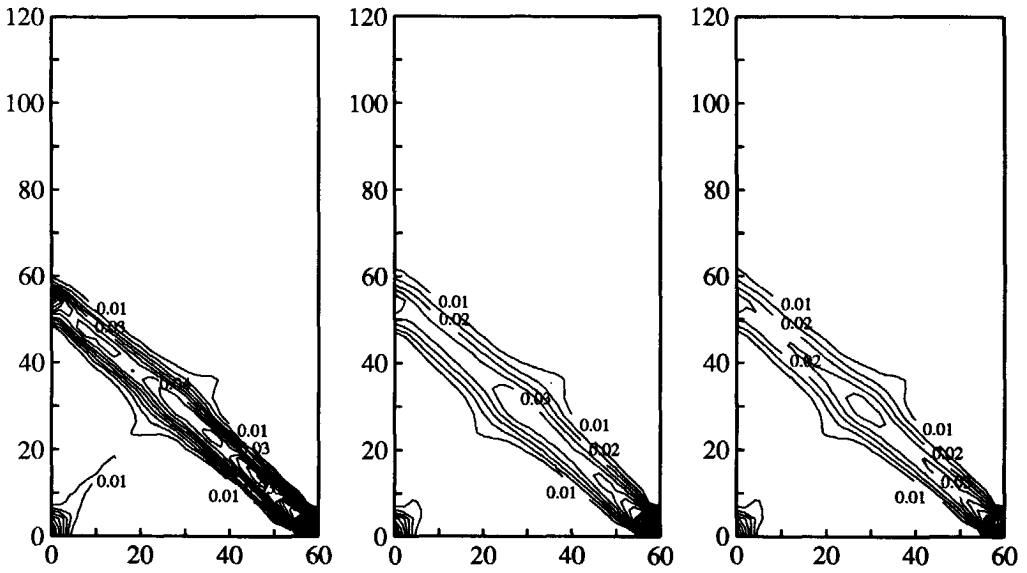
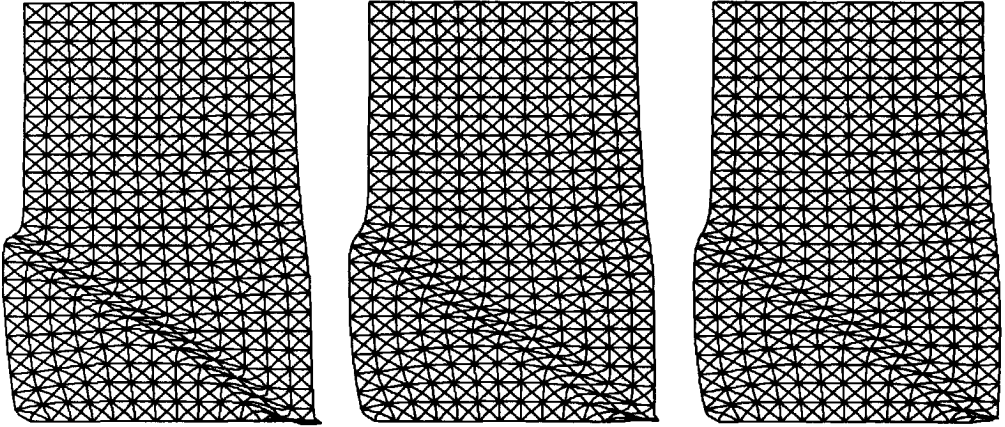


Figure 7.21 Total displacements (top - FA = 15) and equivalent plastic strains (bottom) for reference set of parameters (left), for  $l = 1.875$  mm (centre) and for  $h = -666$  N/mm<sup>2</sup> (right).



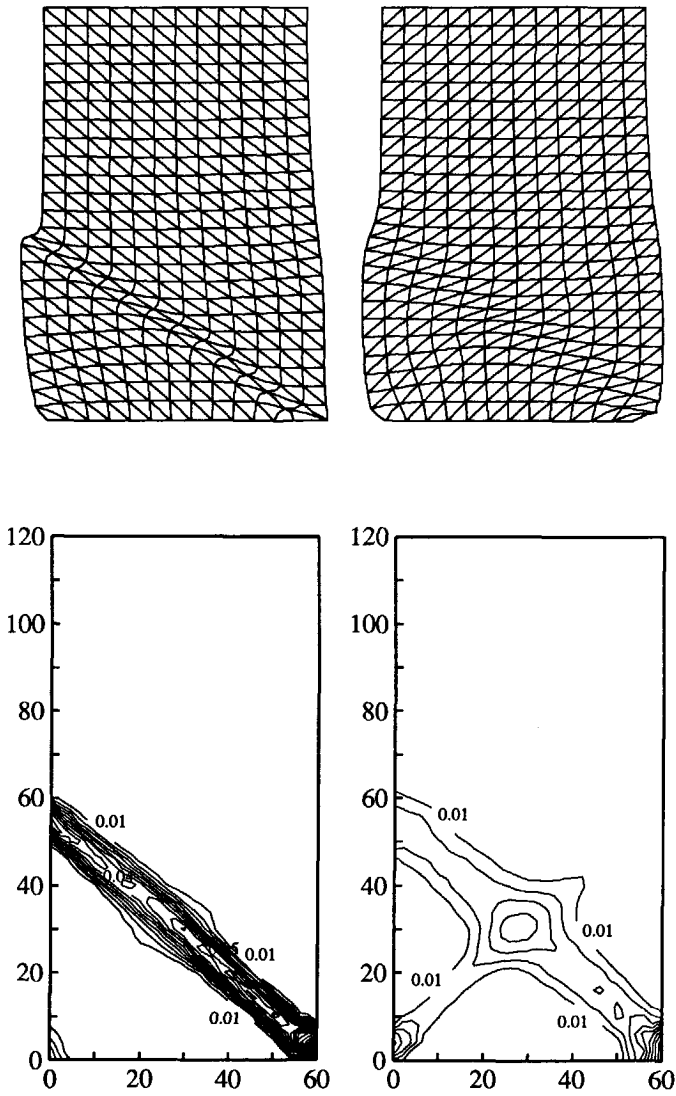


Figure 7.22 Total displacements (top - FA = 15) and equivalent plastic strains (bottom) for biased (left) and unbiased (right) mesh.

Finally, the influence of mesh alignment on the results is investigated with a biased and an unbiased mesh. The results, given in Figure 7.22, show a clear difference between the two analyses. The results for the biased mesh are in agreement with the results for the  $12 \times 24$  mesh in Figure 7.18, but the results for the unbiased mesh deviate markedly. The shear band is substantially wider and the equivalent plastic strains are much smaller. So, for this problem the Cosserat continuum model is too weak as a regularisation method to avoid mesh-alignment problems. In conclusion it can be said that the micro-polar effect partially remedies mesh dependence with respect to the width of the shear band but is not able to exclude the spurious influence of mesh orientation.

### APPENDIX 7A : ANALYTICAL EIGENMODE ANALYSIS OF SHEAR LAYER

If we consider the two solutions belonging to the positive and negative roots for the wave number the static part of the solution for the free response of the shear layer of section 7.4.1 reads

$$u_y(x) = A_1 e^{-ikx} + A_2 e^{ikx} \quad (7A.1)$$

and

$$\omega_z(x) = B_1 e^{-ikx} + B_2 e^{ikx} . \quad (7A.2)$$

To each wave number  $k$  belongs one angular frequency  $\omega_1$  for shear and one angular frequency  $\omega_2$  for micro-rotation. The solution is transformed into sine and cosine functions and if the constants  $C_1 = A_1 + A_2$ ,  $C_2 = A_2 - A_1$ ,  $C_3 = B_1 + B_2$  and  $C_4 = B_2 - B_1$  are introduced the general solution becomes

$$u_y(x) = C_1 \cos kx + iC_2 \sin kx \quad (7A.3)$$

and

$$\omega_z(x) = C_3 \cos kx + iC_4 \sin kx . \quad (7A.4)$$

The following boundary conditions of the unloaded shear layer from Figure 7.7 can be applied

$$1) x=0 \rightarrow u_y = 0 \quad (7A.5)$$

$$2) x=0 \rightarrow m_{xz} = 0 \rightarrow \frac{\partial \omega_z}{\partial x} = 0 \quad (7A.6)$$

$$3) x = 1/2 H \rightarrow \omega_z = 0 \quad (7A.7)$$

$$4) x = 1/2 H \rightarrow \sigma_{xy} = 0 \rightarrow (\mu + \mu_c) \frac{\partial u_y}{\partial x} - 2\mu_c \omega_z = 0 \quad (7A.8)$$

The boundary conditions result in the following system of equations

$$\begin{bmatrix} 1 & 0 & 0 & 0 \\ 0 & 0 & 0 & ik \\ 0 & 0 & \cos 1/2 kH & i \sin 1/2 kH \\ (\mu + \mu_c)k \sin 1/2 kH & (\mu + \mu_c)ik \cos 1/2 kH & -2\mu_c \cos 1/2 kH & -2\mu_c i \sin 1/2 kH \end{bmatrix} \begin{bmatrix} C_1 \\ C_2 \\ C_3 \\ C_4 \end{bmatrix} = \mathbf{0}, \quad (7A.9)$$

which has a non-trivial solution for  $C_i$  when the determinant is equal to zero, which results in

$$(\mu + \mu_c)k^2 \cos^2 1/2 kH = 0. \quad (7A.10)$$

A non-trivial solution for  $k$  can be found if  $\cos 1/2 kH = 0$  which yields

$$\frac{(2n-1)\pi}{H} = k_n \quad n = 1, 2, 3, \dots \quad (7A.11)$$

in which  $n$  represents the number of the eigenmode. The angular frequencies  $\omega_{1n}$  for shear and  $\omega_{2n}$  for micro-rotation follow from eqs.(7.31)-(7.34). From eq.(7A.9) it appears that  $C_1 = C_4 = 0$ , which yields the analytical solution for the free response of the shear layer, written as a summation of  $m$  eigenmodes,

$$u_y(x,t) = \sum_{n=1}^{n=m} (iC_{2n} \sin(k_n x))(e^{-i\omega_{1n}t} + e^{i\omega_{1n}t}) \quad (7A.12)$$

$$\omega_z(x,t) = \sum_{n=1}^{n=m} (C_{3n} \cos(k_n x))(e^{-i\omega_{2n}t} + e^{i\omega_{2n}t}) \quad (7A.13)$$

The constants  $C_{2n}$  and  $C_{3n}$  can be calculated from the initial conditions of the layer.

## 8. CONCLUSIONS

The computational modelling of structural failure in softening materials calls for a proper material modelling of the problem. At incipient failure softening often drives the formation of localisation bands (cracks, shear bands). A conventional material modelling of the softening solid is insufficient because we obtain results which are entirely determined by the finite element discretisation. To state the problem in a clear fashion a first aim of this study was to clarify the problem of mesh sensitivity, while the main goal was to scrutinise solution techniques which remedy mesh sensitivity. We have considered wave propagation problems, which implicitly include static problems as a limit case.

Following the phenomenological approach, a straightforward mapping of load-displacement data with a descending branch beyond peak load onto stress-strain relations provides a negative tangential stiffness in the constitutive equations (strain-softening model). The use of a strain-softening model in the framework of a classical, rate-independent continuum can result in loss of well-posedness of the initial value problem. In the strain-softening region of a structure hyperbolicity of the field equations is lost which is attended by imaginary characteristics and wave speeds. The consequences in a mechanical sense of the loss of well-posedness have been demonstrated by means of the analytical solution of a strain-softening bar. We calculate a localisation zone of zero thickness which develops instantly after the initiation of strain softening. The localisation zone starts to act as a free boundary at which tensile waves reflect as pressure waves. Because the area in which failure occurs is zero the energy consumed in the failure zone is zero. The finite element solution tries to capture the localisation zone of zero thickness and, as a result, strain localisation occurs in a zone which is entirely determined by the element size. Upon mesh refinement we observe convergence to a line crack (Examples 1 and 2) or to a shear band of zero thickness (Example 3). Mesh sensitivity is not only demonstrated with respect to the fineness of the mesh, but it appears that the orientation of the mesh lines also influences the results (mesh alignment). Therefore the severe result is obtained that the direction of crack or shear band propagation is largely influenced by the finite element discretisation.

The basic deficiency of the classical continuum concept is that no characteristic dimensions or necessary spatial interactions in the localisation zone are present. The absence of a length scale parameter leaves the width of the localisation zone unspecified. Secondly, from a dispersion analysis it was demonstrated that propagating waves are non-dispersive in a classical strain-softening continuum, i.e. arbitrarily shaped waves cannot be transformed into stationary localisation waves. However, wave propagation in strain-softening media can only be described properly if the continuum model admits dispersive waves.

To solve the mesh-sensitivity problem the initial value problem must be well-posed and these deficiencies should be overcome to arrive at a solution for the localisation band, which is invariant to size and orientation of the finite elements. For this reason the approach followed

in this study is the enrichment of the softening continuum description with extra or higher-order terms. Three solution techniques have been explored, namely the addition of rate-dependence (RD-model), the addition of second-order strain gradients (GR-model) and the inclusion of micro-polar effects (CO-model). The models do not necessarily lose hyperbolicity at the onset of strain softening and admit a solution with real wave speeds. All models incorporate a length scale parameter which has been related to the width of the localisation band. Wave propagation is dispersive in the enriched continua and therefore transformation of waves is possible in the localisation zone. The three models have been assessed on their numerical performance with respect to mode-I and mode-II failure. Furthermore, the fineness of the mesh and the orientation of the mesh lines have been varied. The results are summarised in Box 8.1.

Box 8.1 : Mesh sensitivity for different types of failure and loading.

	RD-model	GR-model	CO-model
mode-I failure	++	++	-
mode-II failure	++	++	++
static loading	-	++	+
dynamic loading	++	++	+

++ = mesh independent, + = conditionally mesh independent, - = mesh dependent

The inclusion of rate dependence in crack models (mode-I) and plasticity models (mode-II), makes it possible to calculate a finite, unique solution for the localisation band. For some rate-dependent models (power law model, Perzyna model with  $\phi = (f/\bar{\sigma})^N$ ) mesh dependence enters again during localisation because the stabilising viscous effect gradually vanishes when the strain-softening contribution reduces to zero. For the gradient model we also observe convergence to a unique solution for the localisation zone with respect to the size, the wave reflection at the zone and the energy consumption in the zone. It is important that inclusion of rate or gradient effects solves the mesh-alignment problem. For this reason these models differ from a fracture energy model (Bažant and Oh 1983), in which the influence of the orientation of mesh lines on the direction of propagation of a crack or a shear band remains present. Using a fracture energy model mesh adaptation in combination with the exact analytical solution for the orientation of the localisation zone should be used in the analysis procedure, which is, if it is already possible, much more complicated.

A distinct disadvantage of the Cosserat model is that it is only effective as a regularisation method when frictional slip is dominant (mode-II failure). Already in cases where we do not

have pure shear, as for instance the biaxial test (Example 3), the method is weak and not entirely mesh objective with respect to the fineness of the mesh and still shows a large influence of the direction of the mesh lines. This behaviour of the Cosserat model is explainable because the rotational degrees-of-freedom do not become active under pure mode-I loading.

If we combine our results with the results for static analyses with the gradient model (de Borst and Mühlhaus 1992) and with the Cosserat model (de Borst 1990) Box 8.1 can be completed. It is trivial that the inclusion of rate dependence is not a proper solution technique for static analyses. Although the incremental boundary value problem remains well-posed as long as the strain rate is larger than zero, which is always true during failure because a viscous effect is still present, the width of the localisation band approaches zero which is physically unrealistic and contradicts experimental evidence (e.g. Mühlhaus and Vardoulakis 1987). For very low loading rates the viscosity has to be made artificially high to obtain physically realistic results.

Considering the algorithmic aspects of the three models we note that the rate-dependent models and the Cosserat model are relatively easy to implement. The weak formulation of the yield function for the gradient model requires a more difficult algorithm. Furthermore, a disadvantage of the use of a gradient model or a Cosserat model is the need to define additional boundary conditions, which should be chosen with great care but for which physical relevance is lacking.

This study has a fundamental character and the mathematically proper description of the softening solid was more important than the exact simulation of experiments. For simple one- and two-dimensional problems the performance of the enhanced models has been explored thoroughly and the merits and limitations of each of the approaches are now known. Now, efforts should be focused on the proper simulation of the experimentally measured response. An example is the simulation of the impact tensile test on a double-notched specimen (Example 2), in which the additional viscosity parameter was determined by means of the numerical analyses. Since the additional parameters that emerge in the enriched continua models are not directly derivable from experiments such a semi-inverse approach should be followed.

A second topic of research for failure analyses involving localisation of deformation is the limitation of computer time by means of a modification of the spatial discretisation and/or the time integration scheme. The number of finite elements can be limited when the mesh is adapted dependently of the localisation process. If so-called mesh-adaptivity techniques (Ortiz and Quigley 1991, Huerta et al. 1992) are used a fine division of elements can be applied in the localisation zone while keeping the discretisation of the remainder of the body relatively coarse. Criteria for mesh adaptation can be based on the second-order strain gradient (cf. gradient model) or on the strain rate (cf. rate-dependent model). Adaptation of the time integration scheme can also be advantageous in dynamic failure analyses. The small localisation zone often puts a very severe restriction to the time step which is not necessary for the elastic part of the structure and in the pre-failure phase. Therefore, a time step control

algorithm with a variable time step (Thomas and Gladwell 1988) and/or use of subcycling techniques (Belytschko et al. 1984), in which a part of the mesh (localisation zone) is integrated with a smaller time step, should be employed.

A third subject of further research is the extension of the models, developed in this study, to make them suitable for different applications. One is the extension to composite softening materials as (fibre-)reinforced concrete and another is the modelling of propagative instabilities (Lüders bands, Portevin-Le Chatelier effect) in contrast to the static instabilities (cracks, shear band) treated in this study.



## REFERENCES

- ACHENBACH, J.D. (1973) - *Wave propagation in elastic solids*, American Elsevier, New York.
- ASARO, R.J. (1983). Mechanics of crystals and polycrystals, *Adv. Appl. Mech.*, **23**, pp. 2-115.
- BATHE, K.J. (1982) - *Finite element procedures in engineering analysis*, Prentice Hall, New Jersey.
- BAZANT, Z.P. (1976) - Instability, ductility and size effect in strain softening concrete, *ASCE J. Eng. Mech.*, **102(2)**, pp. 331-344.
- BAZANT, Z.P. and OH, B. (1983) - Crack band theory for fracture of concrete, *RILEM Mat. Struct.* **16**, pp. 155-177.
- BAZANT, Z.P., BELYTSCHKO, T.B. and CHANG, T.-P. (1984) - Continuum theory for strain-softening, *ASCE J. Eng. Mech.*, **110**, pp. 1666-1692.
- BAZANT, Z.P. and BELYTSCHKO, T.B. (1985) - Wave propagation in a strain softening bar - exact solution, *ASCE J. Eng. Mech.*, **111(3)**, pp. 381-389.
- BAZANT, Z.P. and PIAUDIER-CABOT, G. (1989) - Measurement of characteristic length of non-local continuum, *ASCE J. Eng. Mech.*, **115**, pp. 755-767.
- BELYTSCHKO, T.B., SMOLINSKI, P. and LIU, W.K. (1984) - 'Multi-stepping implicit-explicit procedures in transient analysis', *Proc. Int. Conf. Innovative Methods for Nonlinear Problems*, Eds. W.K. Liu, T.B. Belytschko and K.C. Park, Pineridge Press, Swansea, pp. 135-153.
- BENALLAL, A., BILLARDON, R. and GEYMONAT, G. (1991) - 'Localization phenomena at the boundaries and interfaces of solids', *Proc. Third Int. Conf. Constitutive Laws for Engineering Materials : Theory and Applications*, Ed. C.S. Desai, Tucson, Arizona, pp. 387-390.
- BOLCK, J. (1992) - *Localisation in visco-plastic media under impact loading*, Graduation thesis, Delft University of Technology, Delft.
- BORST, R. de and NAUTA, P. (1985) - Non-orthogonal cracks in a smeared finite element model, *Eng. Comp.*, **2(1)**, pp. 35-46.
- BORST, R. de (1986) - *Non-linear analysis of frictional materials*, Dissertation, Delft University of Technology, Delft.
- BORST, R. de (1990) - 'Simulation of localisation using Cosserat theory', *Proc. 2nd Int. Conf. Computer Aided Analysis and Design of Concrete Structures*, Eds. N. Bićanić and H.A. Mang, Pineridge Press, Swansea, pp. 931-944.
- BORST, R. de and FEENSTRA, P.H. (1990) - Studies in anisotropic plasticity with reference to the Hill criterion, *Int. J. Num. Meth. Eng.*, **29**, pp. 315-336.
- BORST, R. de (1991) - Simulation of strain localisation: A reappraisal of the Cosserat continuum, *Eng. Comp.*, **8**, pp. 317-332.
- BORST, R. de and SLUYS, L.J. (1991) - Localisation in a Cosserat continuum under static and dynamic loading conditions, *Comp. Meth. Appl. Mech. Eng.*, **90**, pp. 805-827.
- BORST, R. de and MUHLHAUS, H.-B. (1991) - 'Computational strategies for gradient

- continuum models with a view to localisation of deformation', *Proc. 4th. Int. Conf. on Non-linear Eng. Comp.*, Eds. N. Bićanić, P. Marović, D.R.J. Owen, V. Jović and A. Mišanović, Pineridge Press, Swansea, pp. 239-260.
- BORST, R. de and MUHLHAUS, H.-B. (1992) - Gradient-dependent plasticity : Formulation and algorithmic aspects, *Int. J. Num. Meth. Eng.*, to appear.
- BORST, R. de, MUHLHAUS, H.-B., PAMIN, J. and SLUYS, L.J. (1992) - 'Computational modelling of localisation of deformation', *Proc. Conf. on Computational Plasticity, Fundamentals and Applications, Part II*, Eds. D.R.J. Owen, E. Oñate and E. Hinton, Pineridge Press, Swansea, pp. 483-508.
- CORMEAU, I.C. (1975) - Numerical stability in quasi-static elasto/visco-plasticity, *Int. J. Num. Meth. Eng.*, **9**, pp.109-127.
- COSSERAT, E. and COSSERAT, F. (1909) - *Théorie des Corps Deformables*, Herman et fils, Paris.
- CRISFIELD, M.A. (1982) - 'Local instabilities in the non-linear analysis of reinforced concrete beams and slabs', *Proc. Inst. Civil. Engrs.*, **73**, Part 2, pp. 55-62.
- DUVAUT, G. and LIONS, J.L. (1972) - *Les inequations en Mécanique et en Physique*, Dunod, Paris.
- ERINGEN, A.C. and SUHUBI, E.S. (1975) - *Elastodynamics*, Vol.II, Academic Press, New York.
- GUNTHER, W. (1958) - Zur Statik und Kinematik des Cosseratschen Kontinuums, *Abh. Braunschweig. Wiss. Ges.*, **10**, pp. 195-213.
- HILL, R. (1958) - A general theory of uniqueness and stability in elastic-plastic solids, *J. Mech. Phys. Solids*, **6**, pp. 236-249.
- HILL, R. (1962) - Acceleration waves in solids, *J. Mech. Phys. Solids*, **10**, pp. 1-16.
- HOFF, C., HUGHES, T.J.R., HULBERT, G. and PAHL, P.J. (1989) - Extended comparison of the Hilber-Hughes-Taylor  $\alpha$ -method and the  $\Theta_1$ -method, *Comp. Meth. Appl. Mech. Eng.*, **76**, pp. 87-93.
- HUERTA, A., PJAUDIER-CABOT, G. and BODE, L. (1992) - 'ALE formulation in nonlocal strain softening solids', *Proc. Conf. on Computational Plasticity, Fundamentals and Applications, Part II*, Eds. D.R.J. Owen, E. Oñate and E. Hinton, Pineridge Press, Swansea, pp. 2249-2268.
- HUGHES, T.J.R. (1987) - *The finite element method - Linear static and dynamic finite element analysis*, Prentice-Hall, New Jersey.
- KORMELING, H.A. (1986) - *Strain rate and temperature behaviour of steel fibre concrete in tension*, Dissertation, Delft University of Technology, Delft.
- LARSSON, R. (1990) - *Numerical simulation of plastic localization*, Dissertation, Chalmers University of Technology, Göteborg.
- LASRY, D. and BELYTSCHKO, T. (1988) - Localization limiters in transient problems, *Int. J. Solids Structures*, **24**, pp. 581-597.
- LORET, B. and PREVOST, J.H. (1990) - Dynamic strain localization in elasto-(visco-)plastic

- solids, Part 1. General formulation and one-dimensional examples, *Comp. Meth. Appl. Mech. Eng.*, **83**, pp. 247-273.
- MINDLIN, R.D. (1963) - Influence of couple-stress on stress concentrations, *Exp. Mech.*, **3**, 1-7.
- MINDLIN, R.D. (1964) - Microstructure in linear elasticity, *Arch. Ration. Mech. Anal.*, **16**, 51-78.
- MUHLHAUS, H.-B. and VARDOULAKIS, I. (1987) - The thickness of shear bands in granular materials, *Géotechnique*. **37**, 271-283.
- MUHLHAUS, H.-B. and TRIANTAFYLIDIS, Th. (1987) - 'Surface waves in a layered half-space with bending stiffness', *Developments in Geotechnical Engineering*, Ed. A.S. Cakmak, Elsevier and CMP, Amsterdam, pp. 277-290.
- MUHLHAUS, H.-B. (1988) - 'Lamination phenomena in prestressed rock', *Preprints 2nd Int. Symp. on Rockbursts and Seismicity in Mines*, University of Minnesota, Minneapolis, pp. 117-128.
- MUHLHAUS, H.-B. (1989) - Application of Cosserat theory in numerical solutions of limit load problems, *Ing.-Arch.*, **59**, 124-137.
- MUHLHAUS, H.-B. (1990) - 'Continuum models for layered and blocky rock', *Comprehensive Rock Engineering, Vol. 2: Analysis & Design Methods*, Pergamon Press, Oxford.
- MUHLHAUS, H.-B., BORST, R. de and AIFANTIS, E.C. (1991) - 'Constitutive models and numerical analyses for inelastic materials with microstructure', *Proc. Seventh Conf. Int. Assoc. Comp. Methods and Advances in Geomechanics*, Eds. G. Beer, J.R. Booker and J.P. Carter, Balkema, Rotterdam and Boston, pp.377-386.
- MUHLHAUS, H.-B. and AIFANTIS, E.C. (1991) - A variational principle for gradient plasticity, *Int. J. Solids Structures*, **28**, pp. 845-858.
- NEEDLEMAN, A. (1988) - Material rate dependence and mesh sensitivity on localisation problems, *Comp. Meth. Appl. Mech. Eng.*, **67**, pp. 69-86.
- NEEDLEMAN, A. and ORTIZ, M. (1991) - Effect of boundaries and interfaces on shear-band localization, *Int. J. Solids Structures*, **28**, pp. 859-878.
- ORTIZ, M. and SIMO, J. (1986) - An analysis of a new class of integration algorithms for elastoplastic constitutive equations, *Int. J. Num. Meth. Eng.*, **23**, pp. 353-366.
- ORTIZ, M. and QUIGLEY, J.J. (1991) - Adaptive mesh refinement in strain localization problems, *Comp. Meth. Appl. Mech. Eng.*, **90**, pp. 781-804.
- OWEN, D.R.J. and DAMJANIC, F. (1982) - 'Viscoplastic analysis of solids : stability considerations', *Recent Advances in Non-linear Computational Mechanics*, Eds. E. Hinton, D.R.J. Owen and C. Taylor, Pineridge Press Ltd., Swansea, pp. 225-253.
- PAMIN, J. and BORST, R. de (1992) - 'A rectangular element for gradient plasticity', *Proc. Conf. on Computational Plasticity, Fundamentals and Applications, Part II*, Eds. D.R.J. Owen, E. Oñate and E. Hinton, Pineridge Press, Swansea, pp. 2009-2020.
- PERZYNA, P. (1966) - 'Fundamental problems in viscoplasticity', *Recent Advances in Applied Mechanics*, Academic Press, New York, **9**, pp. 243-377.

- PJAUDIER-CABOT, G. and BAZANT, Z.P. (1987) - Nonlocal damage theory, *ASCE J. Eng. Mech.*, **113**, pp. 1512-1533.
- READ, H.E. and HEGEMIER, G.A. (1984) - Strain softening of rock, soil and concrete - A review article, *Mech. of Mat.*, **3**, pp. 271-294.
- RICE, J.R. (1976) - 'The localization of plastic deformation', *Theoretical and Applied Mechanics*, Ed. W.T. Koiter, North Holland Publishing Company, Amsterdam, 207-220.
- RIKS, E. (1979) - An incremental approach to the solution of snapping and buckling problems, *Int. J. Solids Structures*, **15**, pp. 529-551.
- ROTS, J.G. (1988) - *Computational modeling of concrete fracture*, Dissertation, Delft University of Technology, Delft.
- RUDNICKI, J.W. and RICE, J.R. (1975) - Conditions for the localization of deformation in pressure-sensitive dilatant solids, *J. Mech. Phys. Solids*, **23**, pp. 371-394.
- RUNESSON, K., OTTOSEN, N.S. and PERIC, D. (1991) - Discontinuous bifurcations of elastic-plastic solutions at plane-stress and plane-strain, *Int. J. Plast.*, **7**, pp. 99-121.
- SANDLER, I.S. (1984) - Strain softening for static and dynamic problems, *Constitutive Equations - Macro and Computational Aspects - ASME*, pp. 217-231.
- SCHAEFER, H. (1962) - 'Versuch einer Elastizitätstheorie des zweidimensionalen ebenen Cosserat-Kontinuums', *Miszellaneen der Angewandten Mechanik*, Ed. M. Schäfer, Akademie-Verlag, Berlin, pp. 277-292.
- SCHREYER, H.L. and CHEN, Z. (1986) - One-dimensional softening with localization, *J. Appl. Mech.*, **53**, pp. 791-979.
- SIMO, J.C., KENNEDY, J.G. and GOVINDJEE, S. (1988) - Non-smooth multisurface plasticity and visco-plasticity - Loading/unloading conditions and numerical algorithms. *Int. J. Num. Meth. Eng.*, **26**, pp. 2161-2185.
- SIMO, J. (1989) - 'Strain-softening and dissipation : a unification of approaches', *Cracking and Damage: Strain Localization and Size Effect*, Eds. J. Mazars and Z.P. Bažant, Elsevier, London-New York, pp. 440-461.
- SLUYS, L.J. (1989) - *Numerical analyses of impact tensile tests on concrete*, TU-Delft report nr.25.2-89-5-15, Delft.
- SLUYS, L.J. (1990) - *Localisation in a Cosserat continuum under dynamic loading conditions*, TU-Delft report nr.25.2.90.5.15, Delft.
- SLUYS, L.J. and BORST, R. de (1991) - 'Solution methods for localisation in fracture dynamics', *Proc. Conf. on Fracture Processes in Concrete, Rock and Ceramics*, Eds. J. van Mier, J.G. Rots and A. Bakker, Chapman and Hall, London, pp. 661-671.
- SLUYS, L.J., BORST, R. de and MUHLHAUS, H.-B (1991) - 'Wave propagation and localisation in a gradient-dependent elastic plastic solid', *Proc. 4th. Int. Conf. on Nonlinear Eng. Comp.*, Eds. N. Bičanić, P. Marović, D.R.J. Owen, V. Jović and A. Mihanović, Pineridge Press, Swansea, pp. 287-297.
- SLUYS, L.J. and BORST, R. de (1992) - Wave propagation and localisation in a rate-dependent cracked medium: Model formulation and one-dimensional examples, *Int. J. Solids*

- Structures*, to appear.
- STEINMANN, P. and WILLAM, K. (1991) - 'Localisation within the framework of micro-polar elasto-plasticity', *Advances in continuum mechanics*, Eds. V. Mannl, O. Brueller, and J. Najjar, Springer Verlag Berlin, pp. 296-313.
- THOMAS, R.M. and GLADWELL, I. (1988) - Variable-order variable step algorithms for second-order systems, Part 1 : the methods, *Int. J. Num. Meth. Eng.*, **26** , pp. 39-53.
- VALANIS, K.C. (1985) - On the uniqueness of solution of the initial value problem in softening materials, *J. Appl. Mech.*, **52** , pp. 649-653.
- VARDOULAKIS, I. (1989) - Shear-banding and liquefaction in granular materials on the basis of a Cosserat continuum theory, *Ing.-Arch.*, **59** , pp. 106-113.
- WEERHEIJM, J. and REINHARDT, H.W. (1989) - 'Concrete in impact tensile tests', *Proc. First Int. Conf. on Struct. under Shock and Impact*, Cambridge Massachusetts, pp. 29-40.
- WEERHEIJM, J. (1991) - *Properties of concrete under dynamic loading 4, the uniaxial impact tensile test*, PML report nr.91, Rijswijk.
- WHITHAM, G.B. (1974) - *Linear and nonlinear waves*, John Wiley and Sons, New York-London-Sydney-Toronto.
- WILLAM, K.J. (1984) - 'Experimental and computational aspects of concrete failure', *Proc. Int. Conf. Computer Aided Analysis and Design of Concrete Structures*, Eds. F. Damjanić et al., Pineridge Press, Swansea, pp. 33-70.
- WU, F.H. and FREUND, L.B. (1984) - Deformation trapping due to thermoplastic instability in one-dimensional wave propagation, *J. Mech. Phys. Solids*, **32(2)** , pp. 119-132.
- ZIELINSKI, A.J. (1982) - *Fracture of concrete and mortar under uniaxial impact tensile loading*, Dissertation, Delft University of Technology, Delft.
- ZBIB, H.M. and AIFANTIS, E.C. (1988) - On the localization and postlocalization behavior of plastic deformation, I,II,III, *Res Mechanica*, **23** , pp. 261-277, 279-292, 293-305.



## SUMMARY

Localisation of deformation refers to the occurrence of small regions in a structure in which all deformation localises while the remaining part of a structure unloads. This is observed for a wide range of engineering materials including metals, polymers, soils, concrete and rock. In this thesis we address the fundamental issue of developing models for the softening solid that admit localisation of deformation while preserving well-posedness of the initial value problem. This is essential for a proper computational modelling of failure without a spurious influence of the finite element discretisation. Wave propagation problems have been considered, in which wave reflection on the localisation zone and behaviour of waves in the localisation zone are important phenomena.

The occurrence of strain softening causes all further deformation to localise in small bands, which are often a precursor to failure. In Chapter 3 the basic deficiencies of the use of a strain-softening model in the framework of a classical, rate-independent continuum have been discussed. The classical model does not result in a well-posed initial value problem because the field equations lose hyperbolicity at the onset of localisation. Consequently, the strain-softening region becomes elliptic, in which waves with imaginary wave speeds do not propagate (standing waves), while in the remaining hyperbolic part of the structure waves normally propagate. An analytical and numerical solution of a strain-softening bar shows the physically meaningless solution for the localisation zone. Analytically a solution with a localisation band of zero thickness with spurious wave reflection and without energy consumption is calculated, while numerically this solution cannot be captured but is approached upon mesh refinement. This results in a severe dependence on the finite element discretisation, which is also observed for cracking (mode-I localisation) in an impact tensile test on a double-notched specimen and for the formation of a shear band (mode-II localisation) in a biaxial test. In these two-dimensional simulations another severe observation is the dependence of the direction of crack or shear band propagation on the orientation of the mesh lines (mesh alignment). Mesh sensitivity with respect to fineness and alignment is caused by the ill-posedness of the initial value problem. A well-posed problem for the strain-softening solid is needed, in which a length scale parameter preserves the necessary spatial interaction in the localisation zone and in which a dispersion property provides the ability to transform waves into stationary localisation waves.

In the remaining part of the thesis continuum descriptions of the softening solid have been treated which satisfy the abovementioned requirements. The incorporation of extra or higher-order terms in the continuum models conditionally solves the basic deficiencies of the classical continuum model for strain softening.

Chapter 4 treats the inclusion of rate-effects in a smeared crack model as a first regularisation technique to properly capture zones of highly localised deformation. The incorporation of a first-order time derivative term in the constitutive equations prevents the field equations

from becoming elliptic. Dispersive waves are attenuated exponentially in the localisation zone to an extent which is determined by an implicit length scale parameter. The discretisation of the one-dimensional strain-softening bar has no influence on the numerical outcome. Furthermore, the analysis with the double-notched specimen shows a crack band in which the strain localisation is not aligned with the mesh. The calculated response has been compared with experimental data and the additional viscosity parameter was determined in a semi-inverse manner.

In Chapter 5 we have discussed the enrichment of the strain-softening continuum with a second-order gradient term of the equivalent plastic strain. Waves propagate in a dispersive manner through the gradient-dependent medium. By means of a dispersion analysis it was demonstrated that the travelling wave can be transformed into a stationary harmonic wave, of which the wave length represents the width of the localisation zone. Mesh-objective results have been obtained for mode-I localisation (one-dimensional bar) and mode-II localisation (biaxial test). In the latter example the direction of propagation of the shear band complies with the analytical predicted direction and is not influenced by the mesh lines.

In Chapter 6 the inclusion of rate dependence has been done for a plasticity model (viscoplastic model) in order to simulate mode-II localisation. The viscoplastic models according to Perzyna and to Duvaut and Lions give objective results when the fineness of the discretisation has been varied for a one-dimensional shear layer and for the biaxial test. Mesh-alignment problems have been demonstrated to vanish when use is made of viscoplastic regularisation.

A third approach is followed in Chapter 7 and is based on the inclusion of micro-polar (Cosserat) effects. In a Cosserat continuum model extra terms, representing micro-rotations, have been added to the continuum description of the softening solid. The Cosserat continuum consists of micro-elements with a finite length, which implies the introduction of a length scale parameter. Extra rotational degrees-of-freedom have been defined in the finite element representation to take the micro-curvatures and couple stresses into account. In the Cosserat medium wave propagation is dispersive and unconventional wave types emerge such as micro-rotation waves. For an elastic shear layer the dispersive wave propagation of the shear and the micro-rotation wave has been investigated analytically and numerically and perfect agreement was obtained. A disadvantage of the Cosserat model is that it is only effective as a regularisation method for mode-II failure problems, which is due to the fact that the rotational degrees-of-freedom do not become active under mode-I loading. For the biaxial test, in which mode-I components play a role, the method is too weak and a full objectivity of the results on the discretisation cannot be obtained.



## SAMENVATTING

### GOLFVOORTPLANTING, LOKALISATIE EN DISPERSIE IN SOFTENING MATERIALEN

Lokalisatie van deformatie betekent dat in een constructie smalle zones optreden waarin alle deformatie zich lokaliseert terwijl het overblijvende deel ontlast. Dit gedrag wordt geconstateerd voor een brede klasse van materialen zoals metalen, polymeren, grond, beton en rots. In dit proefschrift houden we ons bezig met de fundamentele kwestie van de modellering van het *softening* materiaal, zodanig dat lokalisatie van deformatie wordt toegelaten terwijl het beginvoorwaardeprobleem goed gesteld blijft. Dit is essentieel voor een nette numerieke modellering van bezwijken zonder een valse invloed van de eindige elementen discretisatie. Golfvoortplantingsproblemen zijn beschouwd waarin golfreflectie op de lokalisatiezone en het gedrag van golven in de lokalisatiezone belangrijke fenomenen zijn.

Het optreden van *strain softening* zorgt ervoor dat alle deformatie lokaliseert in smalle banden, wat een inleiding is tot bezwijken. In Hoofdstuk 3 zijn de fundamentele tekortkomingen van het gebruik van een strain softening model in het raamwerk van een klassiek reksnelheidsonafhankelijk continuüm besproken. Het klassieke model resulteert niet in een goed gesteld probleem omdat de veldvergelijkingen hyperboliciteit verliezen op het moment dat lokalisatie optreedt. Als gevolg hiervan wordt de strain softening zone elliptisch, waarbinnen golven met imaginaire golfsnelheden zich niet kunnen voortplanten (staande golven), terwijl in het overblijvende hyperbolische deel van de constructie golven zich gewoon voortplanten. Een analytische en numerieke oplossing van een strain softening staaf laat een oplossing voor de lokalisatiezone zien die fysisch geen betekenis heeft. Analytisch wordt een oplossing gevonden voor de lokalisatieband met een breedte nul, een valse golfreflectie en geen energieconsumptie, terwijl numeriek deze oplossing niet kan worden beschreven maar slechts kan worden benaderd bij verfijning van het elementennet. Dit resulteert in een ernstige afhankelijkheid van de eindige elementen discretisatie, welke ook wordt geconstateerd voor scheurvorming (mode-I lokalisatie) in een dynamische trekproef op een proefstuk met een dubbele zaagsnede en voor de formatie van een afschuifband (mode-II lokalisatie) in een biaxiaaltest. In deze twee-dimensionale simulaties is een ander ernstig probleem de afhankelijkheid van de richting van voortplanting van de scheur of de afschuifband van de orientatie van de mesh lijnen (*mesh alignment*). De gevoeligheid van de resultaten met betrekking tot de fijnheid en de orientatie van de eindige elementen wordt veroorzaakt door de slecht gesteldheid van het beginvoorwaardeprobleem. Een goed gesteld probleem voor het strain softening medium is vereist waarin een lengteschaalparameter zorgt voor de noodzakelijke ruimtelijke interactie in de lokalisatiezone en waarin de dispersie-eigenschap de mogelijkheid biedt golven te transformeren in stationaire lokalisatiegolven.

In de rest van het proefschrift worden continuïmbeschrijvingen van het softening medium behandeld die voldoen aan de bovengestelde eisen. Het meenemen van extra of hogere-orde termen in de continuïmmodellen lost voorwaardelijk de fundamentele tekortkomingen van het klassieke continuïmmodel voor strain softening op.

Hoofdstuk 4 behandelt het meenemen van snelheidseffecten in een uitgesmeerd scheurenmodel als een eerste regularisatietechniek om op nette wijze zones met een sterk gelokaliseerde deformatie te kunnen beschrijven. Door de eerste-orde tijdsafgeleide mee te nemen in de constitutieve vergelijkingen wordt voorkomen dat de veldvergelijkingen elliptisch worden. Dispersieve golven worden exponentieel gedempt in de lokalisatie zone in een mate die bepaald wordt door een impliciete lengteschaalparameter. De discretisatie van de één-dimensionale strain softening staaf heeft geen invloed op de numerieke uitkomst. Bovendien laat de analyse met het proefstuk met een dubbele zaagsnede zien dat de scheurband niet gelijkgericht is met het elementennet. De berekende respons is vergeleken met experimentele data en de additionele viscositeitsparameter is op een semi-inverse manier bepaald.

In Hoofdstuk 5 behandelen we de verrijking van het strain softening continuïm met een term die afhankelijk is van de tweede-orde gradient van de equivalente plastische rek. Golven planten zich op dispersieve wijze voort door het gradientafhankelijke continuïm. Met behulp van een dispersieanalyse is aangetoond dat lopende golven kunnen worden getransformeerd in een stationaire harmonische golf, waarvan de golflengte overeenkomt met de breedte van de lokalisatiezone. Objectieve resultaten met betrekking tot de keuze van het elementennet zijn verkregen voor mode-I lokalisatie (één-dimensionale staaf) en mode-II lokalisatie (biaxiaaltest). In het laatste voorbeeld komt de richting van voortplanting van de afschuifband overeen met de analytisch voorspelde richting en wordt niet beïnvloed door de lijnen van het elementennet.

In Hoofdstuk 6 is het verdisconteren van snelheidsafhankelijkheid toegepast op een plasticiteitsmodel (viskoplastisch model) om mode-II lokalisatie te simuleren. De viskoplastische modellen volgens Perzyna en Duvaut-Lions geven objectieve resultaten wanneer de fijnheid van de eindige elementen discretisatie wordt gevarieerd, zowel voor de één-dimensionale afschuiffiger als voor de biaxiaaltest. Er is aangetoond dat mesh-alignment problemen verdwijnen wanneer gebruik wordt gemaakt van viskoplastische regularisatie.

Een derde aanpak is gevolgd in Hoofdstuk 7 en is gebaseerd op het meenemen van micro-polaire (Cosserat) effecten. In een Cosserat continuïmmodel zijn extra termen, die de micro-rotaties voorstellen, toegevoegd aan de continuïmbeschrijving van het softening medium. Het Cosserat continuïm bestaat uit micro-elementen met een eindige afmeting, wat de introductie van een lengteschaalparameter impliceert. Extra rotatievrijheidsgraden zijn gedefinieerd in de eindige elementen beschrijving om micro-krommingen en koppel-spanningen mee te nemen. In het Cosserat medium is golfvoortplanting dispersief en blijken zich onconventionele golftypes voor te doen, zoals micro-rotatiegolven. Voor een elastische afschuiffiger is de dispersieve golfvoortplanting van de afschuif- en micro-rotatiegolf analytisch en numeriek

onderzocht en is volledige overeenstemming verkregen. Een nadeel van het Cosserat model is dat het alleen succesvol is als regularisatiemethode voor mode-II lokalisatieproblemen, wat een gevolg is van het feit dat de rotatievrijheidsgraden niet actief worden onder mode-I belasting. Voor de biaxiaaltest, waarin mode-I componenten een rol spelen, is de methode te zwak en een volledige objectiviteit van de resultaten met betrekking tot de discretisatie kan niet worden verkregen.



---

## CURRICULUM VITAE

Naam	Lambertus Johannes Sluys
23 december 1964	Geboren te Schoonhoven.
sept. 1977-juni 1983	St. Antonius College te Gouda, afgesloten met VWO-B diploma.
sept. 1983-juli 1988	Studie Civiele Techniek aan de Technische Universiteit te Delft. Onderwerp van het afstudeerproject : niet-lineaire dynamica. Aan dit werk is de Studieprij van de Betonvereniging toegekend.
dec. 1986-juli 1988	Student-assistent bij de vakgroep Mechanica en Constructies.
aug. 1988-juni 1992	Assistent-in-Opleiding aan de Technische Universiteit te Delft, Faculteit der Civiele Techniek. Samenwerkingsproject met het Prins Mauritslaboratorium van TNO.